



HAL
open science

Silicon Nanowires for Photovoltaics : from the Material to the Device

Alienor Togonal

► **To cite this version:**

Alienor Togonal. Silicon Nanowires for Photovoltaics : from the Material to the Device. Micro and nanotechnologies/Microelectronics. Université Paris Saclay (COMUE); Nanyang Technological University (Singapour), 2016. English. NNT : 2016SACLX032 . tel-01496838

HAL Id: tel-01496838

<https://pastel.hal.science/tel-01496838>

Submitted on 27 Mar 2017

HAL is a multi-disciplinary open access archive for the deposit and dissemination of scientific research documents, whether they are published or not. The documents may come from teaching and research institutions in France or abroad, or from public or private research centers.

L'archive ouverte pluridisciplinaire **HAL**, est destinée au dépôt et à la diffusion de documents scientifiques de niveau recherche, publiés ou non, émanant des établissements d'enseignement et de recherche français ou étrangers, des laboratoires publics ou privés.

NNT : 2016SACLX032



THESE DE DOCTORAT
DE
L'UNIVERSITE PARIS-SACLAY
PREPAREE A
L'ÉCOLE POLYTECHNIQUE

ÉCOLE DOCTORALE N° 573
Interfaces : approches interdisciplinaires, fondements, applications et innovation
School of Electrical & Electronic Engineering

Spécialité de doctorat: Physique

Par

Mme Aliénor Togonal

Silicon Nanowires for Photovoltaics: from the Material to the Device

Thèse présentée et soutenue à L'Ecole Polytechnique, le 20 Avril 2016 :

Composition du Jury :

Mr Zhang Qing	Professeur, Nanyang Technological University	Président du jury
Mr Wong Kin Shun Terence	Professeur Associé, Nanyang Technological University	Rapporteur
Mr Thierry Gacoin	Professeur, Ecole Polytechnique	Rapporteur
Mr Professor Ravi Silva	Professeur, University of Surrey	Rapporteur
Mr Pere Roca i Cabarrocas	Professeur, Ecole Polytechnique	Directeur de thèse
Mr Rusli	Professeur, Nanyang Technological University	Co-directeur de thèse

Equipe de Recherche / Laboratoire : LPICM & CINTRA

**Silicon Nanowires for Photovoltaics: from
the Material to the Device**

ALIENOR SVIETLANA TOGONAL

School of Electrical & Electronic Engineering

A thesis submitted to the Nanyang Technological University
in partial fulfillment of the requirement for the degree of
Doctor of Philosophy

2015

To my sunshine Pierre, my love and faithful travel and underwater buddy

*To my parents, Stéphane and Catherine Togonal, for their love, endless support
and encouragement*

Acknowledgements

Here we are: the completion of 4 years of PhD between France and Singapore... What an adventure! I have so many people to thank that have made this experience so fulfilling and fruitful.

Above all, I would like to thank my two supervisors, Prof RUSLI and Prof. Pere ROCA i CABARROCAS for offering me the opportunity to pursue this joint PhD between the Nanyang Technological University in Singapore and the Ecole Polytechnique in France. Their motivation, determination and involvement have played a key role in the establishment of this joint programme. They were both incredible mentors and thesis advisors while giving me great latitude in my PhD studies. I would like to thank Prof RUSLI for his continuous support, scientific guidance and high ethical standard. I have learnt from him the vital skills of critical thinking and technical writing. My deepest gratitude to my advisor Prof ROCA i CABARROCAS for his eternal enthusiasm, inspirational advice and immense knowledge.

I shall then thank Prof. Dominique BAILLARGEAT, the former director of CINTRA for having offered me first an internship then a PhD position at CINTRA. He was always finding arrangements so I can pursue my PhD in the best conditions. He helped me a lot to set the collaboration between France and Singapore. I would like to thank as well the new director of CINTRA, Philippe COQUET.

Then I would like to express my sincere gratitude to Martin FOLDYNA. Martin has been a friend and a research advisor. Our insightful and detailed discussions were precious to me and my research. Martin is always very enthusiastic and a science lover. I have always been impressed by his capacity to see exciting results even when my experiments failed.

Many thanks to all my collaborators for all the fun experiments and insightful discussions we share: Wang Hua CHEN (many thanks for your help with the ARCAM), Bernard GEFROY, Yvan BONNASIEUX, Denis TONDELIER, Jean-Charles VANEL, Ileana FLOREA, Antonin FEJFAR, Soumyadeep MISRA, Romain CARIOU, Igor SOBKOWICZ, Dmitri DAINEKA, Zuzana MRAZKOVA, Rasha KHOURI, Jian TANG, Zheng FAN and my colleagues from my research group in Singapore: Lining HE, Wang HAO, Hong LEI, Ari BIMO PRAKOSO and Li ZEYU.

I am also thankful to all the staff in France and Singapore for having maintained and fixed the equipments so I can work efficiently. A great thank to the N2FC team -Mohamad SHAMSUL BIN MOHAMAD, Mak FOO WAH, Irene CHIA AI LAY, Tan YEW HENG, Chong GANG YIH, Yang XIAOHONG - and the incredible LPICM team - Jérôme CHARLIAC (and his help for the sputtering system), Cyril JADAUD and Eric PAILLASSA.

I would like to thank the administrative staff from France - Laurence CORBEL, Julie DION, Carine ROGER-ROLLING, Gabriela MEDINA - and from Singapore : Jessie QI Jia, Coralie HUSINKER, Jing FEI, Chua-Goh Wei JIAN, Christina WONG Chow Pang, Karen GOH-FONG Lai Peng, FATIMAH Bte Supki and Jennifer LEE-CHUA Siok Moi.

A special thank to my dear friend Loïc, mon acolyte de thèse! Ces 4 années à Singapour n'auraient définitivement pas été les mêmes sans toi. Je me rappelle de nos

révisions acharnées afin de digérer nos milliers de pages de poly, nos galères administratives, nos fous rires, nos discussions animées (scientifiques ou pas), nos voyages, nos soirées... Que de souvenirs! Juliette, quelle bonheur de t'avoir rencontrée. Pierre et moi nous réjouissons d'avoir des amis aussi sincères. On s'est suivi tous les quatres de Singapour à Paris et j'ai hâte de découvrir la prochaine étape!

I would like to thank all my colleagues from CINTRA: Xuan Quyen DINH, Edwin TEO, Christophe COUTEAU, Heinrich DIESINGER, Aurélien OLIVIER and Sébastien PACCHINI. And of course, my fellow PhD students and friends : the CINTRA DREAM TEAM :-): What can I say about our famous coffee break, lunch, trips and party! I would like to thank Ange MAURICE, Etienne RODRIGUEZ, Mathieu COMETTO, Olivier COMETTO, Charles ALTUZARRA, Umar SALEEM, Zeineb BEN AZIZA, Christophe WILHELM, Donny LAI, Riko MADE (and their lovely wives Joyce and Ratih), Shuwen ZENG, Ouyang QUINLING, Dunlin TAN. I want also to thank all the interns from the successive batches: Philippe CASTERA, Romain DUBREUIL, Mathieu BERGONT, Agnès MESSANVI, Camille DEGARDIN, Brieux DURAND, David PEYROT, Eino PERREAU, Mathieu ECOIFFIER, Thibault LAVRIL, Aurélien KIFFER, Laurent ROS, Maxime MALNOU.

I would like to thank all my colleagues and friends from LPICM: Fatima Zahra BOUANIS, Rym BOUKHICHA, Pavel BULKIN, Jean-Luc MAURICE, Costel-Sorin COJOCARU, Marc CHAIGNEAU, Marc CHATELET, Bérengère LEBENTAL, Jean-Luc MONCEL, François SILVA, Frédéric LIEGE, Holger VACH, Enric Garcia CAUREL, Jean-François BESNIER, Lucie LEVEAU, Fluvio MICHELIS, Fatme JARDALI, Dennis LANGE, Prabal GOYAL, Ronan LEAL, Paul NARCHI, Stanislas DEBY, Alice DEFRESNE, Frederico VENTOSINOS, Angelo PIERANGELO, Salome FOREL, Benedict O'DONNELL, Alice CASTAN, Mutaz AL-GHZAIWATAT..

And now of course, I would like to thank my dear love Pierre and my incredible family. Pierre, je t'ai suivi au bout du monde et ces 4 années passées à Singapour ont été une expérience magique, tellement riche intellectuellement, culturellement et émotionnellement. Merci de m'avoir soutenue tout au long de ma thèse. Tu m'as toujours donné des conseils justes et avisés et nos discussions scientifiques ont été extrêmement précieuses à ma recherche. J'admire ton intelligence, ton esprit (ir)rationnel, ta passion pour le sport et ton humour. Tu m'as fait entrée dans ton univers du 2, 4 ou 8 roues! Merci d'avoir partagé avec moi tes passions du roller, du VTT et du voyage. Tu as ce côté rassurant et protecteur tout en ayant gardé la beauté de ton âme d'enfant, ce qui notre vie si heureuse et trépidante. Merci pour tout! Je me réjouis de passer le reste de ma vie à tes côtés...

Papa, Maman, je vous dois tant! Peu de mots peuvent exprimer tout l'amour et toute l'admiration que je vous porte. Vous m'avez offert une vie tellement riche et belle! Merci de votre soutien sans faille, morale et financier, de vos conseils avisés et de votre amour débordant. Vous avez su créer un eldorado familiale que je retrouve avec toujours autant de bonheur et de plaisir. Je chéris ces moments familiales passés à la Folie, si précieux à mon cœur. Merci pour tout! Vous m'avez insufflé la curiosité, le goût des études, le sens aigu de la famille, et surtout ce petit grain de Folie nécessaire à une vie heureuse et épanouie! Papa, merci pour tes blagues et ton humour sans fond! Maman, merci d'être ma confidente et de partager ces purs moments de complicité entre cuisine, shopping et jardinage!

Mes grandes sœurs chéries!! Merci Jéléna de m'avoir appelée si souvent à l'autre bout du monde. Je me rappelle de nos conversations téléphoniques animées,

entrecoupée des pauses "clients". Merci Srdan pour les allers-retours répétés à l'aéroport Charles de Gaulles pour venir me chercher lorsque j'arrivais ou repartais de / à Singapour! Merci à vous deux pour votre accueil toujours aussi chaleureux au sein de votre petite famille qui respire le bonheur! Un grand merci à Zlatan et Artémis pour leurs sourires ravageurs auxquels je ne peux définitivement pas résister. Et enfin un grand merci d'avoir fait de moi le témoin de votre union. Smiliana, Fred, merci d'être venus nous voir à Singapour. Pierre et moi avons été tellement heureux de pouvoir partager avec vous un peu de notre quotidien en Asie. Que de moments exceptionnels passés ensemble en Thaïlande. Je me rappelle avec nostalgie de nos nombreux fous rires, de notre nuit passée dans le train, de la balade sur dos d'éléphants, des massages musclés thaïlandais ou des poissons clowns sur le réfrigérateur. Votre fraîcheur et votre légèreté ont fait de ce voyage un moment inoubliable. Et enfin une dédicace toute spéciale à ce moment exquis où vous avez découvert notre ascenseur Parisien...

Et que dire de la bande des trois G, Guillaume et mes deux petits frères, Grégoire et Goran! Guillaume, mon mousse boy, merci de savoir me transformer en mousse à raser géante! Merci de ton soutien inconditionnel dans la préparation à mon permis, de tes conseils avisés et du temps que tu trouves toujours à me consacrer. Notre randonnée dans la montagne près de Zadar avec Pierre reste un souvenir magique. Greg, merci de ton soutien, de ta passion pour les joujoux technologiques et de ton aide lorsque je suis perdue sur mon ordinateur! Je me rappelle avec beaucoup d'humour ton coaching sur les tests logiques, pour lesquels cela te paraissait si évident. Merci à toi Emilie pour ta bonne humeur. Goran, mon p'tit loup! Merci pour ta gentillesse, tes parties interminables de risks ;p et ta passion de la stratégie militaire. Je me rappelle avec beaucoup de plaisir notre préparation simultanée au permis et nos discussions passionnantes sur le monde végétal où tu m'apprends sans cesse des faits incroyables.

Papy, Jeanine, merci pour votre gentillesse, votre accueil dans votre joli appartement de Sceaux lorsque j'arrivais sur Paris sans aucun pied à terre. Je me rappelle avec beaucoup d'émotions des moments que l'on a partagé tous les trois. Une pensée toute particulière pour toi Jeannine...

Philippe, Daniela, merci de m'avoir accueillie avec tant de naturel et de gentillesse au sein de votre famille. Les dîners en famille sont toujours un moment de complicité et de pur bonheur gustatif. Je comprends aisément d'où vient la glotonnerie de mon petit Pierre. Merci Daniela de m'avoir donné goût à l'art contemporain. J'écoute avec un bonheur toujours renouvelé vos critiques littéraires (merci pour les nombreux livres que j'ai pu vous emprunter) et cinématographiques! Philippe, merci pour votre bonne humeur, votre entrain à la recherche de noms de domaine et vos conseils toujours avisés. Je suis très fier d'arborez une adresse mail en @togonal.fr . Un immense merci également pour l'ordinateur qui m'a permis d'écrire cette thèse. Thomas, Chloé et Valentin, merci pour tous les bons moments passés ensemble sur Paris ou Annecy! Thomas, Chloé, nos futurs "vrais docteurs", merci pour toutes ces parties de jeu de société où j'ai pu admiré toute l'étendue de vos talents de bluff, notamment ceux de Chloé...Val, bon courage pour le développement de tes applications! Mais je n'ai aucun doute de ton succès car tu sais définitivement mener ta barque...

Rossana, Piero, merci pour votre accueil toujours aussi chaleureux au sein de votre jolie maison à Paris. Merci de nous avoir héberger Pierre et moi lorsque nous recherchions un appartement. Merci pour ces joyeux dîners, tellement délicieux et toujours aussi animés, entre la langue italienne et française!

I would like also to thank all the incredible friends I made in Singapore: Florian and his lovely girlfriend Florence who have always been there for me, even when I was alone in Singapore, Thomas and Cécile (and our unforgettable sport session), Sylvia, Leng, Miyuki, Mathilde, Camille, Joe, Sebastian and Jackie, Harish, Yin Teng, Manu and Aziza, Yingying, Stéphane, Samuel, Massy, Jun, Tom and Emily, JB and Jo Pei Hua, Zora, Roman, Claire, Pierre K. and everyone that I may have missed.

I would like to send my thanks and love to my dear friends from France for having been here everytime I was coming back from Singapore: my best friend Marie, my Lycée team - Anne and Anaïs - my Chimie Paris team - Laetitia, Lucie, Célia, Elodie and Emilie - my Classe Préparatoire team - Audrey, Blandine, JB, Norman, Benoît, Ariane, Malik, Rafik, Anne and Alban.

Abstract

Abstract: Silicon Nanowire (SiNW) based solar cells offer an interesting choice towards low-cost and highly efficient solar cells. Indeed solar cells based on SiNWs benefit from their outstanding optical properties such as extreme light trapping and very low reflectance. In this research project, we have fabricated disordered SiNWs using a low-cost top-down approach named the Metal-Assisted-Chemical-Etching process (MACE). The MACE process was first optimized to reduce the strong agglomeration observed at the top-end of the SiNWs by tuning the wettability properties of both the initial substrate and the SiNWs surface. By combining the MACE process with the nanosphere lithography, we have also produced ordered SiNW arrays with an accurate control over the pitch, diameter and length. The optical properties of these SiNW arrays were then investigated both theoretically and experimentally in order to identify the geometrical configuration giving the best optical performance. Disordered and ordered SiNW arrays have been integrated into two types of solar cells: heterojunction with intrinsic thin layer (HIT) and hybrid devices. SiNW based HIT devices were fabricated by RF-PECVD and the optimization of the process conditions has allowed us to reach efficiency as high as 12.9% with excellent fill factor above 80%. Hybrid solar cells based on the combination of SiNWs with an organic layer have also been studied and characterized. The possible transfer of this concept to the thin film technology is finally explored.

Keywords: "Solar cells", "Silicon Nanowires (SiNWs)", "Heterojunction with Intrinsic Thin layer (HIT)", "Hybrid", "Metal Assisted Chemical Etching (MACE)", "Agglomeration", "Optical Properties".

Titre: Nanofils de silicium pour le solaire: du matériau à la cellule photovoltaïque

Résumé: Les cellules solaires à base de nanofils de silicium offrent une alternative intéressante pour la réalisation de panneaux photovoltaïques à haut rendement et à faible coût. Elles bénéficient notamment des excellentes propriétés optiques des nanofils qui forment une surface à très faible réflectivité tout en piégeant efficacement la lumière. Dans cette thèse, nous utilisons et améliorons une méthode de gravure chimique peu coûteuse et industrialisable pour la fabrication de forêts de nanofils de silicium. En adaptant la mouillabilité du substrat et des nanofils, nous avons remédié au problème d'agglomération inhérent à cette méthode lorsqu'on veut obtenir des forêts denses et désordonnées de nanofils. En combinant cette méthode de gravure chimique à la lithographie assistée par nanosphères, nous avons pu fabriquer des réseaux ordonnés de nanofils avec un contrôle précis des propriétés géométriques (diamètre des nanofils et distance entre eux). Les propriétés optiques de ces réseaux ont été étudiées théoriquement et expérimentalement afin d'identifier les configurations optimales. Nous avons ensuite fabriqué des cellules solaires à partir de ces différents types de nanofils et deux types de structures. Le premier type, des cellules solaires HIT (Hétérojonction avec couche mince Intrinsèque) à base de nanofils de silicium, a été fabriqué par RF-PECVD. L'optimisation des conditions de dépôt plasma nous a permis d'obtenir des cellules solaires hautement performantes: rendements de 12,9% et facteurs de forme au-delà de 80%. Le second type, des cellules solaires hybrides, est basé sur la combinaison d'une couche organique et des nanofils de silicium. La caractérisation des cellules fabriquées montre des rendements prometteurs. Enfin, nous présentons des résultats préliminaires pour transférer ces concepts à une technologie couches minces.

Mots clés: "Photopiles", "Nanofils", "Silicium", "Semi-conducteurs-Attaque Chimique", "Agglomération", "Nanofils, Propriétés Optiques".

Substantial Summary in French / Résumé substantiel en français

Les cellules solaires à base de nanofils de silicium offrent une alternative intéressante pour la réalisation de panneaux photovoltaïques à haut rendement et à faible coût. Elles bénéficient notamment des excellentes propriétés optiques des nanofils qui forment une surface à très faible réflectivité tout en piégeant efficacement la lumière. Dans cette thèse, nous utilisons et améliorons une méthode de gravure chimique peu coûteuse et industrialisable pour la fabrication de forêts de nanofils de silicium. Cette méthode permet d'obtenir des forêts denses et désordonnées de nanofils sur de grandes surfaces en quelques secondes. Néanmoins, un problème inhérent à cette méthode est l'agrégation de ces nanofils qui se collent les uns aux autres et forment ainsi de larges paquets. Cette agglomération est souvent citée comme un facteur limitant pour la réalisation de cellules solaires à haute performance à base de nanofils car, en plus de dégrader les propriétés électriques et optiques du système, cela empêche également le revêtement conforme de ces nanofils par le matériau photoactif qui ne peut pénétrer entre les nanofils. Une analyse théorique des forces mises en œuvre pendant le processus de fabrication nous a permis de comprendre que l'agglomération des nanofils résulte de l'interaction entre les forces attractives et répulsives qui s'exercent sur les nanofils. Notamment, l'interaction capillaire est la principale force responsable de l'agrégation des nanofils alors que les forces de Van der Waals deviennent prévalentes lorsque l'interdistance entre les nanofils est de l'ordre du nanomètre. Cet effet est

exacerbé par l'irrégularité des structures fabriquées puisque les forces d'interaction ne se compensent pas, d'où la formation de larges agglomérats. En adaptant la mouillabilité du substrat et des nanofils, nous avons remédié au problème d'agglomération inhérent à cette méthode lorsqu'on veut obtenir des forêts denses et désordonnées de nanofils. En effet, nous avons démontré que l'ajustement des propriétés de mouillage du substrat de silicium initial permet de contrôler la densité et l'uniformité du réseau de nanofils fabriqué, tandis que modifier la mouillabilité de la surface des nanofils après leur fabrication par un traitement hydrophobe permet de réduire de manière très significative l'agglomération des nanofils de silicium. Cela nous a permis d'obtenir des forêts désordonnées de nanofils denses et uniformes avec une agglomération réduite.

Néanmoins, ce procédé de fabrication permet uniquement de contrôler la longueur des nanofils mais ne permet pas de jouer sur les autres paramètres géométriques tel que le diamètre ou l'interdistance. Ainsi, nous décidâmes de combiner cette méthode de gravure chimique à la lithographie assistée par nanosphères. Cela nous permit de fabriquer des réseaux ordonnés de nanofils avec un contrôle précis des propriétés géométriques (diamètre, interdistance et longueur des nanofils).

Dans un second temps, les propriétés optiques de ces réseaux (ordonnés et désordonnés) ont été étudiées théoriquement et expérimentalement afin d'identifier les configurations optimales. Les propriétés optiques des réseaux de nanofils dit désordonnés sont déterminées essentiellement par la longueur des nanofils. La situation est beaucoup plus complexe dans le cas des réseaux de nanofils ordonnés pour lesquels la géométrie a un effet drastique sur les propriétés optiques. Par exemple, la réflectivité moyenne sur la gamme de

longueur d'onde 400-1100 nm varie entre 3 et 20% suivant la géométrie. Cela démontre l'importance de l'optimisation des paramètres géométriques de la structure afin de maximiser le rendement des cellules solaires fabriquées. Nous avons également observé que les réseaux de nanofils ordonnés diffractaient la lumière et que la figure globale de diffraction est une superposition de figures de diffraction hexagonales provenant de différentes zones de l'échantillon ayant des orientations légèrement différentes. Nous avons ensuite modélisé ces réseaux de nanofils ordonnés par la technique RCWA (Rigorous Coupled Wave Analysis) afin de déterminer le potentiel théorique de telles structures. Pour ce faire, nous avons réalisé un grand nombre d'échantillons de réseaux de nanofils ordonnés que nous avons caractérisés. Nous avons alors comparé les résultats expérimentaux avec ceux obtenus par notre modèle. En prenant en compte les défauts inhérents de fabrication des échantillons (distribution du diamètre, de l'interdistance et de la longueur), nous avons obtenu un excellent accord entre les prédictions théoriques et expérimentales. Cela ouvre la porte vers le design et la fabrication de cellules solaires à très haute performance à base de nanofils de silicium.

Par la suite, nous avons fabriqué des cellules solaires à partir de ces différents types de nanofils (ordonné et désordonné) en les intégrant dans deux types de structures. Le premier type, des cellules solaires HIT (Hétérojonction avec couche mince Intrinsèque) à base de nanofils de silicium, a été fabriqué par RF-PECVD. Les cellules solaires HIT reposent sur une jonction p-n entre du silicium cristallin et amorphe. Cette technique, largement répandue dans l'industrie, constitue la technologie la plus performante actuellement disponible sur le marché pour des cellules solaires simple jonction à base de silicium.

L'optimisation des conditions de dépôt plasma de la couche amorphe sur le réseau de nanofils s'est révélé primordial. En effet, un dépôt trop fin ne permet pas le recouvrement conforme des nanofils de silicium, empêchant ainsi la formation de la jonction p-n uniformément à la surface des nanofils. D'un autre côté, si la couche de dépôt amorphe est trop épaisse, cette dernière joue un rôle parasite en absorbant une part importante du rayonnement lumineux. Cette lumière absorbée par la couche de silicium amorphe est alors perdue pour la cellule solaire, réduisant ainsi le courant généré par cette dernière et donc son rendement. Dans un second temps, le dopage de la couche amorphe a été étudié: un réglage fin du gradient de dopage s'est révélé nécessaire afin d'optimiser les performances des dispositifs. Enfin l'épaisseur de la couche intrinsèque, entre le silicium cristallin et la couche amorphe dopée doit être ajustée avec précision. Il faut que cette couche intrinsèque soit assez épaisse pour minimiser la résistance électrique et garantir une passivation uniforme. Ainsi une certaine épaisseur est nécessaire pour obtenir de bon facteurs de formes et tensions en circuit ouvert. Néanmoins une épaisseur trop importante de la couche intrinsèque impacte directement le transport des porteurs de charges (faible conductivité, modification des mécanismes de transport...). L'optimisation des conditions de dépôt nous a permis d'obtenir des cellules solaires hautement performantes: rendement de 12,9% et facteurs de forme au-delà de 80%. L'effet de la longueur des nanofils sur la performances des cellules solaires a également été étudié. Seuls les nanofils courts (longueur inférieure à 1 μm) sont adaptés à des applications dans le photovoltaïque, les performances se dégradant avec de longs nanofils. En effet les nanofils longs sont très difficiles à passiver par le silicium amorphe. Cette pauvre passivation a pour conséquence un nombre

important de défauts de surface qui entraînent à leur tour une durée de vie des porteurs de charges très faible et donc une dégradation des performances. Le courant généré par les cellules solaires a été cartographié par microscopie EBIC (Electron Beam Induced Current). Nous avons observé que les nanofils de silicium sont bien actifs électriquement mais ils génèrent moins de courant que le wafer sous-jacent. Cet effet devient de plus en plus important lorsque la longueur des nanofils augmente. De plus, nous avons prouvé que le principe de cellules solaires HIT à base de nanofils peut être transféré à la technologie couche mince: un rendement de 4.74% a été obtenu sur une couche mince de silicium intégrant des nanofils d'une épaisseur de 5 μm .

Le second type de structure étudié, des cellules solaires hybrides, est basé sur la combinaison d'une couche organique avec des nanofils de silicium. La première configuration étudiée consiste en des nanofils de silicium gravés sur un wafer combinés avec une couche de PEDOT:PSS. La caractérisation des cellules fabriquées montre des rendements prometteurs. En effet des rendements de l'ordre de 9-9.5% ont été obtenus pour les deux types de réseaux de nanofils (ordonné et désordonné), sans qu'aucune différence significative entre ces deux types d'échantillons n'ait été observée. Nous avons également développé une nouvelle méthode de dépôt de la couche organique, basée sur des conditions "basse pression", qui nous a permis d'améliorer significativement le revêtement conforme des nanofils de silicium par la couche de PEDOT:PSS. Cette nouvelle méthode de dépôt a le potentiel d'augmenter la surface de la jonction p-n et d'améliorer la passivation des nanofils de silicium. Enfin, nous présentons des résultats préliminaires pour transférer ces concepts à une technologie couche mince basé sur du silicium amorphe avec une technologie

type p-i-n. Le premier challenge était d'étudier faisabilité de fabriquer des réseaux de nanofils sur une couche mince de silicium amorphe déposé sur un substrat en verre. En adaptant notre procédé de fabrication, nous parvînmes à fabriquer des réseaux ordonnés et désordonnés de nanofils de silicium amorphe. La caractérisation optique de ces nanofils de silicium amorphe a permis de mettre en évidence leur capacité à booster les propriétés optiques du matériaux en réduisant de manière significative la réflectivité. Dans un second temps, nous avons étudié les performances de cellules solaires basées sur une couche mince amorphe de type-n (respectivement de type-p) avec une couche organique de type-p (respectivement de type-n). Malheureusement des cellules solaires peu performantes avec des rendements pauvres furent obtenus. Néanmoins, ces travaux ont permis de mettre en évidence une configuration extrêmement intéressante que nous avons étudiée dans une dernière partie: la possibilité de substituer la couche amorphe de type-n dans une jonction classique p-i-n par une électrode LiF/Al. Cela permet de fabriquer des jonctions de type Schottky. En exploitant ce type de configuration, nous parvînmes à obtenir des rendement élevés de l'ordre de 8.55%. Ce type de jonction constitue un procédé de fabrication simple exempt de gaz toxique tel que la phosphine.

Ce travail de thèse explore le potentiel des nanofils de silicium pour des applications dans le domaine du photovoltaïque. Nous avons réalisé et optimisé chaque étape du procédé, depuis la fabrication des nanostructures jusqu'à leur implémentation au sein de différents dispositifs, tout en réalisant une grande diversité de caractérisation structurels, électriques et optiques afin d'améliorer notre compréhension des cellules solaires à base de nanofils.

Table of content

Acknowledgements.....	7
Abstract.....	11
Substantial Summary in French / Résumé substantiel en français	13
Table of content	19
List of Acronyms:	21
List of Figures	23
List of Tables	33
Chapter 1 : Introduction.....	35
1.1 Solar energy: the Reality and the Future of Photovoltaics.....	35
1.2 PV Technologies	39
1.3 Three Categories of Solar Cells	41
1.4 Motivation, Objectives and Scope of this Thesis.....	42
1.5 Main Contributions of the Thesis.....	46
1.6 Organization of this Thesis	48
Chapter 2 : Literature review	51
2.1 Basics of Solar Cells	51
2.2 Silicon Nanowires: Methods of Fabrication and Properties.....	56
2.3 Silicon Nanowire based Solar Cells	67
2.4 Heterojunction with Intrinsic Thin Layer Solar Cells.....	81
2.5 Hybrid Solar Cells.....	88
Chapter 3 : Fabrication and Characterization Techniques.....	93
3.1 Silicon Nanowires Fabrication by Wet Etching.....	93
3.2 Fabrication of Solar Cells based on Silicon Nanowires.....	105
3.3 Characterization Techniques	115
Chapter 4 : Solving the Agglomeration Effect of Silicon Nanowires fabricated by MACE	127
4.1 Theoretical Basis	127
4.2 Investigation of the Solutions proposed in the Literature to avoid the Bundling of Silicon Nanowires.....	136
4.3 Effect of the wettability on the agglomeration of SiNWs.....	149

Chapter 5 : Optical Properties of SiNW arrays	159
5.1 Comparison between SiNWs and commercial pyramids	159
5.2 Ordered vs Disordered SiNWs: effect of the geometry	161
5.3 Effect of ITO coating	165
5.4 Angle-resolved MM polarimeter.....	169
5.5 RCWA analysis	176
5.6 Dual diameter	182
Chapter 6 : HIT Solar Cells based on SiNWs.....	187
6.1 Understanding the Challenge and Complexity of HIT Solar Cells based on SiNWs.....	187
6.2 Fabrication, Optimization and Characterization of HIT Solar Cells based on random SiNWs.....	189
6.3 Comparison between Ordered and Disordered SiNWs.....	217
Chapter 7 : Hybrid Solar Cells based on SiNWs and Advanced Concepts ..	237
7.1 Hybrid Solar cells based on Disordered and Ordered SiNWs	237
7.2 Hybrid Solar Cells based on amorphous thin films.....	247
7.3 LiF/Al as a back contact for thin film solar cells based on a-Si:H....	256
Chapter 8 : Conclusion and Future Work	269
8.1 Achievements:.....	269
8.2 Future Work	270
References:.....	273
List of Publications	287

List of Acronyms:

AOI	Angle of Incidence
ARMMP	Angle-resolved MM polarimeter
a-Si:H	hydrogenated amorphous silicon
EBIC	Electron Beam Induced Current
c-Si	crystalline silicon
$d_{a-Si:H}$	overall thickness of a-Si:H
DI	Deionized
DMSO	Dimethyl Sulfoxide
EQE	External Quantum Efficiency
H	Solar cell efficiency
FF	Fill Factor
Γ	Interfacial tension
HIT	Heterojunction with Intrinsic Thin layer
HOMO	Highest Occupied Molecular Orbital
IPA	Isopropyl Alcohol
ITO	Indium Tin Oxide
J_{sc}	Short Circuit Current
LPAD	Low-Pressure-Assisted-Deposition
LUMO	Lowest Unoccupied Molecular Orbital
MACE	Metal Assisted Chemical Etching
NSL	Nano-Sphere Lithography
NW	Nanowire
PECVD	Plasma Enhanced Chemical Vapor Deposition
PEDOT:PSS	Poly(3,4-ethylenedioxythiophene):Polystyrene Sulfonate
PS	Polystyrene
PV	Photovoltaic
RCWA	Rigorous Coupled Wave Analysis
RF	Radio-Frequency
RIE	Reactive Ion Etching
R_{series}	Series Resistance
R_{shunt}	Shunt Resistance

SCR	Space Charge Region
SEM	Scanning Electron Microscopy
SiNWs	Silicon Nanowires
TRMC	Time Resolved Microwave Conductivity
TEM	Transmission Electron Microscopy
VLS	Vapor-Liquid-Solid
V_{oc}	Open Circuit Voltage

List of Figures

Figure 1-1: Global and regional cumulative capacity in Megawatt (MW) [4].	36
Figure 1-2: TOP 10 countries in 2014 for cumulative installed capacity [4].	37
Figure 1-3: TOP 10 countries in 2014 for annual installed capacity [4].	38
Figure 1-4: Timeline of the best research cell efficiencies for the different PV technologies [19].	41
Figure 1-5: Illustration of the light trapping effect of SiNWs. This light trapping effect by SiNWs is directly visible with the eye as shown by the back color of SiNWs sample compared to the shiny grey aspect of the planar reference sample. It shows that the light is effectively trapped within the SiNWs.	43
Figure 2-1: (a) Diffusion current at the interface between the p-type and n-type semiconductor in order to equalize the concentration of holes (white circle) and electrons (black circles). The green positive sign symbolize the phosphorus cations and the red negative sign symbolizes the boron anion which are doping the semiconductors.(b) Formation of the space charge region, depleted in charge carriers. The phosphorus and boron dopants create an internal electric field at the p-n junction.	53
Figure 2-2: Equivalent circuit model of a solar cell [39].	55
Figure 2-3: (I,V) curve of a solar cell and definition of the photovoltaic parameters [40].	56
Figure 2-4: Scheme of the VLS Vapor Liquid Solid process [54].	58
Figure 2-5: Mechanism of formation of SiNW by the MACE process. A silicon substrate is dipped in HF/AgNO ₃ solution [61], [62].	60
Figure 2-6: SEM picture of 10 μm SiNWs fabricated by MACE showing the strong agglomeration at the top-end of the SiNWs.	61
Figure 2-7: Reflectance measurement of porous (PSi), polished c-Si and SiNW arrays [26], [27].	62
Figure 2-8: Advantages and drawbacks of the radial, axial and substrate junctions [68].	68
Figure 2-9: Schematic representation of the atomic structure of crystalline silicon (a) and hydrogenated amorphous silicon (b). For c-Si, every Si atom is linked to four other Si atoms and the overall structure is long range ordered. For amorphous silicon, only a short range order is visible because of variation in the angle and length of covalent bonds. Many coordination defects which are not passivated by hydrogen are present within the structure [121].	82
Figure 2-10: Schematic representation of the band diagram of crystalline silicon (a) and hydrogenated amorphous silicon (b). In a perfect crystal, the band gap is well defined and $E_g = E_v - E_c$. Blue color represents states with delocalized wavefunctions. For a-Si:H states are present within the band gap. Orange and purple colors represent the localized wavefunctions, responsible for the reduced mobility properties of a-Si:H. Defects states are due to the dangling bonds defects and tail states are induced by bonding distortion [121].	83
Figure 2-11: Schematics of a standard HIT heterojunction solar cell [125].	85

Figure 2-12: Schematics of the band diagram of a HIT for a n-type c-Si [126].	86
Figure 2-13: Schematic of a HIT structure based on SiNWs. The n-type c-Si wafer has been nanostructured to improve light trapping	88
Figure 2-14: Schematic representation of an ideal nanostructure hybrid silicon/organic material solar cell. The nanowires offer a continuous conductive path to the electrode. L_{exc} is the diffusion length of the exciton. The nanowires are separated by a distance of about $2L_{exc}$, in order to reduce loss in photocurrent due to exciton recombination.	90
Figure 3-1: Schematics of the nanosphere lithography method coupled with the MACE process	94
Figure 3-2: (a) SEM picture of silver dendrites covering the SiNW prior the HNO_3 chemical bath [142], (b) cross-section SEM picture of 30 μm long random SiNWs, (c) inclined (15°) SEM picture of 5 μm long random SiNWs, and (d) inclined (30°) SEM picture of 5 μm long SiNWs.	95
Figure 3-3: Schematics of the nanosphere lithography method coupled with the MACE process	96
Figure 3-4: Schematics of the floating-transferring technique to achieve an hexagonal compact arrangement of PS spheres on a silicon substrate [143].	97
Figure 3-5: (a) Schematics of the flotation capillary forces, the driving force for the self-assembly of the PS spheres [147]. (b) Photograph of the monolayer obtained onto the water surface.	98
Figure 3-6: Photograph of the "transfer" stage where the silicon substrate is placed below the PS monolayer and dragged upward to coat the sample by the PS suspension.	99
Figure 3-7: (a) Photograph of the Si substrate covered by a monolayer of PS spheres. (b) Low-magnification SEM image of perfectly ordered PS spheres arranged into an hexagonal compact arrangement. (c)) High-magnification SEM pictures of perfectly ordered PS spheres arranged into an hexagonal compact arrangement. (d) SEM picture of the PS film showing that the film is not uniform everywhere. Small domains coexist with different orientations.	100
Figure 3-8: Schematics illustrating the effect of the plasma etching treatment on the PS spheres.	101
Figure 3-9: SEM picture of (a) slightly annealed PS spheres. The red circles shows the small area melted. (b) Overheated PS spheres causing the excessive melting of the colloidal particles.	101
Figure 3-10: The etch rate of the PS spheres with initial nominal diameter of 500 nm, 600 nm and 800 nm by oxygen plasma as a function of time.	102
Figure 3-11: SEM picture of the PS spheres arrays after 130s of oxygen plasma treatment. The PS spheres are separated from each other. The initial diameter of PS spheres of 600 nm was reduced down to 392 nm.	103
Figure 3-12: SEM pictures of PS sphere arrays covered by a 25 nm gold thin film.	103
Figure 3-13: (a) SEM pictures of the gold etching mask after the removal of the PS spheres. (b) SEM pictures of SiNWs arrays where the removal stage of PS spheres has been carried out at	

the last step of the process. The PS spheres are not effectively removed since they are trapped inside the nanostructure.	104
Figure 3-14: (a) SEM pictures of (a) high density SiNWs ordered arrays (inclined 30°) samples with 800 nm pitch , (b) low density SiNWs ordered arrays (inclined 30°) with 800 nm pitch, (c) cross section of short SiNWs, and (d) cross section of long SiNWs.	105
Figure 3-15: Schematics illustrating the voltage distribution of a plasma in the case of asymmetric electrodes [148].	108
Figure 3-16: The Paschen curve showing the breakdown voltage as a function of the product of the pressure p with the interdistance between the electrodes d [152].	111
Figure 3-17: Photographs of the (a) ARCAM chamber and (b) ARCAM control panel	112
Figure 3-18: (a) Schematics [154] and (b) corresponding photograph of the e-beam evaporator.	113
Figure 3-19: (a) Schematics [155] and (b) photograph of the sputtering system. (c) O ₂ :Ar plasma during the ITO deposition.	114
Figure 3-20: Schematics illustrating the key steps of the spin coating technique [156].	114
Figure 3-21: The ideal and typical EQE response of a silicon solar cell from www.pveducation.org	116
Figure 3-22: Schematics of TRMC experimental set up [169].	119
Figure 3-23: (a) Schematics of the EBIC set up [178] and (b) photograph of the EBIC equipment.	121
Figure 3-24: Schematics and photograph of the UV/Vis/NIR spectrophotometer (PerkinElmer) using an integrating sphere.	122
Figure 3-25: Schematics illustrating the working principle of Mueller matrix ellipsometer	123
Figure 3-26: Schematics showing the working principle of the Angle-resolved MM polarimeter [179].	124
Figure 4-1: Schematic representation of two cylinders of the same length L and radii R , separated by a distance d and partially immersed in a liquid. Once the water level falls below the tip of the cylinders during the drying process, the surface tension of the liquid/vapor interface γ_{LV} induces a small curvature of the solvent to reduce the active surface area	128
Figure 4-2: Schematic illustration of the forces acting on two SiNWs partially immersed in a liquid. The bending of the SiNWs stems from a balance between the Van der Waals (F_{vdW}) and the surface tension (F_{ST}) attractive forces and the repulsive elastic deformation force F_{ED} . γ_{LV} is the surface tension which characterizes the liquid/vapor interface. δ is the deflection of the NW.	131
Figure 4-3: Schematic model of an array composed of three 2 μ m long-nanowires labeled 1, 2 and 3. Definition of the original geometry- the ideal case (a). Definition of the forces: F_{XY} is the force exerted by SiNW #X on SiNW #Y (b). Definition of the equilibrium position before (nanowire in dotted lines) and after bending (c).	133
Figure 4-4: Equilibrium position of SiNW #2 as function of its initial position. When the interspacing Δ between two nanowires in the array is short, any minor irregularity ($X/\Delta > 0.2$	

or $X/\Delta < -0.2$) lead to adhesion of the nanowires ($X_{eq}/\Delta = 1/-1$) whereas for larger nanowires-interspacing Δ , adhesion occurs for larger irregularities ($X/\Delta > 0.6$ or $X/\Delta < -0.6$).....	134
Figure 4-5: Effect of the length on the Van der Waals, capillary and elastic deformation forces	135
Figure 4-6: (a) Schematic detailing the fabrication process of agglomerated and tapered SiNWs. (b) Schematic showing the effect of KOH post-etching treatment to taper the top-ends of SiNWs [186], [193]	138
Figure 4-7: (a) Cross-section SEM images of the SiNW array after MACE with a scale bar of 10 μm . Inclined (30°) SEM images showing the effect of KOH post-etching treatment on the morphology of SiNWs as a function of the etching time: (b) 0 s, (c) 30 s, (d) 60 s, (e) 120 s, and (f) 240 s. Scale bars in (b)–(f) are 5 μm [186], [193].	139
Figure 4-8: Schematic illustrating the principle of strengthen mechanically the nanowires by a polymer.....	141
Figure 4-9: SEM pictures of SiNWs arrays (a) before and (b) after the replacement of solvent.	143
Figure 4-10: Effect of KOH post-treatment on the morphology of SiNWs for different time of treatment and for different magnification.	145
Figure 4-11: Effect of power on the etching of SiNWs (a) At 100 Watt, the SiNWs collapse and lied on the wafer. (b) At 200 Watt, the SiNWs are completely etched away.	147
Figure 4-12: SEM pictures of SiNWs arrays (a) before and (b) after RIE post-treatment.....	148
Figure 4-13: SiNWs array (a) before and (b) after CO ₂ supercritical drying process.....	149
Figure 4-14: Top view (a), (b) and cross-section (c), (d) SEM pictures: Effect on the morphology of the SiNWs fabricated by MACE with a HF pre-treatment (a), (c) and with a H ₂ O ₂ :H ₂ SO ₄ pre-treatment (b), (d). The insets show high magnification SEM images of the top-view. The scale bar is 500 nm.	152
Figure 4-15: Reflectance of the SiNW arrays fabricated by MACE with a HF pre-treatment (solid black squares), a H ₂ O ₂ :H ₂ SO ₄ pre-treatment (black solid circles) a HF pre-treatment and a HF post-treatment (open squares), and after a H ₂ O ₂ :H ₂ SO ₄ pre-treatment and HF post treatment (open circles).	153
Figure 4-16: SEM pictures - Effect on the morphology of the SiNWs fabricated by MACE after a H ₂ O ₂ :H ₂ SO ₄ pre-treatment (a), after a H ₂ O ₂ :H ₂ SO ₄ pre-treatment and a HF post-treatment (b), after a HF pre-treatment (c), (e), and after a HF pre-treatment and a HF post-treatment (d), (f). The insets show high magnification SEM images of the top-view. The scale bar is 500 nm..	154
Figure 4-17: Measurement of contact angle on SiNWs after the standard MACE process (after HNO ₃ bath) (left) and after HF post-treatment (right).	155
Figure 4-18: Schematic illustration of the water meniscus shape according to the wettability of SiNWs. For hydrophilic SiNWs, the water is wetting on the surface and the meniscus is concave (a) while for hydrophobic SiNWs, the water is non-wetting and the meniscus is convex (b).	157

Figure 4-19: Cross-section SEM pictures of 30 μm long nanowires: Effect on the morphology of the SiNWs fabricated by MACE with no post-treatment (a) and after a HF post-treatment (b). The insets show SEM images of the top-view. The scale bar is 5 μm	157
Figure 5-1: Reproducibility of the measured total reflectance data for 2 different samples. Measurements were performed at different locations of the sample on different days, showing good sample uniformity and measurement reproducibility.	160
Figure 5-2: Comparison of the total reflectance between commercial pyramids (black curve) and ordered SiNWs arrays of ~ 165 nm height and pitch of 330 nm (red curve) and disordered SiNWs with a length of 500 nm (green curve) with the corresponding SEM pictures.....	161
Figure 5-3: Effect of disordered SiNW length on the measured total reflectance plotted as a function of the wavelength.	161
Figure 5-4: Spectral dependence of the total reflectance measured on ordered SiNWs with pitch of 330 nm, diameter of 250 nm (± 10 nm) and lengths of 165 nm, 2 μm , 4 μm and 8 μm	162
Figure 5-5: Cross-section SEM images of ordered SiNW arrays with a pitch of 330 nm, an average diameters between 239-259 nm and lengths of (a) 163 nm, (b) 2.1 μm , (c) 4.2 μm and (d) 8.2 μm , respectively. The inset in (d) shows the corresponding top-view SEM image.	163
Figure 5-6: Figure 5-7: Illustration of SEM image analysis by imageJ: (a) original image, (b) threshold image, (c) image contour analysis and (d) area distribution.	164
Figure 5-8: Effect of the volume fraction on the reflectance of three ordered arrays of SiNWs with a pitch of 600 nm and a length of 2 μm . The diameters for the high, medium and low density SiNW arrays are 503 nm, 436 nm and 158 nm.	165
Figure 5-9: Schematic of the working principle of an anti-reflective coating [221].....	166
Figure 5-10: Effect of increasing the thickness of ITO on the reflectance of ordered SiNW arrays with a pitch of (a) 250 nm and (b) 500 nm.	166
Figure 5-11: Top-view SEM image of ordered arrays of SiNWs with a pitch of 250 nm covered with a thickness of ITO of (a)75 nm and (b) 100 nm.	169
Figure 5-12: Illustration of a diffraction pattern from a periodic diffraction grating [222].....	170
Figure 5-13: Circular diffraction pattern on NWs	171
Figure 5-14: (a) Real space (microscopic) image and (b) corresponding measured normalized Mueller matrices of ordered SiNW arrays with a pitch of 800 nm.	173
Figure 5-15: (a), (c), (e) Real space (microscopic) image and (b), (d), (f) corresponding M_{11} element detail of the measured Mueller matrices for a single domain (a), (b) , exactly 2 different domains (c), (d) and many small domains (e), (f).....	175
Figure 5-16: Definition of the 3 different layers used in our RCWA modeling.	176
Figure 5-17: Effect of the geometrical parameters (pitch and length) on the estimated J_{sc} for a perfect periodic structure.	177
Figure 5-18: Structural imperfections of ordered array of SiNWs fabricated by MACE assisted by NSL such as (a) surface roughness, (b) dislocations, (c) diameter distribution and (d) domain orientations.	178

Figure 5-19: (a) Cross-section and (b) top-view SEM image of short ordered arrays of SiNWs and corresponding modeling (c) , (d) using the "periodic model".	180
Figure 5-20: Comparison between (a) the "periodic model and (b) the "statistical model" for modeling a short periodic array fabricated by MACE assisted by NSL.	180
Figure 5-21: Best fit of Mueller Matrix using the statistical model.	182
Figure 5-22: Representation of the dual diameter SiNW arrays concept with the corresponding Poynting vector at a wavelength of 450 nm. Every black circle represent a nanowire [37], [38].	183
Figure 5-23: Top-view SEM pictures of PS spheres monolayer with a PS sphere (330:600 nm) ratio of (a) (1:2), (b) (2:1) and (c) corresponding SiNW arrays fabricated from (b).	184
Figure 5-24: Reflectance spectra of dual diameter SiNW array with (330 nm : 600 nm) (2:1).	185
Figure 6-1: Schematic of the structure of (a) a HIT solar cells [125] (b) a HIT solar cell where the n-type c-Si wafer has been nanostructured to improve light trapping.	187
Figure 6-2: Illustration of a hexagonal SiNWs arrays with a pitch p and a height h (left) and calculation of the surface ratios for different geometries (right).	189
Figure 6-3: (a) Schematic of the structure of the HIT solar cell where the n-type c-Si wafer has been nanostructured to improve light trapping. (b) SEM cross-section of a fabricated device.	190
Figure 6-4: Process of fabrication of HIT solar cells based on SiNWs.	191
Figure 6-5: Dependence of (a) EQE and (b) (J,V) curves on the thickness of the amorphous layer (see Table 6-1).	192
Figure 6-6: The average value and the standard deviation of J_{sc} (a), FF (b), V_{oc} (c) and η (d) as function of $d_{a-Si:H}$.	194
Figure 6-7: SEM pictures of SiNW solar cells after a-Si:H PECVD deposition of sample D (a) and sample F (b) before ITO deposition and sample F (c) after ITO deposition cross-section and (d) after ITO deposition top-view.	195
Figure 6-8: TRMC signal as a function of time for HIT solar cells with different a-Si:H thicknesses. The inset shows the signal in logarithmic scale.	197
Figure 6-9: Schematic showing the details of the a-Si:H coating.	198
Figure 6-10: Effect of the gradient doping on (J,V) curves of HIT solar cells based on SiNWs.	200
Figure 6-11: Effect of the gradient doping on the EQE of HIT solar cells based on SiNWs.	201
Figure 6-12: Effect of the (i) a-Si:H thickness on the EQE of HIT solar cells based on SiNWs.	203
Figure 6-13: Effects of the SiNWs length on the (a) EQE and (b) reflectance of the cells.	205
Figure 6-14: TRMC signal as a function of time for samples with different SiNW lengths.	206
Figure 6-15: TEM analysis of disordered SiNWs. SiNWs agglomerate (a) and (b). Only the tip of the wire is covered by a-Si:H and the coating depth by a-Si:H is between 370- 500 nm (c), (d) and (e). Small crystal grains can be found within the amorphous coating (f) and (g).	209

Figure 6-16: EBIC mapping of the HIT SiNW cross-section under various accelerating voltages (a) 3 keV, (b) 5 keV and (c) 10 keV.	210
Figure 6-17: EBIC current profile at 10 keV as a function of position of the beam on the sample C with the corresponding EBIC mapping in the inset. The red arrow in the inset indicates the corresponding signal position on the sample. A cross-section schematic of the structure is displayed at the bottom.	211
Figure 6-18: Equation (4) as a function of x, the distance from the junction, obtained from experimental data of zone 2 in Figure 6-17.	212
Figure 6-19: (a) Cross-section SEM image of the bottom of a SiNW partially covered by ITO and (b) corresponding EBIC mapping with the red arrow indicating the corresponding signal position on the sample and (c) the corresponding EBIC current profile at 10 keV as a function of the position of the beam on the sample. (d) Cross-section EBIC mapping of samples with “dead” and electrically active SiNWs. The inset shows the EBIC top-view mapping confirming that only few nanowires are active.	213
Figure 6-20: Modeling of the volume of excitation produced by a 10 keV electron beam impinging on a 550 μm c-Si substrate with (a) no ITO, (b) 100 nm of ITO and (c) 200 nm of ITO.	214
Figure 6-21: EBIC current profiles (a) and cross-section EBIC current mapping (b). The 4 different arrows indicate the localization of the different EBIC profiles measured on the sample.	214
Figure 6-22: EBIC mapping of SiNW solar cells based on 5 μm epitaxial film with low magnification in (a) grey and (b) rainbow magnification and (c) high magnification	216
Figure 6-23: EQE (a) and (I,V) (b) curves of reference planar cell and SiNWs based solar cells on 5 μm Si epitaxial thin film.	217
Figure 6-24: SEM picture of ordered arrays of SiNWs (pitch 550 nm, diameter of 345 nm , length of 1.2 μm) after a-Si:H depositon and before ITO deposition (a) top-view (b) cross-section.....	218
Figure 6-25: Top-view SEM image of ordered arrays of SiNWs covered with a thickness of ITO of (a) 25 nm, (b) 50 nm, (c) 75 nm and (d) 100 nm. (e) shows the cross-section of a single SiNW with various thicknesses of ITO.	219
Figure 6-26: Comparison of EQE response for different C-Si substrates: reference planar cells, ordered SiNW arrays cells, disordered SiNW arrays cells.	221
Figure 6-27: Comparison of EQE response for different epitaxial c-Si substrates: reference planar cells, ordered SiNW arrays cells, disordered SiNW arrays cells.	221
Figure 6-28: Cross-section SEM picture of ordered arrays of SiNWs (pitch 330 nm, diameter 220 nm, length 700 nm) (a) at low and (b) high magnification. The inset (b) shows that the top of the wire is less damaged for short SiNWs (250 nm height).	222
Figure 6-29: EELS analysis of ordered SiNW arrays.	223
Figure 6-30: TEM analysis of ordered SiNW before a-Si:H coating.....	225

Figure 6-31: TEM analysis of ordered SiNW after a-Si:H coating. The coating of SiNWs by a-Si:H is not uniform (a), (b), it is maximum at the tip of the SiNW (c) and present a columnar structure (c) and (d). Finally, some crystalline grains are observed at the bottom of the coating (e).....	227
Figure 6-32: Top-view EBIC mapping of ordered SiNWs arrays (pitch of 500 nm, diameter of 280 nm and height of 460 nm) at different gun energies: 3 keV (a), 10 keV (b) and 20 keV (c) with the corresponding modeling (d), (e) and (f).....	228
Figure 6-33: Cross-section EBIC mapping of short (a), (b) and long (c), (d) ordered SiNWs arrays at 2 different gun energies: 5 keV (a), (c) and 10 keV (b), (d).....	229
Figure 6-34: Top-view EBIC mapping of ordered SiNWs arrays with a length of (a) 500 nm, (b) 2.2 μm and (c) 3 μm	230
Figure 6-35: (a) Top-view SEM image of the silver etching mask after the removal of the PS spheres. (b) Top view SEM image after 20 s wet chemical etching and removal of silver film (c)) Top view SEM image after 45 s wet chemical etching and removal of silver film (d) Cross-section SEM picture of SiNWs fabricated by MACE assisted by NSL with silver catalyst after 1 min etching.	231
Figure 6-36: Illustration of the oxidation process.....	232
Figure 6-37: Top-view SEM picture of ordered arrays of SiNWs (pitch 800 nm, length of 2.7 μm) before (a) and after (b) oxidation process.	232
Figure 6-38: Effect of oxidation treatment on EQE.....	234
Figure 6-39: Top-view EBIC mapping before (a) and after (b) oxidation pre-treatment.	234
Figure 6-40: Cross-section SEM pictures (a) and corresponding EBIC mapping (b) of samples which underwent an oxidation pre-treatment	235
Figure 7-1: Schematic detailing the architecture of the hybrid device	237
Figure 7-2: Process flow of hybrid solar cells	239
Figure 7-3: EQE response of the three arrays of ordered SiNW arrays A, B and C and (b) the corresponding average reflectance on the spectrum range 350-1100 nm.	241
Figure 7-4: (a) (J,V) and (b) EQE of hybrid devices based on disordered and ordered SiNWs.	242
Figure 7-5: Band diagram of the hybrid device.....	243
Figure 7-6: Cross-section view (a), (b), Top-view (c) and Inclined-view (d) SEM pictures of SiNWs coated with PEDOT:PSS.....	244
Figure 7-7: SEM pictures of ordered SiNWs after (a) LPAD1, (b) LPAD2 and (c) LPAD3. ...	246
Figure 7-8: (a) Cross section view of a-Si:H nanowires. (b) Top-view of a-Si:H nanowires. (c) Length of nanowires as a function of the etching time.	249
Figure 7-9: Reflectance measurement of planar a-Si:H thin films and a-Si:H nanowires.	250
Figure 7-10: Top-view (a) and inclined 30° (b) SEM pictures of a-Si:H NWs.	250
Figure 7-11: Architecture of the device studied – Hybrid thin film solar cells based on a-Si:H.	252
Figure 7-12: (a) (J,V) and (b) EQE planar hybrid a-Si:H / PEDOT:PSS heterojunction.....	253

Figure 7-13: Schematic of the hybrid solar cells based on the combination of an organic layer with an amorphous thin film with a LiF/Al rear electrodes.	254
Figure 7-14: Effect of C ₆₀ thickness on the performance of the solar cells.	255
Figure 7-15: Schematic of the vacuum level shift induced by LiF/Al cathode for organic solar cells.	257
Figure 7-16: Schematic of the structure of the LiF/Al rear electrodes on (p+) a-SiC:H/(i) a-Si:H.	258
Figure 7-17: (J,V) curves of the thin film devices with LiF/Al cathode (black) and Al cathode (red).	259
Figure 7-18: EQE curves of the thin film devices with LiF/Al cathode (black) and Al cathode (red)	261
Figure 7-19: Schematic of the band diagram of p-i-n junction and a-Si:H thin film with a LiF/Al rear electrodes.	263
Figure 7-20: (J,V) curves of the thin film devices with LiF/Al cathode (black) and Al cathode (red).	263
Figure 7-21: Light soaking effect on the cells' performances.	265
Figure 7-22: Effect of the electrode size on the solar cells' parameters	266

List of Tables

Table 2-1: Key results and finding on SiNWs based Solar Cells.	72
Table 4-1: Main advantages and drawbacks of the different methods used to separate agglomerated SiNWs.	158
Table 5-1: Average reflectance over the spectral range 400-1100 nm for disordered SiNWs with different lengths.	162
Table 5-2: Geometrical parameters of 4 different ordered SiNW arrays with the corresponding average total reflectance calculated in the range of 400-1100 nm.	163
Table 5-3: Effect of ITO coating on the average reflectance of ordered arrays of SiNWs. J_{sc} is calculated from the absorbed photons and J_{loss} is calculated from the reflected photons.	169
Table 6-1: Summary of various deposition conditions with details of the deposition time of each layer.	192
Table 6-2: The average value and the standard deviation of V_{oc} , J_{sc} , FF and η of core-shell HIT solar cells.	193
Table 6-3: Summary of various deposition conditions with details of the deposition time of every layer and average value of V_{oc} , J_{sc} , FF and η of corresponding core-shell HIT solar cells.	198
Table 6-4: Summary of various deposition conditions with details of the deposition time of every layer and average value of V_{oc} , J_{sc} , FF and η of corresponding core-shell HIT solar cells.	201
Table 6-5: Dependence of the photovoltaic parameters J_{sc} , FF , V_{oc} and η on the length of SiNWs.	204
Table 6-6: Photovoltaic parameters for reference planar cells and SiNWs based solar cells on 5 μm epitaxial layer.	216
Table 6-7: Summary of geometrical characteristics of SiNW arrays and average value of V_{oc} , J_{sc} , FF and η of corresponding core-shell heterojunction solar cells.	220
Table 6-8: Effect of oxidation treatment: summary of geometrical characteristics of SiNW arrays and average value of V_{oc} , J_{sc} , FF and η of corresponding core-shell heterojunction solar cells.	233
Table 7-1: Summary of the geometry of the different SiNW arrays and average value of V_{oc} , J_{sc} , FF and η of corresponding hybrid solar cells.	240
Table 7-2: Average value of V_{oc} , J_{sc} , FF and η of planar hybrid a-Si:H / PEDOT:PSS heterojunction.	253
Table 7-3: Effect of the thickness of C_{60} on the average value of V_{oc} , J_{sc} , FF and η of planar hybrid a-Si:H / C_{60} heterojunction.	254
Table 7-4: Comparison of photovoltaic parameters of thin film devices with Al cathode and LiF/Al cathode.	260
Table 7-5: Photovoltaic Performance - Effect of LiF thickness.	264
Table 7-6: Effect of LiF thickness on the series resistances.	264

Table 7-7: Effect of the electrode size on the series and shunt resistances.....266

Chapter 1 : Introduction

"The ultimate answer to humanity's energy problems rises every morning and sets every evening."

Oliver Morton

Editorial, Nature, 14th August 2008

1.1 Solar energy: the Reality and the Future of Photovoltaics

Energy is undoubtedly the challenge of the century, if not the millennium, because of its potential economic, political and environmental fallouts. Nowadays fossil fuels account for around 80% [1] of the global energy consumption. The world's heavy dependence, especially on oil, is particularly worrying because of the inevitable decline of its supply, and the resulting pollution of water and air by greenhouse gas emissions [2]. As fossil fuel resources are becoming scarce and even more challenging to explore, it is unlikely that the oil industry will be able to keep up with the path of an ever increasing global energy demand, driven by both population and economic growth. Therefore, in response to increasing stress on fossil fuel resources, new concepts such as green energy or sustainable living have emerged, leading to the development of alternative energy sources such as wind energy, solar energy, geothermal energy, tidal energy, biomass, wave power, biodiesel, hydrogen fuel, etc. Among them, solar energy power, as a clean and inexhaustible energy source, is believed to be one of the most promising candidates to help solve the problems of energy shortage and environmental problems

Indeed solar energy has very attractive features. It is a free, clean and infinite energy source which, once installed, produces no pollution, no emission, no carbon footprint and no noise. Solar energy has also the potential

to cover the global energy demand: *every hour, the earth receives more energy from the sun than mankind can consume in a year* [3]. Harvesting a small fraction of this energy could solve the problem of energy shortage, hence many efforts have been put into the research and development of efficient solar cells.

While solar PV was only a niche market one decade ago with small scale applications (calculator, watch, out of grid...), it is nowadays a mature technology and industry on its way to become a mainstream source of electricity. Over the last two decades, the global cumulative installed capacity has grown exponentially from around 5 gigawatt (GW) in 2005 to 177 GW by the end of the year 2014 as shown in **Figure 1-1** [4]. For the year 2014 alone, 38.7 GW were newly installed worldwide, led by China (10.0 GW), Japan (9.7 GW) and USA (6.2 GW). Italy, Greece and Germany are now able to cover respectively 7.9%, 7.6% and 7.0% of their annual energy demand by solar energy [4]. Therefore PV is no longer a chimera, but instead can contribute significantly to a sustainable energetic transition.

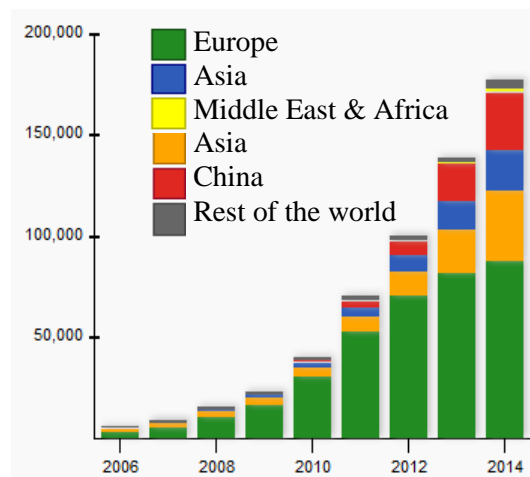


Figure 1-1: Global and regional cumulative capacity in Megawatt (MW) [4].

Japan and Europe have driven for a long time the growth of photovoltaics. In particular, Germany still holds the world record of the highest cumulative solar PV capacity installed in 2014 (38.23 GW) as shown in **Figure 1-2** [4]. However, the competition is fierce and China is expected to take the lead by 2017 with a predicted PV capacity of 70 GW. The European PV market has slowed down over the past 4 years with a significant drop from 22 GW in

2011 to 7 GW in 2014. This is explained by a context of reduced feed-in tariffs, retroactive measures and declining political support which have contributed in the past to the development of the European PV market. European, Japanese and US manufacturers have also suffered from the competition of Chinese and Taiwanese manufacturers which have become today the main module suppliers.

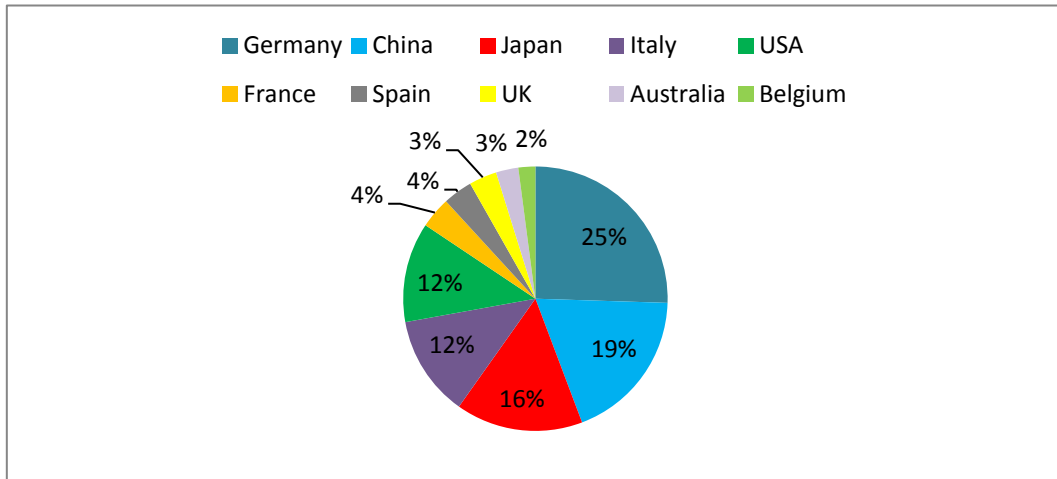


Figure 1-2: TOP 10 countries in 2014 for cumulative installed capacity [4].

Today, the PV market is dominated by Asia which constitutes about 60% of the global PV market. The PV growth is also boosted by emerging markets such as South Africa, Chile, Mexico and Turkey while the European market continues its decline despite the significant growth of the UK installed capacity in 2014 (2.27 GW). **Figure 1-3** shows the added installed capacity country by country for the year 2014 [4]. China and Japan are far beyond the other countries. In 2014, Japan underwent a real boom (9.2 GW) while the Chinese market tends to stabilize (10.6 GW). The landscape of the PV market is therefore changing quickly with new actors entering the play.

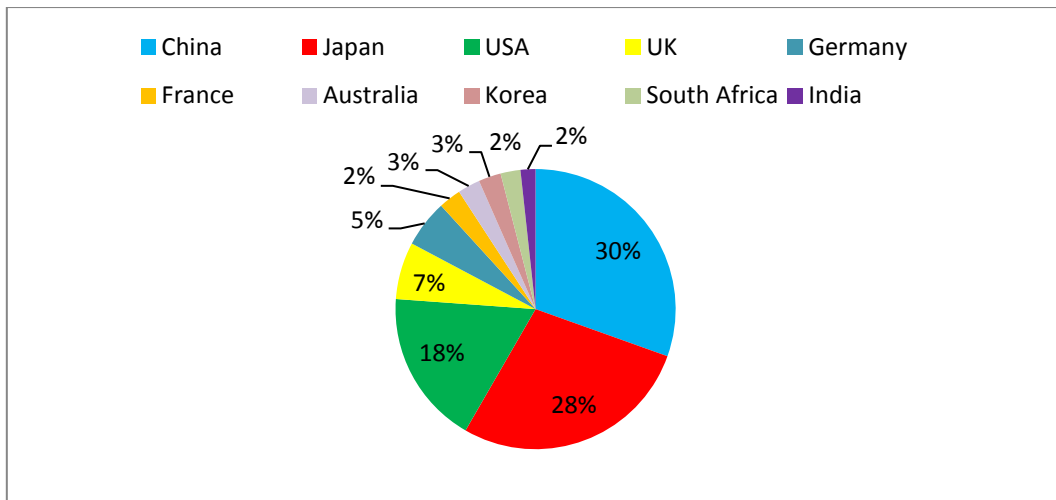


Figure 1-3: TOP 10 countries in 2014 for annual installed capacity [4].

Forecasting the evolution of the PV market is always a delicate and complex issue. Official agencies such as IEA (International Energy Agency) are predicting solar deployment every year but frequently they have to adjust their numbers. For the year 2015, the expected solar growth should be between 35 GW to 57.3 GW, according to the different scenarios established by different agencies or companies [5]–[7]. The market share of crystalline silicon is predicted to increase at the detriment of polycrystalline silicon [8].

Despite the considerable advantages offered by solar energy, cumulative photovoltaic (PV) electricity production represents today only 1% of the total global electricity production [4]. Therefore a legitimate question arises: what are the limitations towards a global PV deployment?

The major limitation, when the subject comes up, remains the initial cost, although it is becoming less and less true. Solar panels and other units for collection and storage are relatively expensive to manufacture, making solar energy a costly option for generating electricity. The time lag of several years for matching initial investment is still prohibitive for many customers. This high cost can be partly explained by the expensive silicon wafer technology which has been widely used as the base component for achieving stable and efficient solar cell devices because of its unique properties. Indeed solar cells based on crystalline silicon (c-Si) wafers have dominated the photovoltaic market since the very beginning of the PV industry, back in the 1950's, maintaining since then a market share of about 80% [9]. In 2014, Panasonic

broke the record of 25.6% for single interdigitated back-contacted silicon heterojunction (IBC-HJ) solar cells [10]. Although silicon is the second most element abundant on earth, it has to undergo high-cost manufacturing processes to be suitable for PV applications, which thus limits the cost competitiveness of the PV market. Although prices are falling rapidly, c-Si wafers still account for 30% of the final module cost. Therefore, new technologies have been developed in order to reduce the cost of standard photovoltaic panels and therefore make solar energy an attractive alternative to fossil fuel.

Finally it is worth to mention that energy is not only an economically-driven industry but also a policy-driven industry. Indeed, costs of PV are really falling down, making solar energy an increasingly competitive alternative to fossil fuel energy. However, it also implies the need for development of building grids, storage, operating and commercial arrangements able to meet the world's electricity demand, which in turn require the right policy support. Financial and political support are thus essential to make the energetic transition a reality.

1.2 PV Technologies

The technological landscape of PV is tremendously vast. If the main PV technologies such as c-Si, hydrogenated amorphous silicon (a-Si:H), Cadmium Telluride (CdTe), Copper Indium Gallium Selenide (CIGS), concentrated photovoltaic (CPV), organic photovoltaic (OPV) are known for at least three decades, they are continuously being improved through new design or materials. The diversity of the PV technologies is illustrated in **Figure 1-4**. As mentioned previously, the PV market is dominated by c-Si, that holds by far the record of power energy conversion for a single junction (25.6%, [10]). There are three types of c-Si: single crystalline silicon, multicrystalline silicon and ribbons. If single crystalline silicon based modules are the most efficient panels on the market, multicrystalline silicon cells are very popular as they are cheaper to manufacture. The thin-film technology represents the second PV market share and reduces drastically the amount of material required for producing a solar cell. Thin-film solar cells have gained popularity over the past 20-30 years as they are relatively cheap, flexible, lighter and easier to integrate. There are

three main types of thin films solar cells : a-Si:H, CdTe and CIGS/CIS. Performance of such devices have reached high efficiency and are consistently being improved. For example, First Solar can fabricate nowadays CdTe modules with an efficiency of 18.6% [11] with their best research cell holding a record of 21.5% [12]. The record CIGS cell is 21.7% [13], [14] and several companies are fabricating nowadays efficient modules (Solar Frontier, TSMC, MANZ). The actual CIGS record module is 16.5% (TSMC, [15]). The major limitation of this type of cells (CdTe, CIGS) is to use rear earth elements such as indium or tellurium that can limit their large scale production. Performance of a-Si based solar cells are lower than their CdTe or CIGS counterparts but their implementation into tandem devices or triple junction have improved their performance to 13.2% [16] and 13.6% [17] respectively (best research cell efficiency). There are many other PV technologies such as CPV that use lenses to focus light on small highly efficient and highly expensive solar cells, generally based on gallium arsenide. There are also OPV cells, with a latest record of 11.5% ([18], [19]). Today, solar cells based on leading-edge technologies have emerged. They cover a wide range of new materials, concepts and innovations and are usually in the research phase. They include for example nanotechnology based solar cells, such as nanowires based devices. More recently, the emergence of the perovskite technology, which has reached efficiency as high as 20.1% (KRICT, [19]) in a few years, has filled with enthusiasm the PV community.

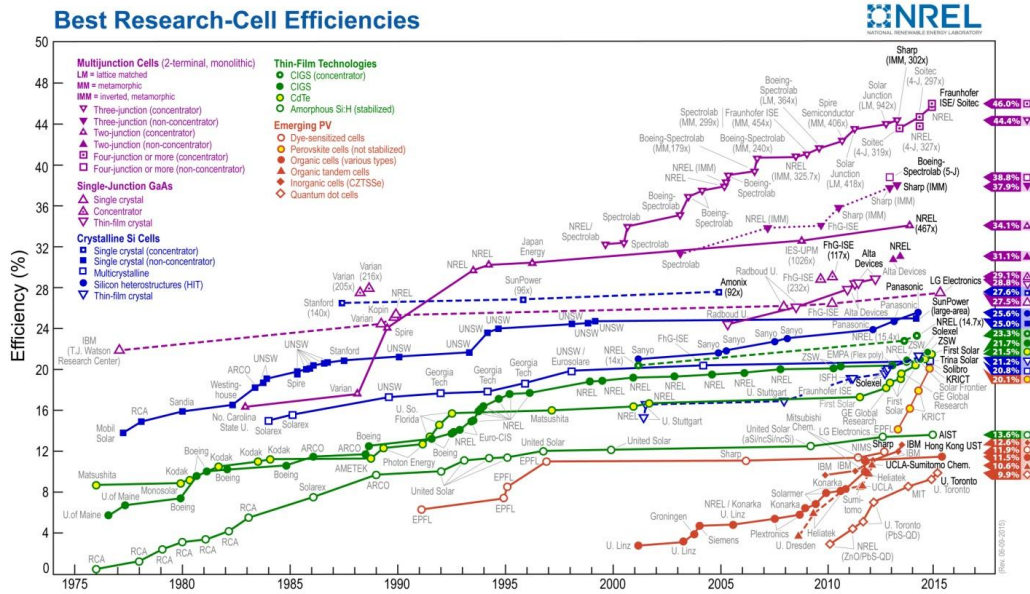


Figure 1-4: Timeline of the best research cell efficiencies for the different PV technologies [19].

1.3 Three Categories of Solar Cells

Solar cells can be divided generally into three main categories:

(1) Inorganic solar cells based on high quality inorganic materials, mainly silicon but also polycrystalline silicon, microcrystalline silicon, CIGS, Cadmium Telluride, etc, which are stable and efficient. As mentioned before, silicon dominates so far the photovoltaic market as it is a well-understood material, and whose manufacturing processes have been developed and optimized over the last fifty years, in particular thanks to the advancement and success of the Si microelectronics industry. Moreover, silicon is abundant, non-toxic and has rather good properties, though not ideal, for photovoltaic applications. However, silicon still suffers from high manufacturing costs arising from the complex and high temperature processes involved in the fabrication of the photovoltaic panels. Therefore price of silicon is still an ordeal that prevents the wide spread use of solar technology worldwide.

(2) Organic solar cells are based on conductive polymers or organic molecules. Organic solar cells have gained popularity in recent years as they offer the possibility to produce flexible, light weight solar cells at low-cost. They are of particular interest for specific applications such as flexible electronics or covering windows and walls. However organic materials have

very poor electrical properties (small dielectric constants and poor dissociation of carriers into free holes and electrons) which prevent them from reaching high efficiency. Moreover organic devices are usually not stable and require encapsulation as they are very sensitive to the environment such as light, humidity, etc.

(3) Recently a new generation of solar cells based on an innovative and challenging approach came to light: the association within a single device of the two families of materials used in solar cells, e.g. inorganic and organic materials. Over the last twenty years, research on organic and inorganic based solar cells has been conducted independently, each technology being developed separately. Would it not be exciting to reconcile the two families and fabricate a device that makes the best use of the two materials? This attractive possibility increasingly studied by the scientific community is to fabricate the so-called hybrid solar cells. Hybrid solar cells are devices that combine both organic and inorganic materials, hence the name hybrid. Inorganic semiconductor nanostructures coupled with organic materials provide not only a good medium for fast carrier transport due to the use of inorganic semiconductor, they can also be fabricated over a very large area at low cost and low temperature using the spin coating or printing technique. Hybrid solar cells include generally the use of inorganic nanoparticles or inorganic nanowires (NWs) embedded in an organic matrix [20]–[23]. More recently the perovskite technology has boosted this field of research by reaching efficiency above 20% in a lapse time of less than 6 years, impacting significantly the photovoltaic community [19], [24], [25].

1.4 Motivation, Objectives and Scope of this Thesis

Progress made in nanotechnology can be used as a driving tool to produce cheaper and more efficient solar cells. A nanowire (NW) is an elongated nanostructure whose diameter is of the order of nanometers scale. NWs have attracted much interest over the past few years as they offer very attractive features which make them good candidates for solar cells applications [26]. In particular, NWs have remarkable optical properties such as antireflection and light trapping effects as illustrated in **Figure 1-5** [26], [27].

Nanowires benefit from outstanding optical properties as they have the potential to address both antireflection and light trapping issues, allowing for efficient light harvesting capabilities. These excellent optical properties are partly due to the subwavelength structure offered by the SiNWs, acting like an antireflective layer. The enhanced absorption is also explained by the electromagnetic wave interaction with the SiNWs. The exceptional optical properties of SiNWs are discussed in detail in section 2.2.2 of this thesis. Moreover, SiNWs can offer enhanced charge carrier collection and interesting electrical properties as we will see in section 2.2.3 and 2.2.4. Many papers have been published recently on NWs based solar cells. Some attempts have already been carried out using CdS, CdSe, CdTe, ZnO or TiO₂ NWs [28]–[36]. Nevertheless, the toxicity of CdS, CdSe and CdTe as well as the high energy gap ($E_g > 3\text{eV}$) of ZnO and TiO₂ NWs make these materials unsuitable for efficient devices. Here we will focus on silicon nanowires (SiNWs) as they are environmental-friendly, abundant, well-understood, and show excellent light trapping and antireflection properties. The properties of SiNWs will be reviewed in more detail in Chapter 2.

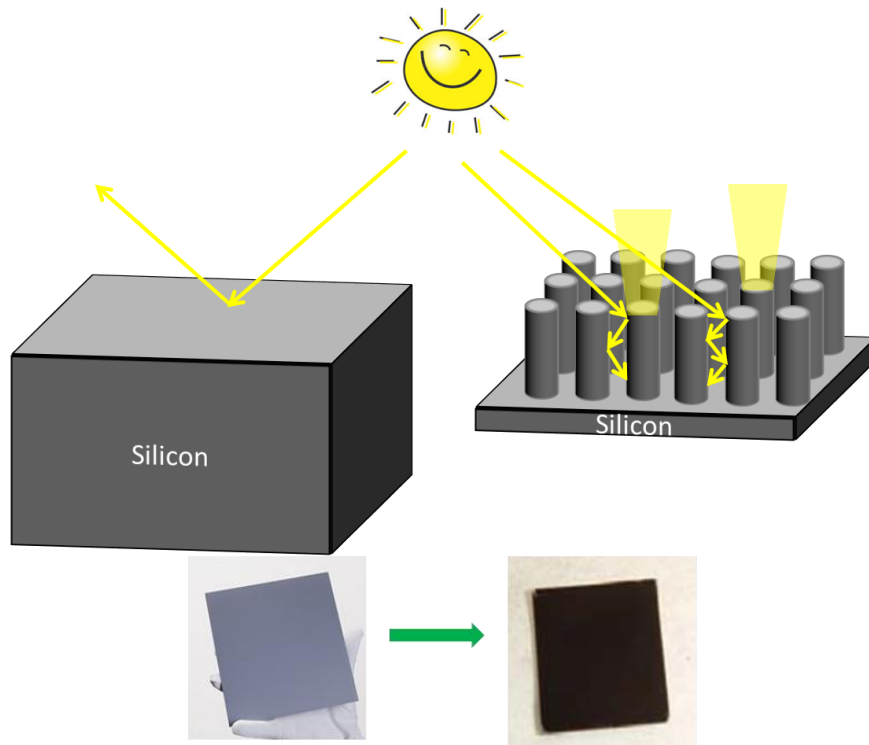


Figure 1-5: Illustration of the light trapping effect of SiNWs. This light trapping effect by SiNWs is directly visible with the eye as shown by the back color of SiNWs sample compared to the shiny grey aspect of the planar reference sample. It shows that the light is effectively trapped within the SiNWs.

One common strategy to reduce the cost of Si based solar cells is to use thinner wafers. However the thickness reduction is detrimental to the optical absorption. Indeed, solar cells based on c-Si are generally thick because of the indirect band gap of Si which requires large thickness to absorb most of the incoming light. SiNWs can be used as a driving force to transfer the bulk c-Si based solar cells to the thin films technology and cut the material and process costs of the PV modules. Indeed, the perfect light trapping properties of SiNW arrays enables high absorption in just 1 μm thick long NW arrays, rendering the transfer to the thin film technology highly desirable. By using crystalline NWs, we are able to produce high quality materials for the thin film technology and therefore high efficiency is expected. The ultimate goal will be to produce high efficiency solar cells based on SiNWs on thin films and bypass the expensive bulk c-Si wafers.

In this thesis, the potential of silicon nanowires (SiNWs) for PV applications is investigated. NWs will be integrated into two different solar cell technologies: hybrid devices and heterojunction with intrinsic thin layer (HIT) devices. The scope of this research work includes the design, fabrication and characterization of SiNWs and solar cells based on SiNWs.

The objectives of the thesis are summarized as follows:

- a) Fabrication of dense arrays of SiNWs using a low-cost and scalable process. The Metal Assisted Chemical Etching (MACE) technique, which is a top down approach based on the wet etching of the bulk material, is used. The principle and advantages of this method are presented in detail in chapter 2 of this thesis. Two types of architectures will be investigated: random and ordered SiNWs arrays. We named random arrays of SiNWs as those where we have no control over the pitch or diameter of the fabricated structures, in contrast to ordered arrays where the geometry of the nanostructures can be controlled.
- b) Optimization of the MACE process by addressing the aggregation issue observed for long SiNWs synthesized by this method. Despite all these advantages, the MACE method suffers from an inherent problem which

is a direct side effect of the method itself: this wet etching process relies on the use of a liquid phase (chemical solution), hence capillary forces arise which is responsible for the agglomeration of the NWs. This agglomeration is highly undesirable and is often considered as a limiting factor to achieve high efficiency solar cells. Indeed large bundles prevent conformal coating of the arrays by photoactive material (inorganic or organic coating), deteriorate the optical properties of the array and may induce higher series resistance. Therefore, finding a simple way to reduce significantly the bundling of nanowires is highly desirable.

- c) Investigation of the optical performances of SiNWs. Random and ordered arrays of SiNWs will be characterized. Characterization techniques include spectrophotometry and Mueller polarimetry. The effect of the geometry on the optical performances will be discussed. This work will be supported by an optical model developed in LPICM [37], [38] that will enable us to find the optimized geometry for SiNWs arrays to achieve strong absorption of solar radiation and deliver high short circuit current density. Results obtained from experiments and the model will be analyzed and compared.
- d) Design and fabrication of HIT solar cells based on deposition of hydrogenated amorphous thin films on crystalline SiNWs. The optical and electrical properties of the cells will be investigated by standard techniques (solar simulator, External Quantum Efficiency (EQE), spectrophotometry) and more advanced techniques such as Time Resolved Microwave Conductivity (TRMC) and Electron Beam Induced Current (EBIC). We will focus on the optimization of the photovoltaic performances of the devices. Finally, some preliminary results on surface treatment to enhance the passivation of SiNWs will be presented.
- e) Design and fabrication of hybrid solar cells based on SiNWs where the junction is simply formed by spin coating a PEDOT:PSS layer on the c-SiNWs. The optical and electrical properties of the cells will be investigated by standard techniques (solar simulator, External Quantum Efficiency (EQE), spectrophotometry). Devices based on both random

and ordered SiNWs will be fabricated and compared. The issue of polymer infiltration within the arrays of SiNWs will be addressed. Some possible surface treatment to improve the surface passivation will be introduced. We will also explore the possibility to transfer this concept to thin film solar cells based on amorphous silicon (a-Si:H). Hybrid solar cells based on a-Si:H will be fabricated. The MACE process will be used to fabricate a-Si:H nanowires. Finally a detailed study of the potential of LiF/Al, a common cathode used for organic solar cells, as the back contact of a schottky thin film solar cells based on a-Si:H will be carried out

1.5 Main Contributions of the Thesis

Random SiNWs with typical diameters of 20-200 nm were successfully fabricated using a low-cost and scalable top-down approach named the Metal Assisted Chemical Etching (MACE). However, the SiNWs fabricated by MACE agglomerate at their top-end to form large bundles. We have developed a theoretical model to understand the origins of this agglomeration. Thanks to a deeper understanding of the physical phenomena involved, we have successfully implemented a new process to prevent the strong agglomeration of SiNWs. A careful adjustment of the wettability properties of the initial substrate and surface of the wires is essential to achieve dense, uniform and well separated SiNWs. The wettability of the initial substrate impacts the density and the uniformity of the fabricated wires while the bundling of SiNWs can be eliminated by changing the surface state of the SiNWs to hydrophobic.

By combining the MACE process with the nanosphere lithography (NSL) method, we have also successfully fabricated ordered SiNW arrays with an excellent control over the pitch, diameter and length of the structure. The pitch of the produced ordered SiNW arrays was varied between 240 to 800 nm.

These two types of SiNW arrays (disordered/ ordered) were then integrated into two different devices: HIT and hybrid solar cells. HIT solar cells were fabricated by depositing successively an intrinsic and doped a-Si:H layer on top of the SiNWs by PECVD. The effect of the thickness and doping of the a-Si:H layer were investigated and revealed to be crucial. By optimizing the

process conditions, we achieved a record efficiency of 12.9% with excellent fill factor above 80% for SiNW based HIT devices. For this type of devices, ordered and random SiNWs gave very different results. We were unable to achieve reasonable V_{oc} for ordered SiNWs. Only HIT devices based on random SiNWs were reaching efficiency up to ~13%. Such result might be related to the porosity observed at the tip of ordered SiNWs. We have then successfully demonstrated the concept of SiNW based HIT solar cells on a 5 μm epitaxial film.

Following that, we fabricated hybrid solar cells based on ordered and disordered SiNWs. The junction was simply formed by spin coating a PEDOT:PSS film on top of the wires. Interestingly, both ordered and disordered SiNWs were working in a similar manner and gave efficiency of about 9-9.5%. We have observed that the PEDOT:PSS film was unable to reach the bottom of the wire and formed like a canopy lying on top of the wires. This reduces the surface of the p-n junction and means that a huge fraction of the Si surface is non-passivated. To solve this problem, we have developed our own method based on low pressure to force the polymer to coat conformally on the SiNWs. We were able to achieve SiNW arrays conformally coated with PEDOT:PSS. We believe that such results might increase significantly the performance of hybrid devices. We have also explored the transfer of hybrid devices to a-Si:H thin film technology. We have successfully fabricated a-Si:H NWs and have produced hybrid solar cells based on the combination of PEDOT:PSS with a thin film of a-Si:H. This work has allowed us to identify an extremely interesting effect between a-Si:H and a LiF/Al electrode, which is a common electrode used in OPV. We have demonstrated that LiF/Al cathode can replace the dead n-layer in standard p-i-n junction, eliminating this way the associated absorption loss and the use of the toxic phosphine gas. We successfully fabricated p-i-n solar cells, without the use of the n-layer, with an average efficiency of 8.3%.

Finally we have characterized the SiNWs and the devices by a wide range of characterization techniques. We have assessed the electrical activity of SiNWs by Electron Beam Induced Current (EBIC). Another key result concerns the investigation of the optical properties of SiNW arrays. We have shown that the optical properties of random SiNWs are essentially determined by the

length of the wires. For ordered SiNWs, we have demonstrated the key role played by the density and diameter of SiNWs. Finally we have successfully developed a model able to simulate the optical response of an ordered SiNW array with excellent accuracy.

1.6 Organization of this Thesis

This thesis is divided into 8 chapters.

Chapter 1 reviews the general context of the PV industry. This chapter also covers the motivation, scope and main objectives of this thesis.

Chapter 2 is a detailed literature review including the working principle and the fundamental concepts of a solar cell, the properties of SiNWs (optical, electrical, charge carrier collection) and their methods of fabrication (top-down and bottom-up). This chapter also reviews the main work reported so far on solar cells based on SiNWs.

Chapter 3 presents the detailed process of fabrication of random and ordered arrays of SiNWs that have been used in this thesis. The different equipment required for the fabrication of HIT and hybrid solar cells are also introduced (Plasma Enhanced Chemical Vapor deposition (PECVD), e-beam deposition, sputtering, spin coating). The non standard characterization tools used during this research work are also presented: Time Resolved Microwave Conductivity (TRMC) and Electron Beam Induced Current (EBIC).

Chapter 4 focuses on the agglomeration issue of silicon nanowires fabricated by Metal Assisted Chemical Etching. A detailed analysis of the forces responsible for the aggregation observed at the top ends of NWs is presented. Following that we propose an elegant way to reduce significantly the agglomeration of SiNWs based on a series of different post and pre-treatments.

Chapter 5 studies the optical properties of random and disorder SiNWs. Arrays of SiNWs are characterized by spectrophotometer and Mueller polarimetry. An optical model is developed and data obtained from the modeling and experiments are compared.

Chapter 6 focuses on the design, performance optimization and characterization of HIT solar cells based on both disordered and ordered SiNWs.

Chapter 7 investigates hybrid devices based on the combination of an organic layer PEDOT:PSS on ordered and disordered SiNWs. The possibility to transfer the concept to amorphous thin films is also explored.

Chapter 8 presents the main conclusions drawn from this research work along with the perspectives.

Chapter 2 : Literature review

This chapter is a detailed literature review. It first describes the working principle and the fundamental concepts of a solar cell. Then we review the properties of SiNWs (optical, electrical, charge carrier collection) and their methods of fabrication (top-down and bottom-up). This chapter also introduces the basics of NW solar cells and reviews the main work reported so far on solar cells based on SiNWs. Finally we describe the working principle and material involved in HIT and hybrid devices.

2.1 Basics of Solar Cells

2.1.1 Working Principle of a Solar Cell

A solar panel/ module is a device that converts the sun's energy into electricity by the so-called photovoltaic effect ("photo" means light and "voltaic" means electricity). Solar modules are divided into cells units (solar cells) which are the basic component of a solar panel. Each cell produces its own electricity and is electrically connected to other solar cells of the panel, contributing this way to the global power of the module. There are basically two key processes involved in the conversion of solar energy into electricity. First, the photovoltaic cell is struck by the sun light, which results in the absorption of a certain fraction of the light by the material. As solar cells are typically made of semiconductors, this absorption results in the formation of positive and negative charges, commonly named an electron-hole pair. The second process is the separation and collection of these 2 charges at different electrodes. Separation of the charges is achieved by the action of a local electric field within the material. The flow of electrons and holes in opposite direction causes an electric current to flow across the device. This generated electric current is collected by contacts usually in the front and rear parts of the device.

As mentioned above, solar cells are made of semiconductors, typically silicon wafers. A solar cell results from the close contact of two silicon layers with different properties: one layer has a high concentration of electrons (commonly named n-type wafer) and the other layer has a high concentration of

holes (commonly named p-type wafers). This is the popular p-n junction. The difference of carrier concentrations between the n-type and p-type materials will result into the formation of a local electric field within the solar cells device, which will act as the driving force for the electron-hole pair separation. To obtain n-type and p-type materials, silicon wafers have to be doped by an appropriate element, phosphorus and boron respectively. Indeed, silicon belongs to group 4 in the periodic table, therefore it needs to form 4 covalent bonds to achieve chemical stability. When being doped by elements from group 3 (such as boron) or group 5 (such as phosphorus), the octet rule is no longer respected. As boron has only 3 electrons to share for covalent bonding, it lacks one electron: there is an empty space, named a “hole” where an extra electron should be. This missing electron – the hole – can wander freely around. Likewise, a silicon atom can be replaced by an element of the 5th group, such as phosphorus, which has one extra electron (5 valence electrons) compared to silicon. Silicon and phosphorus are sharing each 4 electrons to form 4 covalent bonds. However, phosphorus still has one more electron to share. At room temperature, the energy is enough for ionization. This extra electron can move freely in the conduction band and can therefore participate in conduction.

When the p-type and n-type silicon materials are brought into contact, the difference in the concentrations between carriers of the two sides generates a diffusion current, aiming at equalizing the carriers' concentration as illustrated in **Figure 2-1 (a)**. Therefore, holes from the p-side will diffuse to the n-side, leaving behind them negatively ionized atoms (boron). Likewise, electrons from the n-side diffuse to the p-side, leaving behind positively ionized fixed atoms (phosphorous). Indeed dopant atoms are fixed and cannot diffuse. These permanent charges create an electrical field (due to the Coulomb force) in the region located between the n-type and p-type materials. We name this region the space charge region (SCR) or the depletion region as shown in **Figure 2-1 (b)**. This electrical field is essential to the functioning of a solar cell, since it is the driving force for electron-hole pair separation.

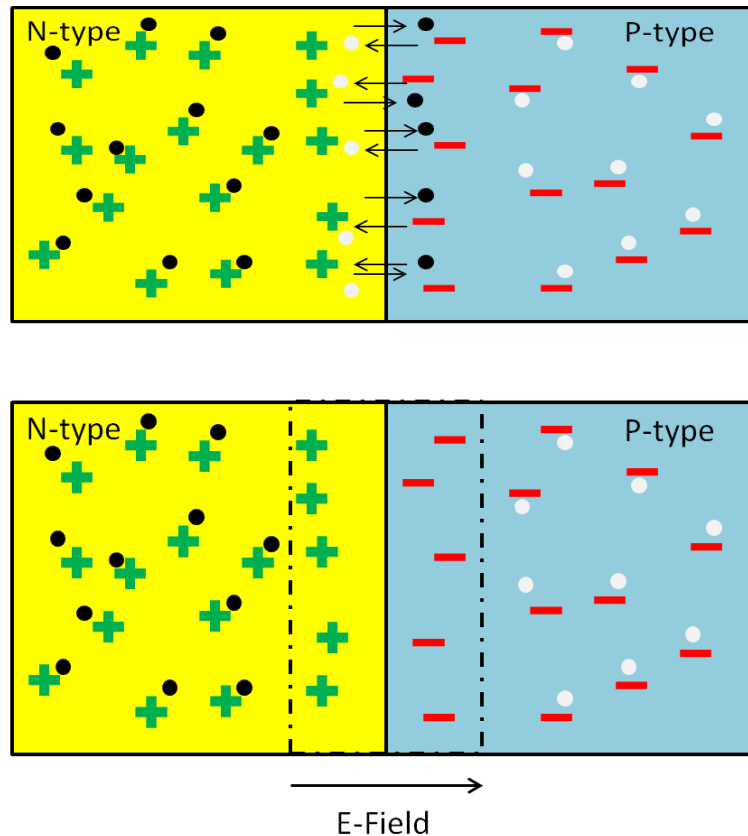


Figure 2-1: (a) Diffusion current at the interface between the p-type and n-type semiconductor in order to equalize the concentration of holes (white circle) and electrons (black circles). The green positive sign symbolize the phosphorus cations and the red negative sign symbolizes the boron anion which are doping the semiconductors.(b) Formation of the space charge region, depleted in charge carriers. The phosphorus and boron dopants create an internal electric field at the p-n junction.

This electric field forces the electrons to return into the n-type material, and the holes into the p-type material, countering in this manner the charge carriers' diffusion. Indeed electrons from the n-type semiconductor are repelled by the anions in the p-type semiconductor while they are attracted by the cations within the n-type material. Therefore two currents are countering themselves: the diffusion current due to disequilibrium in charge concentration and the drift current due to a local electric field at the SCR. At some point equilibrium is reached and an electric field is developing across the junction. This built-in electric field is responsible of the diode characteristic of the junction: it forces electrons to flow from the p-side to the n-side regions and forbid them to flow in the other direction.

When light strikes the cell, a portion of the light energy is absorbed and transferred to the semiconductor material. Atoms bombarded with photons with energy larger than the band gap of the material will give up electrons, generating electron-hole pairs on both sides of the junction. If these electron-hole pairs can be localized in the region of influence of this electric field (either because this electron-hole pair is generated very close or can diffuse to the space charge region), the field will push electrons to the n side and holes to the p-side because of this diode behavior. By placing metallic contacts on the n and p-regions and connecting them, electrons from the n-side will flow through the path to the p-side to recombine with holes that are driven there by the electric field. The solar cell is therefore delivering a power output which is the product of current and voltage of the cell that are generated respectively by the flow of electrons and the built-in electric field.

2.1.2 Definition of the Photovoltaic Parameters

As mentioned previously, a solar cell is acting like a diode, therefore an ideal solar cell can be modeled by a current generator in parallel with a diode. However, in reality solar cells are not ideal and we need to include 2 more electrical components: a series resistance and a parallel resistance (called the shunt resistance). The series resistance is caused by:

- the contact resistance between the silicon and the metallic electrodes,
- the resistance of the top and bottom contacts
- the bulk resistance of the semiconductor materials as semiconductor are not perfect conductors

Shunt resistance is due to current leakage across the p-n junction, due to poor insulation, for example, around the edge of the cells. They are usually attributed to manufacturing defects. **Figure 2-2** displays the equivalent circuit model of a solar cell [39].

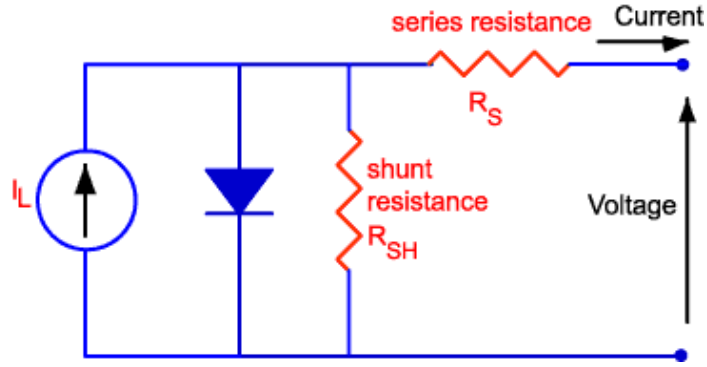


Figure 2-2: Equivalent circuit model of a solar cell [39].

The $J(V)$ characteristic of a solar cell in the presence of series and shunt resistances is given by the Eq. (2.1) below:

$$I = I_L - I_0 \left(\exp \left[\frac{q(V + IR_{series})}{nk_B T} \right] - 1 \right) - \frac{V + IR_{series}}{R_{shunt}} \quad 2.1$$

where I_L is the photo-generated current, I_0 is the diode saturation current, V is the voltage across the cell terminals, k_B is the Boltzmann's constant, q is the charge of the electron, n is the ideality factor, T is the temperature, R_{series} is the cell series resistance and R_{shunt} is the shunt resistance.

The quality of the p-n junction as a solar cell is measured by several factors called the solar cell parameters: the open-circuit voltage (V_{oc}), the short-circuit current density (J_{sc}), the fill factor (FF) and the efficiency (η). These parameters can be extracted from the current-voltage measurements of the cell, the so-called (I,V) curve which provides a lot of information on the junction quality. As illustrated in **Figure 2-3** ([40]), the short circuit current density is the current flowing across the cell when the cell is short-circuited. The open-circuit voltage is the maximum voltage that a solar cell can provide to an external circuit at zero current. The FF is a measure of “how square” the (I,V) curve of a cell is. This is defined as the ratio of the maximum electrical power obtainable from the device to the product of V_{oc} and J_{sc} . FF is therefore the ratio of the area of the dark pink to the light pink rectangles defined in **Figure 2-3**. The FF is given by Eq. (2.2):

$$FF = \frac{V_{mp} J_{mp}}{V_{oc} J_{sc}} \quad 2.2$$

where V_{mp} and J_{mp} , shown in **Figure 2-3** refer to the coordinates of the operating point that maximizes the power output.

Finally the efficiency, which is generally used to compare the performance of solar cells, is calculated as the ratio of the maximum power output to the incident power. The conditions under which solar cells are measured (solar spectrum, light intensity and temperature) have an impact on the performance measured, therefore there is a convention to carry out the measurements with an air mass 1.5 (AM 1.5) at 25°C with an irradiance of 1000 W/m². These conditions are defined as the standard test conditions (STC). The energy conversion efficiency η is then given by Eq. (2.3):

$$\eta = \frac{V_{mp}J_{mp}}{P_{in}} = \frac{V_{oc}J_{sc}FF}{P_{in}} \quad 2.3$$

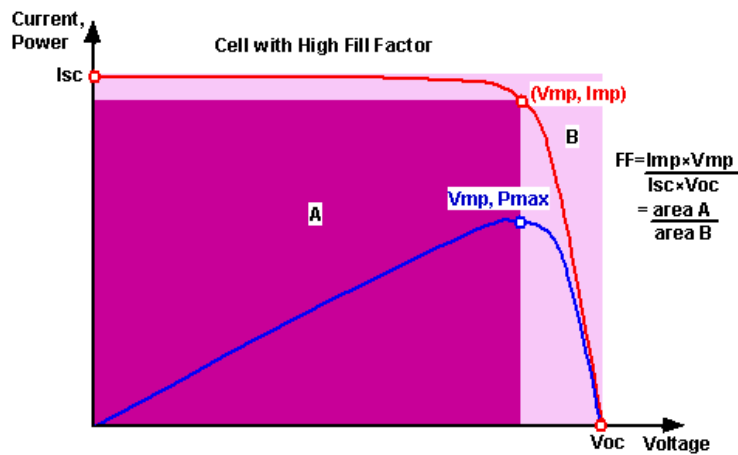


Figure 2-3: (I,V) curve of a solar cell and definition of the photovoltaic parameters [40].

2.2 Silicon Nanowires: Methods of Fabrication and Properties

2.2.1 Methods of fabrication

Many methods have been developed to fabricate silicon nanowires (SiNWs). Basically, they fall into two categories: bottom-up and top-down approaches. The former comprises mainly the vapor-liquid-solid (VLS) growth [41], [42], CVD [43] and Plasma Enhanced Chemical Vapor Deposition (PECVD) [44], [45] processes, while the latter includes dry reactive-ion-etching (RIE) [46]–[48], and solution based wet etching techniques [49].

2.2.1.1 Bottom-up

Chemical Vapor deposition via the Vapor-Liquid-Solid (VLS) process is a popular method used to fabricate dense, high aspect ratio, and vertical SiNWs [41], [42], [50]–[53]. In this approach, crystalline silicon wires are synthesized from gas particles through liquid metal-Si droplets as depicted in **Figure 2-4** ([54]). A thin layer of catalyst agent (generally gold) is first deposited onto a silicon wafer. The temperature is then increased above the catalyst-Si eutectic point, generating alloy droplets on the surface of the wafer. The growth process begins with the decomposition of a precursor gas into a catalyst droplet to create an alloy. Silicon precursor molecules, i.e., monosilane (SiH_4), predominantly crack at the droplet surface and silicon gets incorporated into the droplets by diffusion. Once supersaturation of the droplet is reached, a crystalline nanowire precipitates with a diameter similar to the droplet size at the liquid-solid interface (i.e. supersaturated droplet - substrate). The lateral growth is therefore limited by the droplet. There are two types of growth: the tip growth (the catalyst droplet is rooted at the top of the NWs) and the base growth (the catalyst droplet is rooted at the bottom of the NWs) which occur when the interaction between the metal and the substrate is weak and strong respectively. The bottom-up method can grow SiNWs whose diameter varies between 5 nm and 500 nm. LPICM has developed a strong expertise in the fabrication of SiNWs by PECVD from tin films [55], [56]. However this process induce unavoidable metallic contamination. In particular it is well-known that gold introduces deep-level electronic states in the Si band gap [57] which is detrimental to its use in electronic devices. Therefore a lot of effort has been put in the synthesis of SiNWs using other types of catalysts [44], [45], [55], [58] . Moreover, the control of the geometry (pitch, diameter and length) is challenging as it requires a perfect control of the size and position of the catalyst droplets during the growth.

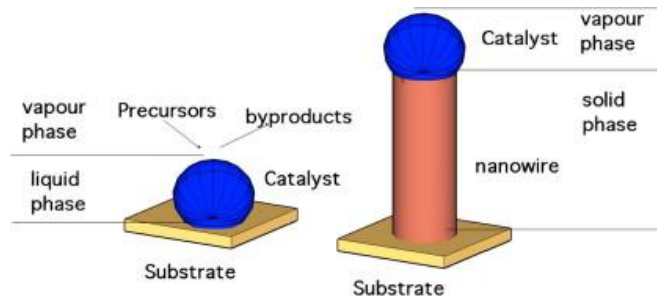
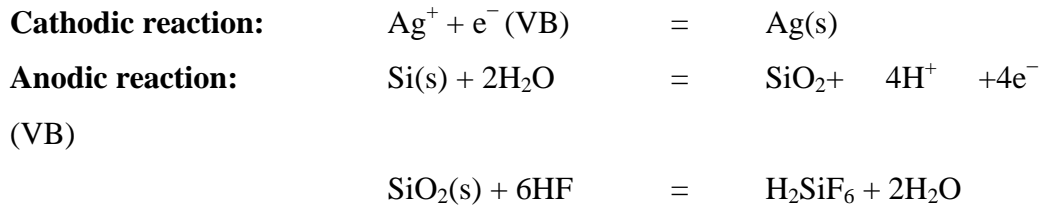


Figure 2-4: Scheme of the VLS Vapor Liquid Solid process [54].

2.2.1.2 Top down

Top down approach prepares SiNWs via the "sculpting" of the bulk Si material by lithography and etching or just catalyzed etching. The reactive ion etching (RIE) and the metal-assisted chemical etching (MACE) techniques are generally used to produce SiNWs. RIE is an etching process used in microfabrication which uses synergistic chemical (reactive species) and physical etching (ion bombardment) at the wafer surface to achieve etching with good anisotropy and selectivity. The plasma is generated at low pressure, usually 10-100 mTorr to achieve a more directional etching. By combining the RIE method with lithography, the size and density of SiNWs array can be well controlled [46]–[48]. Another advantage of this technique is that the SiNWs have the same doping as the original wafer. However the process is time consuming and expensive. Moreover, the roughness of the sidewall is also a problem as the surface is physically damaged by the ion bombardment [59].

The MACE method [49], [60] has been newly developed and is really promising for future industrial applications. This method, being simple and low cost, is able to produce SiNWs with a high aspect ratio over a large area. All there to do is to immerse Si wafers into a HF-AgNO₃ solution at room temperature. The mechanism proposed is a galvanic displacement reaction [61]–[63]. Silver plays the role of etching catalyst in the oxidizing HF solution. The final reaction is composed of the following cathodic and anodic reactions:



The whole reaction can be summed up as follows:



The synthesis of SiNWs is based on a redox reaction between Ag^+ and Si^0 . As Ag/Ag^+ has a more positive redox level than the energy of the valence band edge of Si, there is a preferential charge transfer from Si to Ag^+ as illustrated in step (a) of **Figure 2-5**. The reduction of Ag^+ into Ag nanoparticles occurs at the Si surface. The surface Si atoms are oxidized (anodic reaction) and supply the electrons for the Ag^+ reduction (cathodic reaction). The silicon surface is therefore locally oxidized (only where Ag is directly contacting the Si). The SiO_2 formed is next etched by HF, as shown in step (c) of **Figure 2-5**. We then observe the formation of silver nanoclusters on the surface due to the initial cathodic reaction of Ag^+ . These nanoclusters are restricting further oxidation of the Si surface. Indeed further reduction of Ag^+ in the etching solution occurs on the Ag nanocluster itself as shown in step (b) of **Figure 2-5**. This latter is relatively more electronegative than silicon (easy injection path for holes) and plays the role of a cathode by transferring electrons from the wafer below. The continuous reduction of the silver ions results in the formation of the so-called silver dendrites that are observed at the top of the nanowires. The silver nanoparticles captured in pores drill progressively, leading to the formation of a SiNW array.

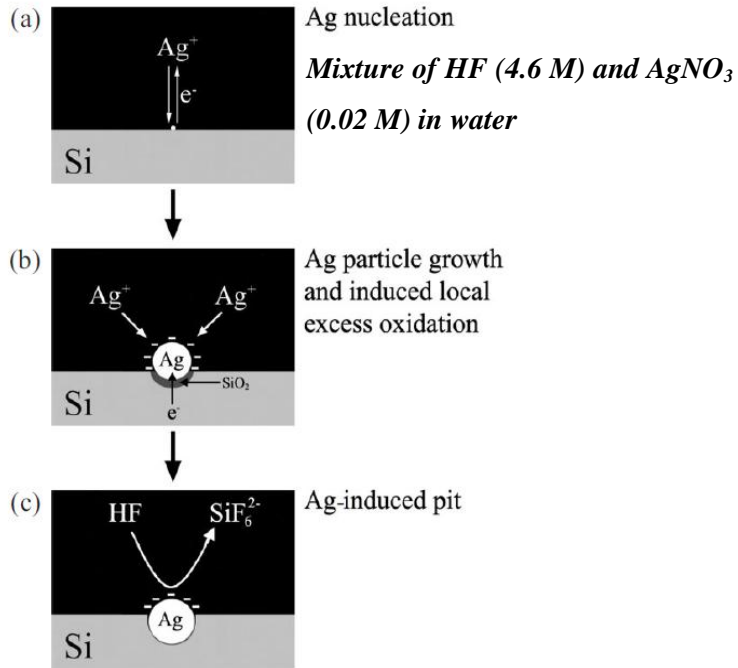


Figure 2-5: Mechanism of formation of SiNW by the MACE process. A silicon substrate is dipped in HF/AgNO₃ solution [61], [62]

SiNWs with different crystalline orientation can be produced by this method. The diameter typically lies in the range of 20 -200 nm while the length is controlled by the etching time. When coupled with some lithography techniques, such as the nanosphere lithography or interference lithography, the MACE method enables the production of nanowire arrays with perfect control over the pitch, diameter and length [60], [64].

Despite all these advantages, the MACE method suffers from an inherent problem which is a direct side effect of the method itself: this wet etching process relies on the use of a liquid phase (chemical solution), hence capillary forces arise, which result in the agglomeration of the SiNWs. This effect is visible in **Figure 2-6** where we show the top-view image of long SiNWs that we have fabricated by MACE. This agglomeration is highly undesirable and is often considered as a limiting factor to achieve high efficiency solar cells. Indeed large bundles prevent conformal coating of the arrays by photoactive material (inorganic or organic coating) [20], degrade the optical properties of the array [65], [66], and may lead to large series resistance [20]. Therefore developing a new process to reduce significantly the bundling of nanowires is of high interest.

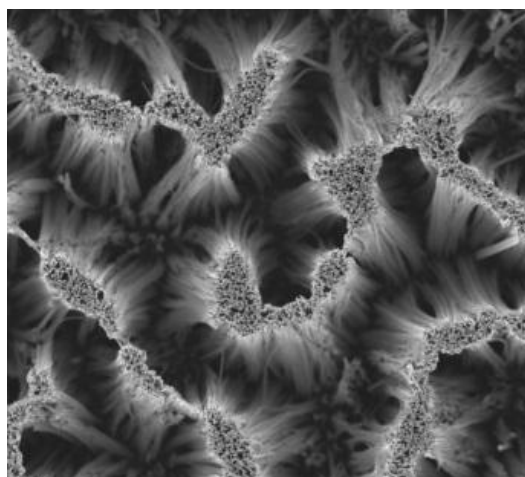


Figure 2-6: SEM picture of 10 μm SiNWs fabricated by MACE showing the strong agglomeration at the top-end of the SiNWs

With the above considerations on the different approaches available for the fabrication of SiNWs, we have decided to focus on the MACE method to fabricate SiNWs because of its undeniable advantages as stated above. Although the agglomeration of SiNWs fabricated by MACE is still problematic, we have proposed an approach to alleviate the issue, which will be presented in Chapter 4 of this thesis.

2.2.2 Optical properties

SiNWs have attracted much interest over the past few years because of their unique properties that can increase significantly the energy harvesting capabilities of solar cells. In conventional solar cells, when the light strikes the front surface of the device, a significant proportion of the light is reflected and does not penetrate into the device, which is a loss for the solar cell. In fact, the light is partially reflected at every interface within the device because of the mismatch in the refractive indices. For example bare Si reflects more than 30% of the light at normal incidence. This absorption loss is very critical and reduces the overall efficiency of the devices. However reflection is not the only absorption loss mechanism to consider: transmission loss which happens for very thin samples or for samples with no sufficient light trapping schemes is also critical. Absorption losses due to reflection and transmission are usually addressed by anti-reflective coating and light trapping schemes respectively.

Nanowires are very attractive candidates to reduce absorption losses as they have the potential to address both antireflection and light trapping issues. First NWs exhibit extremely low optical reflection. It has been demonstrated that SiNWs array reduces drastically the reflectance to less than 1.4% over a wide wavelength range of the solar spectrum from 300-600 nm as illustrated in **Figure 2-7** ([26], [27]) . As these measurements were carried out on thick samples, it does not provide any information on the light trapping capabilities of the device (no transmission is taking place for thick samples). This outstanding antireflection property might be explained by the fact that SiNWs possess diameters smaller than visible wavelength creating a subwavelength structure (SWS) surface, i.e. a surface-relief grating with a period smaller than the wavelength of light. Such a surface behaves like an antireflection surface, suppressing the reflection over a wide spectral range [26], [27]. Moreover, tapered nanowires / nanocones show an enhanced optical absorption as they behave as an effective medium with a gradual change in refractive index that accompanies the gentle change in the diameter of the SiNWs from the top to bottom. Indeed in this approach, the mismatch between refractive index of the two media (wire and air) is not abrupt but instead gradual, eliminating in this way the reflectance over most part of the spectrum [67], [68].

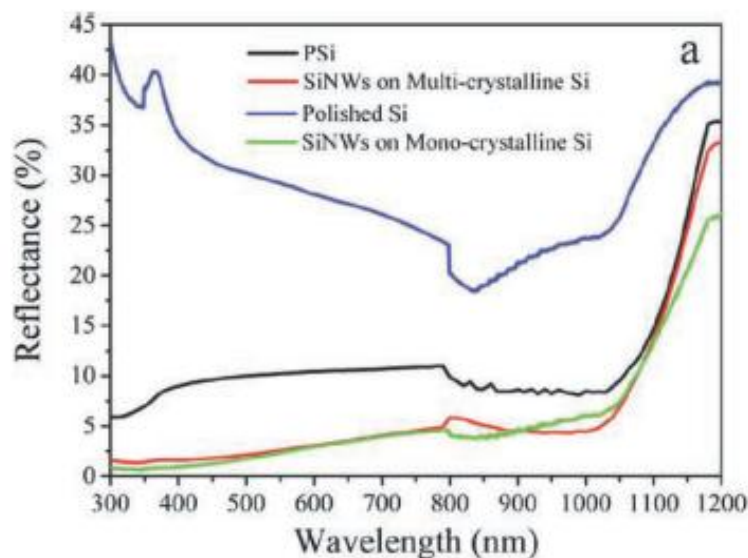


Figure 2-7: Reflectance measurement of porous (PSi), polished c-Si and SiNW arrays [26], [27].

Investigation of the light trapping capabilities of SiNWs is more challenging and only few works have reported on this issue. Indeed to investigate SiNWs light trapping, one should fabricate SiNWs etched on c-Si thin film, which in turn should be prepared on a transparent substrate to ensure no parasitic absorption. Such a structure is technically challenging to realize. Nevertheless, *Sivakov et al.* [69] successfully managed to study the optical properties of MACE mc-SiNWs on glass substrate. The mc-Si thin film was fabricated by laser crystallization of an a-Si:H film deposited on glass by PECVD, and the SiNWs were subsequently fabricated by MACE. They found that SiNWs etched on a 2.5-3 μm thick mc-Si layer do not transmit light between 300-550 nm which proves the light trapping capabilities of the SiNWs.

Nowadays light trapping schemes are commonly used in commercial solar panels and random texturization by pyramids has been adopted as the standard structure for the single crystal silicon texturization [70]. However an anti-reflective coating is still required to achieve low reflectance. Light trapping enhancement provided by standard texturization techniques is limited by the theoretical Yablonovitch limit to $2n^2$ where n is the refractive index of the medium (which is equivalent to an optical path enhancement of $4n^2$ due to angle averaging effects). The theoretical Yablonovitch limit has been established in 1982 [71] and is derived under a statistical ray optics approach. Ray optics is a simple theory where light is modeled as a straight line. It has been used for centuries as it is a simple and powerful concept which is able to explain most of the optical phenomena. However, this model does not take into account the wave nature of light and fails to explain optical phenomena when the wavelength of light is in the same order of magnitude as the dimensions of the objects that light is propagating through. Therefore by using more advanced concepts of the wave optics such as photonic crystal, plasmonic material, dielectric waveguides, sharp features, structured cells or wire-based cells, it has been shown that the theoretical Yablonovitch limit might be exceeded [46], [72]–[76].

As mentioned, SiNW arrays have been shown to exhibit outstanding optical properties with a very low reflectance in the visible range, even without any additional antireflective coating. Many theoretical studies have

demonstrated the potential of SiNWs to boost the optical absorption beyond the classical limit: optimally designed nanowires may significantly increase the absorption of the arrays beyond the theoretical limits of ray optics by a perfect control over the localization of the electromagnetic field. For example, *Garnett et al.* have measured an optical path enhancement of incident solar radiation within ordered SiNW arrays of 73, much higher than the Yablonovitch randomized scattering limit of $2n^2 \sim 25$ for silicon with no back reflector [46]. Theoretical studies usually investigate the interaction of electromagnetic waves with perfectly ordered SiNW arrays of precise dimensions. *Hu et al.* [77] have analyzed the effect of filling ratio (defined as the ratio between the top surface area occupied by the NWs within a unit cell and the top surface area of the unit cell), diameter and length on the optical absorption of SiNW arrays with a period of 100 nm. The results showed that SiNWs could drastically enhance light absorption in the high energy region (>2.8 eV) but not in the low energy region (< 2 eV) because of the small extinction coefficient of silicon, resulting in an overall reduced absorption for SiNWs. This issue can be addressed by using longer SiNWs or a back reflector. *Li et al.* [78] have further investigated the effect of the geometry of the periodic arrangement on the light trapping of SiNWs arrays, and correlated this result to the use of a non-optimal periodicity. Indeed, their work suggested that optimized light absorption is achieved when the periodicity is comparable to the light wavelength, between 250 and 1200 nm, and with a ratio diameter to periodicity of 0.8. With a small periodicity of 100 nm, the wavelength is much longer than the SiNW dimension, in particular in the low frequency regime, and therefore light penetrates through the SiNWs arrays easily “without seeing them”. Consequently, light scattering is reduced and the resulting transmission is very high. When the dimension of the SiNWs array is of the same order as the wavelength, diffraction occurs and scattering becomes dominant, which will then increase the optical path length and improve absorption. In this hypothesis, it is claimed that the periodicity of the SiNWs array is playing a critical role in the light absorption capabilities of the SiNWs.

This point of view has been challenged by *Foldyna et al.* [37], [38] who showed that the periodicity of the arrays is not that a sensitive parameter to light scattering. Indeed, *Foldyna et al.* have also studied optimization of light

trapping in periodic arrays by investigating the effect of geometric parameters such as the diameter, pitch and length on the optical performances. They suggested that the high absorption efficiency of SiNWs come from an efficient light coupling into their localized resonance mode inside the NWs. In fact a NW is behaving like an optical waveguide which guides the light along its length. They found that every nanowire is able to trap the light by confining propagating modes and that the high absorbing efficiency of SiNWs mainly depends on the strong light coupling into the guided modes inside every nanowire. Therefore the high absorption by SiNWs is due to individual effect rather than a group effect. As a consequence, the periodic arrangement is not playing a critical role but rather the volume fraction of SiNWs and their diameter. In particular, the confinement is extremely effective in the situation of matching diameter/wavelength resonance conditions and is still important even for non optimal resonance conditions where a leakage of the electromagnetic field might be observed. They also showed that the light absorbing efficiency is not sensitive to small variations in the geometric parameters, and fabrication processes that deliver perfect and precise geometries are not required. They also reported on the combination of SiNWs with different diameters which might further enhance the optical absorption. Another key point to highlight in understanding the enhanced absorption of SiNWs is their so-called "effective optical cross-section" (larger than their geometrical cross-section) which overlap, in particular in the case of dual-diameter geometry, and can boost the optical absorption in SiNWs.

2.2.3 Enhanced charge carrier collection

The p-n junction in solar cells based on SiNWs is not necessary axial, but can be radial. The radial p-n junction provides a short collection length for charge carriers, reducing their recombination, so that materials of inferior quality can be used. Every SiNW behaves as a tiny p-n junction, commonly named the core-shell structure. When a photon strikes the outer shell of a SiNW, an electron-hole pair is created and the generated carrier travels in the radial direction on very short distances before reaching the electrodes. This architecture is particularly favorable for minority carriers which only need to

diffuse over ten to hundred nanometers to reach the depletion region instead of the typical hundreds of micrometers in conventional Si based solar cells. Light trapping can also enhance the charge carriers generation. By tackling the charge collection and generation issues, solar cells based on SiNWs are expected to offer substantially improved performance [68].

2.2.4 Electronic properties

The size, surface-to-volume ratio, growth direction and morphology can affect the electronic properties of SiNWs. For example the band gap of SiNWs is related to the diameter of the wires. Indeed, when the SiNWs diameter is approaching the Bohr radius, quantum confinement is observed, resulting in a widening of the band gap. The dependence of the bandgap on the wire diameter, in the framework of the EMA-PIB model (Effective Masse Approximation - Particle In a Box), can be expressed as:

$$E_g = E_0 + \frac{C}{d^2} \quad 3.1$$

where E_g is the bandgap of silicon nanowire, E_0 is the bandgap of silicon, C a constant and d is the diameter.

Therefore SiNWs offer an opportunity to adjust the value of the band gap. Tuning of the band gap can be extremely useful to reduce heat losses in a solar cell by the use of optimal and/or complementary band gap materials inside the device. The dependence of the band gap on the SiNW diameter and on the surface terminations has been theoretically studied. Density functional theory calculations (DFT) by *Nolan et al.* [79] have shown that shrinking of SiNWs diameters results in an increase of the band gap and that very small SiNWs (less than 1 nm diameter) have direct band gap while bulk silicon is an indirect band gap material. The surface functionalization can also affect the tailoring of the band gap as investigated by *Nolan et al.* [79] and *Sacconi et al.* [80]. They showed that for the same diameter, different surface terminations will result in different values of the band gap. For example, *Sacconi et al.* showed that the widening of the band gap is larger for H-terminated compared to SiO₂ terminated SiNWs. Such difference is attributed to the reduced confinement provided by SiO₂. *Nolan et al.* explained this effect of surface termination by a

competition between quantum confinement and hybridization effect induced by some terminated groups such as OH or NH₂.

The electrical properties of SiNWs depend on the methods of fabrication. Indeed, SiNWs fabricated by a top down approach have the same electrical properties as the starting bulk material. For bottom-up SiNWs, an additional doping step is required during or after the fabrication process. This is achieved for example, by adding phosphine (PH₃) or trimethylborane (TMB) to silane (SiH₄) gas during the growth. As SiNWs present large surface-to-volume ratio, it is believed that the surface characteristics of SiNWs can have a great impact on their electrical properties. It has been demonstrated that surface modification treatment of SiNWs might result in excellent electrical characteristics. For example annealing treatment or passivation can increase the mobility of carriers in SiNWs [81].

2.3 Silicon Nanowire based Solar Cells

2.3.1 Basics of Nanowire Solar Cells

SiNWs have attracted much interest in the past decade due to their unique optical, structural, electrical, mechanical and thermal properties [26], [82], [83]. A legitimate question arises: What are the benefits of SiNW based solar cells over planar wafers cells? One important point to raise is that it is unlikely SiNWs based solar cells can achieve higher efficiency than the standards limits, but they can cut significantly the cost of production as they reduce the requirements on material purity and the quantity of material needed to reach these limits in conventional solar cells. Moreover, the technology can be transferred to the thin film technology and even on glass substrates, and thus reduces the cost further.

SiNWs offer a wide range of advantages that can improve significantly the photoconversion efficiency including almost perfect light trapping, very low reflection, reduced sensitivity to material defects, tunable band gap, easy strain relaxation due to small diameter and different charge separation mechanisms compared to conventional wafer planar cells. Moreover, NWs made of a wide range of materials or combination of materials have been reported such as

silicon, cadmium, selenide, telluride, zinc oxide, zinc sulfide, germanium, gallium, nitride, arsenide, indium, titanium oxide, copper oxide [28]–[36], [84]–[97], so NWs can be used for many different types of devices.

There are basically 3 concepts under consideration when discussing about SiNWs based solar cells [68].

- The radial p-n junction
- The axial p-n junction
- The substrate p-n junction

The 3 different types of junctions are displayed in **Figure 2-8** ([68]). These 3 types of junctions benefit from the outstanding optical properties of SiNWs which increase light absorption and reduce light reflection. They also benefit from easy strain relaxation and tunable band gap due to the small dimensions involved.

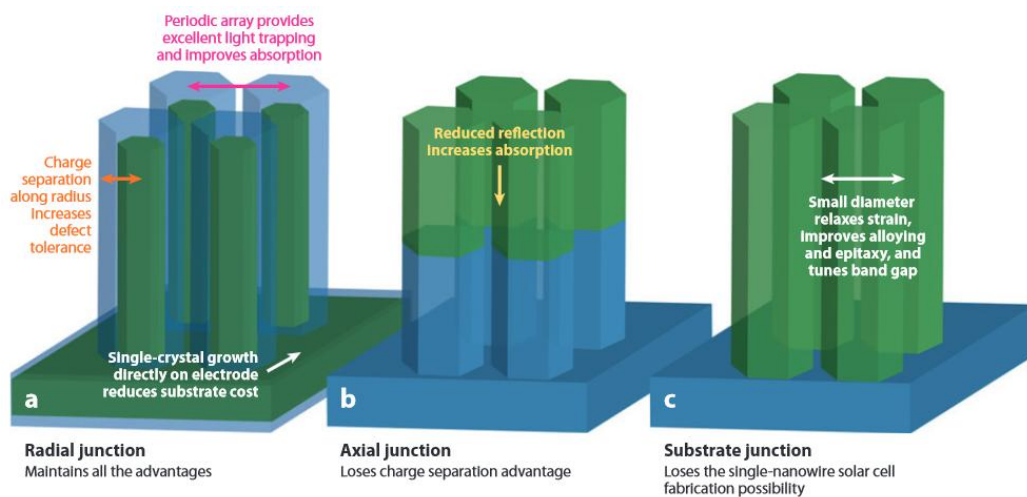


Figure 2-8: Advantages and drawbacks of the radial, axial and substrate junctions [68]

Among the 3 structures, only the radial junction can potentially benefit from all the advantages offered by SiNWs [68]. As for axial and substrate junction, we lose the advantage of radial charge separation with small collection length, and consequently tolerance to defects [68]. Indeed, in both cases, the electrical field is developed in the axial direction as in standard planar cells. Therefore the charge separation mechanism is similar to that in planar cells. Besides, for the substrate p-n junction, it is not possible to detach the nanowires

from the substrate to realize a working solar cell only based on SiNWs (for flexible and thin film applications).

As the p-n junction area of radial junction is very large, we expect lower V_{oc} and lower photo-current density because of surface defects recombination. However, the short distance offered by the radial junction between the charge generation and the p-n junction will in contrary increase the V_{oc} and J_{sc} . As for axial and substrate junction, the area of the p-n junction is much smaller, and therefore we expect a higher V_{oc} and higher photocurrent density.

Finally, for the 3 structures, there is a large outer surface area, which may result in high surface recombination and lower the V_{oc} .

2.3.2 Solar Cells based on Silicon Nanowires: a review

Table 2-1 summarizes the application of SiNWs fabricated by top-down (MACE and RIE) and bottom up approaches (PECVD) in different solar cell technologies. Generally it has been used as an antireflective layer by taking advantage of the low optical reflection (axial and substrate junction) of SiNWs or as a radial / core-shell p-n junction to make the best use of the short collection distance offered by the radial geometry.

Several works have been reported on the use of SiNWs for solar cell applications. Our group has investigated thin film hydrogenated amorphous silicon (a-Si:H) radial junction solar cells by VLS-grown SiNWs with a highest reported efficiency of 9.2% on glass substrate [55], [56]. This architecture uses a 100 nm thick a-Si:H as the active material and the c-SiNWs as the conducting channel. c-SiNWs have also been used as the active material. In this type of devices, the p-n junction is typically formed by the high temperature phosphorus diffusion process. As a consequence, the NWs might be fully converted to n-type (or p-type) materials, making an axial or substrate p-n junction rather than a radial p-n junction. In this case the SiNWs are used for their good anti-reflection and enhanced light absorption, but the benefit of the radial junction is lost [27], [46], [62], [69], [98]–[101]. For example, highly efficient substrate junction solar cells based on SiNWs fabricated by MACE and diffusion process were fabricated with a reported efficiency of 17.11% for an area of 154.83 cm². Moreover an efficiency of 18.2% [102], and more

recently an efficiency of 22.1% [103], was also achieved for black silicon solar cells nanostructured by a wet etching process on a c-Si wafer. Nevertheless, it is very challenging to fabricate a radial junction by the diffusion process since the latter tends to produce axial or substrate junction. However, SiNWs with larger diameter fabricated by deep reactive ion etching (DRIE) have been successfully used in solar cells with a core shell structure fabricated using the phosphorus diffusion process with a reported efficiency of 10.8 % for a few micrometer thick c-Si films [104].

SiNWs have also been used in heterojunction devices resulting in radial type junction. Heterojunction solar cells are devices where the p-side and n-side of the junction are made of different materials. For example heterojunction with intrinsic thin layer (HIT) device is a solar cell where the n-side (respectively p-side) of the junction is made of c-Si while the p-side of the junction (respectively n-side) is made of hydrogenated amorphous silicon [105]. Hybrid devices are also another popular type of heterojunction solar cells where one of the semiconductor of the junction is made of inorganic material like silicon while the other consists of an organic layer. Basically heterojunction solar cells are made by depositing an amorphous silicon or an organic layer on a c-Si substrate. The use of SiNWs in heterojunction solar cells brings an additional challenge of passivation compared to axial or radial homojunctions solar cells mentioned above. Indeed, while diffusion-fabricated p-n junctions are formed inside SiNW bulk, for HIT or hybrid devices the p-n junction is formed at the surface of the SiNW which may present many surface defects.

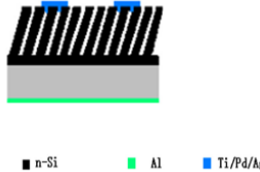
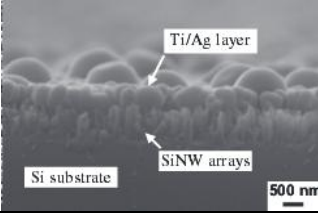
Today, only few works have been published on HIT solar cells based on SiNWs [106]–[109]. So far, the best efficiency reported is 10.04% for SiNWs upon addition of a thin insulating layer of Al_2O_3 to passivate the SiNWs surface [107]. An atomic layer deposition (ALD) technique was used for the Al_2O_3 and contact deposition. Another interesting work claimed an efficiency of 12.2 % for HIT solar cells based on silicon microwires (SiMWs) [110] with radii ranging from 1.5 μm to 50 μm fabricated by DRIE. Nevertheless, SiMWs do not boost the light trapping inside the cells as much as SiNWs can. So far, all the studies published on SiNW based HIT solar cells are based on thick

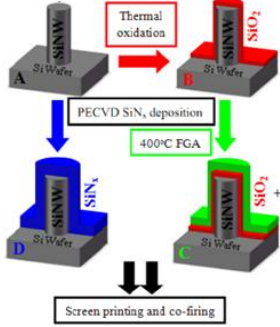
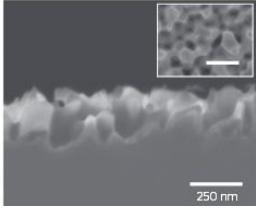
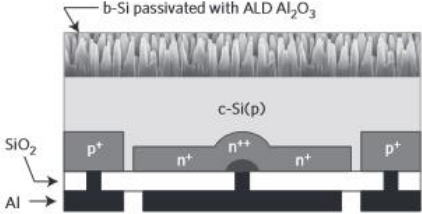
crystalline silicon wafers, while the final objective is to apply this type of architecture to Si thin films.

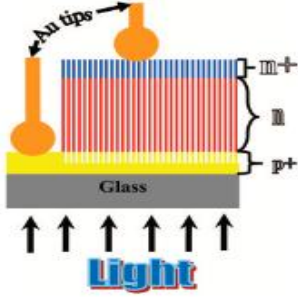
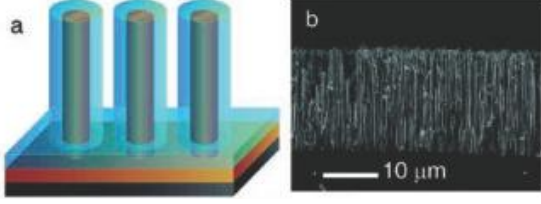
Several works have also been published on the potential of hybrid solar cells based on nanostructures. Our group was the first to report highly efficient hybrid solar cells based on the combination of SiNWs with both a single layer PEDOT:PSS and a dual organic layer of PEDOT/PSS and spiro-OMeTaD, achieving efficiencies of 9 and 10.3% [20], [111] respectively. A deeper understanding of the surface passivation has enabled us to improve the power conversion efficiency up to 12.4% [112].

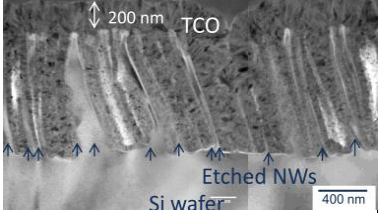
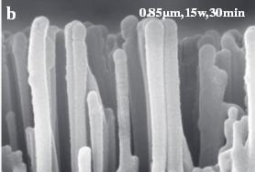
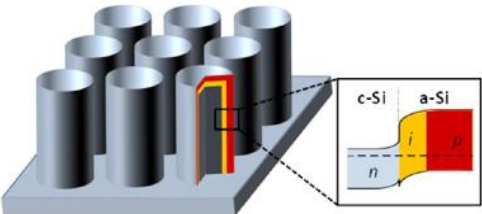
The key results and main findings of SiNWs applied in different types of solar cells are summed up in the following **Table 2-1**.

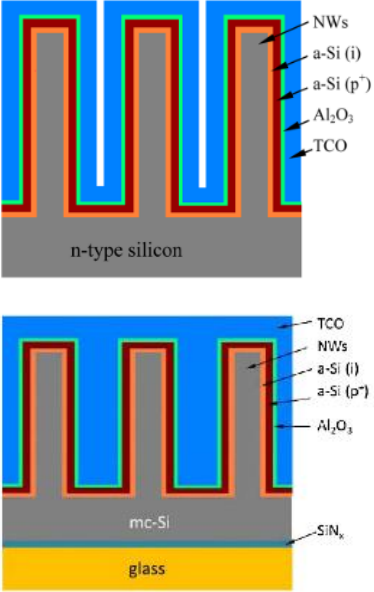
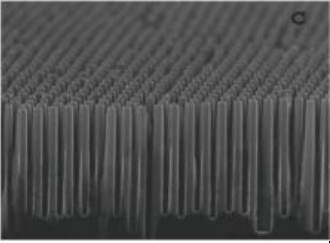
Table 2-1: Key results and finding on SiNWs based Solar Cells.

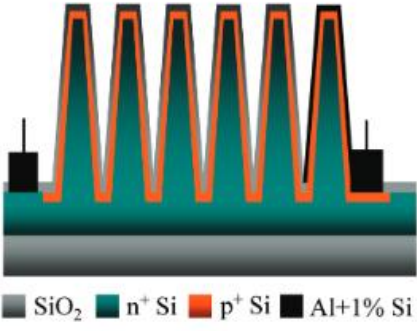
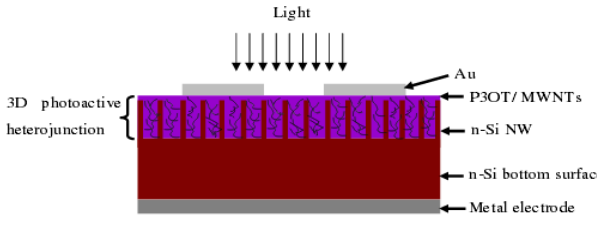
Type of junction	Structure	Efficiency
<p><i>Axial or Substrate junction - Junction formed by phosphorous diffusion - SiNWs are used for their enhanced optical properties</i></p>		
<p>Substrate p-n homojunction (2005) [31]</p>	<p>Conventional phosphorous diffusion on SiNWs fabricated by wet etching on p-type crystalline (100) and polycrystalline substrate.</p>  <p>The SiNW cell fabrication procedure can be applied to c-Si wafer with different orientations and to polycrystalline substrate. SiNWs cell exhibit lower efficiency than their planar counterpart, and this is attributed to strong surface recombination due to the ultra high surface area of SiNWs and the presence of many surface defects and dangling bonds causing short carrier diffusion length.</p>	<p>Crystalline $\eta = 9.31\%$ $V_{oc} = 0.5485V$ $J_{sc} = 26.06 \text{ mA/cm}^2$ $FF = 65.12\%$</p> <p>Polycrystalline $\eta = 4.73\%$ $V_{oc} = 0.4756V$ $J_{sc} = 20.99 \text{ mA/cm}^2$ $FF = 47.4\%$</p>
<p>Substrate p-n homojunction (2008) [98]</p>	<p>Standard phosphorous diffusion on SiNWs fabricated by wet etching on p-type c-Si crystalline (111) wafers. SiNWs length was about 3-5 μm</p>  <p>The high efficiency of the cell is attributed to the very low reflection of SiNW arrays combined with the reduced series resistance of the slanted structure, allowing a better electrical contact.</p>	<p>$\eta = 11.37\%$ $V_{oc} = 0.58V$ $J_{sc} = 27.1 \text{ mA/cm}^2$ $FF = 72.22\%$</p>
<p>Substrate p-n homojunction (2011) [113]</p>	<p>Conventional phosphorous diffusion on SiNWs fabricated by wet etching on p-type c-Si (100) wafers.</p>  <p>Performance improvement is explained by a careful design of the electrodes where SiNWs are selectively etched on the active area and contacts are made over planar surfaces. However, the FF is rather low.</p>	<p>$\eta = 13.7\%$ $V_{oc} = 0.544V$ $J_{sc} = 37 \text{ mA/cm}^2$ $FF = 68\%$</p>

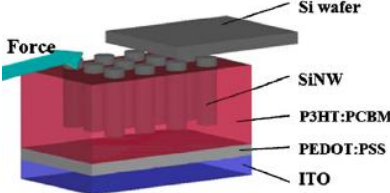
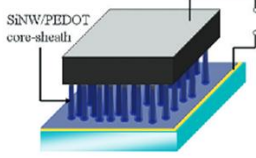
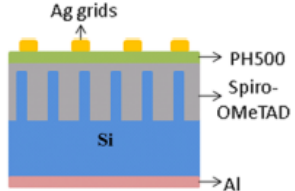
<p>Substrate p-n homojunction (2013) [99]</p>	<p>SiNWs were fabricated by MACE on texturized p-type c-Si with pyramids. The junction was formed by phosphorus diffusion process. After completion of the cell, SiNWs were passivated by SiO₂, SiO₂-SiN_x or SiN_x only. The area of the cell is 154.83 cm².</p> 	<p>$\eta = 17.11 \%$ $V_{oc} = 0.5485V$ $J_{sc} = 35.8 \text{ mA/cm}^2$ $FF = 77.2\%$</p>
<p>Substrate p-n homojunction (2012) [102]</p>	<p>Black silicon was fabricated via wet etching on p-type (100) c-Si wafer. The junction was formed via conventional phosphorous diffusion process. The completed cell was capped by SiO₂ obtained by thermal oxidation to passivate the nanostructure. The area of the cell is 0.8081 cm².</p> 	<p>$\eta = 18.2 \%$ $V_{oc} = 0.628V$ $J_{sc} = 36.5 \text{ mA/cm}^2$ $FF = 79.6\%$</p>
<p>IBC substrate p-n homojunction (2015) [103]</p>	<p>Black silicon was fabricated by using cryogenic deep reactive ion etching (DRIE). The black silicon was passivated by a thin Al₂O₃ layer. The design of the structure was an interdigitated back-contact back-junction (IBC). The area of the cell is 9 cm².</p>  <p>This record efficiency is explained by the excellent surface passivation provided by Al₂O₃ deposited by the ALD technique. As IBC cells are very sensitive to the front surface recombination velocity, these results show that black silicon based solar cells are no longer limited by their surface recombination and the nanostructured surface can be effectively passivated</p>	<p>$\eta = 22.1 \%$ $V_{oc} = 0.665V$ $J_{sc} = 42.2 \text{ mA/cm}^2$ $FF = 78.7\%$</p>

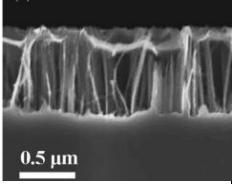
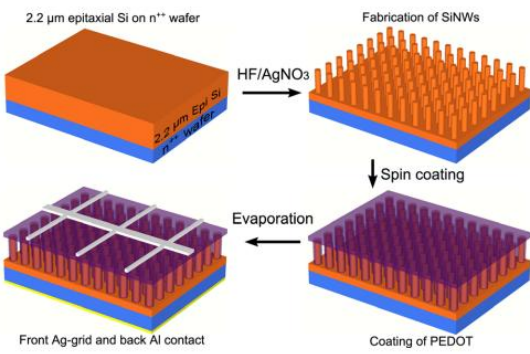
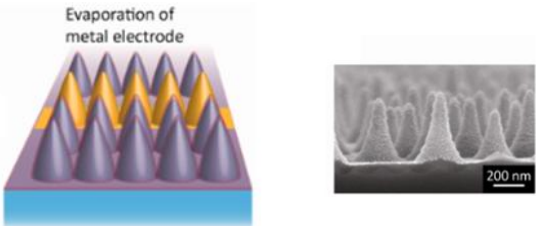
<p>Axial p-n homojunction (2009) [69]</p>	<p>MACE on 2.7 μm multicrystalline p+nn+ doped silicon layers deposited on glass. The multicrystalline layer was obtained through the laser crystallization of a (p) a-Si:H film deposited by electron beam evaporation (EBE). Doping was realized by a standard phosphorus diffusion process.</p>  <p>SiNWs based solar cells were successfully fabricated on glass substrate. High series resistance and shunting of the cell are the main issues to be addressed to improve the cells performance.</p>	<p>$\eta = 1.4 - 4.4\%$ $V_{oc} = 0.45\text{V}$ $FF = 30\%$</p>
<p>Radial or Coreshell p-n junction</p>		
<p>Heterojunction - Junction formed by PECVD</p>		
<p>p-n heterojunction (2008) [114]</p>	<p>n-type SiNWs were fabricated by MACE. (p) a-Si:H film was deposited by Chemical Vapor Deposition (CVD) and further crystallized by Rapid Thermal Annealing (RTP). Extremely long SiNWs were used (18 μm).</p>  <p>Poor performances were attributed to high surface recombination combined with SiNWs roughness and high series resistance due to the poor conductivity of the poly-crystalline shell capping the SiNWs.</p>	<p>$\eta = 0.46 \%$ $V_{oc} = 0.29\text{V}$ $J_{sc} = 4.28\text{mA/cm}^2$ $FF = 33\%$</p>

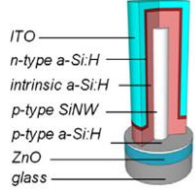
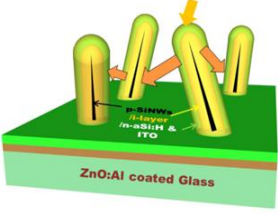
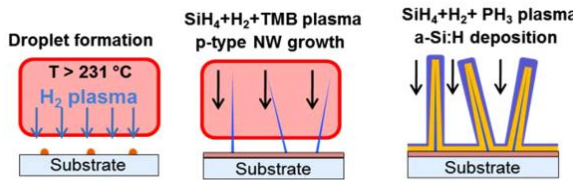
<p>HIT (2012) [106]</p>	<p>SiNWs were etched into n-type c-Si wafer. The core-shell structure was formed by deposition of an a-Si:H heteroemitter by Plasma Enhanced Chemical Vapor deposition (PECVD). Al doped ZnO (AZO) contacts were deposited by Atomic Layer Deposition.</p> 	<p>$\eta = 7.3\%$ $V_{oc} = 0.476V$ $J_{sc} = 27.03 mA/cm^2$ $FF = 56.2\%$</p>
<p>HIT (2013) [109]</p>	<p>SiNWs were fabricated by MACE and the junction was completed by the deposition of a-Si:H heteroemitter on top of the SiNW arrays by PECVD.</p>  <p>Effect of the deposition parameters on the passivation of SiNWs by a-Si:H was investigated. Minority lifetime and a-Si:H thicknesses are strongly depending on the deposition time and on the plasma power. Correlation of the the V_{oc} with the deposition time was more complex to investigate and seems to be depending on the length of SiNWs.</p>	<p>$\eta = 3.97-7.24\%$ $V_{oc} = 0.31-0.37V$ $J_{sc} = 21-23.5 mA/cm^2$ $FF = 61-67\%$</p>
<p>HIT (2012) [110]</p>	<p>Si microwires were fabricated by DRIE on low quality c-Si wafer. The heterojunction was formed by deposition of 12-16 nm of a-Si:H by PECVD. Diameter of the microwires was in the range 1.5 -50 μm. and the length was about 22 μm.</p>  <p>The high efficiency was attributed to the excellent passivation provided by a-Si:H, high collection efficiency and optimization of the radii of the microwires. These results have to be balanced by the fact that the passivation is less challenging as compared to SiNWs as the latter exhibit higher surface-to-volume ratio due to the small diameter involved.</p>	<p>$\eta = 12.2\%$ $V_{oc} = 0.591V$ $J_{sc} = 31.1 mA/cm^2$ $FF = 70.9\%$</p>

<p>HIT (2013 & 2014) [107], [108]</p>	<p>SiNWs were fabricated by MACE and the heterojunction was formed by plasma deposition of a-Si:H film. A thin insulating layer of Al₂O₃ was then deposited on top of the structure by ALD.</p>  <p>This concept was further transferred to the thin film technology. Indeed mc-SiNWs on glass were fabricated by applying the MACE process to a thin layer of mc-Si. The mc-Si layer was obtained through the laser crystallization of a (n) a-Si:H film deposited by PECVD on glass. The SiNWs underwent the same fabrication process described above.</p>	<p>c-Si $\eta = 10.04\%$ $V_{oc} = 0.517V$ $J_{sc} = 26.46 \text{ mA/cm}^2$ $FF = 73.4\%$</p> <p>mc-Si $\eta = 8.8$ $V_{oc} = 0.53V$ $J_{sc} \sim 25 \text{ mA/cm}^2$</p>
<p><i>Homojunction - Junction formed by Diffusion</i></p>		
<p>p-n homojunction (2010) [46]</p>	<p>Combination of RIE and silica bead assembly and boron diffusion on 8 and 20 μm thick epitaxial film on highly doped n++ substrate. The SiNWs were 5 μm long with an average diameter of 390 nm. The junction depth was estimated at 160 nm</p>  <p>Investigation of the effect of SiNW length shows that longer NWs increased both recombination and absorption. A path length enhancement between 1 and 73 was calculated for different SiNW geometries</p>	<p>$\eta = 5-6 \%$</p>

<p>p-n homojunction (2010) [104]</p>	<p>Si nano-conical-frustum (NCF) were fabricated via self-powered parallel electron lithography (SPEL) and RIE. Arrays with a periodicity of 800 nm and a length of 3.5 μm SiNWs on top of a c-Si thin film of 1.5 μm (SOI wafer) were fabricated. The radial junction was formed by boron ion implantation and further annealed at 900°C to activate dopants and repair damages caused by the doping process. The junction depth is estimated at 80 nm. The overall structure was passivated by 20 nm of SiO₂. Planar cells based on 5 μm thick Si-layer were fabricated as a reference.</p> 	<p>$\eta = 10.8\%$ $V_{oc} = 0.59\text{V}$ $J_{sc} = 26.4\text{mA/cm}^2$ $FF = 69\%$</p>
<p><i>Heterojunction - Hybrid Solar cells</i></p>		
<p>Hybrid solar cells p-n heterojunction (2009) [115]</p>	<p>SiNWs were fabricated by MACE on n-type c-Si (111) wafers. The junction was formed by drop casting p-type poly(3-octylthiophene) (P3OT) polymer on the SiNW arrays. Carbon nanotubes were added to the organic mixture to improve carrier transport and exciton dissociation.</p>  <p>Poor band alignment between Si valence band and the HOMO level of P₃OT, the poor transparency of the gold electrode and high series resistance are limiting the PCE of such cells.</p>	<p>$\eta = 0.61\%$ $V_{oc} = 0.353\text{V}$ $J_{sc} = 7.85\text{mA/cm}^2$ $FF = 22\%$</p>

<p>Hybrid solar cells</p> <p>p-n heterojunction</p> <p>(2009)</p> <p>[116]</p>	<p>SiNWs were first incorporated to an organic blend of P3HT/PCBM. SiNWs fabricated by MACE were subsequently separated from the Si substrate by mechanical force, so that the final structure is composed of free standing SiNWs embedded into an organic material. Solar cells with and without SiNWs were fabricated. Upon insertion of SiNWs, the cell's efficiency increases from 1.21% to 1.93%.</p>  <p>SiNWs are believed to improve transport of electrons and exciton dissociation as well as increasing light absorption compared to the reference cell without the SiNWs. The originality from this work relies on the separation of SiNWs from the substrate, therefore the contribution of SiNWs can be really investigated.</p>	$\eta = 1.93\%$ $V_{oc} = 0.425V$ $J_{sc} = 11.61 \text{ mA/cm}^2$ $FF = 39\%$
<p>Hybrid solar cells</p> <p>p-n heterojunction</p> <p>(2010)</p> <p>[65]</p>	<p>SiNWs were fabricated by MACE on n-type c-Si (100) wafers and PEDOT:PSS was spin coated over the arrays in order to form the p-n junction. The length of SiNWs was 2.78 μm.</p>  <p>An efficiency of 5.09% was reported. Long SiNWs agglomerated and changed the morphology of the PEDOT:PSS films, resulting in poor coating and low efficiency.</p>	$\eta = 5.09\%$ $V_{oc} = 0.47V$ $J_{sc} = 19.28 \text{ mA/cm}^2$ $FF = 61\%$
<p>Hybrid solar cells</p> <p>p-n heterojunction</p> <p>(2011)</p> <p>[20]</p>	<p>SiNWs were fabricated by MACE on n-type c-Si wafers. The junction was formed by spincoating PEDOT:PSS combined with spiro-OMeTAD. The effect of the length was investigated.</p>  <p>Highly efficient hybrid solar cells produced at low cost are reported for the first time. The reduced efficiency with increasing length is attributed to SiNWs agglomeration which prevents proper coating of the SiNWs by the organic material.</p>	$\eta = 10.3\%$ $V_{oc} = 0.57V$ $J_{sc} = 30.09 \text{ mA/cm}^2$ $FF = 58.8\%$

<p>Hybrid solar cells</p> <p>p-n heterojunction</p> <p>[111]</p>	<p>SiNWs were fabricated by MACE on n-type c-Si wafers. The junction was formed by spin coating PEDOT:PSS.</p> 	<p>$\eta = 9.0\%$ $V_{oc} = 0.53V$ $J_{sc} = 26.3 \text{ mA/cm}^2$ $FF = 64.2\%$</p>
<p>Hybrid solar cells</p> <p>p-n heterojunction</p> <p>(2012)</p> <p>[117]</p>	<p>SiNWs were fabricated by MACE on 2.2 μm n-type epitaxial thin films deposited on highly doped (n++) substrate. The junction was formed by spin coating PEDOT:PSS.</p> 	<p>$\eta = 5.6\%$ $V_{oc} = 0.57V$ $J_{sc} = 13.6 \text{ mA/cm}^2$ $FF = 71.9\%$</p>
<p>Hybrid solar cells</p> <p>p-n heterojunction</p> <p>(2012)</p> <p>[118]</p>	<p>Si nanocones were fabricated by colloidal lithography. The junction was formed by spin coating PEDOT:PSS</p> 	<p>$\eta = 11.1\%$ $V_{oc} = 0.55V$ $J_{sc} = 29.6 \text{ mA/cm}^2$ $FF = 67.7\%$</p>
<p>SiNWs by VLS - Radial heterojunction</p>		

<p>Radial heterojunction - VLS</p> <p>[119]</p>	<p>SiNWs were grown by PECVD and were covered by (i) a-Si:H and a window layer of n-type a-Si. Effects of the doping and SiNW length on the performance of SiNWs cell were investigated.</p>  <p>J_{sc} was drastically improved when the SiNWs length was tuned from 1 μm (8.8 mA/cm^2) to 3 μm (13 mA/cm^2). Improvement in V_{oc} was achieved by the use of Sn catalyst and by boosting the doping of c-SiNWs. Thinner (n) a-Si:H improved the spectral response in the blue regime but to the detriment of the FF.</p>	<p>$\eta = 5.6\%$ $V_{oc} = 0.80\text{V}$ $J_{sc} = 13\text{mA}/\text{cm}^2$ $FF = 53.8\%$</p>
<p>Radial heterojunction - VLS</p> <p>[55]</p>	<p>The SiNWs based solar cells were fabricated in one pump-down PECVD process. P-type c-SiNWs were first grown on glass substrate, followed by the deposition of (i) a-Si:H and (n) a-Si:H. The absorber a-Si:H thickness was about 100 nm. In this type of junction, charge carriers are generated in the (i) a-Si:H layer and not in the c-SiNWs.</p>  <p>Light induced degradation of such samples is only of 6% while standard light induced degradation of planar p-i-n junction is in the order of 15 to 20%. The improved stability is attributed to the thin thickness of (i) a-Si:H required in radial SiNWs cell. Such high efficiency was achieved through the optimization of the SiNW density.</p>	<p>$\eta = 8.14\%$ $V_{oc} = 0.80\text{V}$ $J_{sc} = 16.1\text{mA}/\text{cm}^2$ $FF = 62.8\%$</p>
<p>Radial heterojunction - VLS</p> <p>[56]</p>	<p>Further optimization was carried out on the VLS SiNWs based solar cells introduced above. Some modifications to the p-type c-SiNWs / (i) a-Si:H / (n) a-Si:H radial solar cells were investigated. The effect of the addition of a (p) a-Si:H with a proper doping gradient on the c-SiNWs prior deposition of (i) a-Si:H was studied. Finally the (n) a-Si:H window layer was replaced by n-type $\mu\text{-SiO}_x\text{:H}$.</p>  <p>Improvement of the V_{oc} up to 0.9V was achieved by the insertion of 10 nm (p) a-Si:H with a doping gradient. The J_{sc} can be improved by replacing the window layer with a material of wider band gap to reduce parasitic light absorption in this layer. This was achieved by replacing the n-type a-Si:H by n-type $\mu\text{-SiO}_x\text{:H}$.</p>	<p>Effect of additional (p) a-Si:H</p> <p>$\eta = 7.6\%$ $V_{oc} = 0.9\text{V}$ $J_{sc} = 13.6\text{mA}/\text{cm}^2$ $FF = 62\%$</p> <p>Effect of n-type $\mu\text{-SiO}_x\text{:H}$ layer</p> <p>$\eta = 9.2\%$ $V_{oc} = 0.82\text{V}$ $J_{sc} = 15.2\text{mA}/\text{cm}^2$ $FF = 73.7\%$</p>

This literature review shows the large diversity of solar cell devices based on SiNWs that have been studied so far. As mentioned earlier, we will be working on SiNWs fabricated by the top-down MACE process. NWs will be integrated into two different solar cell technologies: hybrid devices and heterojunction with intrinsic thin layer (HIT) devices. The best efficiency reported by HIT solar cells based on SiNWs fabricated by MACE is 10.03% [107], [108]. In 2011, our group was the first to report highly efficiency hybrid devices based on the combination of etched SiNWs with an organic layer. These solar cells exhibit efficiency about 10% (9% [111] and 10.3% [20]).

2.4 Heterojunction with Intrinsic Thin Layer Solar Cells

This section is devoted to the description of the heterojunction with intrinsic thin layer (HIT) solar cell structure that we have used in this work. Basically a HIT device relies on the combination c-Si and a-Si:H thin films in order to form the junction at low temperature. HIT is a mature technology that holds the world record efficiency (25.6%) for single junction silicon devices. First we describe the materials used in this structure before introducing the working principle of a HIT device.

2.4.1 Hydrogenated Amorphous and Crystalline Silicon properties

2.4.1.1 Atomic structure

Silicon is the cornerstone of modern electronic industry, being the main material in use in the semiconductor and MEMS industries. Therefore silicon is a well known material which has been extensively studied. As such its characteristics and processing are quite well mastered. In crystalline silicon, atoms are arranged in an ordered structure with a long range order as shown in **Figure 2-9** ([120]). Each silicon atom is systematically coordinated to four other silicon atoms by covalent bonds of the same length with equal angles between them [120]. As displayed in **Figure 2-9**, the atomic structure of hydrogenated amorphous silicon (a-Si:H) differs from that of crystalline silicon. Most of silicon atoms within a-Si:H film are likewise fourfold coordinated, but with small variations in the angle between the bonds ($\pm 10^\circ$) and in the

bonding length [120]. As depicted in **Figure 2-9**, there is nothing like a long-range order in the atomic structure of a-Si:H. Such structure, characterized only by a short-range order over a few atomic distance, is commonly named as a continuous random network. The distorted covalent bonds within a-Si:H films, called the strained bonds, are more energetic than covalent bonds in crystalline structure and are therefore less stable and are more likely to break [120]. Most of the defects in a-Si:H films are consequently coordination defects, in particular one covalent bond missing resulting in apparent dangling bonds (unpaired electron) with some silicon atoms having a coordination of two or three instead of four.

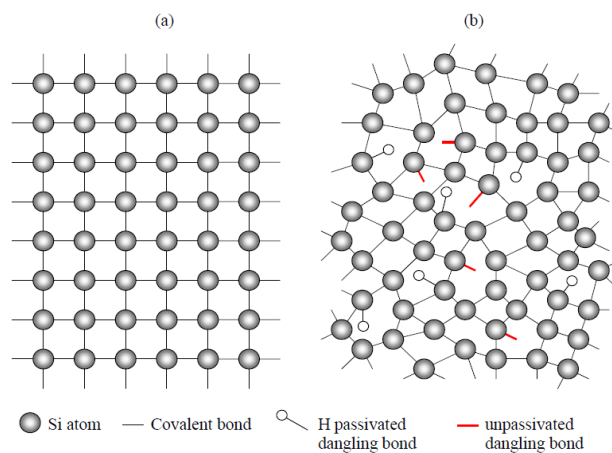


Figure 2-9: Schematic representation of the atomic structure of crystalline silicon (a) and hydrogenated amorphous silicon (b). For c-Si, every Si atom is linked to four other Si atoms and the overall structure is long range ordered. For amorphous silicon, only a short range order is visible because of variation in the angle and length of covalent bonds. Many coordination defects which are not passivated by hydrogen are present within the structure [121].

2.4.1.2 Band diagram

c-Si is an indirect semiconductor with a band gap of 1.12 eV at 300 K. As illustrated in **Figure 2-10** ([121]), there is no forbidden gap for a-Si:H material with a clear separation of the non-localized conduction and valence bands extended states as in crystalline silicon. Instead of the classical transition at the valence and conduction band edges, the density of states of the valence and conduction bands are spreading, forming the so-called “band tail states”, following an exponential distribution [122]. These band tail states have localized wavefunctions and are induced by the bonding distortion in a-Si:H [122]. Moreover, the dangling bonds present within the a-Si:H structure (as

depicted in **Figure 2-9**) are responsible for a continuum of localized states, called the “defect states” within the band gap as illustrated in the **Figure 2-10**. Both band tail and dangling bond states have localized wavefunctions with reduced mobility compared to the non-localized states of the valence band and conduction band extended states [122]. **Figure 2-10** enables us to understand the importance of the incorporation of hydrogenated atoms inside the crystal structure. Indeed pure amorphous silicon is not interesting for electronic applications as it does not have a real band gap. Because of high dangling bonds density in pure amorphous silicon, its electrical properties are very poor. Alloying amorphous silicon with hydrogen can solve this problem. Indeed, hydrogen atoms passivate the dangling bonds and reduce their density by about four orders of magnitude, from about 10^{21} cm^{-3} in pure amorphous silicon to 10^{15} - 10^{16} cm^{-3} in a-Si:H [121]. By passivating these dangling bonds, the density of the localized states is lower than the delocalized density of states of both the conduction and valence bands, hence resulting in the formation of a kind of band gap, called the mobility gap [121]. Typical band gaps of a-Si:H are suitable for photovoltaic application and range between 1.5 eV and 1.9 eV [123]. Both localized band tail and dangling bond states have a great impact on the electrical properties of a-Si:H, as they act as recombination and trapping centers respectively.

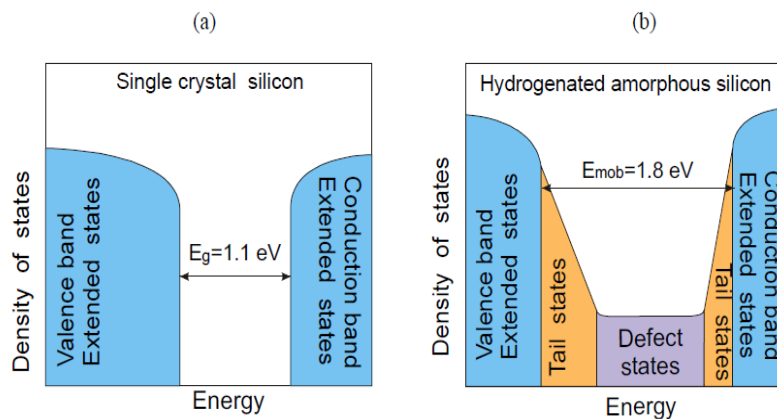


Figure 2-10: Schematic representation of the band diagram of crystalline silicon (a) and hydrogenated amorphous silicon (b). In a perfect crystal, the band gap is well defined and $E_g = E_v - E_c$. Blue color represents states with delocalized wavefunctions. For a-Si:H states are present within the band gap. Orange and purple colors represent the localized wavefunctions, responsible for the reduced mobility properties of a-Si:H. Defect states are due to the dangling bonds defects and tail states are induced by bonding distortion [121].

2.4.1.3 Optical properties

Contrary to crystalline silicon, amorphous silicon behaves like a direct band gap semiconductor [120]. As a consequence, a given thickness of a-Si:H absorbs about 100 times more than c-Si (in the visible spectral range) which means that only 1 μm thick a-Si:H film is enough to absorb about 90 percent of usable solar energy [121]. To achieve similar absorption in c-Si, a thickness of about 180 μm is required. As illustrated in **Figure 2-10**, the density of states diagram of a-Si:H presents both a quadratic and exponential parts responsible for band-to-band and tail-to-tail optical transitions respectively. The optical band gap can be extrapolated from the study of the absorption coefficient according to the following equation: $\alpha(h\nu)=(A/h\nu)(h\nu-E_T)^2$ where E_T is the so-called Tauc gap and is generally used as the value of the optical band-gap. From this study, a band gap of 1.75 eV is commonly obtained, although deposition conditions have a great impact on this value. An interesting optical property of a-Si:H is the ability to vary its optical band gap over a wide range by alloying the material with carbon or germanium [121]. Small variations of the hydrogen content of a-Si:H can also modify the optical band gap of a-Si:H to a smaller extend.

2.4.1.4 Electrical properties

As for all amorphous materials, the carriers' motilities are lower than in crystalline but are still acceptable with typical mobilities in the order of 10 $\text{cm}^2\text{V}^{-1}\text{s}^{-1}$ for electrons and 1 $\text{cm}^2\text{V}^{-1}\text{s}^{-1}$ for holes [121]. As a reference, mobilities in the range of 1500 $\text{cm}^2\text{V}^{-1}\text{s}^{-1}$ for electrons and 450 $\text{cm}^2\text{V}^{-1}\text{s}^{-1}$ for holes have been measured for silicon with a doping concentration of 10^{14} cm^{-3} . Conduction in a-Si:H can be accounted for by three main mechanisms [121]:

- a) band conduction as in crystalline silicon in the delocalized extended band states (valence and conduction),
- b) hopping between band tail states and
- c) tunneling within deep dangling bond states

2.4.2 Heterojunction with Intrinsic thin layer (HIT) devices:

HIT stands for heterojunction with intrinsic thin layer (HIT). HIT [124] solar cells are devices based on crystalline silicon wafer coated by thin films of a-Si:H as illustrated in **Figure 2-11** ([125]). This technology, pioneered by Sanyo back in 1992 [105], is a combination between the c-Si and the thin film technologies. The name HIT summarizes the main features of this type of devices:

- Heterojunction = two different semiconductors (c-Si and a-Si:H) form the p-n junction.
- Intrinsic = an intrinsic layer of a-Si:H is sandwiched between the c-Si and the doped a-Si:H layers.
- Thin films = The total thickness of a-Si:H films is in the order of 20 nm.

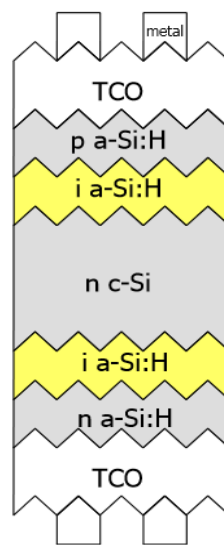


Figure 2-11: Schematics of a standard HIT heterojunction solar cell [125].

The main advantage of HIT solar cells over the standard homojunction c-Si solar cells is the possibility to manufacture the device, including formation of the p-n heterojunction and back surface field, by the PECVD technique at low temperature (200°C) while classical c-Si solar cells require diffusion, passivation and photomasking steps (up to 1000°C). Recently, Panasonic, adapting the HIT to a back contact architecture has broken a new world

efficiency record of 25.6% [10], making HIT solar cells the most efficient Si based technology.

The main feature of heterojunction is the band gap mismatch between the 2 materials as shown in **Figure 2-12**, resulting in band offsets. Indeed band gaps of c-Si and a-Si:H differ by 0.5 to 0.7 eV. The conduction and valence bands cannot be therefore continuous over the entire junction as for homojunctions. The bending of the band is essentially supported by c-Si, the energy bands of a-Si:H being almost flat. This is explained by the concept of “charge neutrality level” where bands are bending in order to achieve charge neutrality. As a-Si:H has much more rechargeable state, most of the bending is observed in the c-Si.

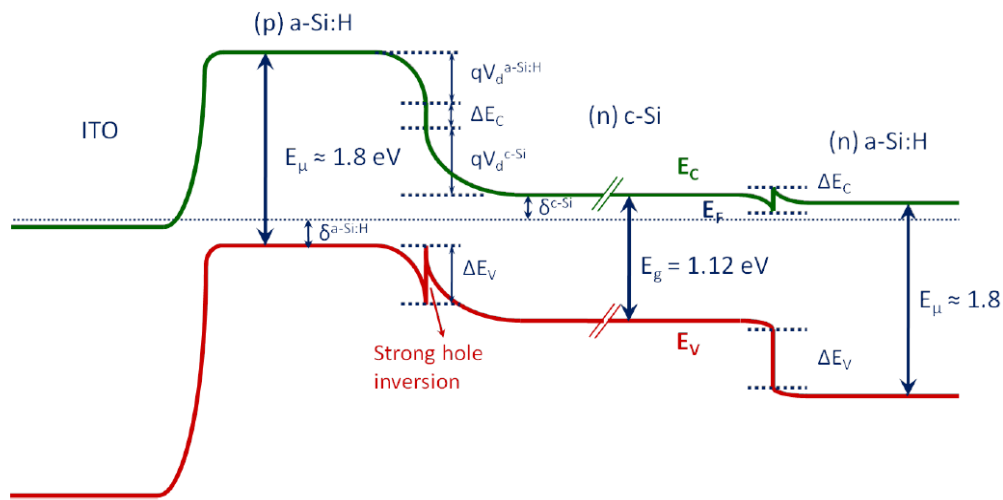


Figure 2-12: Schematics of the band diagram of a HIT for a n-type c-Si [126].

At the I/N heterojunction interface (on the right of the band diagram) holes are the minority carriers and electrons the majority carriers while at the P/I heterojunction interface (on the left of the band diagram), electrons and holes are the minority and majority carriers respectively [127]. At each interface, the band offsets due to the difference in the band gaps between a-Si:H and c-Si is responsible for an unfavorable blocking barrier for majority carriers and a favorable reflection barrier for minority carriers. The barrier experienced by the electrons on the (n) a-Si:H side is quite small and several works have shown that electrons are effectively collected and this barrier does not pose any problem. At the (p) a-Si:H, the barrier height experienced by the holes is more problematic. Majority carriers have to overcome the barrier by tunneling, trap-

assisted tunneling or thermionic emission which is only possible if the a-Si:H layers are really thin and the (p) a-Si:H layer heavily doped. In the case of poor hole collection, s-shape curves (I,V) curves can be observed.

Another key feature of HIT devices is the excellent passivation of c-Si provided by (i) a-Si:H with reported surface recombination velocities below 5 cm/s. If the thickness of the (i) a-Si:H layer is kept very thin, charge carriers transport will not be affected significantly. The optimal thickness of (i) a-Si:H is about 4-5 nm. This intrinsic thin layer was first introduced by Sanyo. Upon insertion of this “buffer” layer, the V_{oc} improved by 30 mV, and a FF of 80% was achieved. The efficiency increases from 12.3% to 14.8% [105]. Since then, continuous improvement of the structure [105], [128]–[132] (textured surface, BSF, symmetrical structure, reduction of absorption in a-Si:H and TCO, grids electrode, improvement of the a-Si:H and c-Si interface, back architecture....) has led recently to a new world record efficiency of 25.6% achieved by Panasonic [10].

Finally, it is worth to mention the excellent stability of HIT devices under light and temperature exposure.

We will now introduce the standard structure used in our work. We used n-type wafer with typical resistivity of 1-5 Ω .cm whose surface has been nanostructured by SiNWs fabricated either by MACE or MACE assisted by nanosphere lithography. The front contact consists of a thin (i) a-Si:H layer recovered by a thicker (p) a-Si:H layer. The BSF is made of a thin (i) a-Si:H layer capped by a (n) a-Si:H layer. The symmetrical structure has been shown to reduce both thermal and mechanical stress. ITO is then sputtered both at the front and backside of the cells. ITO on the front side serves as a transparent electrode and an anti-reflective layer. Backside ITO, whose role is to increase the reflection, is then covered by a metallic back contact. The structure is summarized in **Figure 2-13**.

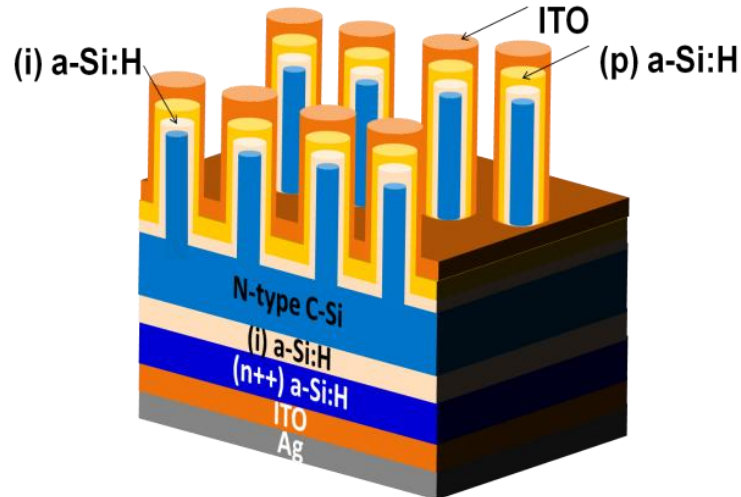


Figure 2-13: Schematic of a HIT structure based on SiNWs. The n-type c-Si wafer has been nanostructured to improve light trapping

2.5 Hybrid Solar Cells

In this section, we review the concept of hybrid devices as we will study the potential of SiNWs for hybrid solar cells in this thesis. A hybrid device is composed of an organic layer combined with an inorganic semiconductor. Light absorption and charge transport in organic solar cells is ensured by the use of conductive small organic molecules or polymers instead of the classical silicon wafers. The principle is similar to that of inorganic solar cells, except that there are no valence or conduction bands involved but we talk rather of the Highest Occupied Molecular orbital (HOMO) and the Lowest Unoccupied Molecular Orbital (LUMO). When light of sufficient energy is absorbed by the organic material, electrons in the HOMO state will be excited above the LUMO level, leaving holes in the HOMO and generating excitons. This kind of solar cells, though less efficient, offer many advantages such as low material cost and simpler fabrication process. Due to their processability, organic materials have great potential in terms of realizing cheap and large scale solar cells fabrication. Moreover, organic materials have a very high optical absorption coefficient, in the order of 10^7 cm^{-1} [133], thus enabling the use of very thin layers. On the other hand, some typical features of organic semiconductors prevent them from reaching high efficiency. These include small dielectric constants and poor dissociation of carriers into free holes and electrons. The latter is attributed to

the high binding energy of photogenerated excitons of about 400 meV [134], which is much higher compared to just several meV in inorganic semiconductors. Besides, the exciton diffusion length, that is, the distance over which an exciton can travel before recombination, is typically very low, about 10 nm [135]–[137]. Therefore, only the part of organic material that is near the interface and within the diffusion length contributes significantly to the photocurrent. Typical lifetime of an exciton is in the order of hundreds of picoseconds [136], [138] before it undergoes recombination. Thus carrier mobility in conducting polymer is a limiting factor: hole mobility typically ranges from 10^{-1} to 10^{-7} $\text{cm}^2\text{V}^{-1}\text{s}^{-1}$ [137], [138] and electron mobility from 10^{-4} to 10^{-9} $\text{cm}^2\text{V}^{-1}\text{s}^{-1}$ [139], [140]. Therefore, organic solar cells are still characterized by rather poor efficiency, and furthermore are not sufficiently stable enough to compete with inorganic devices.

In this work, we have mainly used PEDOT:PSS as the organic material because of its high conductivity and quite high transparency to visible radiation. PEDOT:PSS is a transparent hole conducting mixture of polymers. It is composed of two polymers: a sulfonated polystyrene (PSS) and a conjugated polymer Poly(3,4-ethylenedioxythiophene), commonly named PEDOT. PEDOT is made of repetitive units of the monomer EDOT. PSS plays the role of dopant for PEDOT, making PEDOT both conductive and soluble. With proper additives, conductivity of PEDOT as high as 1000 S/cm can be achieved. As PEDOT:PSS is highly doped, it is sometimes considered as a metal.

As mentioned in the introduction, hybrid solar cells generally include the use of inorganic nanoparticles or inorganic nanowires embedded in an organic matrix. The idea behind is to overcome the poor charge carrier transport properties of organic materials by coupling them with inorganic semiconductor nanostructures that provide a good medium for fast carrier transport while keeping the advantage of fabricating the devices at low cost and low temperature using the spin coating or printing technique. Hybrid solar cells based on the use of nanowires have been investigated in this research work, as this design is theoretically more suitable to achieve morphological requirements for an efficient charge carriers collection than hybrid solar cells based on nanoparticles. Indeed for hybrid solar cells based on nanoparticles, the carrier

transport is limited to hopping between the inorganic nanoparticles while hybrid solar cells based on nanowires offer a continuous path for charge transport from the interface to the electrode as depicted in **Figure 2-14**. Although we expect most of the charge carriers being generated in the c-Si, hybrid solar cells based on SiNWs can improve exciton dissociation if the separation distance between two nanowires is about two times the diffusion length of an exciton.

Until 2010, best hybrid SiNW based solar cells, consisting of a transparent polymer (PEDOT) on an n-SiNWs array fabricated by electroless etching [13] and reactive ion etching coupled silica bead assembly [21] , showed a promising efficiencies of 5.08% and 6.1% respectively. The research in the field has undergone a remarkable progress in 2011 when our group reported an efficiency as high as 9% [111] for a similar structure, and 10.3% [20] and 9.7% [141] for a structure using a new small organic molecule (SPIRO-O-MeTAD). Such enhancement was possible through the use of more suitable organic material and a better understanding of the interface between the organic and inorganic materials. Such results are highly promising for future industrial application and prove that the concept of hybrid solar cells is valuable.

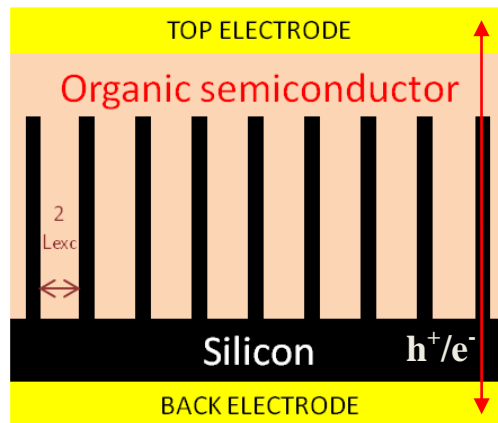


Figure 2-14: Schematic representation of an ideal nanostructure hybrid silicon/organic material solar cell. The nanowires offer a continuous conductive path to the electrode. L_{exc} is the diffusion length of the exciton. The nanowires are separated by a distance of about $2L_{exc}$, in order to reduce loss in photocurrent due to exciton recombination.

Conclusion:

In this chapter, we have discussed the working principle and the most fundamental concepts of a solar cell. Then we did a detailed literature review on the properties of SiNWs (optical, electrical and charge carrier collection) and their methods of fabrication (top-down and bottom-up). In particular, we have introduced the wet etching technique, MACE, used in this research work. The key features of NWs based solar cells have been explained and the most significant research work related to solar cells based on SiNWs were reviewed and summarized. Finally, we have described the main features of the two solar technologies studied in this project, HIT and hybrid solar cell, and introduces the main properties of the materials involved (a-Si, a-Si:H, c-Si and PEDOT:PSS).

Chapter 3 : Fabrication and Characterization Techniques

This chapter describes the methods of fabrication of random and ordered SiNWs by MACE and by MACE assisted by nanosphere lithography respectively. We also detail the working principle of all the equipments needed to complete HIT and hybrid solar cells. Finally, we describe the different characterizations tools used for this research work.

3.1 Silicon Nanowires Fabrication by Wet Etching

Experiments were carried out in a class 100 cleanroom (100 denotes the maximum number of particles of diameter 0.5 μm or larger that are allowed per cubic foot of air).

Two types of SiNW arrays have been fabricated and characterized: random and ordered SiNW arrays. SiNWs were fabricated either by direct use of the standard Metal Assisted Chemical Etching (MACE) process or by coupling the MACE process with the nanosphere lithography (NSL) method. While the cost-effective MACE process allows the fabrication of high density with high aspect ratio random SiNWs arrays, the NSL step further allows for an almost perfect control of the geometry of fabricated arrays in terms of pitch, length and diameter.

3.1.1 Random / Disordered Silicon Nanowires

SiNWs directly fabricated by MACE are considered as random, as there is no control over the pitch or the diameter. The only controlled parameter is the length of the SiNWs which is tuned by the etching time.

The fabrication of SiNW arrays by MACE is simple and straightforward. SiNWs were fabricated as follows: single-crystal n-type wafers [100] were successively cleaned in acetone, IPA and deionized (DI) water for 10 min each by an ultrasonic bath at room temperature. A solution of 4.6 M HF (Sigma Aldrich) and 0.02 M AgNO_3 (Sigma Aldrich, Purity = 99.9999%) at room temperature was used for the etching process. The silicon substrates were

introduced into the etching solution and the length of the NWs was tuned by the etching time. Typically NWs with lengths of 500 nm, 2 μm and 5-6 μm were obtained for etching times of 5 min, 12 min and 25 min respectively. **Figure 3-2** displays the length of the SiNWs as a function of time with χ^2 being the fitting error of the experimental curve by the theoretical model.

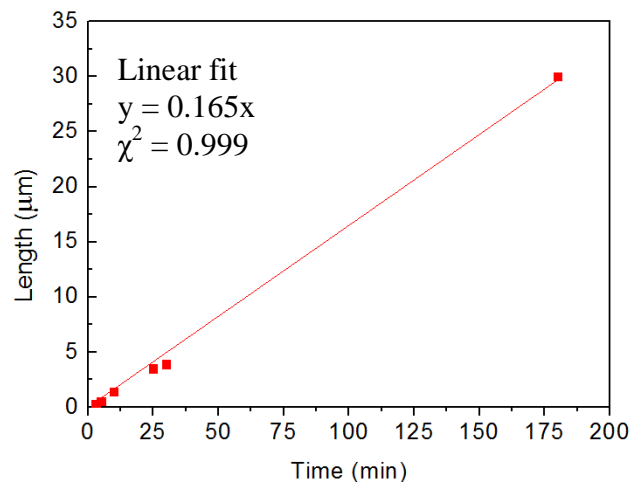


Figure 3-1: Schematics of the nanosphere lithography method coupled with the MACE process

Following this etching step, the SiNWs are capped by a dense greyish foam, called the silver dendrites. These silver dendrites, which resulted from the continuous reduction of the silver ions, have the shape of a tree with ramifications as shown in **Figure 3-2(a)** ([142]). The silver dendrites were subsequently removed by a 15 minutes concentrated nitric acid bath (65%, sigma Aldrich). The samples were finally rinsed through fully in DI water. **Figure 3-2** shows the top-view and the cross-section of the typical SiNW arrays we produce by this method. As illustrated, the SiNW arrays are straight and extremely dense. Typical diameters of the SiNWs lie in the range 20 - 200 nm.

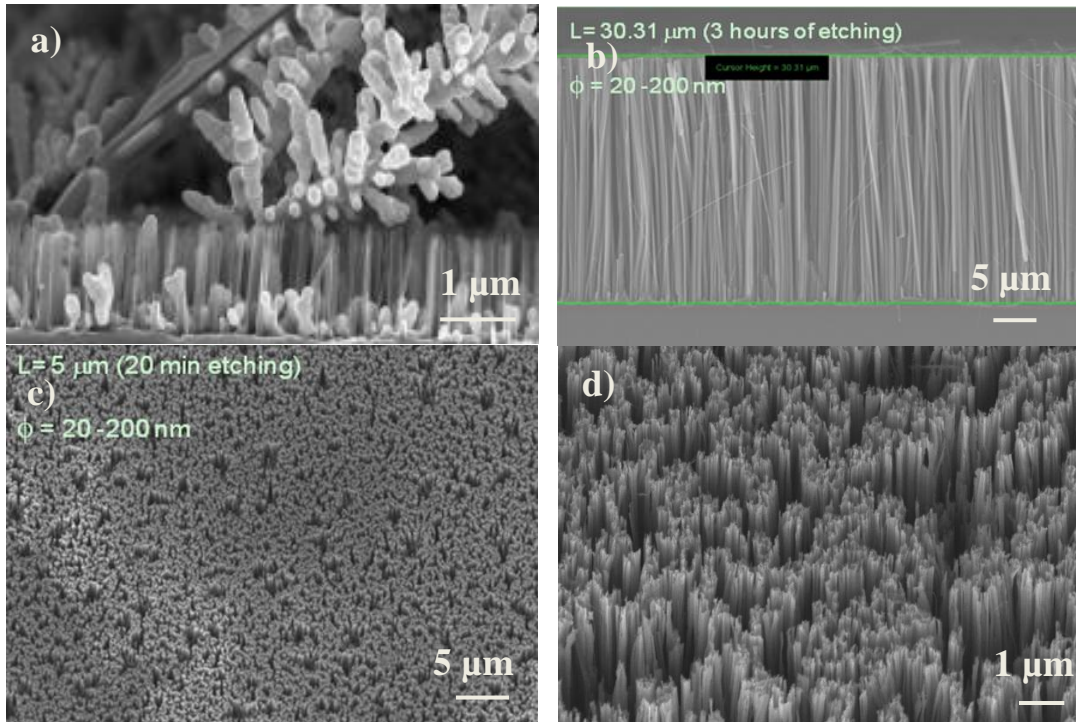


Figure 3-2: (a) SEM picture of silver dendrites covering the SiNW prior the HNO_3 chemical bath [142], (b) cross-section SEM picture of 30 μm long random SiNWs, (c) inclined (15°) SEM picture of 5 μm long random SiNWs, and (d) inclined (30°) SEM picture of 5 μm long SiNWs.

3.1.2 Ordered Silicon Nanowires

The fabrication of an ordered SiNW array requires additional steps to form a metallic mask which will serve as a template during the etching procedure [64].

The overall process is summarized in **Figure 3-3**. Single-crystal n-type wafers ([100]; resistivity 1-5 $\Omega\text{-cm}$) were successively cleaned in acetone, IPA and deionized (DI) water for 10 min each by an ultrasonic bath at room temperature. A monolayer of Polystyrene (PS) balls was first deposited on the Si wafers using a floating–transferring technique which will be detailed later on. The initial diameter of the PS balls determined the pitch (center to center distance) of the fabricated structure. Next step included the reduction of the PS balls diameter by an oxygen plasma treatment (30 Watt, 20 sccm). The time of etching determined the diameters of the fabricated SiNWs. Therefore different treatment times will result in different diameters. Finally a thin film of gold of 25 nm was deposited by e-beam evaporation. The PS balls were subsequently removed by immersing the sample into a toluene solution leading to the

formation of a gold membrane with holes. A solution mixture of HF, H₂O and H₂O₂ was used for the etching procedure. The length of the resulting nanowires was again tuned by the etching time. At the end of the etching process, the gold film was etched away by potassium iodide, completing the fabrication of an array of SiNWs with a controlled geometry.

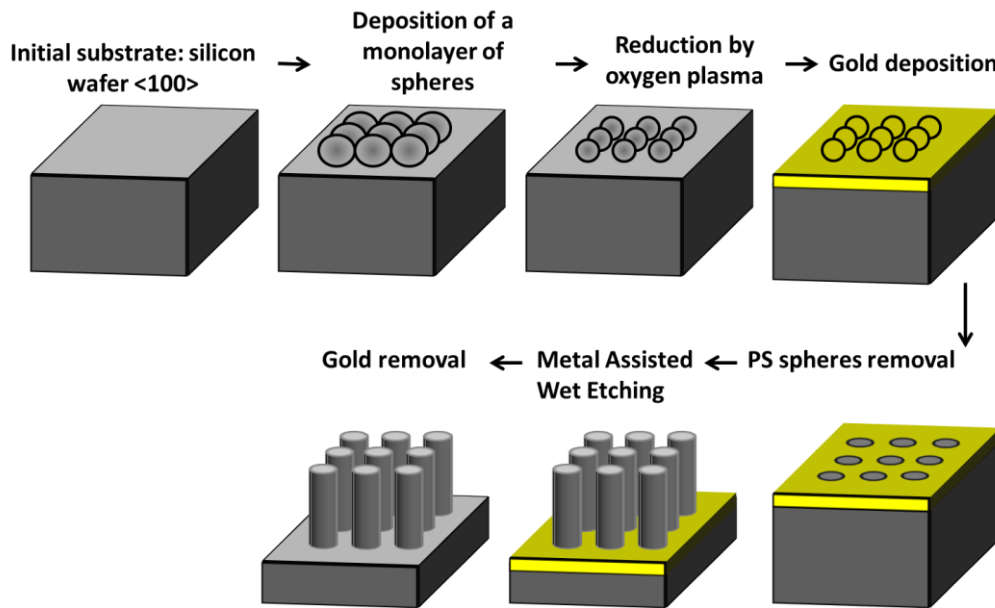


Figure 3-3: Schematics of the nanosphere lithography method coupled with the MACE process

In this section, we will review the details of the different steps of fabrication.

We first deposit a compact monolayer of PS balls on a c-Si substrate by the floating transferring technique. Polystyrene (PS) balls (microParticles GmbH, Germany) with different nominal diameters of 330 nm ± 7 nm (10% w/w aqueous suspension), 476 nm ± 14 nm (5% w/w aqueous suspension), 617 nm ± 20 nm (10% w/w aqueous suspension), 803 nm ± 26 nm (10% w/w aqueous suspension) were used for the self-assembly deposition process. These commercial aqueous suspensions of PS spheres were first mixed with ethanol (1:1) and the solutions were ultrasonicated for 10 minutes. Ethanol, a low-surface tension solvent, is used as a spreading agent.

Figure 3-4 ([143]) shows a schematic of the floating transferring technique. In this method, a high quality monolayer of colloidal particles was first formed on the water surface before being transferred to a substrate. The

floating transferring process was carried out inside a glass Petri dish. The Petri dish was treated under plasma oxygen (60 watt, 20 sccm, 200 mTorr) for 15 minutes in order to achieve a highly hydrophilic surface, before it was filled with highly resistive DI water (about 18 M Ω).

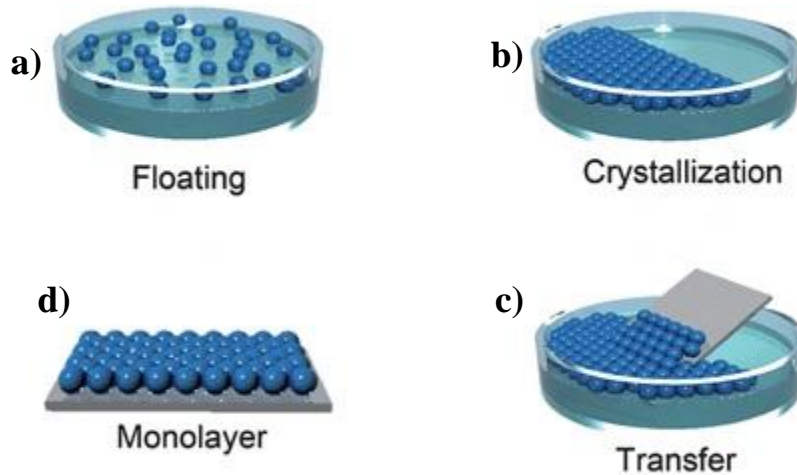


Figure 3-4: Schematics of the floating-transferring technique to achieve an hexagonal compact arrangement of PS spheres on a silicon substrate [143].

The colloidal dispersion of PS spheres in ethanol was pipetted on a clean water surface. A long sharp tip glass Pasteur pipette, whose tip was subsequently sharpened (tens of microns) and bended by thermal treatment, was used. This helped to control the flux of the colloidal solution when dispersed on the water surface. The pipette was then placed towards the sidewall of the Petri dish, just in contact with the water surface. This is a critical step, as the addition of the PS suspension on the surface of water has to be adjusted carefully in order to achieve a high quality monolayer with no sedimentation. The introduction of the PS spheres was stopped when about 70-80% of the water surface was covered by the colloidal solution. Indeed, this will ensure that the PS spheres can freely diffuse at the surface of the water to find their configuration of lowest energy. The spreading of the colloidal suspension at the surface of the water is a direct consequence of the Marangoni effect, commonly named “the tears of wine” phenomenon. The Marangoni effect describes the effect of a surface tension gradient along an interface on the movement of a fluid. The presence of a surface tension gradient forces the low surface-tension liquid to be pulled towards the region of high surface-tension. The large

difference of surface tension between water (72 mN/m) and ethanol (22 mN/m) creates a gradient in surface tension which induces a Marangoni flow of ethanol containing the PS spheres along the fluid-fluid interface and into the water, pulling the nanospheres/suspension towards the edges of the Petri dish [144], [145]. During the next crystallization step (b), the PS spheres formed a compact hexagonal arrangement because of attractive forces between the particles. Indeed, strong attractive flotation capillary forces arose between the PS spheres with the evaporation of ethanol which is much more volatile than water [146], [147]. **Figure 3-5 (a)** illustrates the effect that flotation capillary forces induce by the deformation of the water surface because of the weight of the PS particles. These attractive forces cause reorganization of the PS balls into a compact hexagonal arrangement. The compact hexagonal arrangement is thermodynamically favored because this is the configuration with the minimum Gibbs free energy. This process required about 4 hours. **Figure 3-5 (b)** shows the PS spheres monolayer obtained on the water surface inside the Petri dish. This shiny aspect is due to the arrangement of the PS spheres into a hexagonal compact arrangement.

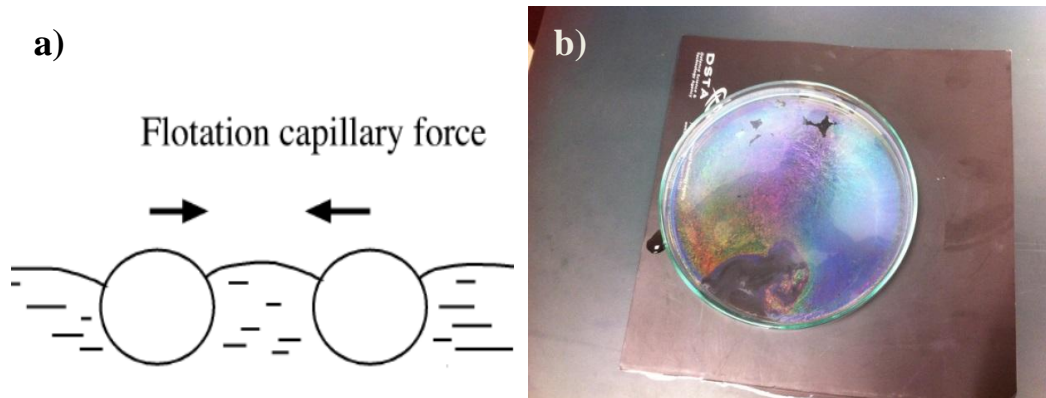


Figure 3-5: (a) Schematics of the flotation capillary forces, the driving force for the self-assembly of the PS spheres [147]. (b) Photograph of the monolayer obtained onto the water surface.

In the meantime, silicon substrates (1-5 ohm. cm, n-type, [100]) were cleaned in acetone, IPA and deionized (DI) water for 10 min each by an ultrasonic bath at room temperature to ensure the hydrophilicity of the surface. The silicon substrate was then inserted below the monolayer of PS spheres

inside the water and then the substrate is dragged upward, so that the monolayer is deposited on the wafer surface as shown in **Figure 3-6**. The samples were then allowed to dry naturally in air for a few hours.

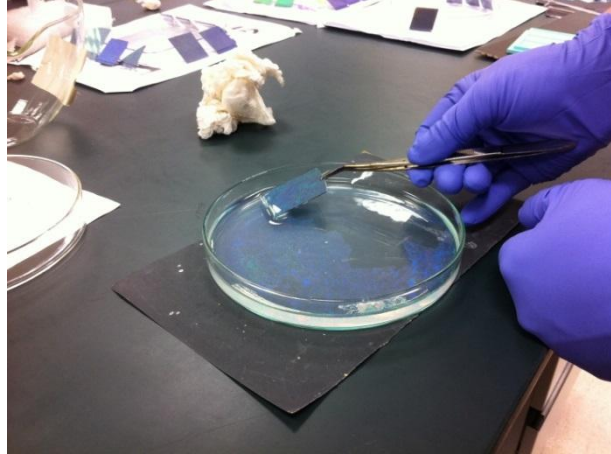


Figure 3-6: Photograph of the "transfer" stage where the silicon substrate is placed below the PS monolayer and dragged upward to coat the sample by the PS suspension.

Figure 3-7 shows (a) a photograph and (b) low magnification and (c) high magnification SEM pictures of the PS monolayer we achieved for an initial diameter of 800 nm. The PS spheres formed a compact hexagonal arrangement as shown in **Figure 3-7(c)**. **Figure 3-7(d)** shows that the PS self-assembly is not always perfect in the long range. The smaller the PS spheres, the more difficult it is to obtain a perfect order. Usually we obtained a kind of multicrystalline structure in the sense we observed uniform domains with different size, each of them is organized hexagonally but with different domain orientation.

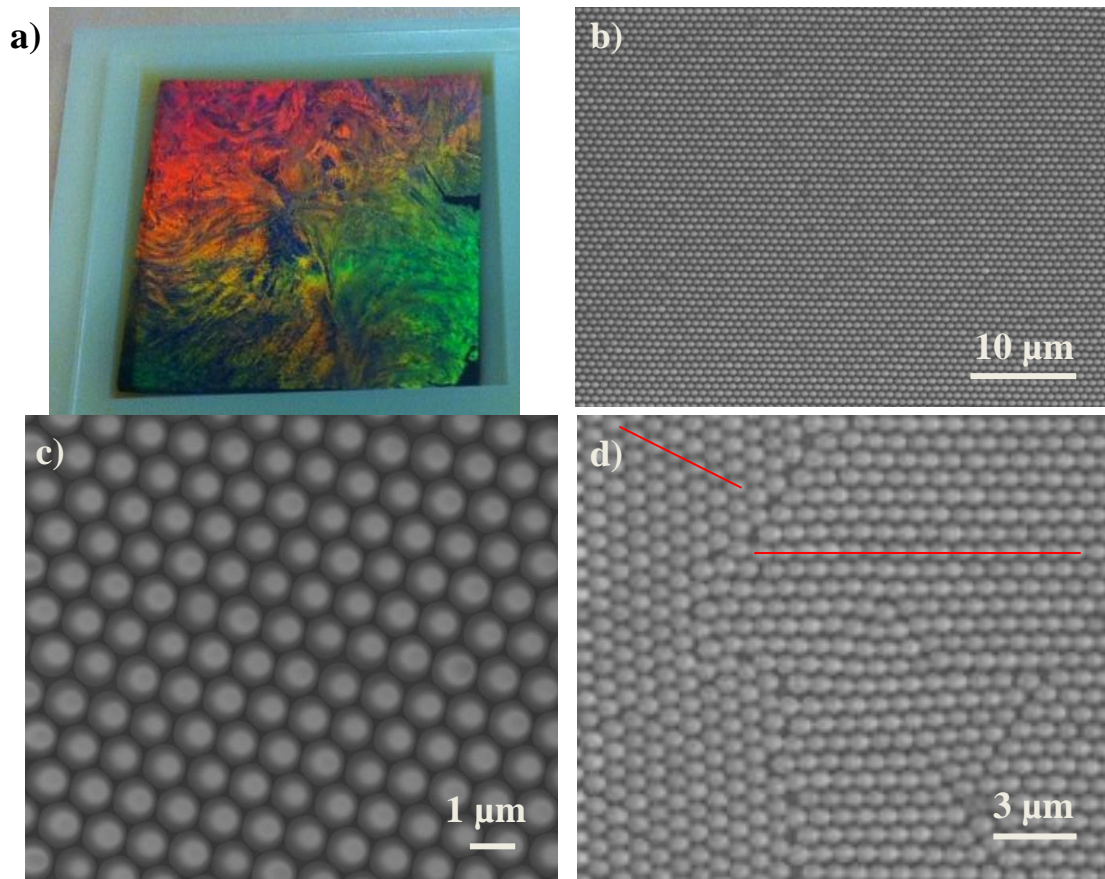


Figure 3-7: (a) Photograph of the Si substrate covered by a monolayer of PS spheres. (b) Low-magnification SEM image of perfectly ordered PS spheres arranged into a hexagonal compact arrangement. (c) High-magnification SEM pictures of perfectly ordered PS spheres arranged into a hexagonal compact arrangement. (d) SEM picture of the PS film showing that the film is not uniform everywhere. Small domains coexist with different orientations.

The next step is the reduction of these PS spheres by a oxygen plasma treatment. The initial diameter of the PS spheres determines the pitch (center to center distance) of the fabricated structure. A flow rate of 20 sccm, a power of 30 Watt and a pressure of 180 mTorr was used. The time of the oxygen plasma treatment defines the diameter of the fabricated structures. Different treatment times will result in different PS spheres diameters that will consequently produce SiNWs with different diameter as illustrated in **Figure 3-8**.

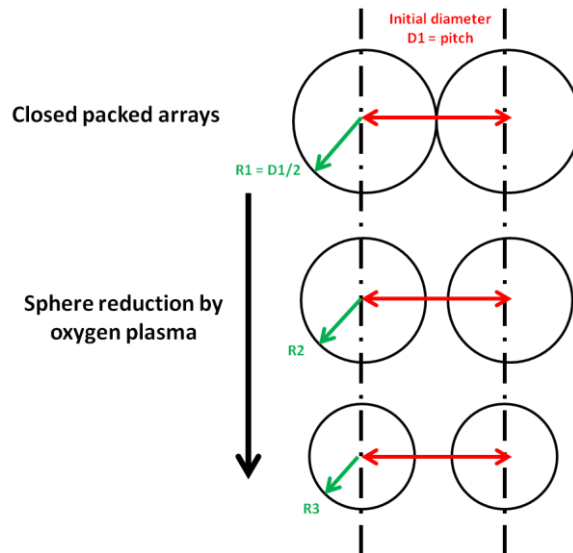


Figure 3-8: Schematics illustrating the effect of the plasma etching treatment on the PS spheres.

Prior to the plasma treatment, the samples were annealed at 90°C for 5 min in order to improve the adhesion of the PS spheres to the substrate. The objective is to allow the PS spheres to melt a little bit in order to adhere more to the surface as illustrated in **Figure 3-9 (a)**. The temperature has to be carefully adjusted. Indeed, there is a risk of melting the PS spheres and to form rings of melted PS around the PS balls, as observed for annealing treatment of 105°C shown in **Figure 3-9 (b)**.

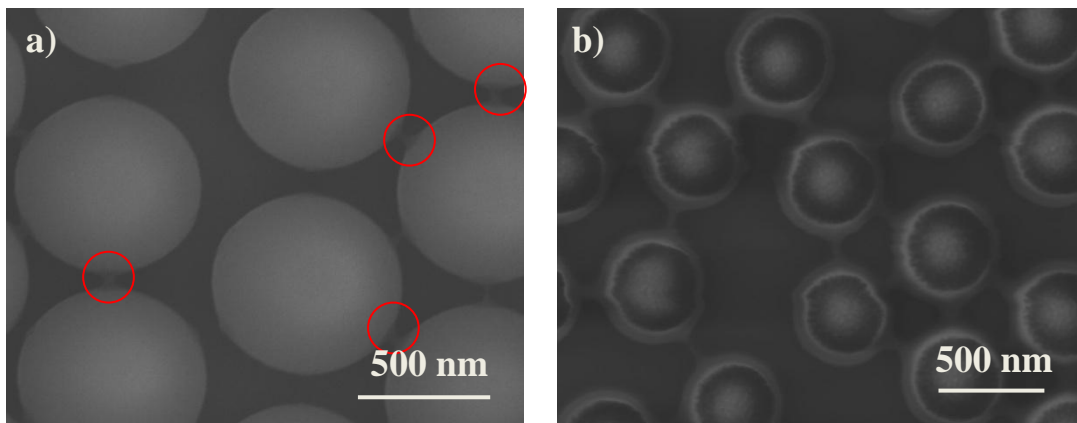


Figure 3-9: SEM picture of (a) slightly annealed PS spheres. The red circles shows the small area melted. (b) Overheated PS spheres causing the excessive melting of the colloidal particles.

The etch rate of the PS spheres varies slightly with the nominal diameter of the initial PS spheres. The etch rate typically lies in the range of 0.70-1 nm/s.

Figure 3-10 shows the evolution of the PS spheres diameter as a function of the plasma treatment time, for different initial nominal PS spheres diameters of 800 nm, 600 nm and 500 nm. We observe that the etch rate varies linearly with the etching time and that the smaller the PS sphere the faster is the etch rate. Note that at some point all the PS spheres are etched away when the plasma treatment time is too long as the adhesion of the PS spheres on the substrate is becoming too weak.

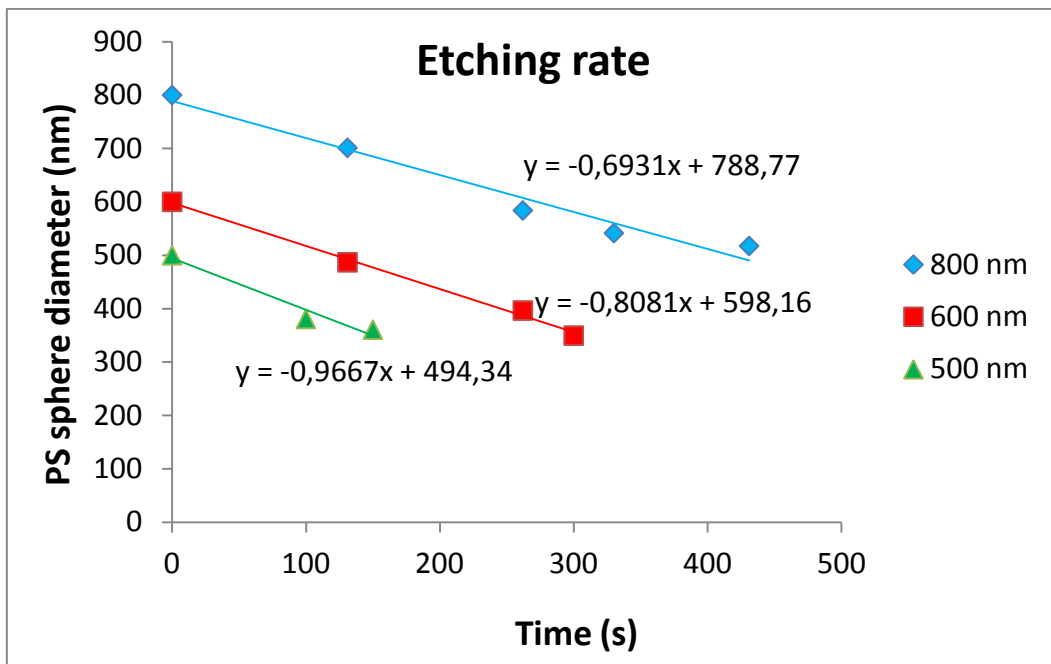


Figure 3-10: The etch rate of the PS spheres with initial nominal diameter of 500 nm, 600 nm and 800 nm by oxygen plasma as a function of time.

Figure 3-11 shows typical SEM pictures of PS spheres treated by oxygen plasma. The initial diameter of the PS spheres was ~600 nm and the plasma oxygen treatment lasted 250s, resulting in a new average diameter of 392 nm.

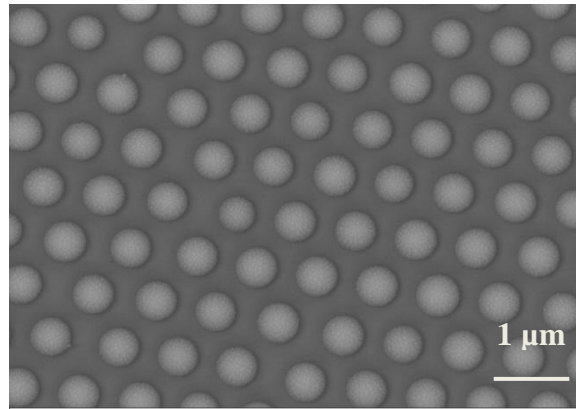


Figure 3-11: SEM picture of the PS spheres arrays after 130s of oxygen plasma treatment. The PS spheres are separated from each other. The initial diameter of PS spheres of 600 nm was reduced down to 392 nm.

Following this step, a 25 nm thick film of gold is deposited on the substrate. The film was deposited by e-beam evaporation at a deposition pressure of $3\text{-}5 \times 10^{-6}$ Torr. The sample holder was rotating during the deposition to ensure a uniform deposition of the metallic film. **Figure 3-12** displays a typical SEM picture of this fabrication step, showing the PS spheres covered by a thin film of gold of 25 nm.

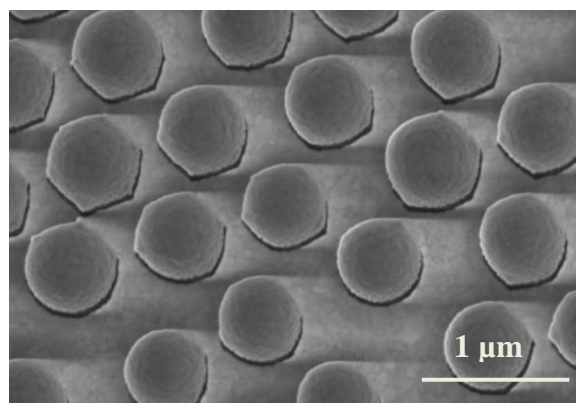


Figure 3-12: SEM pictures of PS sphere arrays covered by a 25 nm gold thin film.

The next step is the removal of the PS spheres. To remove the PS spheres, the samples were ultrasonicated at low power in toluene. The PS spheres with small diameter required more time to be completely removed. **Figure 3-13 (a)** shows the SEM pictures of the sample after removal of the PS spheres. A gold film with holes is obtained which forms the etching template mask. It is easier to remove the PS spheres at this stage of the process when the

surface is still flat, rather than after the fabrication of the SiNWs. When the SiNWs have been formed, the PS spheres can fall between them, making the removal more challenging, as illustrated in **Figure 3-13** that shows the two cases when the PS spheres have been removed after the metallic deposition (a) or after the wet etching procedure (b). In **Figure 3-13(b)**, we still observed many residual PS spheres present within the SiNWs.

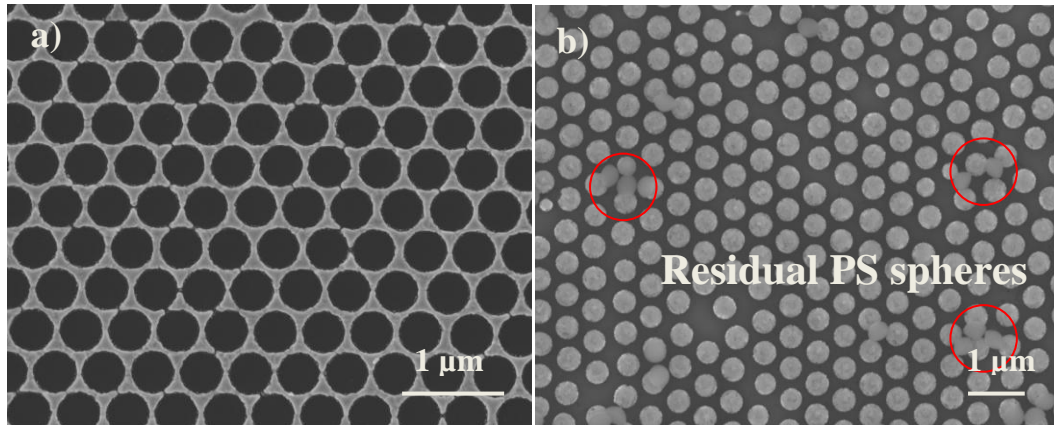


Figure 3-13: (a) SEM pictures of the gold etching mask after the removal of the PS spheres. (b) SEM pictures of SiNWs arrays where the removal stage of PS spheres has been carried out at the last step of the process. The PS spheres are not effectively removed since they are trapped inside the nanostructure.

The samples were then immersed into a chemical etching solution to produce SiNWs. A solution mixture of HF, H₂O and H₂O₂ was used for the etching procedure. The concentration of HF and H₂O₂ are 4.6 m and 0.44 M respectively. The length of the SiNWs were tuned by the etching time. Note that an addition of an oxidizing agent was required in comparison with the standard MACE process as the metallic film was already in the “reduced” form and therefore it could not oxidize the Si wafer. As a consequence H₂O₂ was used to oxidize the silicon wafer. The etching would take place everywhere where the metallic film is deposited. Indeed, the silicon surface in contact with Ag is etched preferentially due to a much faster etching rate compared to bare Si surface. This is explained by the role of microscopic cathode played by the silver which promotes charge transfer (holes injection). Finally the metallic film was removed. The gold film was etched away by potassium iodide (28 Å/s). **Figure 3-14** shows typical SiNWs produced by this method. We are able to produce SiNW arrays with various geometries (different pitches and diameters)

with different densities (low, medium, high density) and different lengths (from 100 nm to tens of μm) as shown in **Figure 3-14**. The NSL process coupled with the MACE process is extremely interesting as it a versatile method which provides an easy and almost accurate control over the pitch, diameter or length of the fabricated structures.

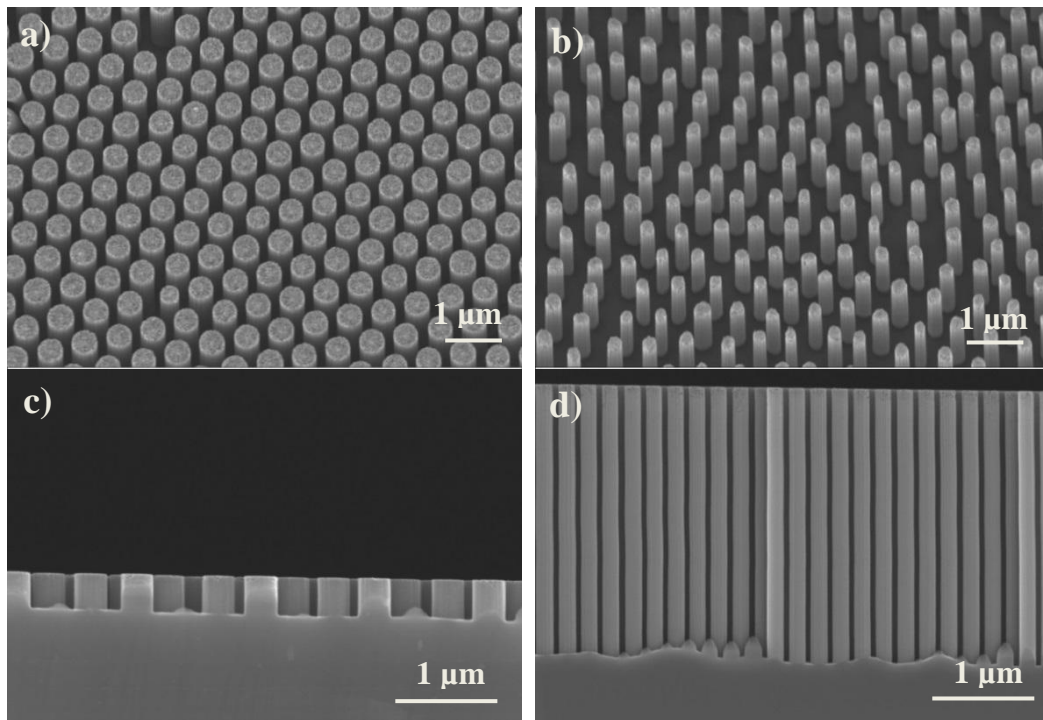


Figure 3-14: (a) SEM pictures of (a) high density SiNWs ordered arrays (inclined 30°) samples with 800 nm pitch , (b) low density SiNWs ordered arrays (inclined 30°) with 800 nm pitch, (c) cross section of short SiNWs, and (d) cross section of long SiNWs.

3.2 Fabrication of Solar Cells based on Silicon Nanowires

3.2.1 Plasma Enhanced Chemical Vapor Deposition System

In this section, we describe the working principle of a Plasma Enhanced Chemical Vapor Deposition (PECVD) system. We first review the physics of plasmas before introducing the PECVD reactor "ARCAM" that we have used in our experiments.

Thin films are commonly deposited by the chemical vapor deposition (CVD) or by the plasma enhanced chemical vapor deposition (PECVD) techniques. The PECVD is in fact derived from the CVD technique. In a CVD

process, gas precursors are reacting on a hot substrate via chemical reactions which require usually quite high temperatures (500-800°C) to take place. In the PECVD process, an electrical discharge is used to decompose the precursors, generating reactive species such as radicals or ions which will induce chemical reactions and result into the growth of a film at lower temperature (100-350°C). The PECVD technique is therefore a low temperature process which enables the growth of films with good adhesion and uniformity properties. Another possible technique includes the hot wire chemical vapor deposition (HWCVD), another derivative from the CVD, where gas species are dissociated upon a catalytic reaction by a hot filament. The main advantage of the HWCVD technique is its high deposition rate. However the uniformity and quality of the films are still not as good as those of films grown by the PECVD technique

3.2.1.1 The Physics of Plasma

Plasma is often considered as the 4th state of the matter, the others being the solid, liquid and gas states. Interestingly, plasma is the most common form of matter, since more than 99% of the visible universe is comprised of plasma. Plasmas have unique properties which differentiate them from the other states of matter.

Plasma is basically an ionized gas, i.e. a gas which has been provided with enough energy to release electrons from a significant number of gas atoms/molecules, so that a mixture of electrons, ions and neutral particles can co-exist. Plasma is therefore a collection of electrons, ions (multiple or singly charged) with neutral atoms / molecules / molecular fragments. The type of gas, the ratio of ionized particles to neutral particles, and the particles energy can affect significantly the properties of the plasma and therefore we are able to generate different types of plasmas suitable for a wide range of applications that include etching and growing of materials.

Plasma can be generated by applying an electric field between two electrodes. Negatively charged electrons will be accelerated towards the positive electrode (the anode) and will undergo on their way a series of collisions with the different plasma components. These collisions can either lead to further ionization and excitation of the neutral species (inelastic

collisions) or lead to neutralization via collisions with the reactor wall. At some point, equilibrium is reached and the average number of charged particles remains the same. The ions and the electrons density are equal to ensure overall balance of charges, so that the global charge neutrality is respected.

The disparity between the electronic and ionic mass can account for the plasma electrical properties. Indeed, the very light and fast moving electrons are faster drained to the electrodes while the movement of the heavy ions is much slower. At the cathode, we observe a zone depleted of electrons because they are repelled from the negative electrodes. This area, where only few excitations are taking place is named the dark space or the cathode sheath. Although ions are attracted toward the cathode, because of their large mass, only a few of them will reach the interface between the plasma and the dark sheath and be effectively attracted. The situation is different at the anode where the negatively electrons are strongly attracted by the positive electrode. At some point, the charged surface of the anode is becoming negative that will cause a balance flux between the attracted positive ions from the plasma and the repulsed electrons. This is the so-called anode sheath. The density of electrons falls to zero at the walls while the density of the ions is small because of their low mobility. Therefore the charge neutrality is broken in these dark sheath regions. The term dark sheath comes from the fact that in these zones, only very few ionization or excitations are taking place due to the quasi-null density of electrons, and therefore there is less luminosity. These dark sheaths induce positively biased plasma with respect to the electrodes. **Figure 3-15** displays the case where the two electrodes have different sizes. In symmetric RF systems, the voltage distribution is symmetric while for asymmetric systems, the voltage drop at the smaller electrode with respect to the plasma is much more important. The relationship between the surface area of two electrodes A_1 and A_2 and the observed electrode voltage drop V_1 and V_2 is as follows, with q being an exponential factor typically comprises between 1 and 2:

$$\frac{V_1}{V_2} = \left(\frac{A_1}{A_2}\right)^q \quad 3.1$$

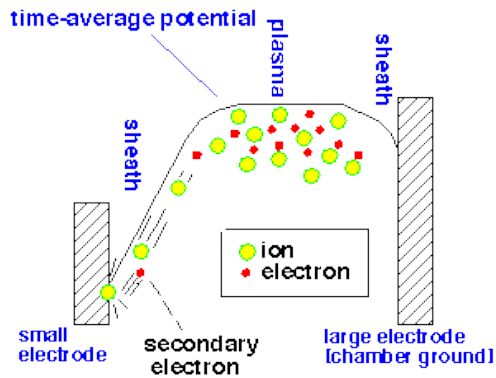


Figure 3-15: Schematics illustrating the voltage distribution of a plasma in the case of asymmetric electrodes [148].

3.2.1.2 Plasma Key Parameters

A key parameter to describe the local non neutrality of plasma is the Debye length (λ_D) [149]. Indeed, plasmas are conductors but there is no electrical field. This is due to the screening of the electrostatic fields by the free charges in the plasma. The Debye length is the distance over which a significant charge separation may exist. Beyond a few λ_D , the perturbation is screened and its effect on the charge density or potential of the plasma is negligible. The Debye length can be expressed in the case of electrons screening by:

$$\lambda_D = \sqrt{\frac{\varepsilon k_B T_e}{n_0 e^2}} \quad 3.2$$

where n_0 is the number of electrons, k_B the Boltzmann constant, T_e the effective temperature and ε the dielectric constant. Dark space or plasma sheaths for example are in the order of a few Debye lengths.

Another fundamental parameter of plasma is the plasma frequency [149] which is basically the frequency of oscillations of the electrical charges in the plasma. For example if electrons are moved from a zone of the plasma, the ions in this zone will attract back the electrons via columbic interactions as they only have slightly moved due to their heavy mass. Electrons will be pulled back and so on, leading to oscillations. Note that the observed movement is a collective

effect, caused by the coordinated motion of many particles. The plasma frequency can be expressed by [149]:

$$\omega_{p,j} = \sqrt{\frac{4\pi n_j e^2}{m_j^*}} = \sqrt{\frac{n_j e^2}{m_j^* \epsilon_0}} \quad 3.3$$

where n_j is the species density, e is the electrical charge, ϵ_0 the permittivity of vacuum and m_j^* the effective mass of the considered species.

The plasma frequency is dependent on the effective mass and will be therefore different for ions and electrons. As the effective mass of electrons is much smaller than that of ions, the frequency of electrons is the most important and usually we refer to the plasma pulsation of electrons when we refer to the plasma frequency. This plasma frequency is of high interest as it dictates the behavior of the oscillating species in the plasma when a periodic external electrical stimulation ω_s is applied. If $\omega_s < \omega_p$, the species will have enough time to react to the perturbation and electrons will oscillate at the same frequency of the applied stimulation. On the other hand, if $\omega_s > \omega_p$, the species will not react and remain fixed.

A common way to categorize plasmas is to consider their electron density and their electrons energy (or temperature). In this work, we are interested in RF-PECVD powered plasma which shows typical electron density of $1 \times 10^9 \text{ cm}^{-3}$ - $1 \times 10^{11} \text{ cm}^{-3}$ and electron energy of 1-10 eV. RF-PECVD powered plasma is a low-temperature plasma. In low-temperature plasmas, there is still an important proportion of neutral species which are playing an essential role by contributing to energy exchange or transport via collisions. A plasma can be described by its degree of ionization α [149], the ratio between the electron density to the total density of both electrons and neutral species:

$$\alpha = \frac{n_e}{n_0 + n_e} \quad 3.4$$

where n_0 is the density of the neutral species and n_e is the density of electrons.

This ionization degree is in the range of 0.1%-6% for the reactor we used. Reactions happening in the plasma are generally divided into two main categories: primary and secondary reactions. The primary reactions concern the interaction of the electrons with the parent neutral gas. They are the most important reactions in the sense they are generating the key plasma particles:

ions and radicals, excited species and photons which gives the plasma its “glow” aspect. These species can further react with the substrate, electrons or even with themselves. These reactions are named the secondary reactions.

In this work, we have mainly used the PECVD system to deposit thin films of hydrogenated amorphous silicon (a-Si:H). Depositions of such films are usually taking place at low pressure and RF power. Under such conditions, primary reactions are playing a crucial role while secondary reactions are limited. The number of secondary reactions can be increased by raising the pressure or the temperature.

3.2.1.3 Description of a capacitive coupled RF-PECVD reactor

A RF-PECVD reactor is composed of two parallel metal electrodes, separated by a short distance d . One electrode is connected to a radio frequency (RF) power supply (the RF electrode) while the other one is grounded (the ground electrode). An alternative potential with a frequency of 13.56 MHz (or multiples) is applied between the two electrodes. In this system, thin films are deposited by interaction between a vapor phase and a heated substrate (170°C-200°C) which is placed on the grounded electrode. Electrical energy (RF voltage) is used to create a glow discharge (the plasma) between the two plates, the energy being transferred by capacitive heating to the gas mixture, which will generate reactive species such as radicals and ions. Another interesting point is that the walls are usually also grounded, therefore the area of the ground electrode is larger than that of the RF electrode. According to Eq. 3.1, we will observe a larger voltage drop at the RF electrode than at the ground electrode as shown in **Figure 3-15**.

The minimum voltage required to start the plasma is called the breakdown voltage and is a function of the product of the distance d between the two electrodes and the gas pressure p . This relationship is known as the Paschen law and is given by Eq. (3.5) [150], [151]:

$$V = \frac{apd}{\ln(pd) + b} \quad 3.5$$

where V is the breakdown voltage, d is the distance between the two electrodes, p is the gas pressure and a and b are both constants depending on the gas mixtures.

Figure 3-16 ([152]) shows the typical breakdown voltage of a plasma V as a function of the product ($p \times d$).

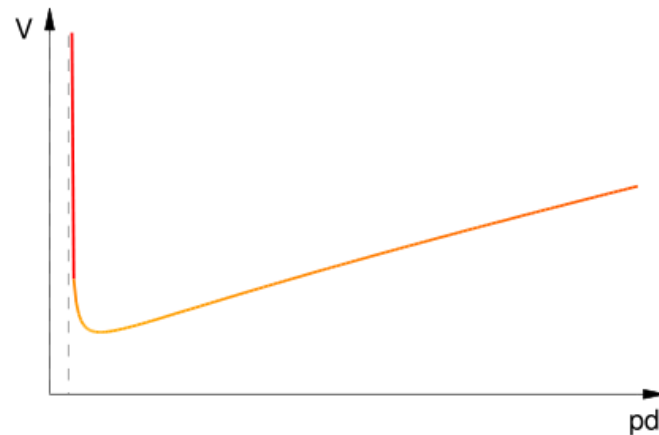


Figure 3-16: The Paschen curve showing the breakdown voltage as a function of the product of the pressure p with the interdistance between the electrodes d [152].

Finally an impedance matching network between the RF source and its load is required in order to maximize power transfer. This is achieved by the use of a matching box which will also protect the RF generator from excessive reflected power.

3.2.1.4 The ARCAM reactor

In this work, we have used the ARCAM reactor to deposit amorphous silicon thin films. The ARCAM reactor is at the centre of the LPICM research activities. Specificities of the ARCAM reactor have been described in details in *Cabarrocas et al.* [153]. The main features of the ARCAM reactors which differentiate them from standard RF PECVD reactors include:

- Temperature homogeneity which is achieved by the use of a thermocoax cables installed in the reactor's walls.
- This is a multiple chamber system with 3 RF chambers. Therefore deposition of different films such as (i) a-Si:H, (n) a-Si:H and (p) a-Si:H can be carried out in the same pump down process, in separated chambers with no cross contamination.

- Finally, ARCAM, by a smart rotating system of substrate holders, allow us to deposit up to three different conditions in a single run.

Typical conditions used in our experiment include an electrode distance of 28 mm and a temperature of 200°. **Figure 3-17** shows photographs of the ARCAM reactor.

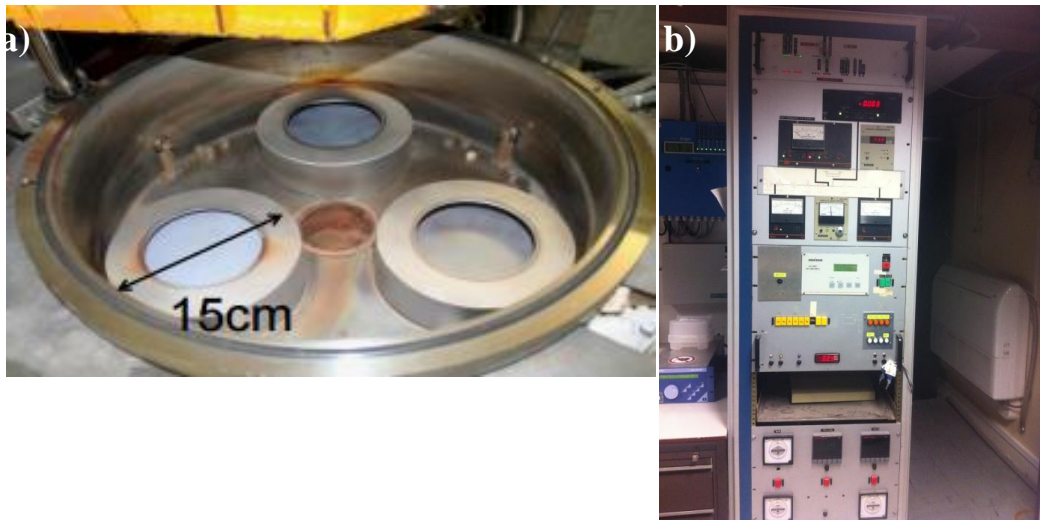


Figure 3-17: Photographs of the (a) ARCAM chamber and (b) ARCAM control panel

3.2.2 E-beam deposition

The contacts were deposited by e-beam evaporation. This technique allows an accurate control of the deposition rate. An e-beam is an ultra-high vacuum system (10^{-7} Torr) which uses a beam of electrons to evaporate a metal on a substrate. During the first stage of the process, a hot filament is heated in order to produce a beam of electrons by thermionic emission. Basically electrons are released from the hot filament as they gain enough energy to be in an excited state and to move freely. This high kinetic beam of electrons is further directed at the centre of the crucible containing the material to be deposited. The path of the electron beam is controlled by two magnets: a focusing magnet whose role is to attract the beam of electrons and a deflecting magnet which will deflect the path to the crucible. Conversion of this kinetic energy to thermal energy will heat and evaporate the target material. The

released molecules inside the chamber can move freely due to the high vacuum and therefore condensate on all the surfaces, including the substrate. The thickness is monitored by a quartz crystal. Various materials were deposited during this PhD work (Titanium, Gold, Silver, Palladium, Aluminum...). **Figure 3-18** shows the schematics of the e-beam set up (a) ([154]) and the corresponding photograph (b).

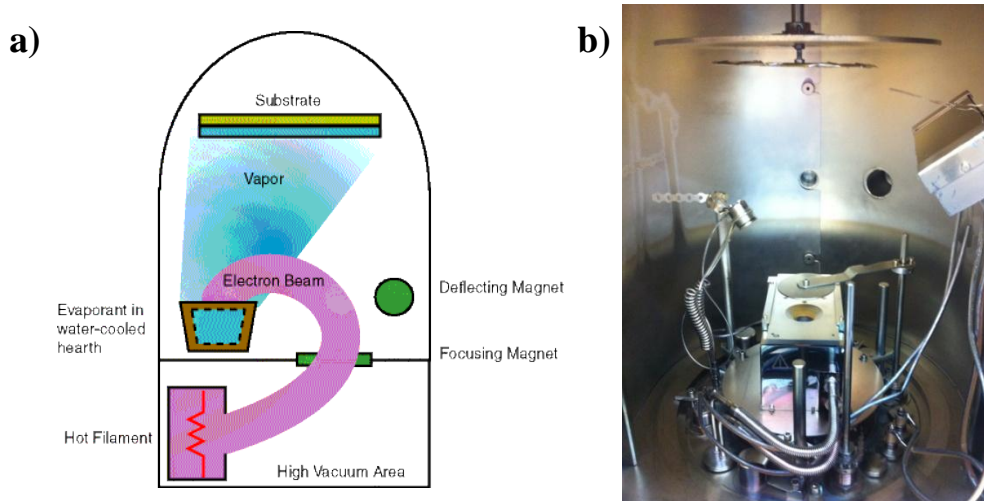


Figure 3-18: (a) Schematics [154] and (b) corresponding photograph of the e-beam evaporator.

3.2.3 Sputtering

ITO (Indium Tin Oxide) was deposited by sputtering. The principle is the same as e-beam evaporation in the sense that a material is released from a source and is then deposited on a substrate. Both techniques are classified as Physical Vapor Deposition processes. Sputtering is a low temperature process which is one of its main differences over other evaporation techniques. The working principle of a sputtering system is to use an ionized gas (a plasma) to bombard the source material, commonly named the target, inside a vacuum chamber. An inert gas such as argon is commonly used. The highly energetic ions will cause atoms to break off and to be ejected from the source. The substrate is then placed in the path of these ejected particles, resulting in the coating of the substrate by the source material. The working principle of a sputtering system is summarized in **Figure 3-19**.

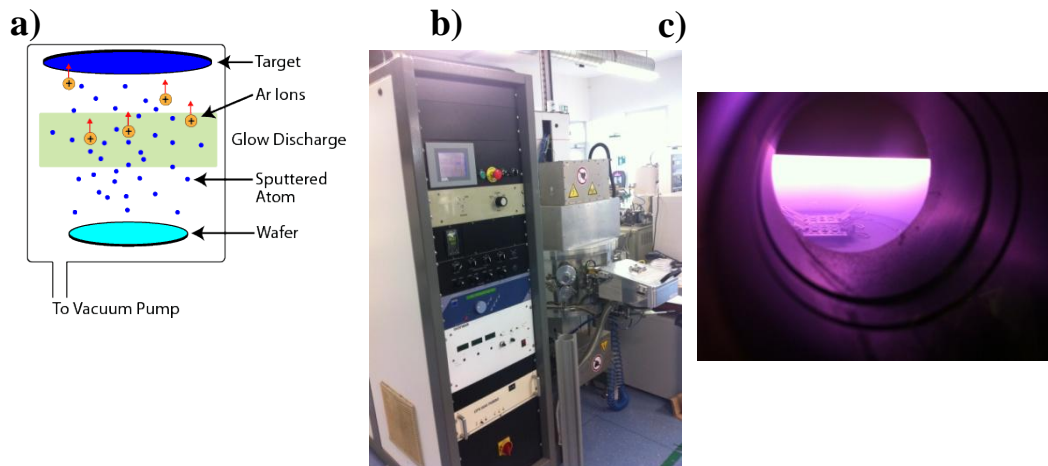


Figure 3-19: (a) Schematics [155] and (b) photograph of the sputtering system. (c) O₂:Ar plasma during the ITO deposition.

3.2.4 Spin coating

The working principle of a spin coater is very simple and allows the uniform deposition of a thin film on a substrate. The substrate is fixed on a substrate holder by vacuum suction. A small quantity of the coating material is dropped in the middle of the sample. The substrate is then simply rotated at very high speed and the film is spread homogeneously under the action of centrifugal forces as shown in **Figure 3-20** ([156]).

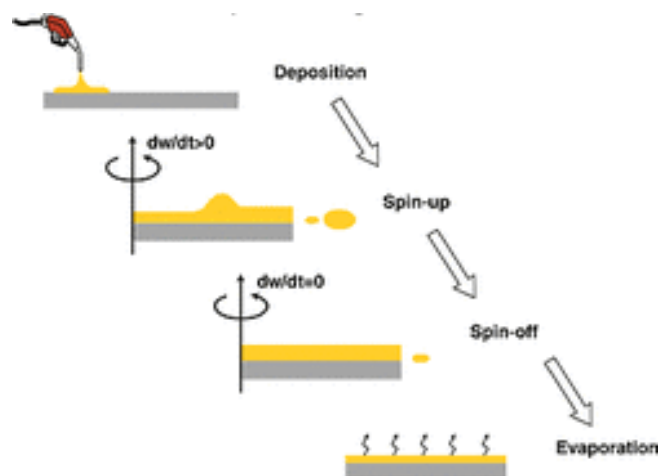


Figure 3-20: Schematics illustrating the key steps of the spin coating technique [156].

3.3 Characterization Techniques

3.3.1 J-V characteristics

The current density-voltage (J-V) characteristics of cells were measured under 100 mW/cm^2 illumination (AM 1.5G) with a commercial solar simulator (Oriel AAA) at 25°C . This corresponds to the standard conditions under which performances of the devices should be measured [157], [158]. Indeed solar radiation reaching the surface of our planet is not constant and depends on the location, the atmospheric conditions (clouds, ozone layer ...), the day time, the distance between the earth and the sun, the sun rotation, etc... To standardize the analysis, the American Society for Testing and Materials (ASTM) has chosen to use the AM 1.5 spectra "because they are representative of average conditions in the 48 contiguous states of the United States" [158]. AM stands for air mass coefficient. The value 1.5 indicates that the solar zenith angle is 48.2° . The letter G means that the spectrum is received at a surface tilted of 37° . Therefore the solar simulator reproduces the standard AM 1.5G spectrum. The equipment is driven by a Keithley SourceMeter unit that sets the voltage across the electrode and measures the corresponding current flowing through the solar cell. The intensity of the light source was calibrated using a crystalline Si reference cell before each series of measurements. A cooling system is used to set the temperature to 25°C during the measurement.

3.3.2 EQE Measurements

The spectral response (SR), which is expressed as a function of the wavelength, is defined as the ratio between the current produced by a solar cell to the power incident on the latter (in A/W). This a powerful tool that can provide unique information on the generation of current inside a device under illumination by giving the contribution of each wavelength to the global photocurrent. ASTM has also defined standardized conditions under which these measurements should be carried out (E1021-15) [159]. The system consists of a mechanical chopper, used to create a pulse source of light from a white lamp and of a monochromator that filtered this incident light. Calibration

of the set up before each series of measurements was carried out using a photodiode.

The EQE response, defined as the ratio of charge carriers collected to the incident number of photons is derived from the spectral response SR according to Eq. (3.6):

$$EQE = \frac{hc}{\lambda q} SR(\lambda) \quad 3.6$$

In fact the EQE response represents the probability that an incident photon provides one electron to the external circuit. Therefore, the EQE of a device at a certain wavelength is equal to 1 if all the photons of this particular wavelength are absorbed and if all the corresponding generated minority carriers are collected. Front surface recombination, small diffusion length, reflection or poor passivation are common factors that can reduce the overall EQE response. **Figure 3-21** summarizes the ideal and the typical experimental EQE response measured for a silicon solar cell.

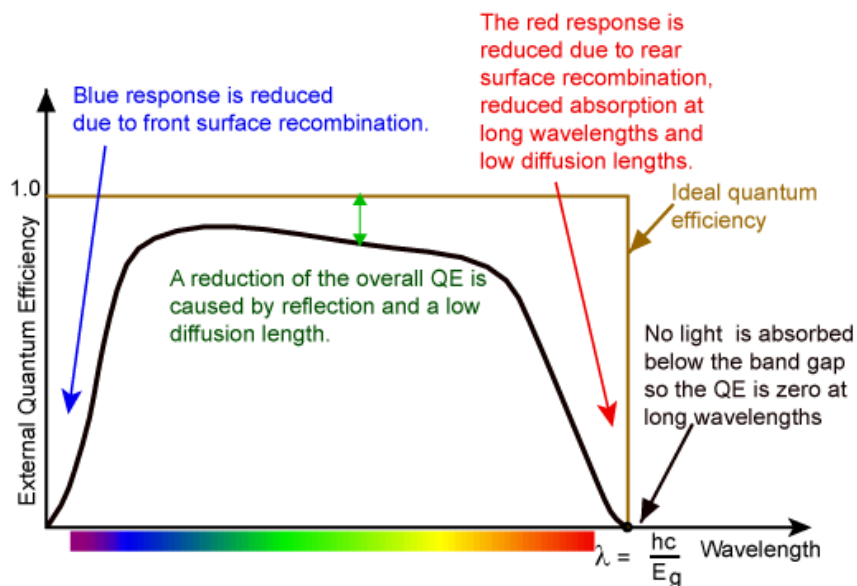


Figure 3-21: The ideal and typical EQE response of a silicon solar cell from www.pveducation.org.

3.3.3 Time Resolved Microwave-Conductivity

3.3.3.1 Theory

The quality of the passivation provided by a-Si:H can be investigated by the time resolved microwave conductivity (TRMC) technique [160]–[165]. This method has initially been implemented to analyze the interface between insulator and semiconductor before being used to investigate amorphous silicon and its alloys. The principle of the non-invasive and contactless TRMC technique is to measure the change in the microwave power reflected by a sample [160]. A laser pulse is used to generate an excess amount of free carriers $n_k(t)$ which modifies the conductivity of the sample and therefore its refractive index at microwaves frequency. The relative change in the microwave power - the so-called microwave photoconductivity or TRMC signal $\Delta P(t) / P$ - is proportional to the variation of the sample's conductivity $\Delta\sigma(t)$ for small perturbations. Therefore we can write:

$$TRMC\ signal = \frac{\Delta P(t)}{P} = A\Delta\sigma(t) = A \sum_k e\mu_k n_k(t) \quad 3.7$$

where $n_k(t)$ is the number of excess charge carriers k at time t , μ_k is the mobility of the carrier k , e is the electron charge and A is a constant.

TRMC enables us to monitor the kinetic decay of excess charge carriers caused by recombination or trapping and can be used to evaluate the effective carrier lifetime and assess the surface passivation in a non-destructive way [160], [161], [163]–[166]. TRMC signals can usually be fitted by an exponential decay using the following expression:

$$y = A_0 e^{-\frac{1}{\tau_e} t} \quad 3.8$$

with τ_e being the effective lifetime.

It is important to mention that the TRMC effective lifetime we are measuring is different from lifetime obtained by other methods such as the Eddy-current method (SINTON measurement) [167]. This is because the physics behind is not the same. For example the principle of the SINTON measurements is based on the Eddy-current method. The excess charge carriers are generated by a light pulse from a white lamp and the evolution of the excess charge carriers is monitored by a coil sending electromagnetic waves. The data

are analyzed by transient photoconductance and the Quasi-steady-state photoconductance techniques.

The general minority carrier equation can be expressed as:

$$\frac{d\Delta n}{dt} = -J(x + dx) + J(x) + G - R \text{ with } J = -D \frac{dn}{dx} \quad 3.9$$

where n is the minority carrier concentration, D is the diffusion constant, G is the generation rate and R is the recombination rate.

For TRMC measurements on silicon, the general minority carrier equation can be simplified. Indeed, we can neglect the generation rate after the excitation. As for the recombination mechanisms, we can only consider the Shokley Read Hall recombination which is the most likely to happen and which is almost constant at the minority carrier concentration we are carrying out the experiment. Therefore, a constant recombination time τ_{bulk} is assumed. The new minority carrier equation becomes [168]:

$$\frac{d\Delta n}{dt} = D \frac{d^2 \Delta n}{dx^2} - \frac{\Delta n}{\tau_{bulk}} \quad 3.10$$

where n is the minority carrier concentration, D is the diffusion constant and τ_{bulk} is the constant recombination time.

When solving the minority carrier diffusion equation, we can show that under some assumptions, the general solution is a linear combination of periodic functions with both a spatial configuration and time decay term that we named “modes solutions” [168]. If we treat the distribution of free carriers as a sum of these decay modes, what we are effectively monitoring with TRMC is the fundamental mode. This mode presents the longest time decay term and the flattest spatial configuration term. This corresponds to the diffusion of the free carriers to homogenize the carrier distribution and their recombination. Other modes have a lower typical decay time and their observation is limited by the duration of the initial excitation. Therefore these modes are happening during the laser pulse and cannot be analyzed and fitted accurately.

3.3.3.2 TRMC set up

Carrier lifetime measurements were carried out by using the time resolved microwave conductivity (TRMC) technique [162]. **Figure 3-22**

([169]) shows the schematic of the TRMC set up. The set up consists of an optical, a microwave source and an acquisition part.

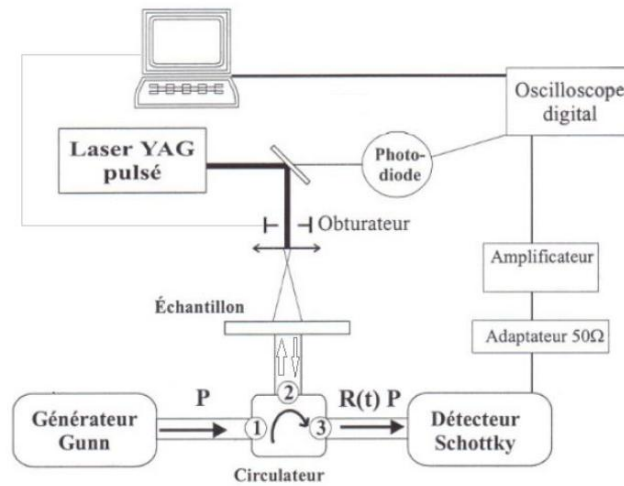


Figure 3-22: Schematics of TRMC experimental set up [169].

The pulse light source used in our experiments was a Nd:YAG laser operating at 1064 nm that will generate the charge carriers. Non-linear crystals could be used to change the wavelengths to 532 nm, 355 nm and 266 nm. In our experiment we used a wavelength of 532 nm. We obtained laser pulses with 4 ns full width at half maximum (FWHM). The laser beam diameter was less than 3 mm and its stability was in the order of a few percents. A beam splitter was used to direct one part of the light to the sample and the other part to a photodiode that would trigger the acquisition. The light directed in the sample direction would first pass through an obturator whose role was to cancel parasite signals such as electromagnetic interferences from the laser. A divergent lens allowed the laser beam to spread over the sample's surface. Another calibrated photodiode was used to measure the intensity of the incident flux.

The microwave part of the set up consists of a gunn diode (Quinstar QTM 2720) generating microwaves at a power of 100 mW at 27 GHz (Ka band), a circulator to direct the generated and reflected microwaves to the samples and the Schottky detector respectively. The Schottky diode (Microwave Resources Inc, S/N 347, Mod Ka D) was used to detect the reflected microwave signal and convert it to an electrical signal. The sensitivity

of the detector was in the order of 1000 mV/mW. Three waveguides were used to connect the samples, the gunn generator and the Schottky diode to the circulator.

The signal was acquired via a digital oscilloscope directly connected to the PC. An amplifier consisting of a low-pass filter with a cut-off frequency of either 10 or 100 MHz could be used to amplify the signal. The gain could be varied between 10-60 dB. The amplifier was used only for devices with very weak response such as very long nanowires. To minimize the noise during our acquisition, the measurement was iterated 100 times and the final signal was an average over these 100 iterations.

3.3.4 Electron Beam Induced Current

SiNW based solar cells were characterized by the electron beam induced current (EBIC) technique [170]. EBIC has been extensively used to characterize nanowires and provides a unique tool that gives insight into the electrical parameters of nanowire devices [171]–[177]. This technique uses the interaction between a device and a focused beam of electrons to generate carriers which flow and produce the so-called EBIC current. In fact the energetic electrons from the focused beam excite the p-n junction in a similar way as photons do, except that electron-hole pairs are generated by an electron beam instead of light. The electron beam whose size is very small (less than 10 nm) is scanned over the cross-section of the sample with measured variation in the EBIC current. This EBIC current is used as the imaging signal, enabling a mapping of the electronic activity of the samples. These mappings are therefore mapping of currents. The EBIC signal is collected at zero bias. It is extremely sensitive to electron-hole pair recombination, therefore it is a powerful tool to analyze defects and their impact on the performances of a device.

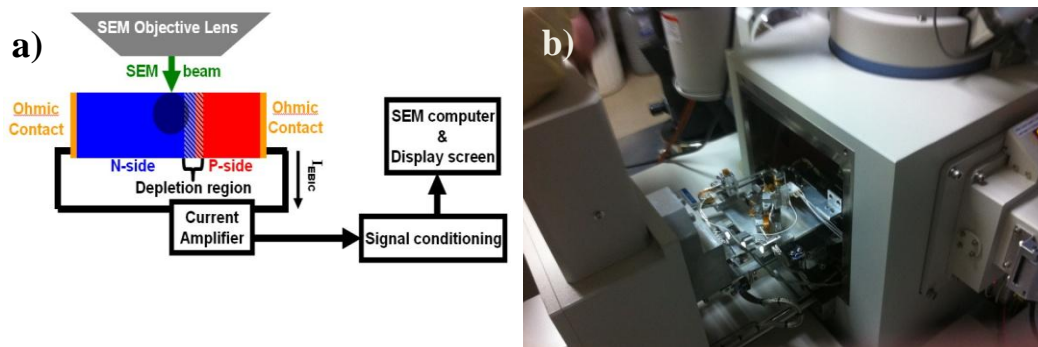


Figure 3-23: (a) Schematics of the EBIC set up [178] and (b) photograph of the EBIC equipment.

Figure 3-23 shows a schematic of the experimental set up. Measurements were carried out at a room temperature in a Hitachi SU8000 SEM system. Micro-manipulators are used for contacting the device. The beam of electrons is scanning the surface of the sample at normal incidence. The EBIC current signal is amplified via a low-noise Stanford Research System SR570 preamplifier directly connected to the micro-manipulators. The system is then connected to a synchronized monitor to visualize the mappings of currents.

3.3.5 Spectrophotometer

SiNWs were characterized by using a UV/Vis/NIR spectrophotometer (PerkinElmer) using an integrating sphere with at the angle of incidence (AOI) of 8°. The total reflectance was measured in the spectral region between 250 nm to 1500 nm. The spot size corresponded to an area of a few square millimeters.

Figure 3-24 shows a picture and a schematic of the equipment. A tungsten and a deuterium lamp are used to generate light in the visible and ultra-violet regions respectively. The wavelength is selected by passing the light through a monochromator. The integrating sphere is a spherical chamber whose walls are coated with spectralon, a highly reflective material that ensures maximum reflectance over the entire visible spectrum. The spectrophotometer can be used to measure both transmittance and reflectance. A baseline is first recorded before each series of measurement by placing a spectralon reference sample in the reflectance port. The sample is then mounted on the rear mount of the equipment to measure reflectance. Basically light of the desired wavelength

is entering the chamber through an aperture and is reflected on the sample. The light reflected at the surface of the sample is subsequently reflected by the highly reflective internal surface of the chamber, whatever the angle of reflection. This ensures that all the light reflected from the sample is effectively collected by the detector. The system can measure both total and diffuse reflectance. We use the system in the total reflectance mode, i.e. a specular white plate is placed at the specular reflectance angle. To measure in the diffuse reflectance mode, a specular light trap should be used instead. Both configurations are summarized in **Figure 3-24**.

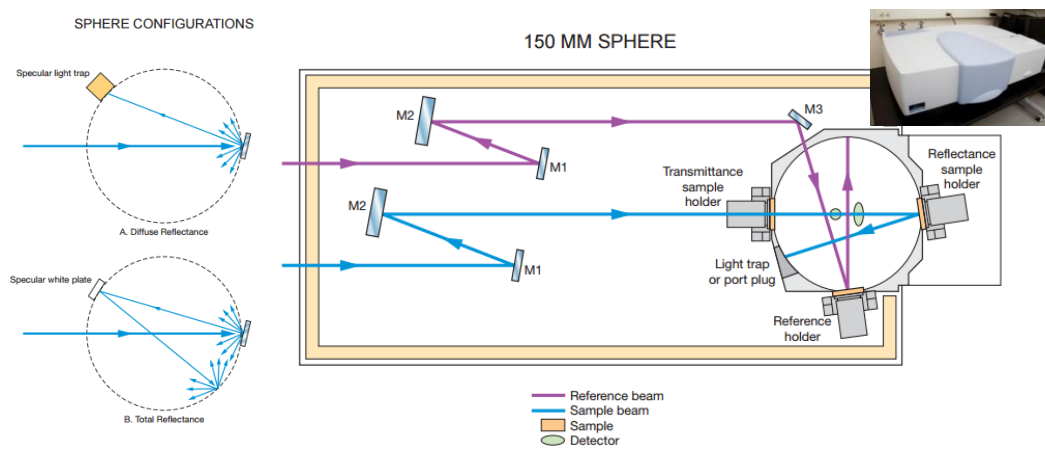


Figure 3-24: Schematics and photograph of the UV/Vis/NIR spectrophotometer (PerkinElmer) using an integrating sphere.

3.3.6 Mueller Matrix Ellipsometer

The Mueller matrix is an extremely powerful tool to characterize the optical properties of a sample. The principle is to study the response of a medium to an excitation with a polarized light (either in a reflection or transmission configuration). Mueller matrices were acquired via a SmartSE Mueller matrix ellipsometer. Measurements were taken at AOI of 60° with a spectral range from 450 to 1000 nm. This is a specular optical system (angle of incidence = angle of reflection). This technique consists of measuring the change in polarization of light induced by its reflection on the sample of interest. This change of polarization is dependent on the properties of the sample such as thickness and refractive index. First an electromagnetic wave passes through a polarizer whose role is to polarize linearly the light before

falling on the sample. This light is reflected and passes through another polarizer named analyzer which analyzes the new polarization of the light before reaching a detector. Compensators or phase modulators can be added on the incident and reflected beam path. The schematic of the set up is presented in **Figure 3-25**.

Data are further analyzed by the Mueller formalism which describes the electromagnetic wave as a stoke vector. The transformation is expressed as a 4x4 real-values matrices named the Mueller Matrices. Therefore, by comparing the polarization change induced by the medium between the incident stoke vector S_i and the reflected stoke vector S_r , the Mueller matrix M can be defined as:

$$S_i = MS_r \quad 3.11$$

Therefore the Mueller matrix is a mathematical tool that describes perfectly the polarization change induced by a medium. A wide range of optical properties can then be derived from the Mueller matrix such as the reflectance, the isotropic ellipsometry parameters, the depolarization effects...

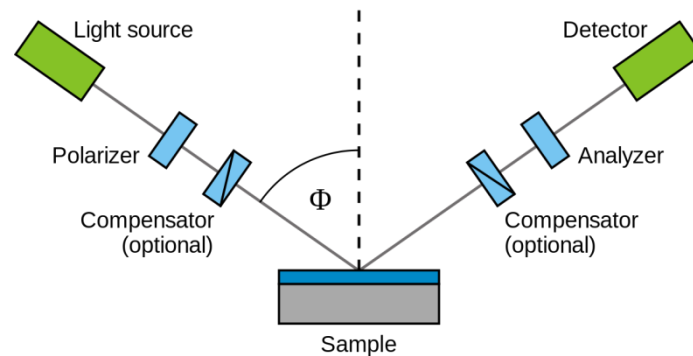


Figure 3-25: Schematics illustrating the working principle of Mueller matrix ellipsometer

3.3.7 Angle-resolved MM polarimeter (ARMMP)

Ordered arrays of SiNWs were characterized by angle-resolved Mueller Matrix polarimeter (ARMMP) [179]. ARMMP is an advanced polarimeter set up based on liquid crystals and a microscope objective, able to measure all incidence and azimuthal angles without involving any mechanical

displacement, hence its advantage over standard MM polarimeters. It is possible to measure a small spot on the sample in the range of few to tens of microns. ARMPP can achieve fast calculations of complete Mueller matrices over a wide range of polar and azimuthal angles and the setup also provides real space (microscopic) image.

Figure 3-26 ([179]) shows a schematic of the set up. Both the PSG (Polarization State Generator) and PSA (Polarization State Analyzer) parts of the equipment are composed of two nematic liquid crystals in association with a linear polarizer. Nematic liquid crystals are special transparent/ translucent liquids able to change the polarization of the light that is passing through them. Different polarizations are achieved by changing the intensity of the electric field applied to the liquid. The light is generated by a white halogen lamp whose incident angles are determined by a mask. This light is partly illuminating a Nikon microscope objective with a high nominal numerical aperture (0.95) that will ensure a wide range of polar (from 0° to 60°) and azimuthal angles (from 0° to 360°). Polar angles are limited by the numerical aperture while all azimuthal angles are possible. Imaging lenses are used to image the back Fourier plane of the objective on a CCD detector (512 x 512 pixels). This gives a picture in the Fourier space while the use of a microscope gives access to real-space pictures. Finally the wavelength of the light on the CCD was selected by an interferential filter of 633 nm.

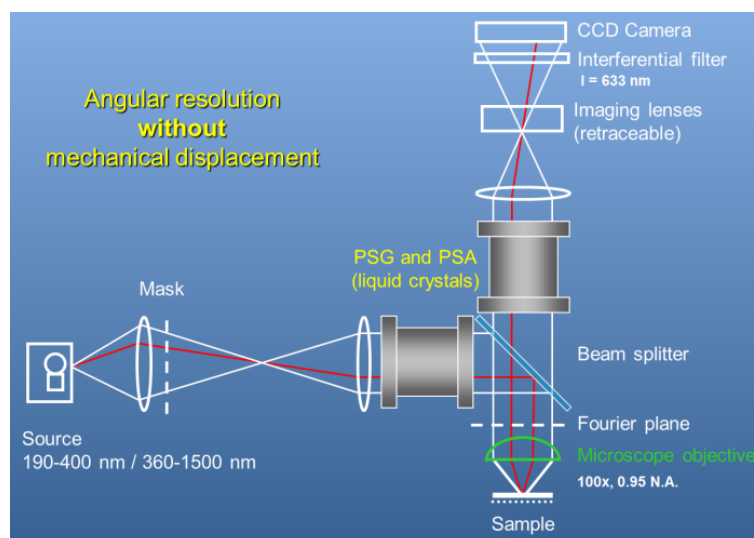


Figure 3-26: Schematics showing the working principle of the Angle-resolved MM polarimeter [179].

Chapter 4 : Solving the Agglomeration Effect of Silicon Nanowires fabricated by MACE

The metal-assisted chemical etching (MACE) [180]–[182] process offers a simple and low-cost procedure to fabricate SiNWs with a high aspect ratio over large areas. The key step of the MACE technique consists of immersing Si wafers into an etching solution (commonly HF-AgNO₃) at room temperature. The SiNWs' diameters typically lie in the range of 20-200 nm while their length is controlled by the etching time. Despite all these advantages, the MACE process suffers from an inherent problem, which is a direct side effect of the method itself. Indeed this wet etching process relies on the use of a liquid phase (chemical solution) which leads to an inherent undesirable effect: the SiNWs bend progressively until agglomeration occurs near their tips, leading to the formation of large bundles of SiNWs as illustrated in **Figure 2-6**. The Van der Waals forces [183]–[186], the capillary forces and the associated liquid bridging are often held responsible for the coalescence of the nanowires [187]–[190]. This agglomeration is an issue and is often considered as a limiting factor to achieve high efficiency solar cells. Indeed large bundles prevent from coating conformally the arrays by a photoactive material [191] (inorganic or organic coating), deteriorate the optical properties [192], [193] of the array and may induce higher series resistance [191]. Therefore finding a simple way to reduce the bundling of nanowires is highly desirable [194].

4.1 Theoretical Basis

To understand the tendency for SiNWs to clump into bundles, an investigation of the forces acting on them during the etching process is essential. There are mainly three forces: the Van der Waals force (F_{VdW}), the force arising from the solvent surface tension (F_{ST}) and the elastic deformation force (F_{ED}). Agglomeration of SiNWs results from the interaction and balance between them [194].

4.1.1 Van der Waals force

Van der Waals force is a weak intermolecular force between two bodies that arise from mutual electric interaction. Although often neglected at the macro/micro scale, it becomes non-negligible and plays a fundamental role at the nanometer scale. This interaction energy is generally attractive between two bodies of the same material and depends on the geometry and material properties. The expression for the Van der Waals force between two parallel cylinders or rods of radii R_1 and R_2 separated by a distance d , as depicted in **Figure 4-1**, is well assessed [195], [196]:

$$F_{vdw} = -\frac{AL}{8\sqrt{2}d^5} \left(\frac{R_1 R_2}{R_1 + R_2} \right)^{\frac{1}{2}} \quad 4.1$$

where A is the Hamaker constant of the silicon-water-silicon system ($A=8.88 \times 10^{-20}$ J [197], [198]).

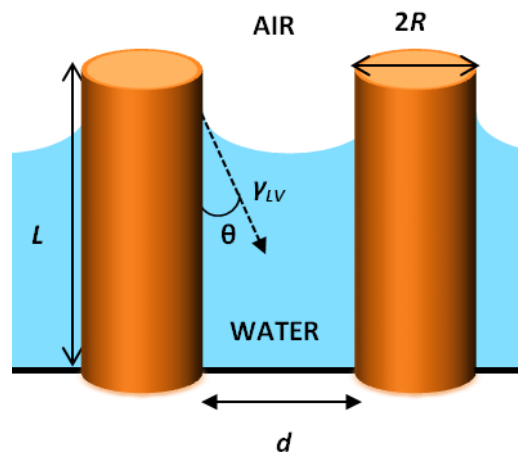


Figure 4-1: Schematic representation of two cylinders of the same length L and radii R , separated by a distance d and partially immersed in a liquid. Once the water level falls below the tip of the cylinders during the drying process, the surface tension of the liquid/vapor interface γ_{LV} induces a small curvature of the solvent to reduce the active surface area

4.1.2 Surface Tension/ Capillary effect

The experimental procedure to fabricate SiNWs involves the use of solvents. Once the solvent level falls below the tip of nanowires during the drying process, a Liquid (solvent)-Vapor (air) interface appears, characterized by an interfacial tension γ which tends to reduce the active surface area by

inducing a small curvature of the liquid as illustrated in **Figure 4-1**. The interfacial tension γ is at the origin of the capillary phenomena. Indeed the latter are due to surface tension forces acting on all points of the meniscus. The exact way interfacial tensions and capillary forces act on nanowires is still not well clarified, however different models have been developed to explain the aggregation due to surface tension. It has been suggested that the bending would most likely be due to the surface tension force of the advancing water-gas interface during the drying process [188], [199].

In the literature, the collapse has also been attributed to Laplace pressure variation in an array [200]–[203]. The Laplace pressure is the difference of pressure between the inside and outside of a curved surface. The Laplace pressure arises from the difference in pressure at the Liquid-Vapor interface and balances the surface tension force. Irregular spacing between nanowires induces different values of pressure since the pressure is inversely proportional to the diameter of the pore. This kind of isolated capillary bridge is often held responsible for the bending of NWs, all the more because the pressure variance induced by surface tension can be very large owing to the irregular spacing between nanowires, which can vary from 20 to 100 nm.

However this point of view has been challenged in the case of 2-D arrays [204]. Indeed Chandra and Yang explained that the previous hypothesis is only valid and proven for 1-D cases [205], [206]. The 2-D array should be surrounded by a continuous liquid body, therefore the mean curvature and the Laplace pressure may be constant everywhere. As a result, there should be no Laplace pressure variation and hence no bending of the SiNWs. The bundling is instead due to the lateral capillary meniscus interaction between two adjacent nanowires. This interaction force, which can either be attractive or repulsive, has been estimated between two cylinders partially immersed in a liquid [204], [207]:

$$F_{ST} = - \frac{\pi\gamma_{LV}R^2 \cos^2 \theta}{\sqrt{\left(\frac{d+2R}{2}\right)^2 - R^2}} \quad 4.2$$

where θ is the contact angle (e.g. the angle that the tangent to the liquid/air interface makes with the solid/liquid interface ($\theta \sim 0^\circ$ [188])) and γ_{LV} is the surface tension of the liquid/air interface ($\gamma_{LV}(\text{water}) = 72.8 \text{ mN/m}$ [208]).

It should be emphasized that even though it is commonly recognized that the driving force for the nanowires agglomeration stems from capillary forces, the interaction between liquid and arrays of nanowires of high aspect ratio is very complicated, and not yet clarified. For example, the relation between the size of the bundles, the chemical and mechanical characteristics of the nanowires (diameter, wettability, etc...) and that of the solvent is not clearly established.

4.1.3 Elastic deformation force

Due to their own stiffness, SiNWs can hold out, to a certain extent, against the deformation forces they experience. To make two nanowires contact each other, the bending force has to overcome the parallel elastic deformation force due to the tensile strength of the material. The relation between the lateral displacement δ perpendicular to the nanowire and the resulting elastic deformation force on the top of the nanowires is given by [209]:

$$F_{ED} = \frac{3EI\delta}{L^3} \quad 4.3$$

where L , E , I and δ are respectively the length, Young's modulus ($E= 1.30 \times 10^{11}$ Pa [210]–[212] for SiNWs), moment of inertia and deflection of the SiNWs.

The moment of inertia of a circular cross section nanowire is $I = \pi R^4/4$. Therefore, the elastic deformation force is as follows:

$$F_{ED} = \frac{3\pi ER^4\delta}{4L^3} \quad 4.4$$

All the fundamental forces acting on the nanowires are summarized in **Figure 4-2**.

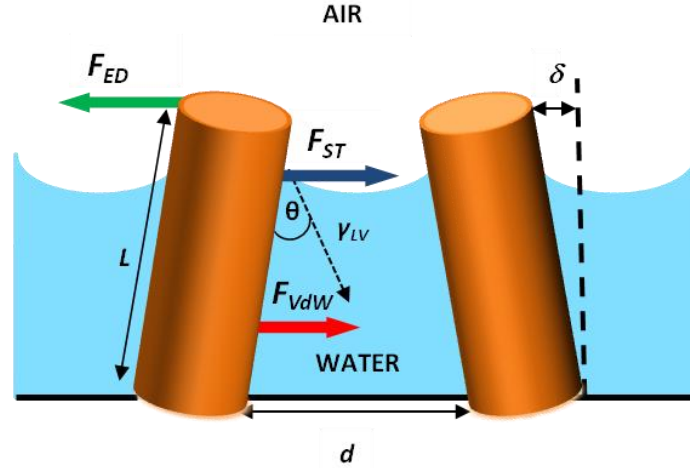


Figure 4-2: Schematic illustration of the forces acting on two SiNWs partially immersed in a liquid. The bending of the SiNWs stems from a balance between the Van der Waals (F_{vdW}) and the surface tension (F_{ST}) attractive forces and the repulsive elastic deformation force F_{ED} . γ_{LV} is the surface tension which characterizes the liquid/vapor interface. δ is the deflection of the NW.

4.1.4 Modeling - array of three nanowires

First we consider the simple case of a pair of identical SiNWs partially immersed in a liquid as depicted in **Figure 4-2**. We assume two SiNWs with a radius R of 30 nm and a length L of 2 μm separated by a distance d of 50 nm. Assuming contact at $d_{adhesion} = 0.5$ nm of distance [213], [214], adhesion between the two symmetric SiNWs occurs when the attractive forces (sum of the surface tension F_{ST} and Van der Waals F_{vdW} forces) overcome the recovery elastic deformation force for $(d - d_{adhesion})/2$ displacement. The force required to bend a nanowire is computed as the value of F_{ED} for $\delta = (d - 0.5 \text{ nm})/2$, where the deflection undergone by the nanowires enables the contact. Note that the bending moment is maximal when the meniscus is at the tip top of the nanowires. Each specific geometry has given values of F_{ST} , F_{vdW} and F_{ED} . For such geometry, the calculations gave: $F_{ST} = 4.47 \times 10^{-9}$ N, $F_{vdW} = 3.44 \times 10^{-12}$ N and $F_{ED} = 7.68 \times 10^{-10}$ N. We note that the Van der Waals and capillary forces differ by three orders of magnitude. Therefore the capillary forces are the driving force for the SiNWs agglomeration. Nevertheless, calculation shows that the Van de Waals forces increase by more than five orders of magnitude and become stronger than the capillary forces at $d = 1.3$ nm. SiNWs can therefore be plastically deformed when the capillary bending force overcomes the elasticity resistance deformation limit of the material or when this force

pushes the SiNWs so close that the Van der Waals force becomes prevalent, making the SiNWs irremediably stick together. Once the nanowires are too close, the adhesion of the nanowires will persist.

However the situation in an array is much more complex since superposition of pairwise interactions between one SiNW and its neighboring SiNWs have to be taken into account. A nanowire undergoes interaction forces from the surrounding environment and its bending results from a complex equilibrium between all these forces. To exemplify this point, a simple model composed of one nanowire (labeled SiNW #2) situated between two fixed nanowires (SiNW #1 and SiNW #3) is considered, as shown in **Figure 4-3**. The distance d' between SiNW #1 and #3 at the edges is a constant defined by $d' = 2\beta = 2\Delta + 4R$ where β and Δ are defined in **Figure 4-3**. The position of SiNW #2 is varied within the range $[-\Delta, \Delta]$ in order to enlighten the effect of superposition of pairwise interaction according to the distance. F_{XY} is the force exerted by SiNW #X on SiNW #Y. The forces exerting on SiNW #2 are added up to obtain the resulting force F_{TOTAL} :

$$F_{TOTAL} = F_{ST\ 3/2} - F_{ST\ 1/2} + F_{VdW\ 3/2} - F_{VdW\ 1/2} - F_{ED}.$$

At equilibrium, the different forces balance each other so that $F_{TOTAL} = 0$. By using the expressions of the forces defined above and equating F_{TOTAL} to zero, the bending displacement X_2 as defined in **Figure 4-3 (b)** can be retrieved:

$$X_2 = \frac{8L^3\gamma \cos \theta^2}{3ER^2} \left(\frac{1}{\sqrt{(\beta - X)^2 - 4R^2}} - \frac{1}{\sqrt{(\beta + X)^2 - 4R^2}} \right) + \frac{AL^4}{12\pi ER^2} \left(\frac{1}{(\beta - X - 2R)^{5/2}} - \frac{1}{(\beta + X - 2R)^{5/2}} \right) \quad 4.5$$

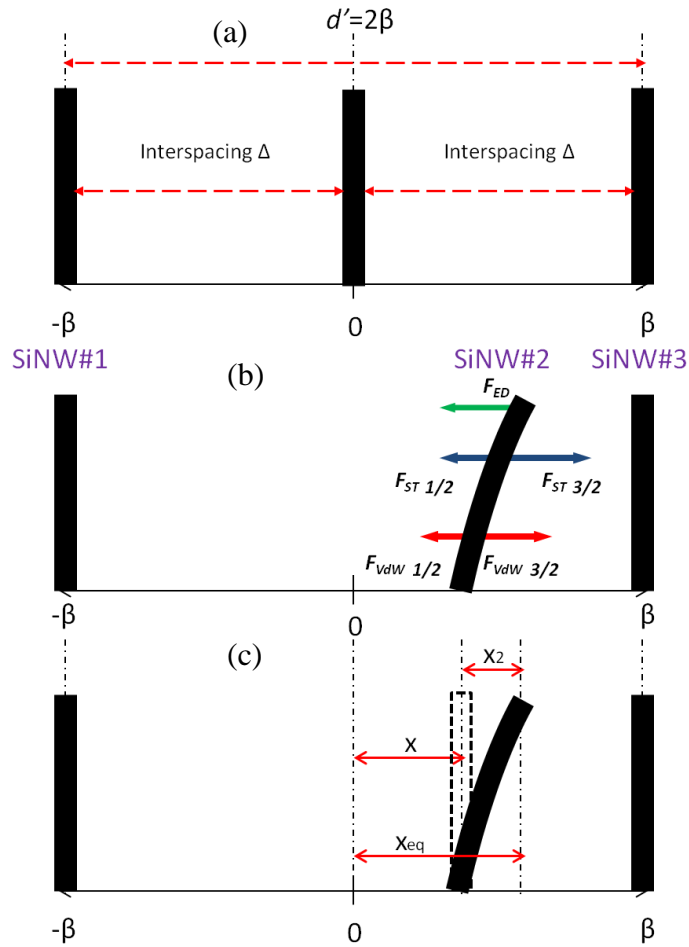


Figure 4-3: Schematic model of an array composed of three 2 μm long-nanowires labeled 1, 2 and 3. Definition of the original geometry- the ideal case (a). Definition of the forces: F_{XY} is the force exerted by SiNW #X on SiNW #Y (b). Definition of the equilibrium position before (nanowire in dotted lines) and after bending (c).

We considered three identical SiNWs of 2 μm length with a diameter of 30 nm. We vary the position X of SiNW #2 and study its resulting equilibrium position X_{eq} . **Figure 4-4** shows the equilibrium position X_{eq} of SiNW #2 as a function of its initial position X . Different values of Δ have been investigated and the results normalized to Δ for comparison. We only display results for X varying from 0 to Δ , the case being symmetric for X varying from 0 to $-\Delta$. The line $X_{\text{eq}} = X$ is the ideal case when the nanowires do not bend, e.g. the tip and the bottom of the nanowire are aligned. X enables the quantification of the regularity of an array. In a perfect array, i.e. $X = 0$, all the forces exerting on the nanowires are supposed to balance each other: therefore no bending should be observed. For $X \neq 0$, we step aside from the ideal case, since the interspacing

between the nanowires varies. Each curve in **Figure 4-4** shows that for a critical value $X = X_{\text{cri}}(\Delta)$, adhesion of the nanowires occurs. Indeed, when $X_{\text{eq}}/\Delta = 1/-1$ (e.g. $X_{\text{eq}} = \Delta$ or $X_{\text{eq}} = -\Delta$), SiNW # 2 touch SiNW #3 ($X_{\text{eq}} = \Delta$) or SiNW #1 ($X_{\text{eq}} = -\Delta$) respectively.

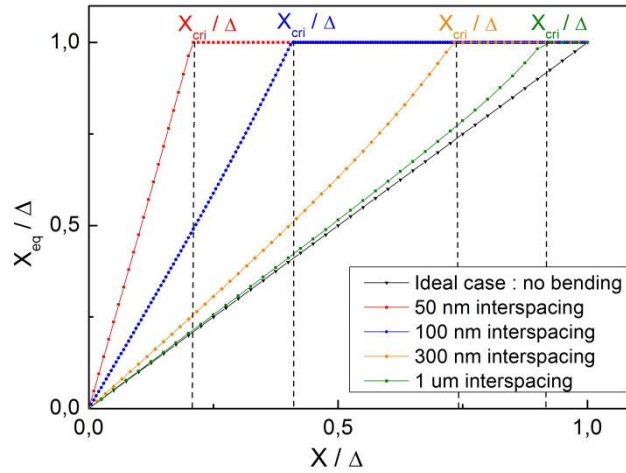


Figure 4-4: Equilibrium position of SiNW #2 as function of its initial position. When the interspacing Δ between two nanowires in the array is short, any minor irregularity ($X/\Delta > 0.2$ or $X/\Delta < -0.2$) lead to adhesion of the nanowires ($X_{\text{eq}}/\Delta = 1/-1$) whereas for larger nanowires-interspacing Δ , adhesion occurs for larger irregularities ($X/\Delta > 0.6$ or $X/\Delta < -0.6$).

When the NWs interspacing in an array is short ($\beta < 50$ nm in our case), any irregularity of the array i.e. small variations of X around its initial position, leads to an adhesion of the nanowires (X_{cri} small). For larger values of β (the case of case $\beta = 1$ μm), the adhesion only occurs very close to the extrema, and the behavior is close to the ideal case where no bending is observed (i.e. $X = X_{\text{eq}}$). An array fabricated by the MACE technique is characterized by very small interspacing (in the order of tens of nanometers) and irregularly spaced NWs. This can explain why large bundles are usually observed for the MACE process. Such calculations prove that the inherent irregularity of the nanowires array fabricated by MACE is responsible for the bundling as pairwise interactions between nanowires do not compensate and that the larger the irregularity is, the more likely the bundling is [194].

4.1.5 Effect of the SiNW length on the agglomeration

The length of the SiNWs has a drastic effect on the agglomeration. The longer the SiNWs are, the larger are the bundles observed. To understand this effect, we can consider the simple case of a pair of identical SiNWs partially immersed in a liquid as depicted in **Figure 4-2**. We assume two SiNWs with a radius R of 30 nm separated by a distance d of 50 nm. **Figure 4-5** is depicting the effect of the length on the different forces acting on the SiNWs and responsible for their agglomeration. We can observe that:

- the elastic deformation force is plummeting with the increasing SiNW length,
- the capillary forces are independent of the SiNW length,
- the Van der Waals forces are increasing slightly with the length of the SiNWs.

The Van der Waals forces being weaker than the capillary forces of several order of magnitude, the agglomeration of SiNWs is observed when the blue curve depicting the capillary forces (attractive force) is crossing the green curve of the elastic deformation force (repulsive force).

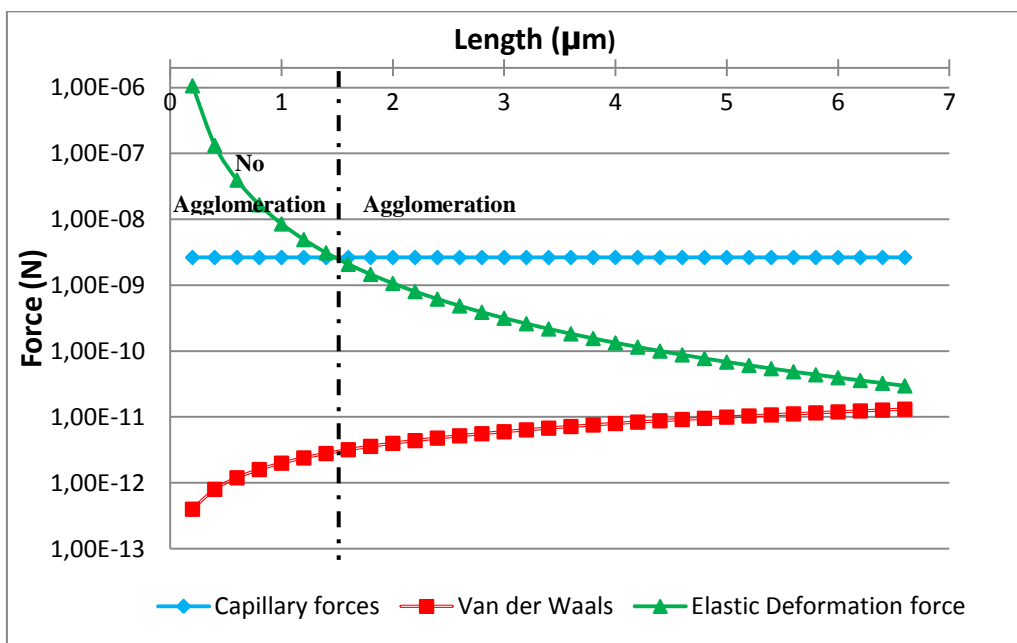


Figure 4-5: Effect of the length on the Van der Waals, capillary and elastic deformation forces

From this graph, we can clearly observe that the strong agglomeration observed for long SiNWs is due to the collapsing of the value of the elastic deformation force with the increasing length of SiNWs (4 orders of magnitude when the length is increasing from 200 nm to 7 μm). This is due to the fact that the elastic deformation force is inversely proportional to the cube of the length of the nanowire. Basically, the stiffness of the wires is decreasing drastically with the length of the nanowires. As a consequence, long SiNWs have more difficulty to counter balance the attractive force, hence the strong agglomeration observed for long SiNWs.

4.2 Investigation of the Solutions proposed in the Literature to avoid the Bundling of Silicon Nanowires

Several attempts have been reported in the literature to solve the agglomeration issue of the SiNWs. They basically fall into 3 categories: use of low surface-tension solvent, post-treatment and special drying technics. We first investigate and test the different methods reported in the literature:

Then, in the next section, we proposed our own method to reduce significantly the bundling of SiNWs. Our method enables to overcome the main drawbacks of the methods listed above. Our process shows that the control of the wettability properties of both the initial wafer substrate and the SiNWs' surface can be an effective way to achieve dense and uniform SiNW arrays with good lateral separation.

4.2.1 Literature Review

4.2.1.1 Low surface-tension solvent

One way to reduce agglomeration of SiNWs is to reduce the attractive forces exerting on the SiNWs. According to equation 4.2, the capillary forces F_{ST} , responsible for SiNWs agglomeration, are directly proportional to the surface tension γ_{LV} of the solvent used. Therefore a straightforward way to minimize the attractive forces is to use a solvent with a low surface tension. The etching process is normally conducted in water whose surface tension γ_{LV} is high ($\gamma_{water} = 75.64\text{mN/m}$). Water can be replaced by solvents with a lower

interfacial tension [215] such as ethanol ($\gamma_{ethanol} = 22.27$ mN/m), methanol n ($\gamma_{methanol} = 22.6$ mN/m), n-hexane ($\gamma_{n-hexane} = 18.4$ mN/m), n-octane ($\gamma_{n-octane} = 21.8$ mN/m). Using such solvents might considerably reduce the strength of the capillary forces. For example, using ethanol instead of water can decrease more than 3 times the amplitude of the capillary forces ($\frac{\gamma_{water}}{\gamma_{ethanol}} = 3.4$). The replacement of solvent can be done at different stages of the fabrication process. For example, we might prepare the HF based etching solution by replacing water by another solvent. Nevertheless, it has been reported that the solvent can greatly influence the etching process which is undesirable. Indeed, *Li and al.* [215] have used ethanol as a low-surface-tension solvent and found that the ideal ethanol concentration is about 12.5%. Another possibility is to perform the last step of the SiNWs fabrication process - the rinsing step - with low-surface-tension liquids.

4.2.1.2 Post treatment

Two kinds of post-treatments were tested: wet etching and dry etching. These processes took place after completion of the SiNWs fabrication, e.g. SiNWs are already forming large bundles and the objective of these post-treatments is to separate them.

4.2.1.2.1 Wet etching:

Jin-Young Jung et al. [193] have proposed to taper the top-end of the NWs by a post-wet etching treatment based on KOH solution. The principle is to use the typical anisotropic etching of silicon by KOH solutions, whose etch rate depends heavily on the surface bond strength of the silicon atoms. Indeed, strong alkaline solutions like KOH (Potassium Hydroxide) or TMAH (Tetramethylammonium Hydroxide) etch silicon anisotropically according to the following reaction: $\text{Si} + 4 \text{OH}^- \rightarrow \text{Si}(\text{OH})_4 + 4\text{e}^-$.

It is more common to use KOH solutions instead of TMAH solutions because KOH has an etch ratio eight to nine times more than TMAH. The etching by KOH or TMAH is not diffusion but etch rate limited. Si is etched anisotropically because the bonding strength of the Si atoms are depending on the crystal plane considered: for example KOH has no effect on the (111)

planes whereas the (100) and (110) crystal planes are attacked by the etching solution [216]. According to the wafer orientation, we observe:

- (111) c-Si wafers are stable and are almost left intact by the etch
- (100) wafers lead to the formation of pyramids with (111) surfaces. This is a common process to form pyramids for enhancing absorption and reduce reflection on c-Si solar cells.
- (110) wafers are resulting in the formation of vertical trenches whose sidewalls are (111) oriented. This is a common process to form microchannels.

Atoms located on the edge of the NWs present weaker bonds and will be etched faster, hence the formation of tips. The principle of the method is summarized in **Figure 4-6**.

The idea is therefore to achieve separation by sharpening the top end of the SiNWs. *Jin-Young Jung et al.* [186], [193] claimed to obtain vertically aligned, tapered SiNWs through this simple and cheap method. They used an aqueous solution of 30 wt% KOH at 20 °C just after metal-assisted etching. The SEM images in **Figure 4-7** show the results they have obtained.

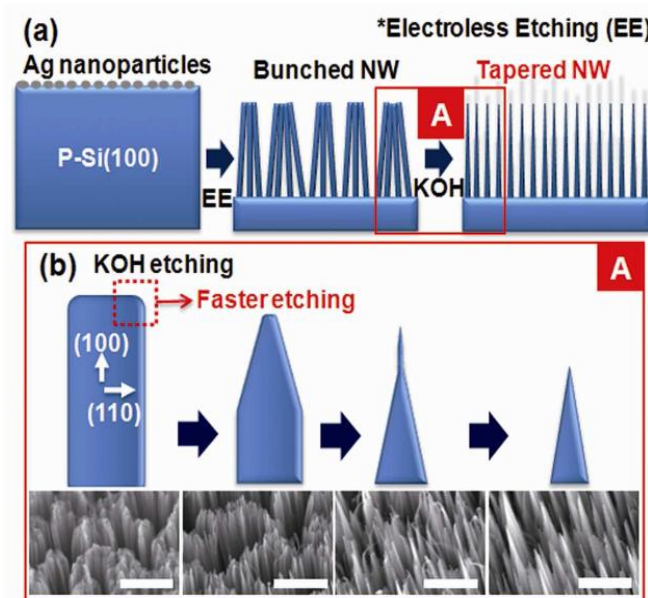


Figure 4-6: (a) Schematic detailing the fabrication process of agglomerated and tapered SiNWs. (b) Schematic showing the effect of KOH post-etching treatment to taper the top-ends of SiNWs [186], [193]

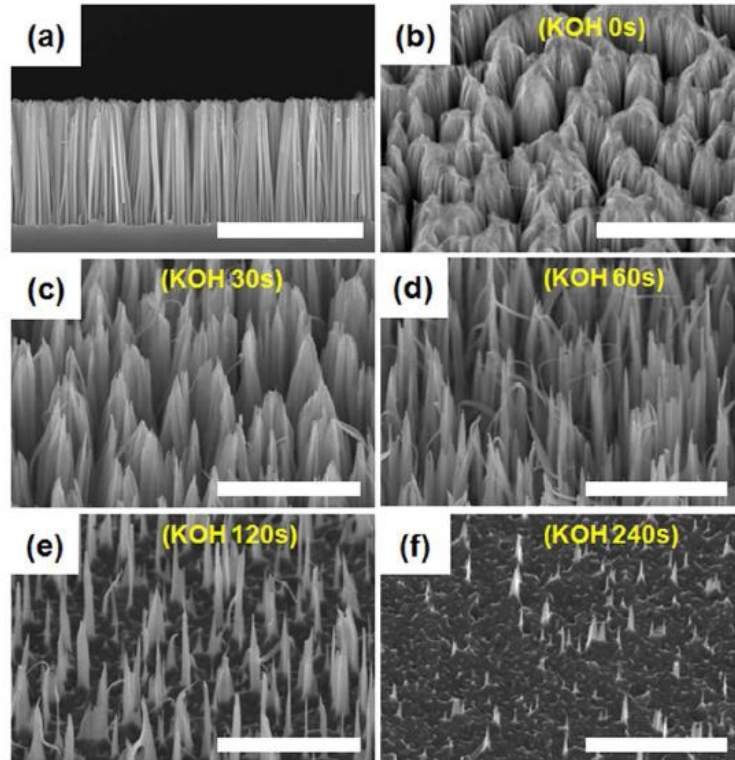


Figure 4-7: (a) Cross-section SEM images of the SiNW array after MACE with a scale bar of 10 μm . Inclined (30°) SEM images showing the effect of KOH post-etching treatment on the morphology of SiNWs as a function of the etching time: (b) 0 s, (c) 30 s, (d) 60 s, (e) 120 s, and (f) 240 s. Scale bars in (b)–(f) are 5 μm [186], [193].

First we observe that this is a destructive method, as the density of the SiNWs reduces drastically with the etching time. Moreover, from the observation of the SEM images (**Figure 4-7**), it is not true to claim that individual nanowires are sharpened and separated from each other. We cannot see the sharp tip-shape of the nanowires themselves, as this is more the bundles of SiNWs that show a sharp tip-shape rather than individual nanowires. Finally, the post-treatment still took place in liquid phase, which means that capillary forces are still there and are still exerting attraction between the SiNWs.

4.2.1.2.2 Dry etching

Another possibility includes a post-dry etching process [215]. The NWs array undergoes a post-plasma treatment in a RIE system. The positive aspect of this method is that the post-treatment is carried out in dry-phase, therefore at this stage, no more capillary forces are underwent by the NWs. NWs are stuck to each other only by the Van der Waals forces. A good separation of the NWs

is achieved. However the process induces slimming of the NWs and formation of surface defects, without mentioning the extra-cost and process-time induced by RIE.

4.2.1.3 Special Drying techniques

An effective way to eliminate the capillary effect would be to suppress its origin by preventing the formation of a liquid-gas interface in the first place. In the ordinary drying process, liquid evaporates and capillary forces arise as a result of the surface tension of the Liquid–Vapor interface. Two special drying techniques are often considered to eliminate the surface tension: the freeze-drying process and the supercritical drying process. The first method, the freeze-drying process, enables the removal of liquids by first freezing the system before decreasing the pressure and supplying enough heat so that the frozen water in the system can directly sublime from the solid phase to the gas phase. *Li et al.* successfully managed to achieve separation of NWs using this method [215]. In the supercritical drying process the liquid is transferred to vapor via the supercritical phase. Carbon dioxide is generally used because of its low critical temperature and pressure ($T_c = 31,1^\circ\text{C}$, $P_c = 72,8 \text{ atm}$). During evaporation of the supercritical carbon dioxide, no Liquid–Vapor interface exists, so there are no capillary forces involved, and the driving force of the agglomeration is suppressed. In this way, SiNWs with reduced agglomeration have been fabricated [188]. Although good results have been reported with these methods, they make the NWs fabrication process more complicated and expensive to implement.

4.2.1.4 Other approaches

Two other approaches can be considered to avoid the bundling of SiNWs. According to Eq. (4.2), the capillary forces F_{ST} , responsible for SiNWs agglomeration, are directly proportional to the contact angle θ . Therefore by changing the combination of the surface and the liquid to be dried, a contact angle close to 90° (i.e. $\cos(\theta)=0$) can be achieved in order to suppress the capillary forces. However, in practice, it will be very challenging if not impossible to obtain a contact angle equal to zero.

Another approach is to strengthen the nanowires mechanically [217]. The idea is to erect momentary polymer structures to reinforce flexible microstructures during the drying stage. The polymer is at the end of the process removed by plasma since plasma does not involve any liquids (no phenomenon of interfacial tension). It enables to counteract the surface tensional forces during drying. The principle of this method is illustrated in Figure 4-8. To prevent the sticking of the structures, *Kozłowski and al.* [217] have substituted the rinsing liquid by a monomer (divinylbenzene) which polymerization was initiated by irradiation under ultraviolet light. The solid polymer obtained was then removed by oxygen plasma. We think that this approach is quite complex and the risk of impurity (residual polymer structure between the SiNWs) will be a problem for subsequent integration of these SiNWs into solar cells.

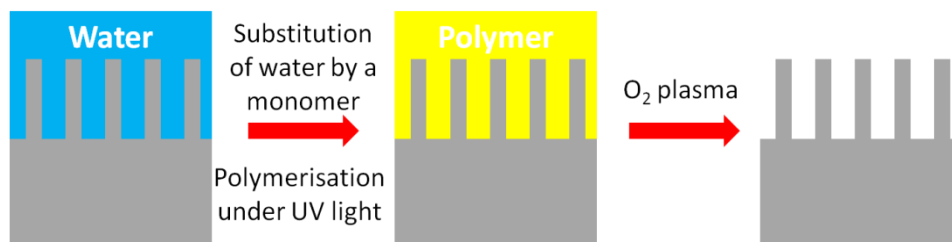


Figure 4-8: Schematic illustrating the principle of strengthen mechanically the nanowires by a polymer.

We have just reviewed the different approaches that can be considered to solve the problem of agglomeration of SiNWs. We have decided to focus our attention on low-surface tension solvent, the post-treatment methods (wet etching and dry etching) and the supercritical drying process as they appear as good candidates to reduce SiNWs agglomeration. In the next section, we have tested and evaluated the relevance of these different methods.

4.2.2 Experimental Section

SiNWs were fabricated by the standard MACE process. Experimental details can be found in the section 3.1.1 of this thesis.

4.2.3 Low surface-tension solvent

As mentioned in section 4.2.1.1, one way to minimize the bundling of SiNWs is to use a solvent with a low surface-tension such as ethanol ($\gamma_{ethanol} = 22.27$ mN/m at 20°C), acetone ($\gamma_{acetone} = 25.20$ mN/m at 20°C) or isopropanol (IPA) ($\gamma_{isopropanol} = 23.00$ mN/m at 20°C). The solvent replacement can be conducted at different stages of the SiNWs fabrication process: during the chemical etching step, during the removal of silver dendrites step, or during the rinsing step. However, capillary forces arose during the drying process, the last step of the fabrication procedure. Therefore SiNWs have to be immersed in the low-surface tension solvent for the drying stage when attractive forces are at play. To replace the solvent in the previous stages is not supposed to have a critical impact on the SiNWs morphology. Moreover, we need to consider the different chemical incompatibilities. Strong acids should be never mixed with organic solvents as they may react. In particular sulfuric acid and nitric acid may react highly exothermically and cause fires. Therefore we cannot mix our solvent with nitric acid during the stage of silver dendrites removal. The mixing of ethanol with silver nitrate is also an explosive combination. For safety reasons, we have decided not to change the solvent during process but rather at the end of the process, prior to the drying stage which is the critical step in SiNWs agglomeration.

After immersion in nitric acid bath, samples were fully rinsed in DI water to clean any nitric acid residual. Ethanol was used since it has the smallest surface-tension. The replacement of solvents was achieved by immersing the samples in several baths of ethanol with different concentrations for at least 15 min each:

- Immersion of the samples in 70% Ethanol solution for 15 minutes.
- Immersion of the samples in 85% Ethanol solution for 15 minutes.
- Immersion of the samples in 100% Ethanol solution for 15 minutes.
- Immersion of the samples in 100% Ethanol solution again for another 15 minutes.

As shown in **Figure 4-9**, no convincing results were obtained: bundles, although smaller, are still observed. It means that the reduction of the force magnitude was not enough to suppress the agglomeration of SiNWs. Moreover,

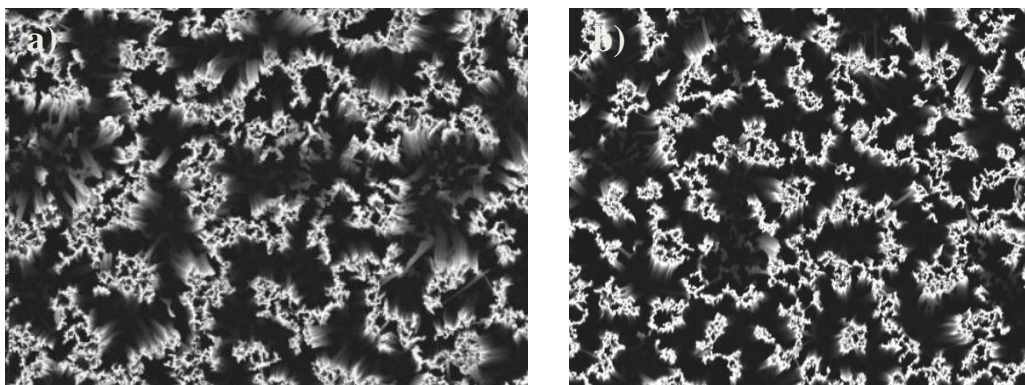


Figure 4-9: SEM pictures of SiNWs arrays (a) before and (b) after the replacement of solvent.

when replacing the solvent, samples were transferred quickly from one bath to another. Even if the transfer was fast, as ethanol evaporates quickly, it was also possible that the sample started to dry when outside the liquid solution. Capillary forces were present and some nanowires might have started to bend and stuck to each other.

4.2.4 Etching post-treatment

4.2.4.1 Wet etching

We also tested the wet etching post treatment by KOH solution to taper SiNWs [186], [193] in order to achieve SiNWs with total separation after the metal-assisted electroless etching treatment. For that purpose after the last rinsing step of the SiNWs fabrication procedure, the samples were immersed in a 30% w/w KOH solution for 30s, 45s, 60s and 75s. The solution was prepared from pellets of potassium hydroxide (30g of KOH in 70g of water). Dissolution of KOH pellets in water is strongly exothermique, meaning that the process gives off significant heat. Therefore it is very important to allow the solution to cool to ambient temperature before using it: otherwise the etch reaction is highly reactive and the results are not reproducible. **Figure 4-10** shows the effect of KOH post-treatment on the morphology of SiNWs for different treatment times and for different magnification (x 7 KeV, x 12 KeV, x 23 KeV and x 35 KeV). SEM pictures of the samples before post-treatment are also displayed for reference. From the SEM pictures of **Figure 4-10**, we can make the following observations:

- (i) Good lateral separation of SiNWs is not achieved.

(ii) The SiNWs bundles present a sharp-tip shape, but the nanowires are still stuck to each which is consistent with our analyze of the work by *Jin-Young Jung et al.* [186].

(iii) This method is also destructive as the nanowires were completely etched away, leading to a drastic reduction of the nanowires density. The effect is more prominent with increasing etch-time.

Since the driving force for SiNWs agglomeration is the capillary effect, this method does not suppress the cause of the problem. Indeed this post-treatment is a solution based process and therefore the capillary forces are not eliminated, hence agglomeration of SiNWs is still observed.

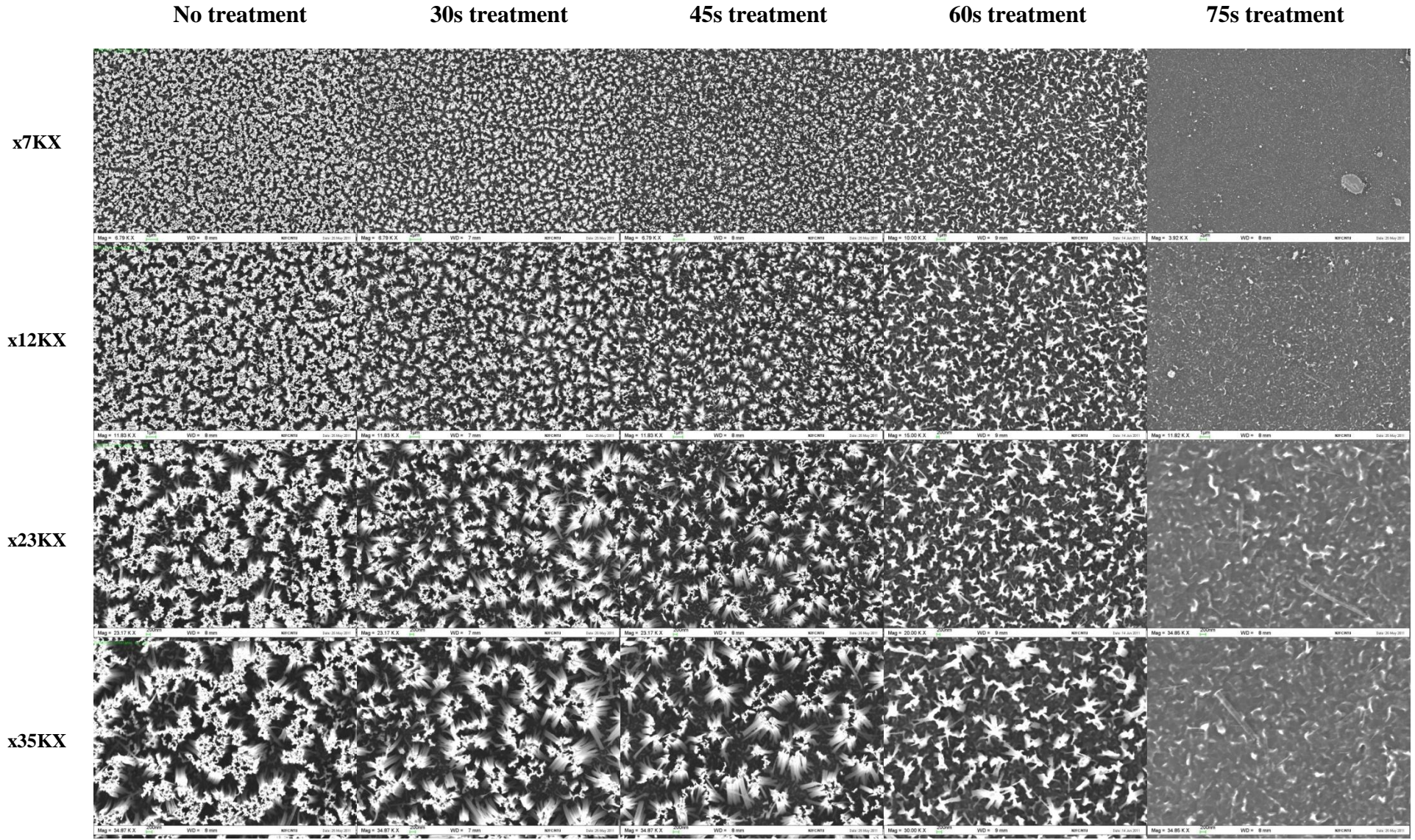


Figure 4-10: Effect of KOH post-treatment on the morphology of SiNWs for different time of treatment and for different magnification.

4.2.4.2 Dry etching

The use of the RIE technique [69] to help reduce the size of the SiNWs bundles appears as a more relevant method than the wet etching process. Indeed, as there is no solvent involved in this etch post-treatment, there is no capillary tension involved. The idea is to etch the top tips of the nanowires in order to achieve separation of the SiNWs, and reduce the big bundles to smaller ones. The experiments were carried out in a RIE system (OXFORD INSTRUMENT) which utilizes reactive radicals generated in the plasma. These radicals undergo a series of chemical reactions with the Si surface. The volatile by-products produced by these reactions are then pumped away by the system. The different parameters to be optimized are as follows: time, nature of the gas, flow rate, the pressure and the power. Each parameter has been tuned while maintaining the other parameters constant in order to understand its impact. The RF power was revealed to be a critical parameter. When the power was varied from 100 to 200 Watt, the SiNWs collapsed and lied on the wafer. When the power is exceeded 200 watt, the SiNWs arrays were completely etched away as shown in **Figure 4-11**.

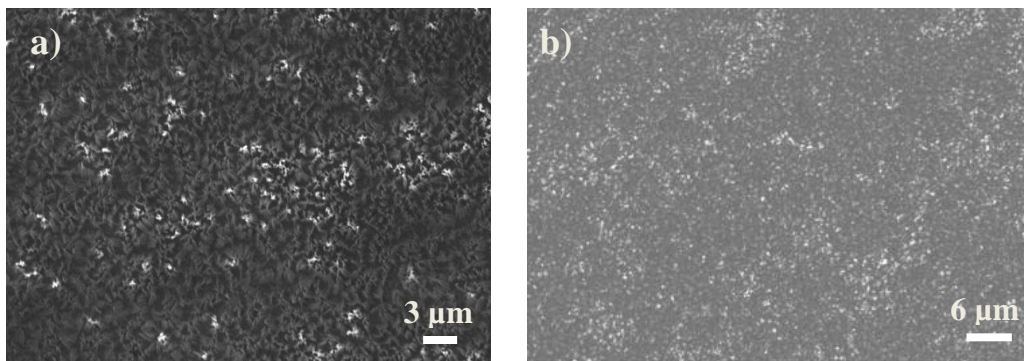


Figure 4-11: Effect of power on the etching of SiNWs (a) At 100 Watt, the SiNWs collapse and lied on the wafer. (b) At 200 Watt, the SiNWs are completely etched away.

A mixture of SF_6/O_2 was used. Our best results were achieved with the following recipe:

- Pressure: 120 mTorr
- Power: 50 Watt
- Gas: SF_6 (15 sccm) and O_2 (5 sccm)

- Time: 20s

Our results show that the SiNWs can be separated by the RIE etching as shown in **Figure 4-12**. However, this RIE post treatment complicates the fabrication process of SiNWs. Moreover the RIE process induces both slimming of NWS and roughness which is undesirable for solar cells application since surface recombination might be enhanced [69]. We should not forget that this method relies on the physical etching of SiNWs, which means partial destruction of SiNWs.

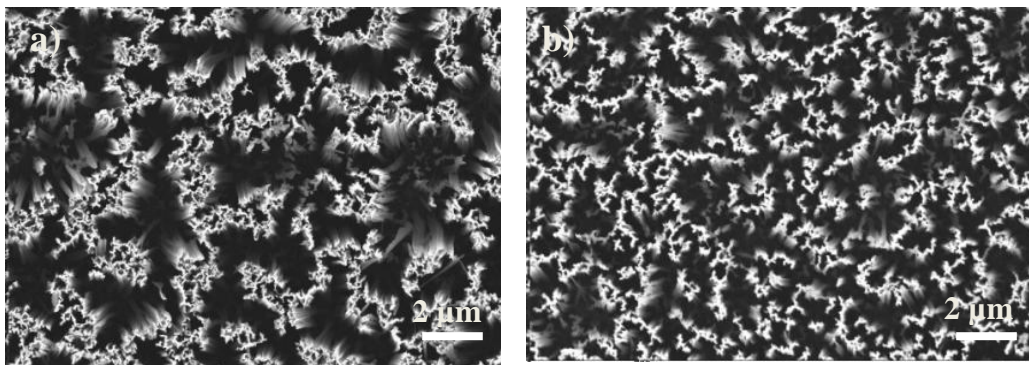


Figure 4-12: SEM pictures of SiNWs arrays (a) before and (b) after RIE post-treatment.

4.2.5 Supercritical drying process

Some special drying techniques can be applied to solve the agglomeration problem of SiNWs as discussed in section 4.2.1.3. We have investigated the potential of the supercritical drying process. After fabrication of the SiNWs, a series of dehydration were performed to replace any water in the specimen by acetone. Indeed carbon dioxide is not miscible with water. Therefore we have to use a third medium, which is termed the intermediate fluid. The replacement of water by acetone was achieved by immersing the samples in several baths of acetone with different concentration for at least 15 min each:

- Immersion of the samples in 30% acetone solution for 15 minutes
- Immersion of the samples in 70% acetone solution for 15 minutes
- Immersion of the samples in 85% acetone solution for 15 minutes
- Immersion of the samples in 100% acetone solution for 15 minutes

- Immersion of the samples in 100% acetone solution again for another 15 minutes

Samples were directly transferred to a CO₂ pressure chamber. We use a Critical Point Drier (EMS 850). This system allows a precise temperature control by a built-in thermo-electric heating and adiabatic cooling. The chamber was first cooled down, to allow the samples to be filled by liquid CO₂. We applied a temperature of 34°C and a pressure of 1200 psi, just above the critical drying point in order to bring CO₂ to its supercritical state. A needle valve was used to vent the CO₂ to prevent samples distortion. Good results were obtained as illustrated in **Figure 4-13** although SiNWs bundles are still observed. However, the process is expensive and very sensitive. The transfer to the CO₂ pressure chamber has to be fast in order to not allow the sample to dry. Indeed, once the sample is out of a solution, it starts to dry: the capillary forces appear and bend the nanowires which start to form large bundles.

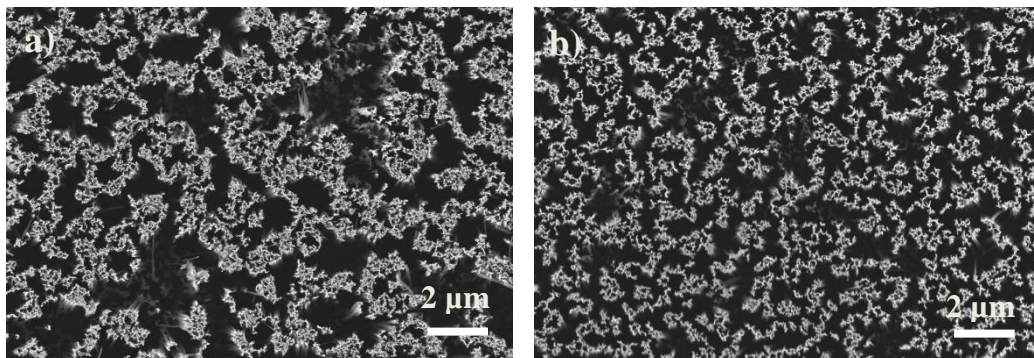


Figure 4-13: SiNWs array (a) before and (b) after CO₂ supercritical drying process.

4.3 Effect of the wettability on the agglomeration of SiNWs

In the following section, we propose a simple way to reduce significantly the size of the bundling of SiNWs. Indeed, we demonstrate that controlling the wettability properties of both the wafer and the nanowires surfaces has a drastic effect on the agglomeration of SiNWs [194].

4.3.1 Experiments

Single-crystal n-type wafers ([100]; resistivity 0.7-0.9 Ω-cm) were successively cleaned in acetone, IPA and deionized (DI) water for 10 min each

by an ultrasonic bath at room temperature. The samples were then divided into two sets A and B. Samples from set A were dipped into a piranha solution, consisting of a mixture of sulfuric acid (H_2SO_4) and hydrogen peroxide (H_2O_2) with the proportion 3:1, while samples from set B were dipped into a solution of 5% HF for 1 minute. Therefore, the surface state of samples from set A was hydrophilic while the one from set B was hydrophobic prior to the etching procedure of SiNWs. Following that, the samples from set A and B underwent the same etching conditions described in the section 3.1.1 of this thesis. After having rinsed thoroughly the samples in DI water, each set (A and B) of the fabricated samples was then divided again into 2 sub-sets: set A1/A2 and set B1/B2 respectively. For set A1 and B1, the as-fabricated nanowires were dried under nitrogen gas environment as the final step. For set A2 and B2, the samples were dipped into a 5% HF solution for 1 min before being dried under nitrogen gas environment.

4.3.2 Results and Discussion

4.3.2.1 HF as a pre-treatment

As a pre-treatment, we mean a treatment of the initial wafer substrate prior the etching process to form the SiNWs. **Figure 4-14** shows that the initial surface state of the wafer has a drastic effect on the morphology of the SiNW arrays. When the surface of the initial wafer is hydrophobic, large bundles are observed as illustrated in **Figure 4-14 (a)** (top-view) and **Figure 4-14 (c)** (cross-section) while for hydrophilic surfaces (treated by piranha) the bundling, although still present, is much reduced (**Figure 4-14 (b)** and **Figure 4-14 (d)**). We suggest that the wettability of the wafer has an impact on the distribution of the silver particles on the top surface of the wafer during the etching procedure. The initial contact of the substrate with the solution is critical since the first deposited silver particles will impact the overall etching process. Indeed the initial reduction of Ag^+ results in the formation of Ag nanoclusters on the substrate surface which restrains further oxidation of silicon surface below the cluster, hence the etching process takes place locally, below the Ag nanoclusters themselves, as the latter are relatively more electronegative than silicon and thus constitutes an easy injection path for holes. *Shu-Chia Shiu et al.*

have observed SiNWs with a reduced density and uniformity for initial H-terminated substrate [218]. They suggested that the H-terminated bonds could form a protection layer which prevented the oxidation of silicon, and contributed to the results observed. They showed the effect of the surface state on the morphology of the silver nanoclusters. For hydrophilic surfaces, silver ions were reduced in particles while for hydrophobic surface silver flakes were formed. A hydrophilic surface tended to form dense and uniform arrays of SiNWs while for hydrophobic surface the SiNW array was less dense and uniform.

For a hydrophilic substrate, the high density of silver nanoclusters results in a more regular array (separated nanoparticles), so that the nanowires undergo capillary forces of about equal magnitude in all directions, resulting in reduced bundling. On the contrary, for hydrophobic surface, silver flakes result in non-uniform SiNW arrays, so that the irregularity of the arrays becomes much more important. The capillary forces are less counterbalanced and large bundles are formed, as suggested by our calculations in section 4.1.4. Moreover there is a clear color difference between samples with initial hydrophilic and hydrophobic surface state. Samples which underwent $\text{H}_2\text{O}_2\text{:H}_2\text{SO}_4$ pre-treatment were dark black while the samples with HF pre-treatment were dark brown. This difference might be explained by the reduced reflectivity for initial hydrophilic substrate which comes from the higher density of the arrays. This hypothesis is confirmed by the reflectivity measurements of the samples with initial hydrophilic and hydrophobic substrates as depicted in **Figure 4-15**. These measurements show that the pre-treatment has a significant impact on the optical properties of the SiNW arrays: for SiNWs of the same length, the average reflectance (in the range 250-1100 nm) decreases down to 3.8% for samples with a piranha pre-treatment, hence a reduction of 28% of the reflectance compared to samples with a HF pre-treatment (average of 5.3% in the range 250-1100 nm). Therefore the use of a substrate with hydrophilic properties is essential to get more regular and dense SiNW arrays with excellent optical properties.

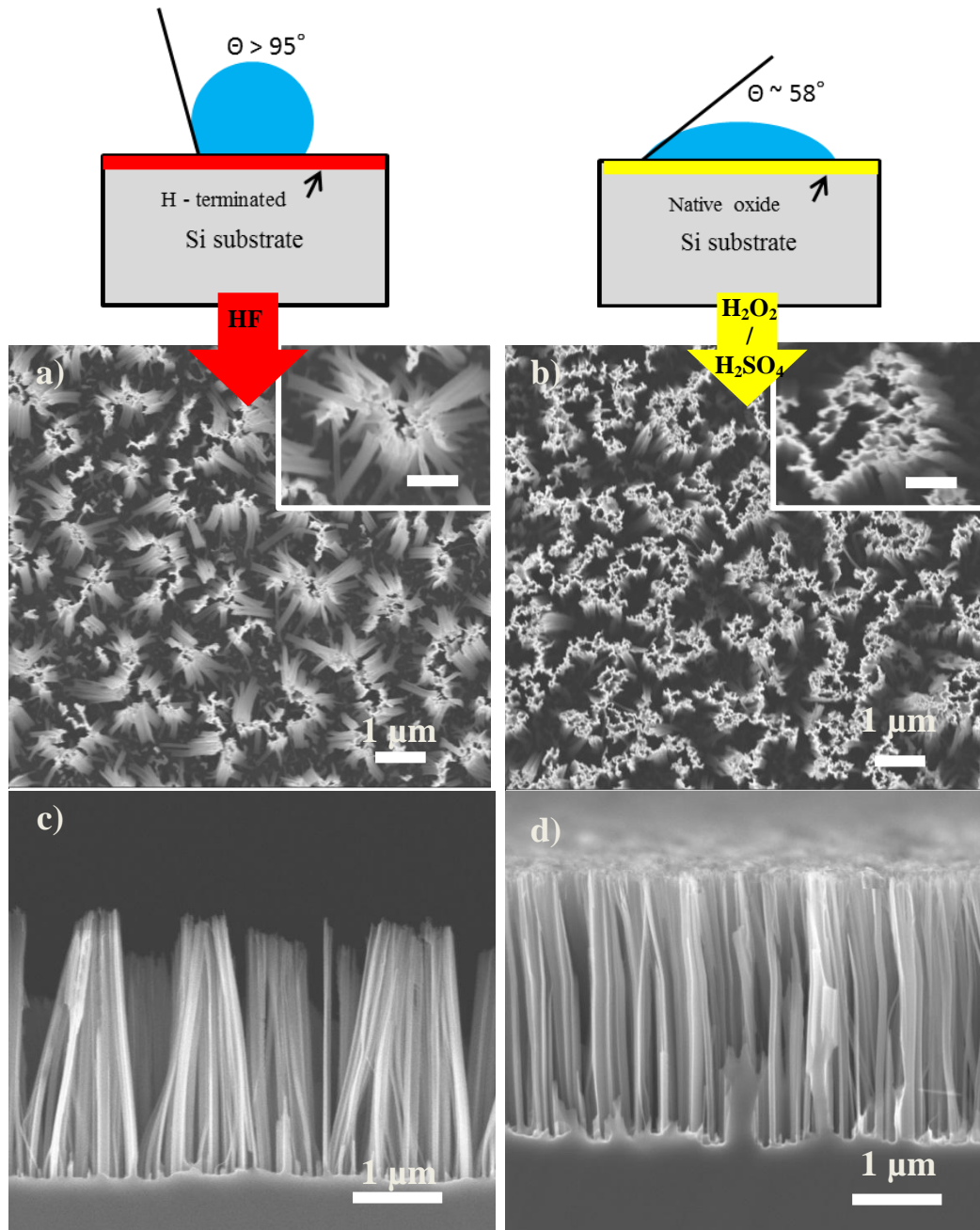


Figure 4-14: Top view (a), (b) and cross-section (c), (d) SEM pictures: Effect on the morphology of the SiNWs fabricated by MACE with a HF pre-treatment (a), (c) and with a $H_2O_2:H_2SO_4$ pre-treatment (b), (d). The insets show high magnification SEM images of the top-view. The scale bar is 500 nm.

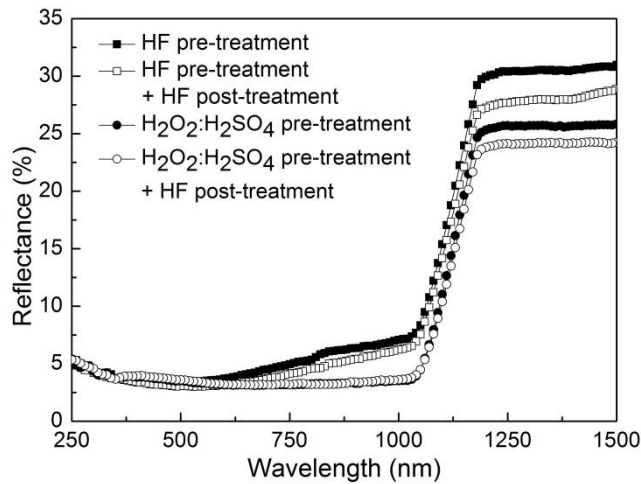


Figure 4-15: Reflectance of the SiNW arrays fabricated by MACE with a HF pre-treatment (solid black squares), a $\text{H}_2\text{O}_2:\text{H}_2\text{SO}_4$ pre-treatment (black solid circles) a HF pre-treatment and a HF post-treatment (open squares), and after a $\text{H}_2\text{O}_2:\text{H}_2\text{SO}_4$ pre-treatment and HF post treatment (open circles).

4.3.2.2 HF as a post-treatment

A HF as a post-treatment, i.e. a treatment after the etching procedure, has a drastic effect on the agglomeration of SiNWs: SiNWs treated by HF after the etching procedure are well separated and the bundling is significantly minimized (**Figure 4-16 (b)**, **Figure 4-16 (d)** and **Figure 4-16 (e)**) whereas for as-fabricated samples large bundles are observed (**Figure 4-16 (a)**, **Figure 4-16 (c)** and **Figure 4-16 (e)**).

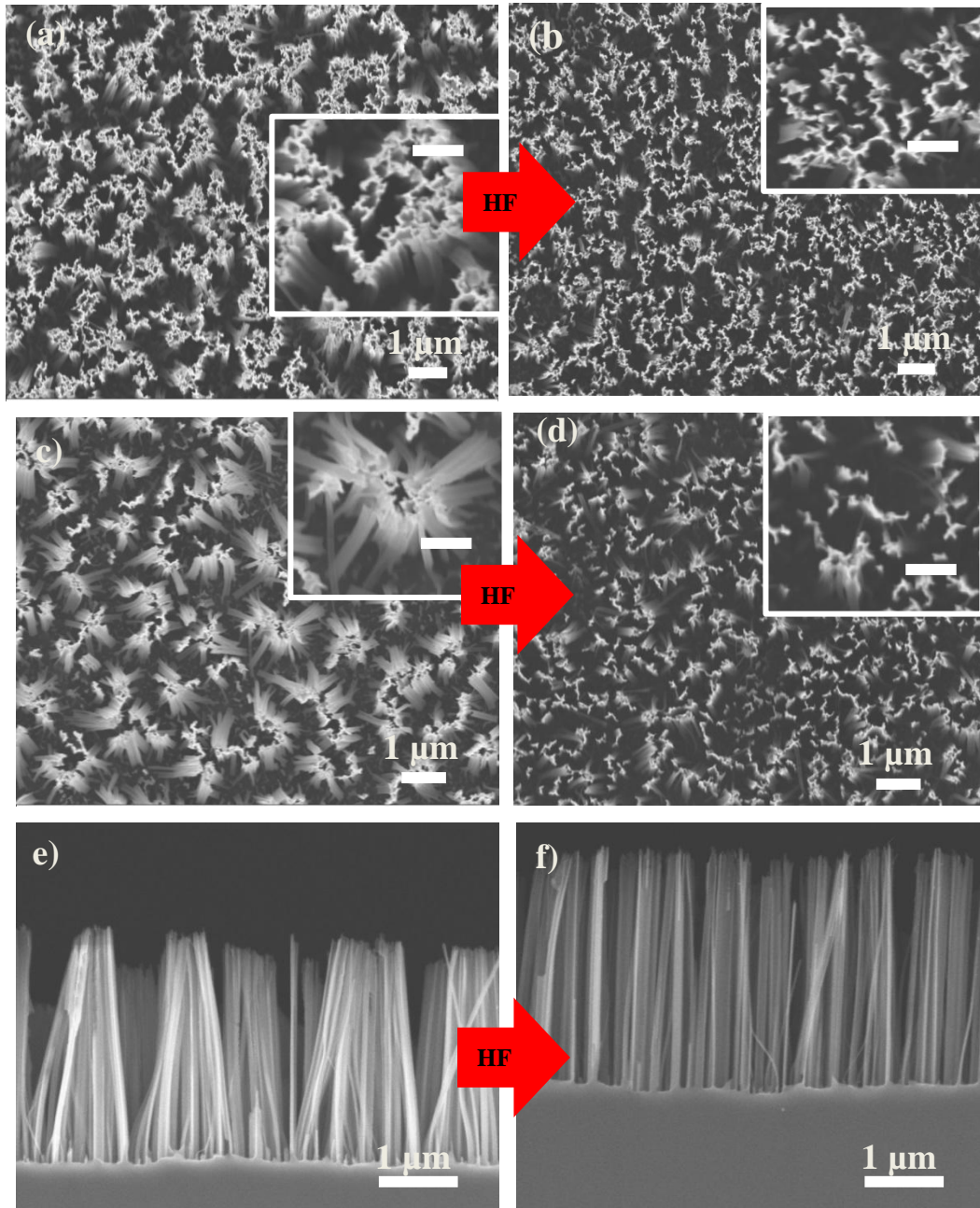
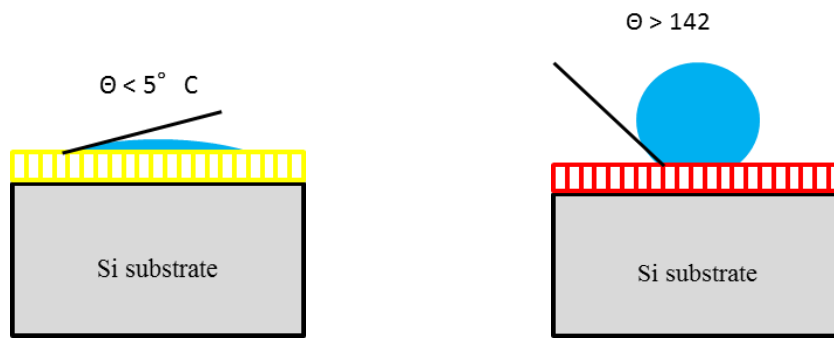


Figure 4-16: SEM pictures - Effect on the morphology of the SiNWs fabricated by MACE after a $\text{H}_2\text{O}_2:\text{H}_2\text{SO}_4$ pre-treatment (a), after a $\text{H}_2\text{O}_2:\text{H}_2\text{SO}_4$ pre-treatment and a HF post-treatment (b), after a HF pre-treatment (c), (e), and after a HF pre-treatment and a HF post-treatment (d), (f). The insets show high magnification SEM images of the top-view. The scale bar is 500 nm.

According to our experiments, the bundling of nanowires strongly depends on the surface-state of the nanowires. The objective of a HF post-treatment is to change the wettability of the nanowires. Indeed as fabricated SiNWs by the standard MACE method are hydrophilic. After a bath in nitric acid (HNO_3) and a water rinse, SiNWs are functionalized by hydrophilic groups. The surface of SiNWs can be partially oxidized by a concentrated HNO_3 solution according to the following reaction: $2x\text{HNO}_3 + \text{Si} \rightarrow \text{SiO}_x + 2x\text{NO}_2 + x\text{H}_2\text{O}$. The surface is therefore functionalized by the following groups: Si-O-Si , Si=O , Si-OH . When the samples are dipped in a 5% HF bath, we expect the surface state of the nanowires to become hydrophobic. When dipping in HF solutions, H-terminated bonds form on the silicon surface. The surface is therefore functionalized by Si-H. To confirm this change in the wettability, measurements of the contact angle of the SiNWs samples after a 15 min HNO_3 bath and after a 1 min HF bath were carried out using a contact angle analyzer. As illustrated in **Figure 4-17**, the wettability of the samples can be changed from superhydrophilic with a contact angle less than 5° to highly hydrophobic with a contact angle exceeding 142° .

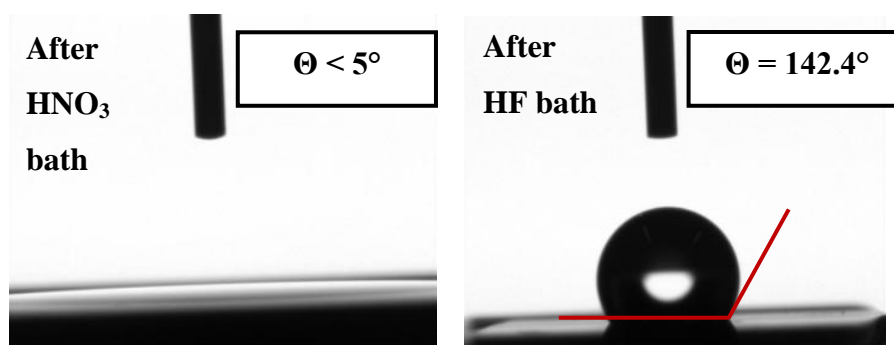


Figure 4-17: Measurement of contact angle on SiNWs after the standard MACE process (after HNO_3 bath) (left) and after HF post-treatment (right).

The Liquid (solvent)-Vapor (air) interface is characterized by an interfacial tension γ which tends to reduce the active surface area by inducing a small curvature of the liquid. This meniscus can either curve upwards or downwards according to the liquid's wettabilities on the solid surface. The H-terminated bonds on the silicon may lead to a convex form (the meniscus curve up) since the water is non-wetting on hydrophobic surfaces. On the other hand,

the hydrophilic NWs may lead to a concave form (the meniscus curves down) as the water is wetting on the surface as illustrated in **Figure 4-18**. When the main mechanism of adhesion is due to capillary forces, as it is the case here, the surface state of the NWs can have a dominant effect on the stiction of the nanostructure. By using a hydrophobic surface, the free energy of their surface is reduced, which can decrease significantly the adhesion forces as the number of water molecules adsorbed on the SiNWs' surface and responsible for the formation of the water meniscus is minimized. We propose that the H-terminated bonds on the silicon surface can reduce significantly the size of the bundles of nanowires and enables a very good lateral separation as shown in **Figure 4-16**. The water is responsible for the stress exerting on the NWs and with the very narrow gaps between SiNWs, it is very difficult to remove the trapped liquid entirely during drying. Similar results are obtained with the special freeze or supercritical drying process but in comparison our technique is very fast, easy and cheap. The effect of the HF post-treatment on the reflectivity of the arrays is quite small, which shows that the density of the arrays is not affected by the HF bath. We observe a reduction of 11.4 % (**Figure 4-15**) of the reflectivity for well separated SiNWs (**Figure 4-16 (d)**) compared to the SiNWs sample with large bundles (**Figure 4-16 (c)**) for the case of initial substrate with hydrophobic surface-state, which may be explained by the better light trapping capabilities of the well separated SiNWs. As a summary, we can conclude that the agglomeration of SiNWs has surprisingly a small impact on the measured reflectivity. Instead, the density of the wires which is modified by the pre-treatment (HF or H₂SO₄) is impacting significantly the reflectivity of the samples. We also tested our method for longer SiNWs. The etching time was set to 3 hours and SiNWs with a length of 30 μm were fabricated. As illustrated in **Figure 4-19**, excellent lateral separation was obtained for 30 μm SiNWs post-treated by HF after the etching procedure while strong bundling is observed on non-treated samples.

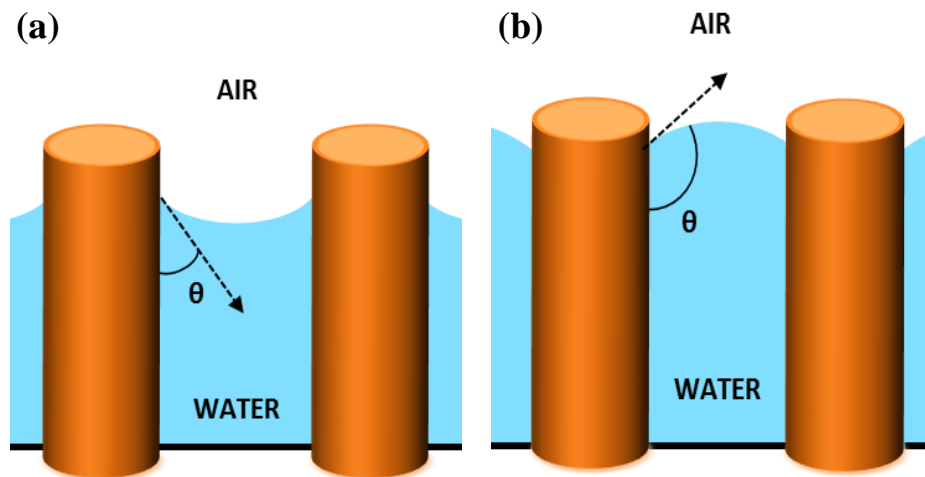


Figure 4-18: Schematic illustration of the water meniscus shape according to the wettability of SiNWs. For hydrophilic SiNWs, the water is wetting on the surface and the meniscus is concave (a) while for hydrophobic SiNWs, the water is non-wetting and the meniscus is convex (b).

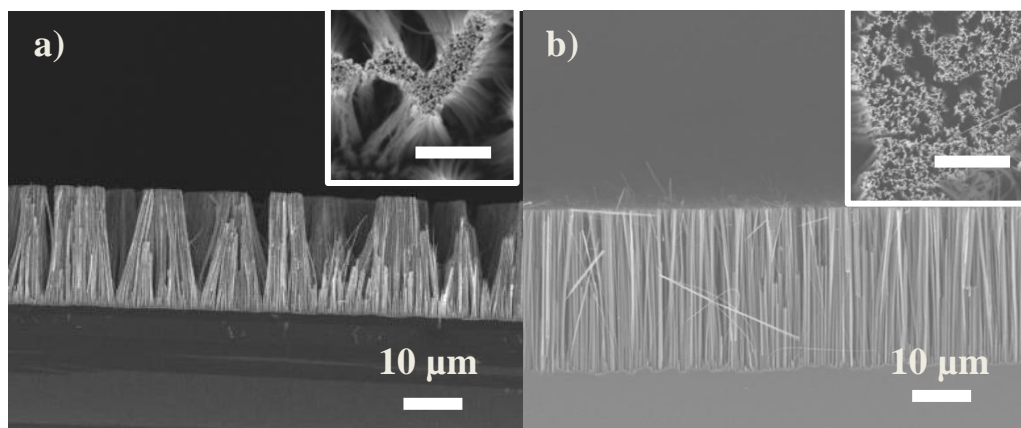


Figure 4-19: Cross-section SEM pictures of 30 μm long nanowires: Effect on the morphology of the SiNWs fabricated by MACE with no post-treatment (a) and after a HF post-treatment (b). The insets show SEM images of the top-view. The scale bar is 5 μm .

Table 4-1 summarizes the advantages and drawbacks of the different methods to achieve lateral separation of SiNWs.

Table 4-1: Main advantages and drawbacks of the different methods used to separate agglomerated SiNWs.

Technology	Advantages	Disadvantages
Wet Etching	Simple and Low-cost.	SiNWs are still stuck to each other's. Good lateral separation is not achieved.
Dry Etching	Good separation of SiNWs is achieved.	Additional process adding some damages.
Supercritical Drying process	Good lateral separation.	Additional expensive process.
Our solution (Control of the wettability)	Simple, fast and low-cost process. Easy to implement. Significant reduction of the agglomeration of SiNWs is achieved.	Although HF is widely used in the MEMS industry, this chemical is still very hazardous.

Conclusion

In this section we have shown that the surface state (hydrophilic vs hydrophobic) of the c-Si substrate undergoing the MACE procedure has a big impact on the morphology of the SiNWs arrays fabricated. A hydrophilic wafer surface is essential to achieve a dense and uniform array of SiNWs with reduced agglomeration. The bundling is further reduced by functionalizing the surface of the fabricated SiNWs by hydrophobic groups in order to reduce the stress exerted by water in the form of capillary forces. The pre-surface treatment enables a reduction of the reflectance down to 3.8% in the spectral range 250 nm-1100 nm for SiNWs of the same length. The good lateral separation of the SiNWs by the post-treatment has a little impact on the optical properties of the arrays. However, the good lateral separation might be crucial for the conformal coating of the active material to form the junction in solar cells.

Chapter 5 : Optical Properties of SiNW arrays

This chapter is devoted to the investigation of the optical properties of both random and ordered SiNW arrays. We have fabricated and studied the optical properties of a large set of SiNW arrays and compared them with the performance of Si with the standard pyramid texturization. SiNWs are characterized via various techniques such as a spectrophotometer system (PerkinElmer, Lambda 950/UV/Vis/NIR), an angle-resolved Mueller matrix polarimeter (ARMMP) and a Mueller matrix ellipsometer. This experimental work is supported by modeling of the optical properties of the arrays using the rigorous coupled-wave analysis method (RCWA) [219], [220] which provides guidelines to analyze and optimize the geometry to minimize the total reflectance.

5.1 Comparison between SiNWs and commercial pyramids

Random and ordered SiNWs were fabricated using the standard and NSL assisted MACE process, respectively, as described in section 3.1 of this thesis. The optimization of the recipe, presented in Chapter 4, was implemented to achieve well separated SiNWs. Random SiNWs are mainly characterized by their length, which can be controlled by the etching time, while the diameters and pitches are not directly controllable. In contrast, the ordered SiNW arrays are defined by their pitch (center to center distance), diameter and length, which can all be controlled in the fabrication process. We have prepared a large set of ordered samples with nanowire diameters varying from 190 to 650 nm and pitches from 250 to 800 nm. The samples were characterized by UV/Vis/NIR spectrophotometer using an integrating sphere at the angle of incidence (AOI) of 8°. The spot size was a few square millimeters large.

To confirm the reproducibility of our measurements, as well as the uniformity of the SiNW arrays, the total reflectance of the samples was measured on different days and at different positions on the samples. As shown in **Figure 5-1**, the total reflectance data are highly reproducible and the uniformity of the samples is well assessed.

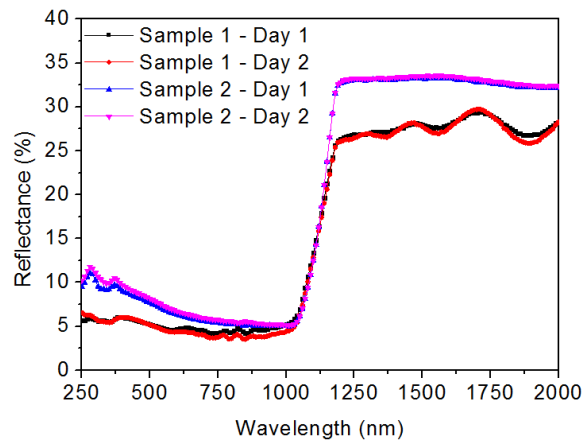


Figure 5-1: Reproducibility of the measured total reflectance data for 2 different samples. Measurements were performed at different locations of the sample on different days, showing good sample uniformity and measurement reproducibility.

As illustrated in **Figure 5-2**, SiNWs show better optical performance as compared to commercial random pyramids. For example, carefully designed short ordered SiNWs arrays, with a length of only 165 nm and a pitch of 330 nm, show reduced reflectance over the whole spectral range, with an average total reflectance of 7.6% in the range between 400 and 1100 nm, compared to the average 13.1% reflectance of the commercial pyramids. Likewise, short random SiNWs with a length of 500 nm have an average reflectance of 7.5% over the spectral range of 400-1100 nm. This demonstrates that the efficient light trapping offered by the SiNWs that is suitable for photovoltaic applications. Indeed the challenge is to improve light trapping in thin crystalline silicon solar cells using a low-cost approach, while avoiding the typical removal of about 10 μm of c-Si material induced by the standard random pyramid texturization. Moreover, the proposed light trapping scheme is efficient even when reducing the thickness of the absorber layer down to a few micrometers.

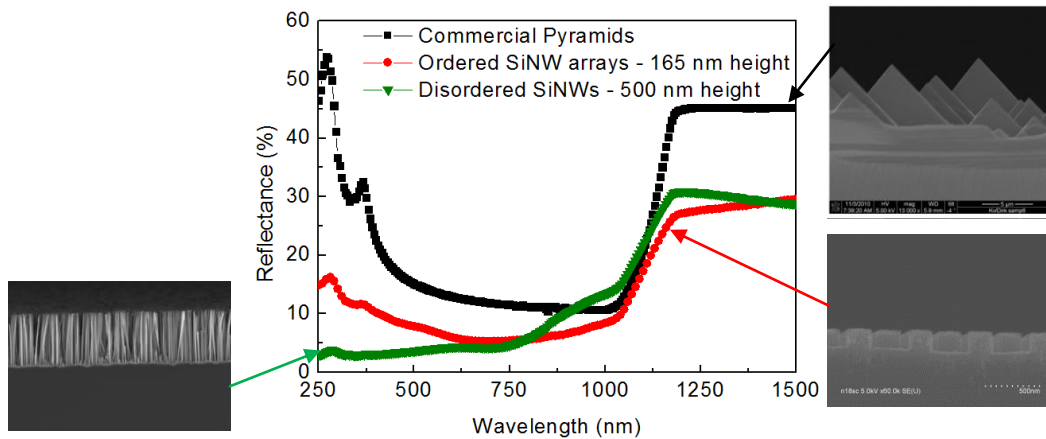


Figure 5-2: Comparison of the total reflectance between commercial pyramids (black curve) and ordered SiNWs arrays of ~165 nm height and pitch of 330 nm (red curve) and disordered SiNWs with a length of 500 nm (green curve) with the corresponding SEM pictures

5.2 Ordered vs Disordered SiNWs: effect of the geometry

Figure 5-3 shows the wavelength dependence of the reflectance of random SiNWs with increasing length. We observe a clear trend: the longer the SiNWs, the lower the reflectance, which is explained by better light trapping capabilities of very long SiNWs. At the same time, we can observe the saturation (for heights from 1.5 μm and higher) where further increase of SiNW length does not significantly improve the reflectance anymore. **Table 5-1** summarizes the average reflectance over the spectral range 400-1100 nm acquired from measured total reflectance of the corresponding arrays. To conclude, the optical properties of shorter random SiNWs are strongly depends on the SiNW length, while the decrease of the reflectance for very long nanowires does not pay off the increased fabrication time.

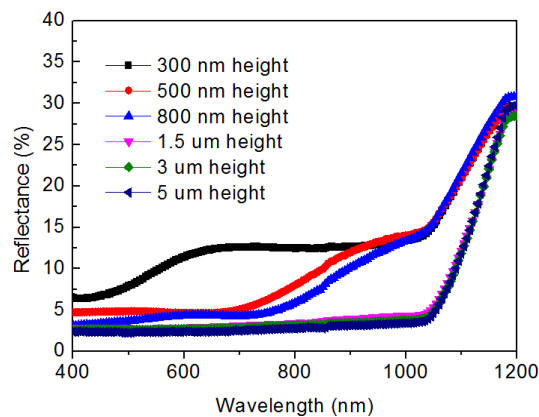


Figure 5-3: Effect of disordered SiNW length on the measured total reflectance plotted as a function of the wavelength.

Table 5-1: Average reflectance over the spectral range 400-1100 nm for disordered SiNWs with different lengths

Random SiNWs	300 nm	500 nm	800 nm	1.5 μm	3 μm	5 μm
Average Reflectance (%) (400-1100 nm)	11.92	8.62	7.54	3.73	3.41	3.11

In contrasts, for ordered SiNWs, there are other critical parameters which can be considered and have impact on the performance. **Figure 5-4** shows the measured reflectance of ordered SiNW arrays with the same pitch (330 nm) and with similar diameters (within tens of nanometers), but with different lengths. Details of the geometrical parameters and average reflectance are displayed in **Table 5-2** with corresponding SEM images in **Figure 5-5**. The average diameter was determined by analyzing the SEM image using the software ImageJ. This is a powerful tool which allowed us to acquire the average diameter and the distribution. **Figure 5-6** shows the image treatment applied to SEM images to extract the average diameter of the arrays. As illustrated on **Figure 5-4**, the sample with 2 μm SiNW lengths shows lower reflectance than samples with 2 or 4 times longer SiNWs, which may come as a surprise. This is caused by the 10 nm difference in average diameter, which significantly changes the optical properties and highlights the critical effect of ordered SiNW geometry. Moreover, we observe agglomeration in the case of 8.2 μm length (see inset of **Figure 5-5 (d)**), similar to that reported for MACE SiNWs in Chapter 4, which may impact the optical performance of the array.

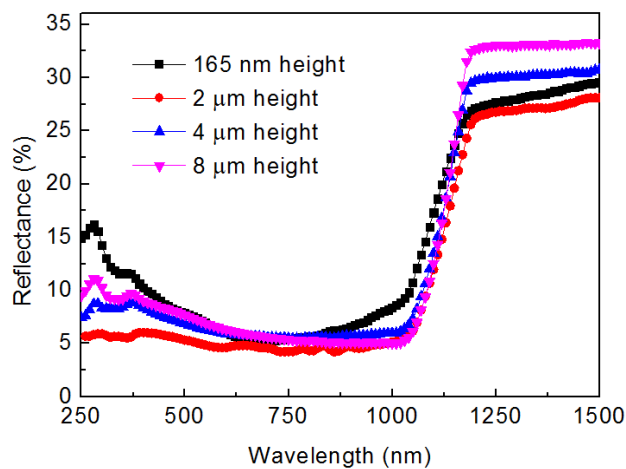


Figure 5-4: Spectral dependence of the total reflectance measured on ordered SiNWs with pitch of 330 nm, diameter of 250 nm (+/- 10 nm) and lengths of 165 nm, 2 μm , 4 μm and 8 μm .

Table 5-2: Geometrical parameters of 4 different ordered SiNW arrays with the corresponding average total reflectance calculated in the range of 400-1100 nm.

Sample	Ordered A	Ordered B	Ordered C	Ordered D
Pitch (nm)	330	330	330	330
Diameter(nm)	239.1	254.2	259	250.7
Length (nm)	165 nm	2.1 μm	4.2 μm	8.2 μm
Average Reflectance (%) (400-1100 nm)	7.66	5.33	6.47	6.34

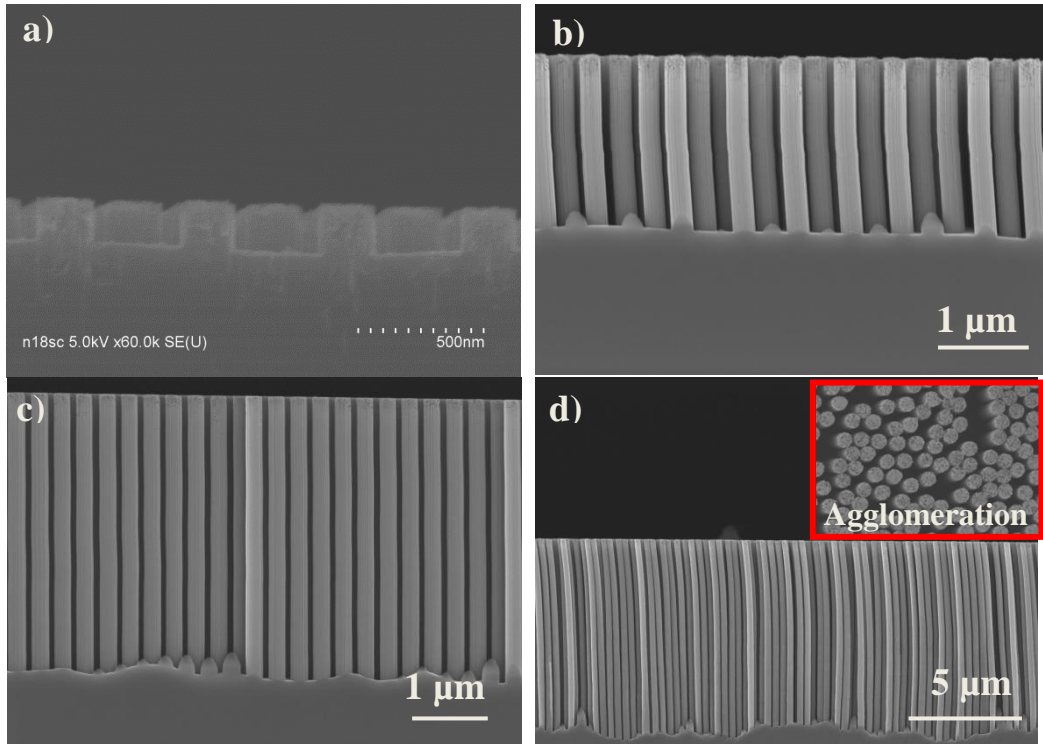


Figure 5-5: Cross-section SEM images of ordered SiNW arrays with a pitch of 330 nm, an average diameters between 239-259 nm and lengths of (a) 163 nm, (b) 2.1 μm , (c) 4.2 μm and (d) 8.2 μm , respectively. The inset in (d) shows the corresponding top-view SEM image.

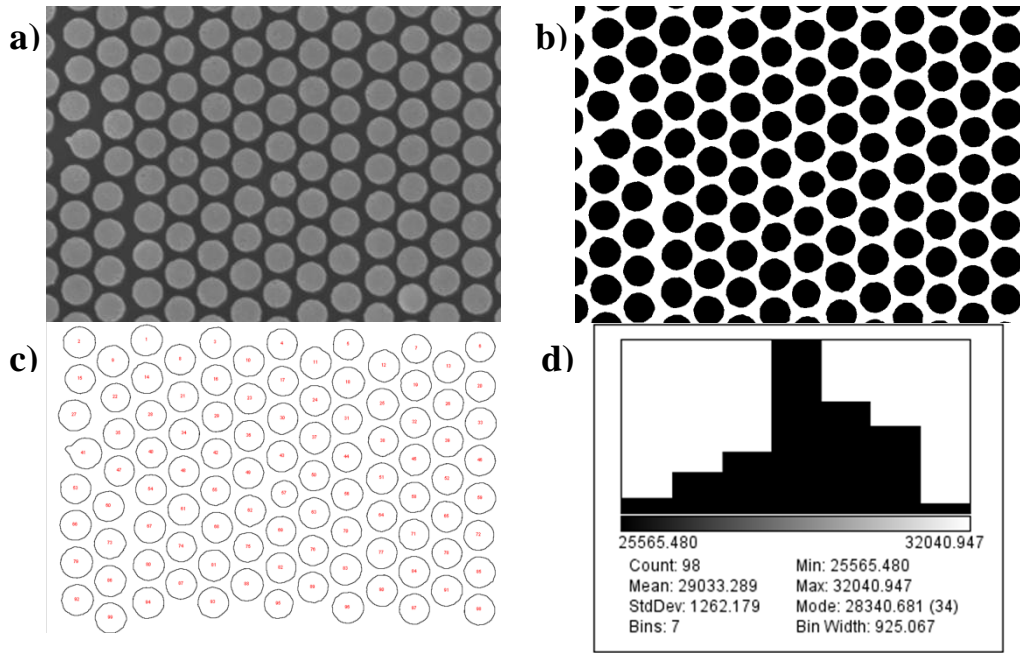


Figure 5-6: Figure 5-7: Illustration of SEM image analysis by imageJ: (a) original image, (b) threshold image, (c) image contour analysis and (d) area distribution.

To highlight the effect of the density and diameter, we also compare the reflectance of three ordered SiNW arrays that have the same length of 2 μm and pitch of 600 nm, but different diameters and therefore different material density. The three arrays have an average diameter of 550, 424 and 306 nm, respectively. We have calculated the filling fraction (%) of ordered SiNWs organized in an hexagonal arrangement using Eq. (5.1):

$$D_h = \frac{2\pi r^2}{\sqrt{3}p_h^2} \quad 5.1$$

with p_h being the pitch of the hexagonal arrays (center to center distance).

The corresponding filling fraction has been calculated and we found a filling fraction of 0.51, 0.45 and 0.24 for an average diameter of 550, 424 and 306 nm, respectively. We have obtained an average total reflectance of 6.5%, 5.1% and 9.9% in the spectral range of 400 nm to 1100 nm for the high, medium and low density arrays, respectively. The measured total reflectances are plotted in **Figure 5-8** as functions of the wavelength.

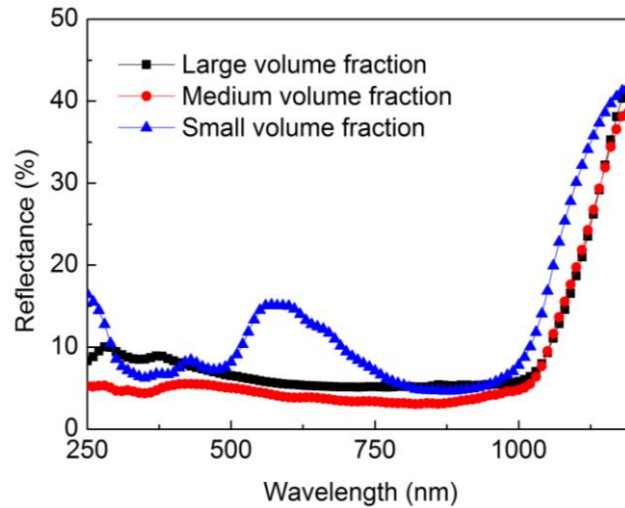


Figure 5-8: Effect of the volume fraction on the reflectance of three ordered arrays of SiNWs with a pitch of 600 nm and a length of 2 μm . The diameters for the high, medium and low density SiNW arrays are 503 nm, 436 nm and 158 nm.

The SiNW diameter and the material density are critical parameters that determine the optical properties of the ordered arrays, thus confirming the theoretical predictions of *Foldyna et al.* [37] from the optical model of the optimized nanostructures. As the geometry of the ordered SiNW arrays has a drastic effect on the optical properties, with the average total reflectance in the 400-1100 nm range varying from more than 20 % to less than 3.8 % for the different fabricated geometries, a careful optimization is needed to maximize the performance of fabricated SiNW arrays.

5.3 Effect of ITO coating

We have also investigated the effect of ITO coating on the reflectance of the SiNW arrays as ITO also plays the role of an anti-reflective coating. The objective of an antireflective coating is to create a double interface leading to the formation of two reflected waves, by depositing a thin layer of material on the top of a substrate. If these two reflected waves are out of phase, they will interfere destructively and will eventually cancel each other out, thus less light is being reflected as illustrated in **Figure 5-9** ([221]).

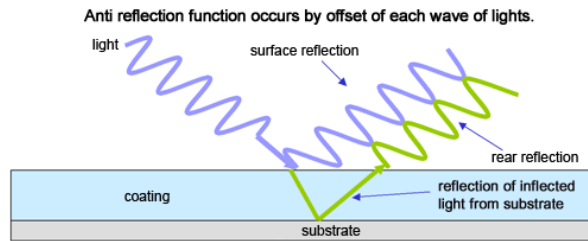


Figure 5-9: Schematic of the working principle of an anti-reflective coating [221].

An effect of ITO thickness on the total reflectance was investigated for two ordered SiNW arrays characterized respectively by a pitch of 250 nm and 500 nm, a diameter of 219 nm and 314 nm and a height of 242 nm and 2 μm . Results are displayed in **Figure 5-10 (a)** and **Figure 5-10 (b)**.

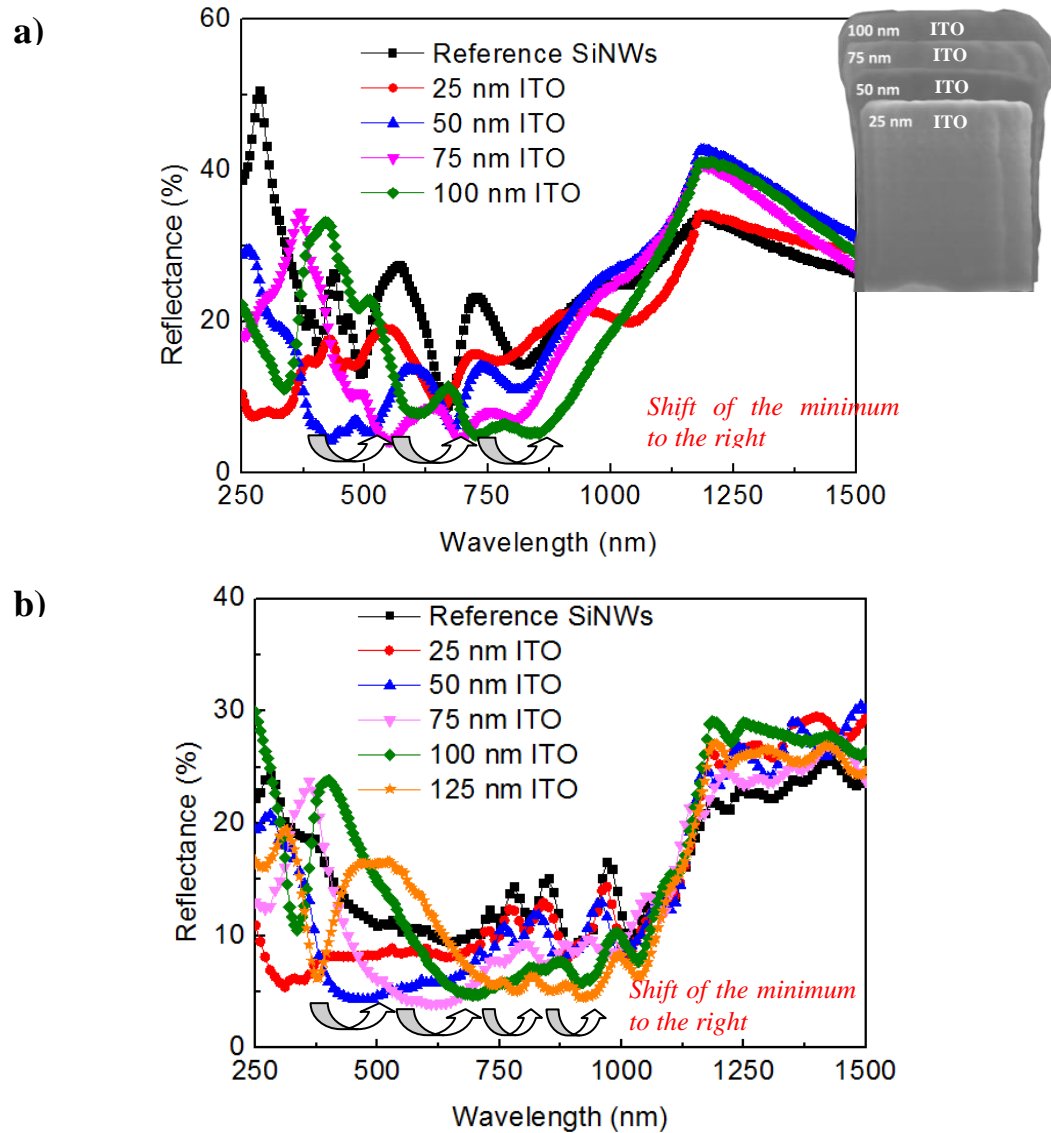


Figure 5-10: Effect of increasing the thickness of ITO on the reflectance of ordered SiNW arrays with a pitch of (a) 250 nm and (b) 500 nm.

When comparing the reflectance spectra, we can see a combination of two effects. First, we observe that the spectra minima are shifting to the right with increasing thickness of ITO for the two arrays with a pitch of 250 and 500 nm as shown by the arrows in **Figure 5-10**. This is a common effect observed for planar structures with increasing thickness of the antireflective coating. The standard flat antireflective (AR) coating theory is relevant in our case since we can consider that the main effect of ITO during the first penetration into the SiNW is coming from the ITO on the top of the SiNWs. The cross-section SEM image in the inset of **Figure 5-10 (a)** shows the superimposing of a single SiNW covered with increasing thickness of ITO. We observe that the coverage by ITO is not uniform: large bumps are observed at the top of the SiNWs while the thickness of ITO decreases from the top to the bottom of the wire. Thus the thickness of ITO on the sidewall is very small. Therefore we can use flat AR theory as a first approximation. Naturally, for more accurate modeling, RCWA should be used. This right shift of the minimum is therefore not related to the nanostructuration. In the case of planar AR theory, the two reflected waves should be in opposite phase to achieve minima. For normal incidence, the phase shift between the two reflected waves induced by an optical path difference δ is given by:

$$\Delta\varphi = \frac{2\pi\delta}{\lambda} = \frac{4\pi t}{\lambda} \quad 5.2$$

where t is the thickness of the film and λ the wavelength inside the antireflective coating.

To be out of phase, $\Delta\varphi$ should be equal to π , therefore we achieve the following condition for the destructive interference:

$$t = \frac{\lambda}{4} \quad 5.3$$

When the thickness of the film increases slightly, the corresponding wavelength which gives the minima is shifted towards longer wavelength, hence the observed shift to the right of the minima with increasing thickness of ITO in **Figure 5-10**.

The second effect is a decrease of the reflectance curve peaks. The reference cell with no ITO shows a reflectance spectrum with several peaks due

to the nanostructuration. No drastic changes in the reflectance curve shape is observed with increasing thickness of ITO, but peaks get smaller and slightly shifted.

We also observe a decrease in the average reflectance in the range between 400 and 1100 nm with increasing thickness of ITO, until it reaches a minimum at 75 nm and starts to slightly increase again. This can be related to the morphology of the ITO film coating. Indeed, from 100 nm, the large ITO bumps on the top of the wires are touching each other as shown in **Figure 5-11**. Therefore, we achieve a kind of planar structure that is less efficient at trapping the light. However, these data are not calibrated by the solar 1.5 AM spectrum and did not take into account the number of photons. Therefore we also compare the theoretical upper limit of the J_{sc} estimated from the absorption spectra $A(E)$ by assuming $A(E) = 1 - R(E)$ (for $\lambda < 1100$ nm) since very thick wafers of 550 μm were used. From $A(E)$, we have obtained values of ultimate J_{sc} by using the following formula:

$$J_{sc} = e \int_{E>E_g}^{\infty} A(E)N(E)dE \quad 5.4$$

where $A(E)$ is the spectral absorptance, $N(E)$ is the number of photons per unit area per second, E is the photon energy, E_g is the band gap energy and e is the electron charge. We assumed an ideal internal quantum efficiency of 100%. Therefore this equation gives a numerical estimation of the theoretical solar cell performance (upper limit) which allows us to evaluate the potential of a specific geometry.

Results are summarized in **Table 5-3**. We have also included results for J_{loss} , which is the integrated current from the reflected photons. We obtained consistent results with the average reflectance. Indeed, the lower the reflectance, the smallest is the J_{loss} (or higher is the estimated J_{sc}).

$$J_{loss} = e \int_{E>E_g}^{\infty} R(E) \frac{dN_{AM1.5G}(E)}{dE} dE \quad 5.5$$

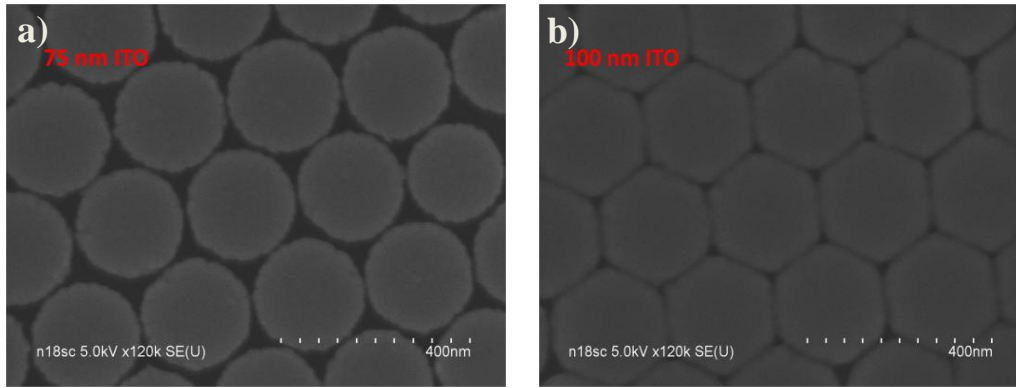


Figure 5-11: Top-view SEM image of ordered arrays of SiNWs with a pitch of 250 nm covered with a thickness of ITO of (a) 75 nm and (b) 100 nm.

Table 5-3: Effect of ITO coating on the average reflectance of ordered arrays of SiNWs. J_{sc} is calculated from the absorbed photons and J_{loss} is calculated from the reflected photons.

Sample		No ITO	25 nm ITO	50 nm ITO	75 nm ITO	100 nm ITO	125 nm ITO
Pitch 250 nm	Average reflectance (%) (400-1100 nm)	20.59	17.09	14.84	13.48	14.47	
	J_{sc} estimated (mA/cm ²)	34.64	36.30	37.32	37.92	37.52	
	J_{loss} (mA/cm ²)	8.84	7.19	6.17	5.57	5.97	
Pitch 500 nm	Average reflectance (%) (400-1100 nm)	11.78	9.84	8.12	8.07	9.72	9.35
	J_{sc} estimated (mA/cm ²)	38.36	39.30	40.0	40.0	39.35	39.40
	J_{loss} (mA/cm ²)	5.13	4.19	3.49	3.49	4.14	4.09

5.4 Angle-resolved MM polarimeter

If ordered SiNWs are well organized into a periodic hexagonal arrangement, we should be able to observe light diffraction for suitable pitch and wavelength of the light. One first and easy to execute experiment is to illuminate the SiNW sample with a laser pen and observe the subsequent diffraction pattern on a white background. For this experiment, we used an array of SiNWs with a pitch of 800 nm, a diameter of ~540 nm and a length of 2.6 μm . The wavelength of the laser pen was 532 nm. This is a case of a reflective diffraction grating, when the incident and diffracted rays are on the same side of the grating as illustrated in **Figure 5-12**.

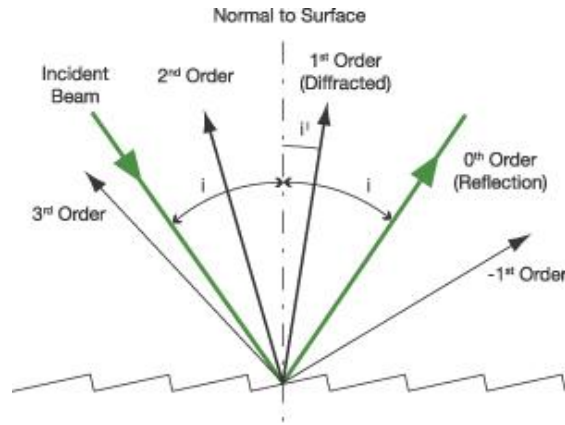


Figure 5-12: Illustration of a diffraction pattern from a periodic diffraction grating [222]

The light diffraction is therefore depending on the pitch of the structure and on the wavelength used. In the case of normal incidence, the diffracted orders appear at angle θ_k given by the following formula [223]:

$$p \sin \theta_k = k\lambda \quad 5.6$$

with p being the pitch (center to center distance), k the diffraction order (an integer) and λ the wavelength of the light. In the case of an arbitrary angle of incidence θ_i , we obtain the so-called grating equation [223]

$$(\sin \theta_i + \sin \theta_k)p = k\lambda \quad 5.7$$

We can only observe a limited number of diffraction orders as the norm of $\sin \theta_k$ must be smaller or equal to one. Assuming $\theta_k = 0$, the following criteria holds true:

$$k = \frac{p}{\lambda} \sin \theta_k < \frac{p}{\lambda} \text{ so } k_{max} = \text{integer part} \left(\frac{p}{\lambda} \right) \quad 5.8$$

Therefore, to observe at least the first order of diffraction ($k = 1$), we need to respect the condition $p > \lambda$, and if we want to observe the second order of diffraction we should have $p > 2\lambda$, etc. Hence we have chosen a pitch p of 800 nm and a light wavelength of 532 nm such that $p > \lambda$. **Figure 5-13** shows the pattern obtained when illuminating the sample by the green laser. We observe the specular reflection, additional diffusion and the first diffraction order. The diffraction pattern is circular instead of the expected well-defined six points in hexagonal pattern.

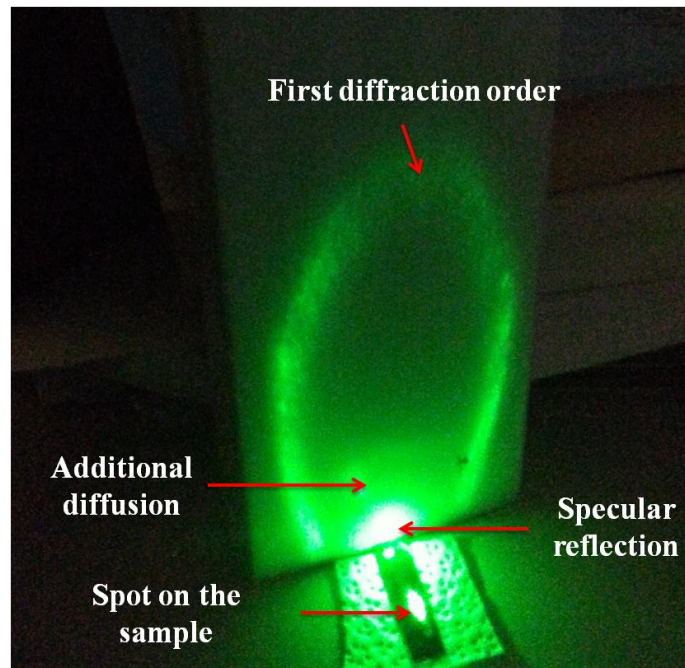


Figure 5-13: Circular diffraction pattern on NWs

In order to understand this diffraction pattern, SiNWs were further characterized by angle-resolved MM polarimeter whose working principle has been detailed in section **Erreur ! Source du renvoi introuvable.**. The key features of this characterization technique include:

- Spot size of a few tens of micrometers,
- Accessibility to the real space (microscopic imaging (**Figure 5-14 (a)**))
- Complete measurements of Mueller matrices (**Figure 5-14 (b)**),
- All incidence and azimuthal angles are measured at once.

The instrument operating in Fourier space measures Mueller matrices for all combination of angular (ϑ) and polar angles (φ). Every pixel in the image described by polar coordinate (r, θ) corresponds to (ϑ, φ) coordinates in the Fourier space with $r \propto \sin(\vartheta)$ and $\theta = \varphi$. Therefore, each point on **Figure 5-14 (b)** is an element of the Mueller matrix measured at (ϑ, φ) incidence.

The polarization state of completely polarized light can be described by using the Jones calculus. In the Jones calculus, the polarized incident light is defined as a Jones vector \vec{J}_i while the optical system is represented by a 2×2 matrix, named the Jones matrix. The new polarization state of the light, described by the emerging vector \vec{J}_e , is equal to the product of the Jones vector of the incident light with the Jones matrix of the system as follows [224]:

$$\vec{J}_e = \begin{bmatrix} J_{11} & J_{12} \\ J_{21} & J_{22} \end{bmatrix} \vec{J}_i \quad 5.9$$

However, Jones calculus is only useful for fully polarized light. When the light is incoherently or partially polarized, we need to use the Mueller calculus [225]. The Mueller matrix can be also uniquely derived from the Jones matrix elements if the system is non-depolarizing, where the relation between the Jones matrix and the corresponding Mueller matrix MM can be described using the following relationship [226]:

$$MM = \begin{bmatrix} \frac{1}{2}(|J_{11}|^2 + |J_{22}|^2 + |J_{12}|^2 + |J_{21}|^2) & \frac{1}{2}(|J_{11}|^2 - |J_{22}|^2 - |J_{12}|^2 + |J_{21}|^2) & \text{Re}(J_{11}^* J_{12} + J_{21}^* J_{22}) & -\text{Im}(J_{11}^* J_{12} + J_{21}^* J_{22}) \\ \frac{1}{2}(|J_{11}|^2 - |J_{22}|^2 + |J_{12}|^2 - |J_{21}|^2) & \frac{1}{2}(|J_{11}|^2 + |J_{22}|^2 - |J_{12}|^2 - |J_{21}|^2) & \text{Re}(J_{11}^* J_{12} - J_{21}^* J_{22}) & \text{Im}(-J_{11}^* J_{12} + J_{21}^* J_{22}) \\ \text{Re}(J_{11}^* J_{21} + J_{12}^* J_{22}) & \text{Re}(J_{11}^* J_{21} - J_{12}^* J_{22}) & \text{Re}(J_{11}^* J_{22} + J_{12}^* J_{21}) & \text{Im}(-J_{11}^* J_{22} + J_{12}^* J_{21}) \\ \text{Im}(J_{11}^* J_{21} + J_{12}^* J_{22}) & \text{Im}(J_{11}^* J_{21} - J_{12}^* J_{22}) & \text{Im}(J_{11}^* J_{22} + J_{12}^* J_{21}) & \text{Re}(J_{11}^* J_{22} - J_{12}^* J_{21}) \end{bmatrix} \quad 5.10$$

with J_{ij} being the element of the row i and column j of the Jones matrix.

The M_{11} element is the absolute intensity of the total nonpolarized light. For non-depolarizing Mueller matrix, it is defined as the sum of squares of the absolute values of all elements of Jones matrix. In our measurements, all elements of Mueller matrix are normalized by M_{11} . Therefore we have $-1 \leq M_{ij} \leq 1$.

Measured Mueller matrices are shown in **Figure 5-14 (b)** with all elements normalized except M_{11} , which shows raw measured light intensity. Some elements of the Mueller matrices are very close to zero (M_{13} , M_{14} , M_{23} , M_{24} , M_{31} , M_{32} , M_{41} and M_{42}), while others have the shape of a ring (M_{12} , M_{21} , M_{34} and M_{43}). For the diagonal elements of the matrix (M_{11} , M_{22} , M_{33} and M_{44}), this external ring pattern is combined with additional circle in the center.

From zero block off-diagonal elements (M_{13} , M_{14} , M_{23} , M_{24} , M_{31} , M_{32} , M_{41} and M_{42}), we can conclude that $J_{12} = J_{21} = 0$, or at least are negligible with respect to the experimental errors, thus signifying that there is no change of polarization.

As $M_{21} \neq 0$ and $M_{12} \neq 0$, we can deduce that there is a difference between reflectance of TE or TM polarized light with TE and TM standing for Transverse Electric mode and Transverse Magnetic mode, respectively. Indeed as we have $J_{21}=J_{12}=0$, we can rewrite M_{12} and M_{21} as :

$$M_{12} = M_{21} = \frac{1}{2} (|J_{11}|^2 - |J_{22}|^2) \quad 5.11$$

where J_{11} and J_{22} represent reflectances for TE and TM polarized light, respectively. That means, if M_{12} and M_{21} are zero, there will be no difference between reflectance of TE or TM polarized light. In our case, we have $M_{21} \neq 0$ and $M_{12} \neq 0$ for the diffracted light, so we can deduce that $J_{11} \neq J_{22}$.

We have observed some depolarizing properties of MM in the center. It has been demonstrated that a necessary and sufficient condition for a given Mueller matrix to describe a non-depolarizing optical system is to follow the following rule introduced by Gil and Bernabeu [227]:

$$\text{Tr}(M^T M) = \sum_{i,j}^4 M_{i,j}^2 = 4M_{11}^2 \quad 5.12$$

where Tr is the trace of the matrix, M^T the transposed matrix of M and $M_{i,j}$ are the elements of the Mueller matrix M .

Regarding the measured circle in the center of images, we observe that the intensity of M_{22} element is clearly larger than that of M_{33} and M_{44} , i.e. $1 \geq M_{22} > M_{33}$ or M_{44} . It means that $\text{Tr}(M^T M)$ is strictly smaller than 4 (considering that all other off-diagonal elements appear to be zero), thus indicating a diagonal depolarizer, for which the degree of polarization decreases depending on the incoming light polarization.

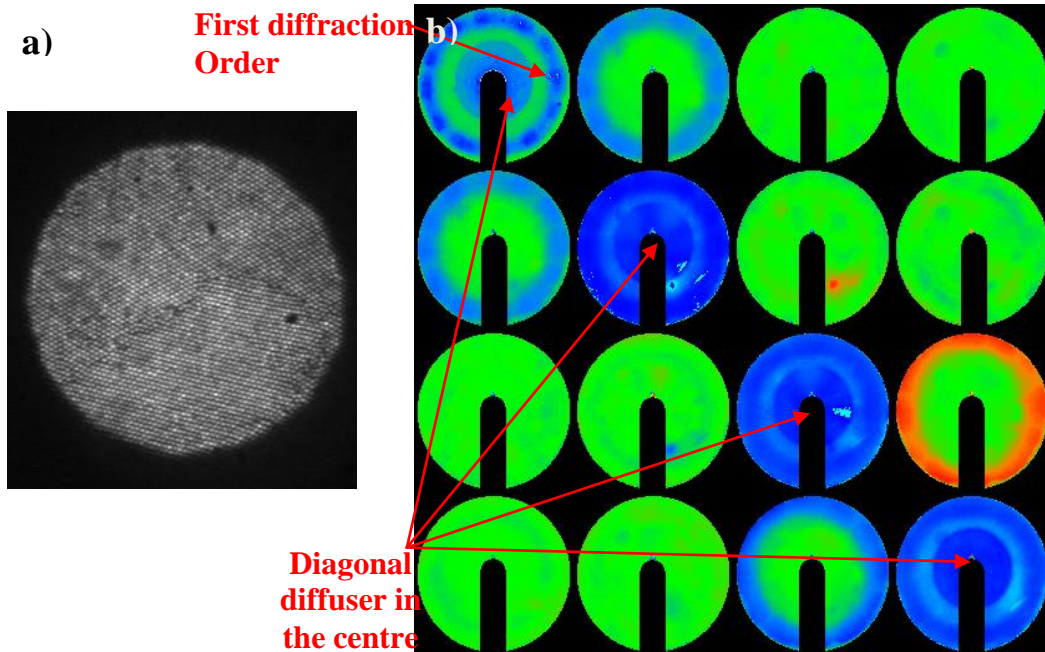


Figure 5-14: (a) Real space (microscopic) image and (b) corresponding measured normalized Mueller matrices of ordered SiNW arrays with a pitch of 800 nm.

The external ring corresponds to the diffracted light from the first order. This ring is located at a specific distance from the center at angles corresponding to the condition from Eq. (7.4). In our case, the distance d of the diffraction pattern from the center is such that:

$$d = \frac{\lambda}{p} \quad 5.13$$

As explained previously, SiNW arrays fabricated by MACE assisted by NSL are not perfect and different domain orientations can be observed in SEM images at different parts of the sample. **Figure 5-15** shows the microscopic image and M_{11} element detail of the measured Mueller matrices on the SiNW arrays with normal incidence illumination for three different situations: one single domain, exactly two domains and several domains. Domains are called areas with the same hexagonal periodicity, while different domains have usually symmetry axis rotated to each other – that makes them possible to distinguish. As shown in **Figure 5-15 (b)**, in the case of a single domain, we observe a single hexagonal diffraction pattern. When the number of domains is increased to 2, we observe the superposition of 2 diffraction patterns, slightly rotated from each other (**Figure 5-15 (d)**). Finally, when there are many different domains (**Figure 5-15 (f)**), there is a superposition of the diffraction patterns. We cannot distinguish the patterns from each other anymore and all together form the continuous circular diffraction pattern, similar to **Figure 5-13**. The measurements show a very good periodicity of the pattern fabricated using nanosphere self-organizing and that the most significant deviation from the perfect periodicity is the existence of domains with rotated symmetry axes.

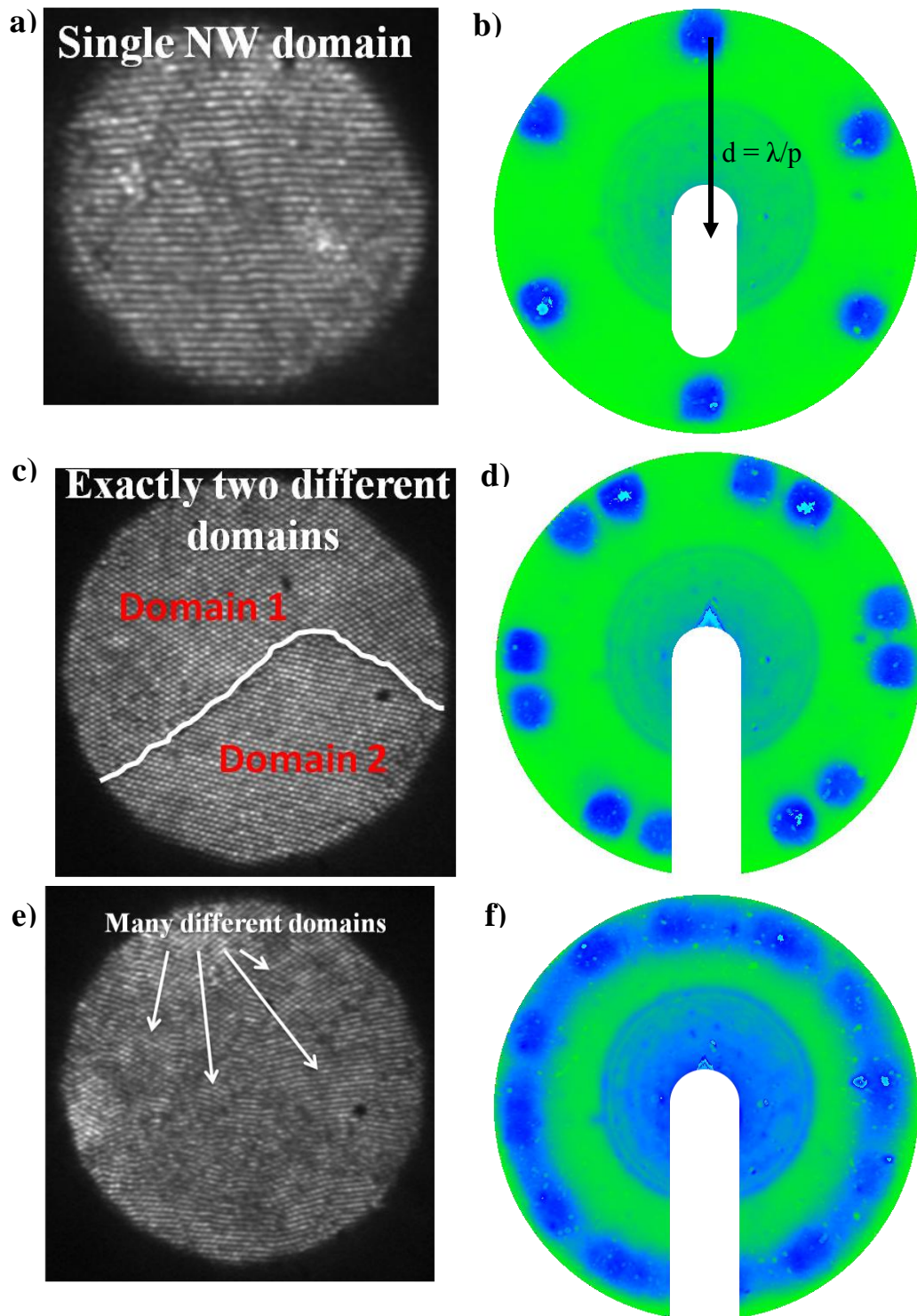


Figure 5-15: (a), (c), (e) Real space (microscopic) image and (b), (d), (f) corresponding M_{11} element detail of the measured Mueller matrices for a single domain (a), (b) , exactly 2 different domains (c), (d) and many small domains (e), (f).

5.5 RCWA analysis

It is possible to model the optical response of a perfect periodic arrangement of SiNWs using the rigorous coupled wave analysis (RCWA) method [37], [38]. SiNWs are modeled as nanostructures organized into a hexagonal arrangement since they correspond to the type of arrays fabricated via MACE assisted by NSL. We consider a polarized plane wave of the desired wavelength illuminating the structure at a normal incidence. In the RCWA approach, the nanostructure is basically divided into lateral layers that are uniform in the z -direction. In our case, we divide our system into three layers as illustrated in **Figure 5-16**: the dielectric superstrate layer, the grating (the SiNWs) layer and the substrate.

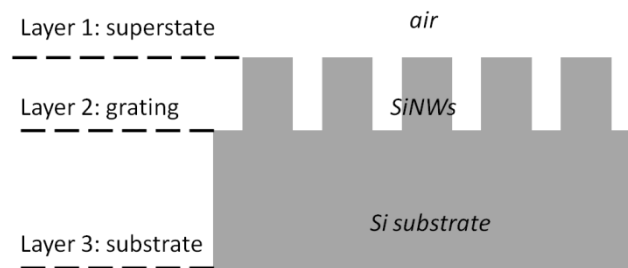


Figure 5-16: Definition of the 3 different layers used in our RCWA modeling.

A staircase approximation is implemented for the grating profile, i.e. the optical properties are graded along the z -direction, (which is not the case for vertical NWs), based on the work of Moharam and Gaylord [228], [229]. The RCWA method is based on the Fourier series expansion of the periodic electromagnetic field inside the SiNW array, which allows us to calculate propagating and evanescent modes. At first, electromagnetic Bloch modes are calculated for every layer. Then, boundary conditions are applied at each interface between the layers to match tangential electromagnetic field components. As a result, we can calculate reflectance and transmittance of every diffracted order, absorptance inside NWs and the complete electromagnetic field inside SiNW arrays can also be reconstructed. The convergence of the model was further improved by using factorization rules [230], [231]. The model was also improved by using the scattering matrices technique [232] for deeper grating structures. To model the three dimensions,

we use a 3D generalization formulation of RCWA [233] with adapted factorization rules [234]. In the following text, we will refer to this model as "the periodic model". From RCWA, we can determine the amount of light absorbed by the system from the reflection and transmission coefficients. For each configuration, the spectral absorptance $A(E)$ as a function of the wavelength was calculated. From $A(E)$, we have obtained values of ultimate J_{sc} by using Eq (5.4). All the RCWA calculations were realized using the optical model developed by Martin Foldyna from LPICM [37], [38].

From calculations for a wide range of parameters, we can obtain a map of the best theoretical J_{sc} (upper limit) as a function of the pitch and the diameter as shown in **Figure 5-17**. This gives us a valuable guidance for the design of SiNW arrays with excellent optical properties. On this map, we have included the theoretical J_{sc} calculated from the reflectance data measured on 8 different ordered SiNW arrays using Eq (5.4). Absorptance was assumed to be $A(E)=I-R(E)$ in the wavelength region below 1100 nm. Therefore each black cross on the map refer to a fabricated SiNW array whose coordinates gave the pitch and diameter of the fabricated structure.

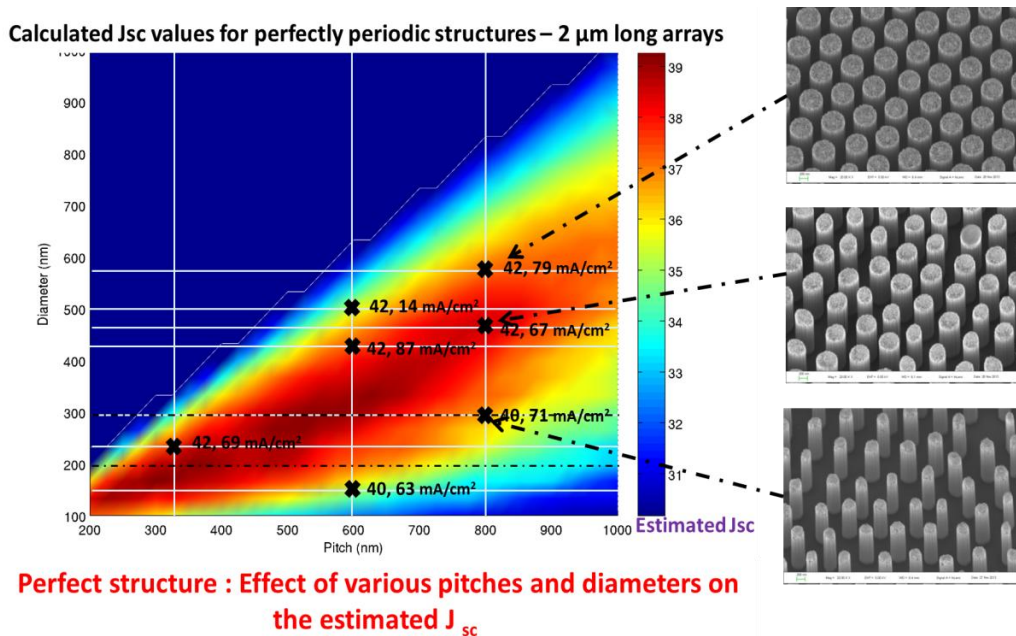


Figure 5-17: Effect of the geometrical parameters (pitch and length) on the estimated J_{sc} for a perfect periodic structure.

We have compared the theoretical J_{sc} values obtained from the model with the ones obtained from the experimental total reflectance measurements of the fabricated samples. The experimental values do not seem to follow the trend predicted by the periodic model, with about 3 mA/cm^2 , higher J_{sc} values than provided by the model. This difference can be explained by the structural imperfections of the arrays. Indeed, even if the SiNWs are quite well ordered, there are still some imperfections such as surface roughness, dislocations, different domains' orientations and distribution of the diameters and heights as shown in **Figure 5-18**. All those imperfections contribute positively to a reduction of the total reflectance.

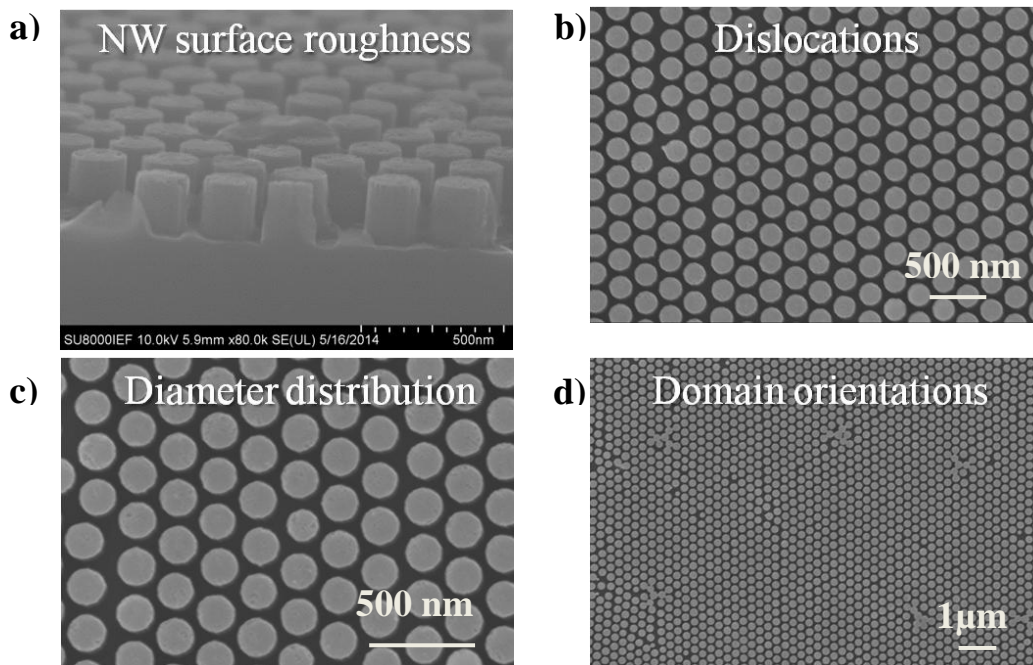


Figure 5-18: Structural imperfections of ordered array of SiNWs fabricated by MACE assisted by NSL such as (a) surface roughness, (b) dislocations, (c) diameter distribution and (d) domain orientations.

We have confirmed the effects of these imperfections on the optical properties by the model by integrating the periodic model into a statistical approach. In this new method, the total reflectance is first calculated by RCWA. Then, the optical response is statistically weighted to achieve a more adequate model, named "the statistical model". There are different optical responses, coming from different areas of samples with different geometrical parameters within the statistical distribution, that contribute to the total detected signal. The

idea behind the "statistical model" is to consider that the total response is composed of incoherently combined responses originating from different illuminated areas on the sample. Therefore, the total response R_T can be re-write as:

$$R_T = \frac{1}{\sum_n S_n} \sum_n S_n R_n \quad 5.14$$

where n denotes the n -th incoherent component and S_n the corresponding illuminated area.

The best fitting values for the diameters and heights of the NWs are acquired by minimizing χ^2 defined by the following formula:

$$\chi^2 = \frac{1}{N-1} \sum_n \frac{(R_{c,n} - R_{m,n})^2}{\sigma_n^2} \quad 5.15$$

where N is the number of points in the spectrum, $\sigma_n = 0.01$, $R_{c,n}$ is the reflectance calculated at the spectral point n and $R_{m,n}$ is the reflectance measured at the spectral point n . The minimum of χ^2 was found using the Levenberg-Marquardt algorithm [235], [236].

Figure 5-19 shows the results we have achieved for the modeling of an ordered array using the periodic model and parameters obtained from SEM with the blue line and red points representing the modeled and measured data, respectively. The SEM images of the corresponding SiNW array are also displayed for the reference (**Figure 5-19 (a) and (b)**). **Figure 5-19 (c) and (d)** shows direct forward calculations using parameters from SEM image. We can see that none of the values are able to perfectly reproduce the measured data. Using SEM data can be misleading as it does not necessarily provide parameters which will give appropriate optical response.

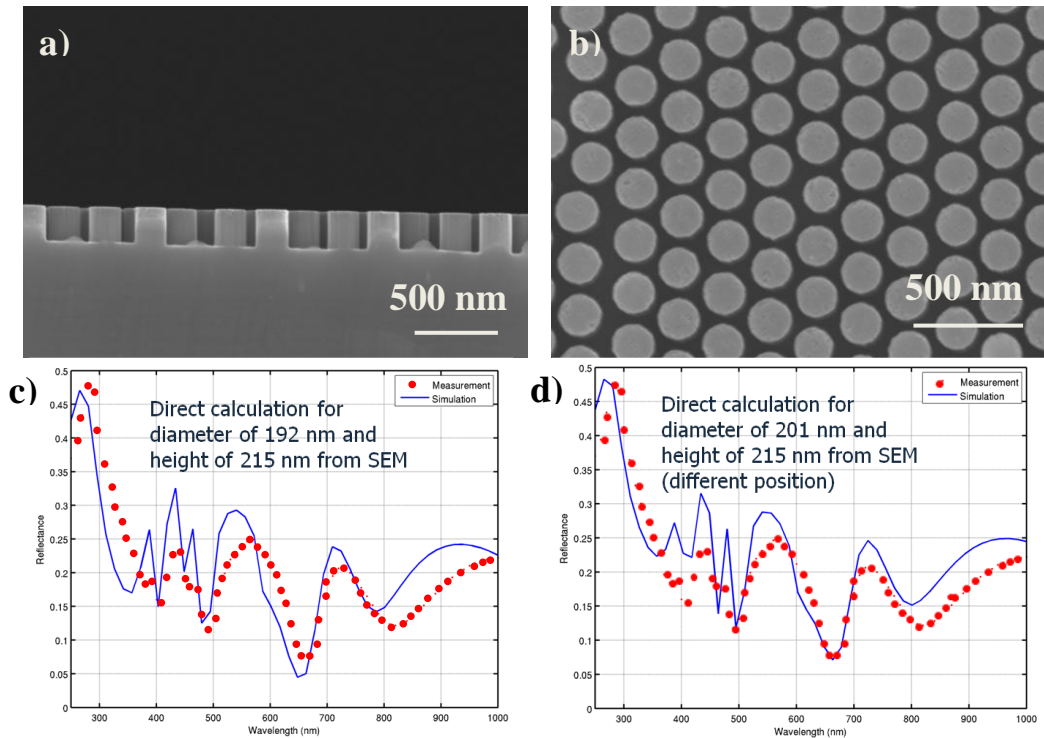


Figure 5-19: (a) Cross-section and (b) top-view SEM image of short ordered arrays of SiNWs and corresponding modeling (c) , (d) using the "periodic model".

Therefore it is essential to find the best fitting values and develop a good optical model which can more accurately describe the optical properties of fabricated SiNW arrays. **Figure 5-20 (b)** shows the fit we achieved using the statistical model compared with the best fit we obtained for the periodic model (**Figure 5-20 (a)**) There is an excellent agreement between the model and the measured total reflectance when these imperfections are taken into account, with a much better results in terms of small χ^2 values.

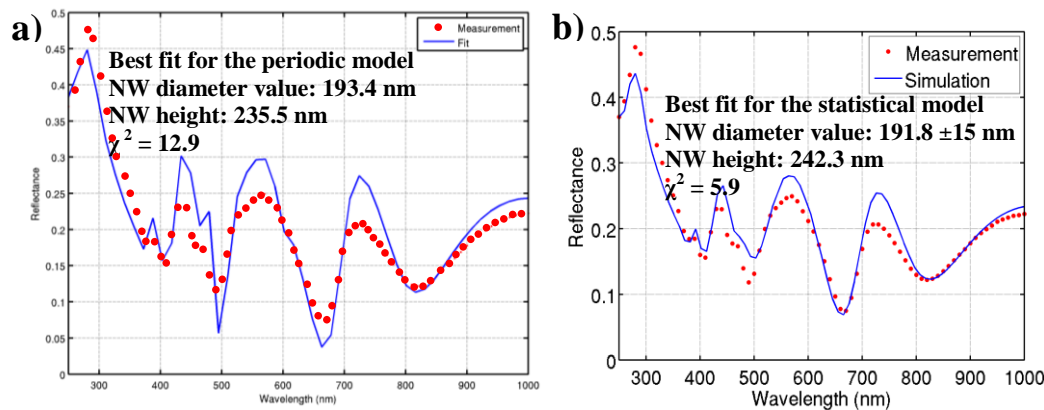


Figure 5-20: Comparison between (a) the "periodic model and (b) the "statistical model" for modeling a short periodic array fabricated by MACE assisted by NSL.

Likewise, we can model the Mueller matrices using RCWA and compare the data with measurements obtained from a Mueller matrix ellipsometer. Measurements were carried out at an angle of incidence of 60° in the spectral range from 450 nm to 1100 nm with a spot size of $250 \times 250 \mu\text{m}$. The tool measures all 15 elements of normalized Mueller matrices.

We observed previously that different Mueller matrices were obtained at different locations on the sample and that the total response is a combination of responses coming from different illuminated areas of the samples (**Figure 5-15**). If we assume that the measured response with a Mueller matrix ellipsometer is composed of mutually incoherent responses originating from different illuminated areas on the sample, we can re-write the Mueller matrix as:

$$M_{ij} = \frac{1}{\sum_n S_n} \sum_n S_n M_{ij}^n \quad 5.16$$

where n denotes the n -th incoherent component and S_n the corresponding illuminated area.

As shown in **Figure 5-21**, a good agreement between the measured data and the statistical model developed from a superposition of incoherent Mueller matrices has been achieved. We needed to include more details to the model, such as surface roughness or azimuthal angle because of the high sensitivity of MM data. We achieved SiNW diameters of 182 ± 8 nm, SiNW heights of 256 nm, a surface roughness 13.3 nm, an azimuthal angle 1.9° and $\chi^2 = 21$ with $\sigma = 0.01$ for all points.

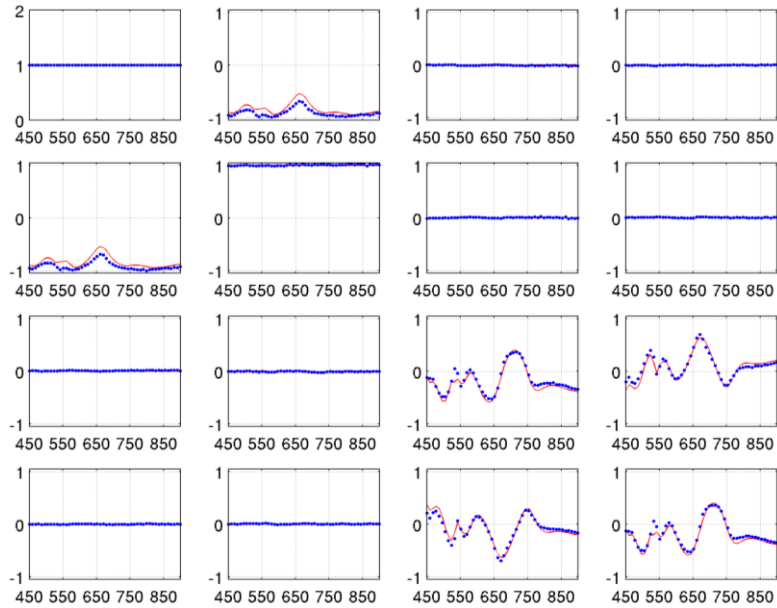


Figure 5-21: Best fit of Mueller Matrix using the statistical model.

The good agreement between the measured data and optical model enables to not only identify the structural parameters of fabricated samples using a fast and non-destructive technique, but also to use such model as a reliable tool leading the optimization of SiNW arrays for the best optical performance.

5.6 Dual diameter

Foldyna et al. have demonstrated that the more optimal configuration for vertical SiNW arrays is based on two diameters instead of the standard concept of a single diameter SiNW arrays [37], [38]. This is related to the reduced light efficiency of coupling short wavelength light into the guided modes of large diameter NWs and the impossibility to couple light with large wavelengths into localized modes of too small NW diameters. Indeed, the performance can be boosted by overlapping of the effective optical cross section of the neighbouring SiNWs. The concept is illustrated in **Figure 5-22** showing coupling of short wavelength light into the small and large diameter NW array.

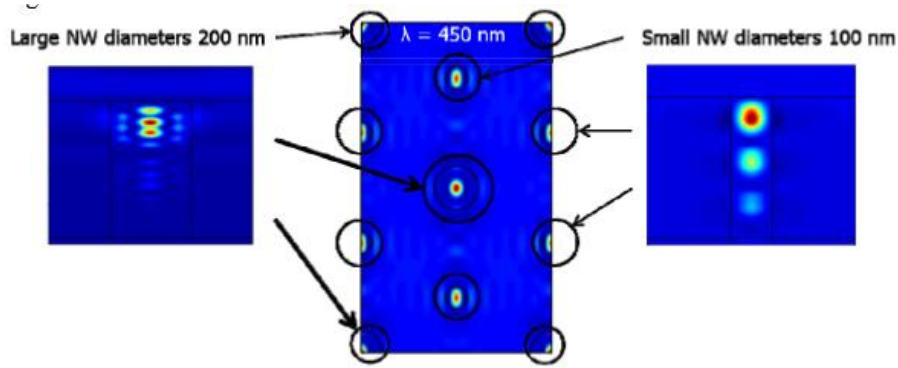


Figure 5-22: Representation of the dual diameter SiNW arrays concept with the corresponding Poynting vector at a wavelength of 450 nm. Every black circle represent a nanowire [37], [38].

This work is now in the phase of the experimental realization. We have tried to fabricate SiNW arrays with dual diameters. To this end, we have mixed two solutions of PS spheres of 330 and 600 nm with different ratios. We show the results we achieved for two ratios (2:1) and (1:2) of (330 nm : 600 nm) PS nanospheres in **Figure 5-23**. Interestingly, we achieve a monolayer. We can observe that small spheres form a compact monolayer with the big spheres distributed in this monolayer. SiNW arrays successfully fabricated from these PS nanospheres covered substrate are shown in **Figure 5-23 (c)**. Note the high density is due to a very short oxygen plasma reduction step.

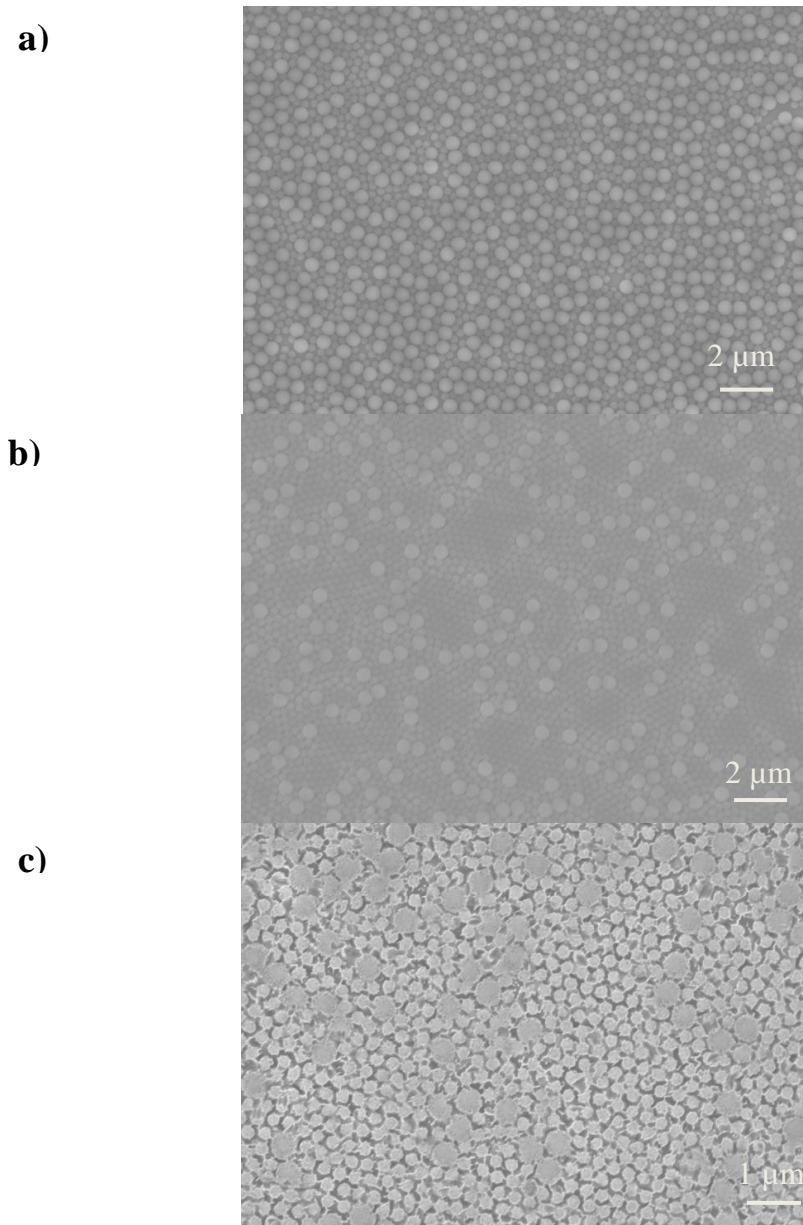


Figure 5-23: Top-view SEM pictures of PS spheres monolayer with a PS sphere (330:600 nm) ratio of (a) (1:2), (b) (2:1) and (c) corresponding SiNW arrays fabricated from (b).

Figure 5-24 shows the experimental reflectance spectrum we obtained for a dual SiNW array (330 nm : 600 nm) (2:1). We achieve an average reflectance of 5.4 % in the spectral range of 400-1100 nm for very short SiNWs (< 150nm), which is the best average reflectance we achieved for ordered SiNWs arrays with similar lengths. To exemplify this point, we have added the reflectance spectra of single diameter SiNW array with a pitch of 330 nm and with a similar length. This is a proof of concept of the viability of dual diameter fabrication of SiNW arrays. More work is required to optimize the fabrication

process of dual diameter SiNW arrays and boost the optical properties of SiNW arrays further.

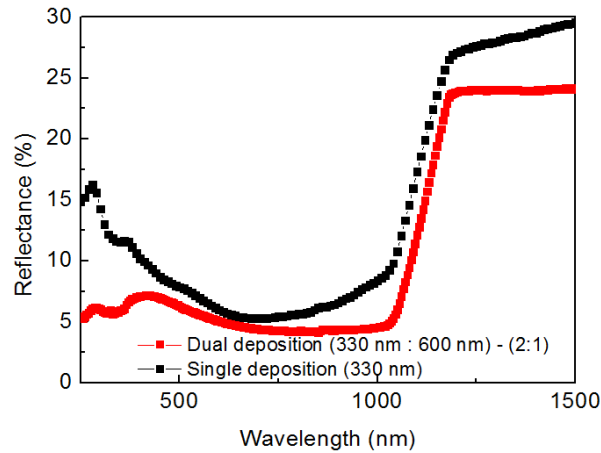


Figure 5-24: Reflectance spectra of dual diameter SiNW array with (330 nm : 600 nm) (2:1).

Conclusion:

This chapter demonstrates the enhanced light trapping of SiNW arrays of different lengths and geometries. Optical properties of random SiNWs are mainly determined by the length of the nanowires as there is no other parameter to control. The case of ordered SiNW arrays is more complex. Indeed, the geometry of the SiNW arrays has a drastic effect on the optical properties, with the average reflectance in the 400-1100 nm wavelength range varying from more than 20 % to ~3 % as a function of the geometry. This work highlights the importance of optimally designed nanoscale features for improving the light trapping within devices and confirms the theoretical predictions from the optical model of the optimized nanostructure. We observe that ordered SiNW arrays are diffracting the light and that the diffraction pattern is a superposition of hexagonal diffraction patterns coming from different areas of the sample with different domain orientations. Optical properties of SiNW arrays were also modeled using the RCWA technique in order to give a numerical estimation of the theoretical solar cell performances. By taking into account the inherent defects of the arrays due to the process of fabrication, we were able to obtain

good agreement between the model and experimental data which opens the door towards the design and realization of highly efficient SiNW arrays.

Chapter 6 : HIT Solar Cells based on SiNWs

In this Chapter 6, we focus on the fabrication and characterization of heterojunction with intrinsic thin layer (HIT) solar cells based on SiNWs fabricated either by the standard MACE process or by the MACE process assisted by nanosphere lithography (NSL). This includes the optimization of the process of fabrication, the characterization by specific techniques such as electron beam induced current (EBIC) and time resolved microwave-conductivity (TRMC) and the investigation of specific surface treatments to enhance the efficiency. We also report on the possible transfer of the SiNWs based HIT device to the silicon thin film technology.

6.1 Understanding the Challenge and Complexity of HIT Solar Cells based on SiNWs

We already have introduced the main features of HIT solar cells in the section 2.4.2 of this thesis. As a reminder, a HIT device consist of the subsequent deposition of a thin intrinsic and doped a-Si:H layer on the top of the silicon substrate to form the heterojunction. **Figure 6-1 (a) and (b)** show the schematic architecture of a HIT and SiNWs based HIT devices. HIT planar cells were fabricated as well to serve as a reference.

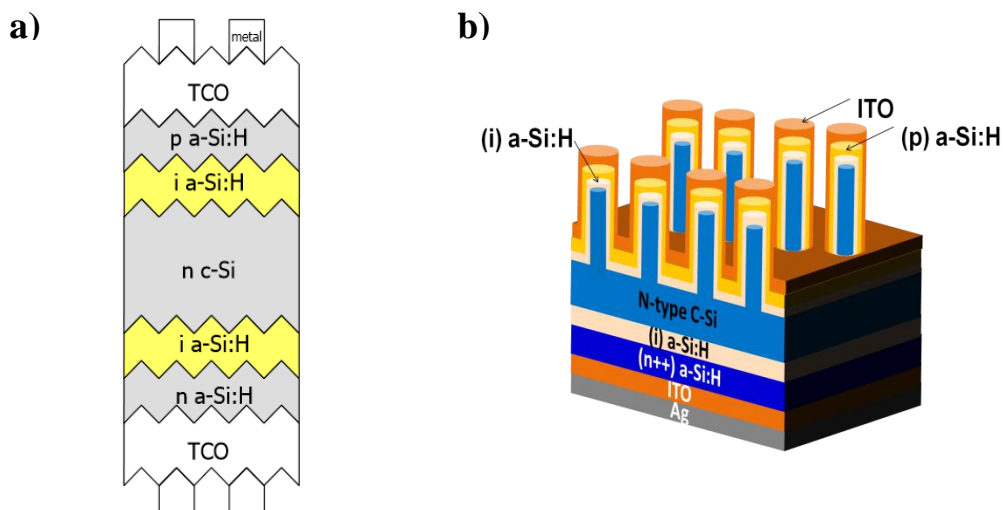


Figure 6-1: Schematic of the structure of (a) a HIT solar cells [125] (b) a HIT solar cell where the n-type c-Si wafer has been nanostructured to improve light trapping.

The main difficulty faced in SiNW based solar cells is the proper passivation of SiNW surface by a-Si:H. Indeed, the small size and the high aspect ratio of NWs make achieving conformal coverage extremely challenging. Considering this aspect, the SiNW cells are much more complex to fabricate than planar ones. Besides, the deposition conditions have to be optimized for SiNW based solar cells.

For example, a simple calculation can show us how big is the surface enlargement due to the presence of SiNWs with respect to the planar structure. It is complex to calculate accurately the surface enlargement due to disordered SiNWs as the diameter or pitch of the fabricated array is random. However, as the MACE process coupled with the NSL enables control over the geometry of the arrays in term of pitch, diameter and length, as shown in the Chapter 3 of this thesis, we can calculate accurately the surface increase ratio for different geometries. In the MACE process assisted by NSL, the SiNWs form a dense hexagonal arrangement as displayed in **Figure 6-2**. We consider six SiNWs arranged hexagonally, with a pitch p (center to center distance). We defined S , the planar surface defined by the black rectangle as the reference area. We have:

$$S = \sqrt{3}p^2 \quad 6.1$$

In this rectangle, we have 2 SiNWs (one in center and $\frac{1}{4}$ at each of the 4 edges). Therefore, the total surface S' including the SiNWs is given by the sum of the planar surface and the total area of the SiNWs as follows:

$$S' = 2(2\pi rh) + S \quad 6.2$$

So the surface ratio S_r is given by the following formula:

$$\begin{aligned} S_r &= \frac{S'}{S} = \frac{2(2\pi rh) + S}{S} = \frac{2(2\pi rh) + \sqrt{3}p^2}{\sqrt{3}p^2} \\ &= 1 + \frac{4\pi}{\sqrt{3}} * \frac{rh}{p^2} \end{aligned} \quad 6.3$$

We have calculated S_r for different geometries that we have fabricated and the results of calculations are tabulated in **Figure 6-2**.

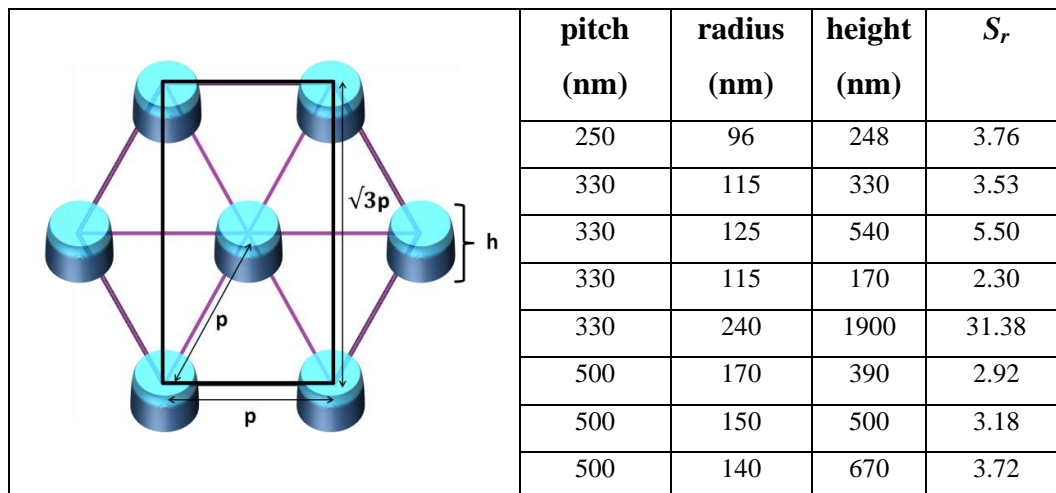


Figure 6-2: Illustration of a hexagonal SiNWs arrays with a pitch p and a height h (left) and calculation of the surface ratios for different geometries (right).

As shown in **Figure 6-2**, the increase in surface area is significant and we need to keep this in mind when optimizing the experimental conditions for HIT solar cells based on SiNWs. The first assumption we can draw is that we need more a-Si:H material to cover the SiNW arrays compared to standard deposition conditions for planar solar cells as the area of the p-n junction is much bigger.

6.2 Fabrication, Optimization and Characterization of HIT Solar Cells based on random SiNWs

6.2.1 Fabrication of HIT devices by PECVD and finalization of devices

The SiNW samples previously prepared by the standard MACE (see section 3.1.1 and Chapter 4) were transferred to a RF PECVD reactor (ARCAM,[153]) after a prior removal of the native oxide layer by a 5% HF bath. The plasma deposition process was performed at 200 °C. **Figure 6-3 (a) and (b)** show the schematic architecture of our device and its scanning electron microscopy (SEM) image respectively. The structure is as follows: indium tin oxide (ITO)/(p) a-Si:H/(i) a-Si:H/(n) c-Si/(i) a-Si:H/(n++) a-Si:H/ITO/Ag.

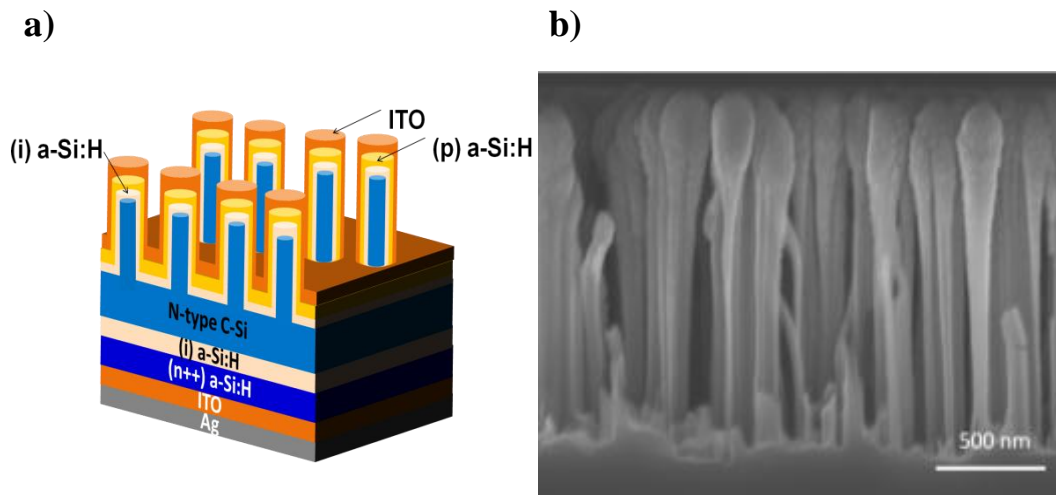


Figure 6-3: (a) Schematic of the structure of the HIT solar cell where the n-type c-Si wafer has been nanostructured to improve light trapping. (b) SEM cross-section of a fabricated device.

First, a very thin layer of intrinsic amorphous silicon carbide (i) a-SiC:H was deposited on the top of the nanowires from the dissociation of a gas mixture of $\text{SiH}_4:\text{CH}_4$ (25:50) for 30 seconds with a low plasma power of 1 watt. This layer prevents the epitaxial growth of silicon which has a detrimental effect on the surface passivation and carrier lifetime. A thin intrinsic hydrogenated amorphous silicon layer (i) a-Si:H was then deposited using pure SiH_4 (50 sccm, 1 watt). Finally, the window layer (p) a-Si:H was deposited from a gas mixture of SiH_4 :trimethylboron (TMB) in argon. The gas ratio was varied during deposition, initially 50:10 and then 50:20 to achieve a doping gradient. Different doping gradients were obtained by varying the deposition time. For the backside, a thin a-SiC:H layer (30s) followed by an (i) a-Si:H (1 min) layer were deposited. Following that, an (n++) a-Si:H layer was deposited from a gas mixture of $\text{SiH}_4:\text{PH}_3$ with ratio of 50:1 and 50:2 for 1 and 3 minutes, respectively, on the back of the samples, providing both surface passivation and an ohmic contact to the ITO electrode. Finally the top and bottom ITO were deposited by sputtering while the bottom Ag was deposited by thermal evaporation. The process flow is summarized in **Figure 6-4**.

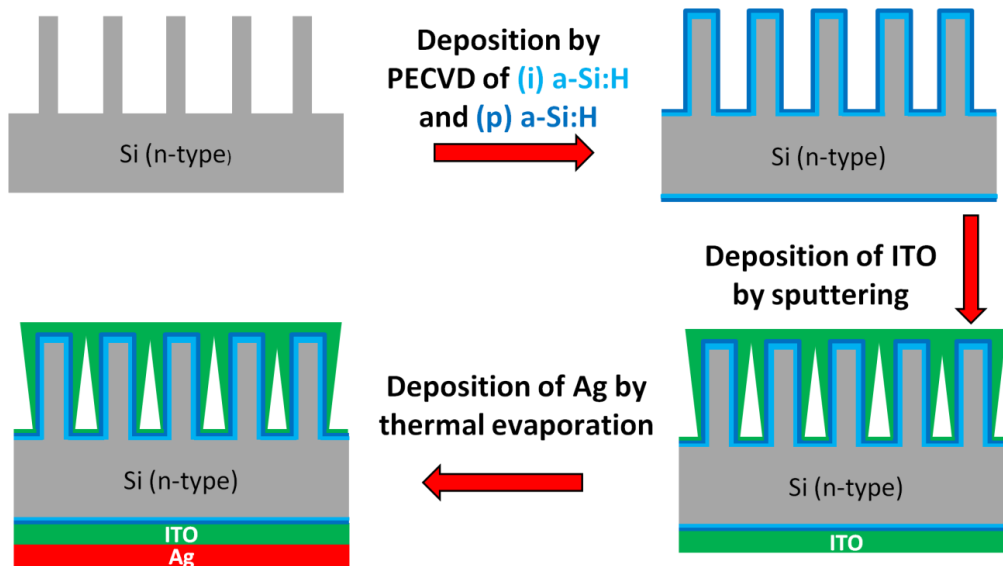


Figure 6-4: Process of fabrication of HIT solar cells based on SiNWs.

6.2.2 Optimization of the process conditions

6.2.2.1 Effect of the overall thickness of deposition

Optimization of the process conditions was carried out on random SiNWs. To optimize the passivation scheme for SiNWs, we have tested 6 different deposition conditions for the two front layers (i) a-Si:H and (p) a-Si:H. Disordered SiNWs with a height of 500 nm were used in the experiments. Six different samples were obtained, labeled as sample A, B, C, D, E and F, with their deposition conditions summarized in **Table 6-1**. All the samples have the same back contact, and only the front deposition conditions are different. The area of each cell is 0.126 cm². The nominal thickness corresponds to the overall thickness of a-Si:H ($d_{a-Si:H}$) measured on flat reference thin films deposited under the same conditions, i.e. $d_{a-Si:H}$ corresponds to the total thickness of both the (i) a-Si:H and (p) a-Si:H layers. The thicknesses have been deduced from spectroscopic ellipsometry measurements and modeled using the Tauc Lorentz dispersion law [237], [238].

Table 6-1: Summary of various deposition conditions with details of the deposition time of each layer.

Samples	A	B	C	D	E	F
Total deposition time (p) a-Si:H + (i) a-Si:H	4 min	7 min	8 min	13 min	17 min	21 min
Overall thickness measured on planar Si ($d_{a-Si:H}$)	14 nm	28 nm	32 nm	48 nm	64 nm	80 nm

The current density versus voltage ($J(V)$) curves of the cells are displayed in **Figure 6-5 (a)**. The averaged values and the standard deviation of the corresponding solar parameters are summarized in **Table 6-2**. The $J(V)$ curve of sample C presents the smallest series resistance compared to samples with other thicknesses. A record efficiency of 12.9% was achieved for the best cell from sample C.

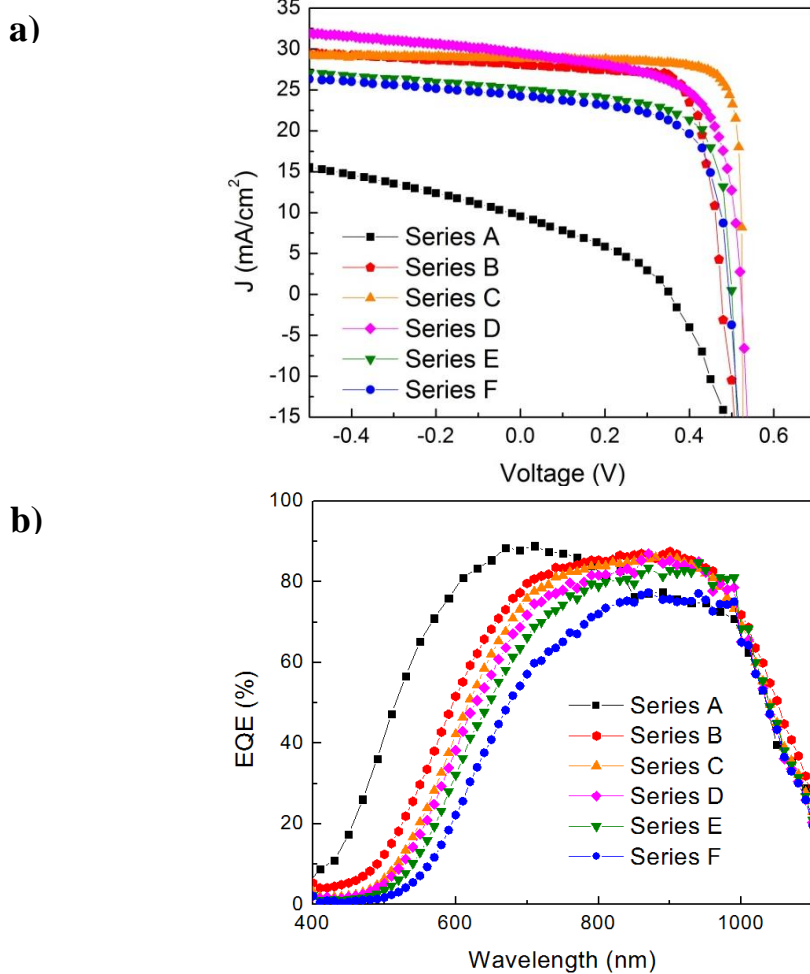


Figure 6-5: Dependence of (a) EQE and (b) (J,V) curves on the thickness of the amorphous layer (see Table 6-1).

Table 6-2: The average value and the standard deviation of V_{oc} , J_{sc} , FF and η of core-shell HIT solar cells.

Sample	A	B	C	D	E	F
V_{oc} (V)	0.33 ± 0.01	0.48 ± 0.01	0.53 ± 0.01	0.52 ± 0.005	0.53 ± 0.004	0.52 ± 0.005
J_{sc} (mA/cm ²)	14.21 ± 2.5	28.71 ± 0.44	29.27 ± 1.1	30.17 ± 0.50	25.03 ± 0.11	23.71 ± 0.51
FF (%)	41.44 ± 1.9	77.33 ± 5.0	81.05 ± 5.2	61.91 ± 2.0	66.41 ± 1.3	64.43 ± 0.42
η (%)	4.015 ± 0.31	10.73 ± 0.81	12.43 ± 0.33	9.66 ± 0.35	8.31 ± 0.13	7.64 ± 0.21

Figure 6-6 summarizes the effects of the amorphous layer thickness $d_{a-Si:H}$ on the photovoltaic parameters (J_{sc} , FF , V_{oc} and η) of the fabricated devices. It can be seen that $d_{a-Si:H}$ has a drastic effect on the performances of solar cells. If $d_{a-Si:H}$ is too thin (series A, 14 nm), the samples are characterized by V_{oc} , J_{sc} , FF and η that are the lowest among all the samples. It indicates a poor passivation by a-Si:H most likely due to an insufficient a-Si:H covering at the bottom of the NWs. When $d_{a-Si:H}$ is increased to 32 nm, the open-circuit voltage reaches 0.53V as seen **Figure 6-6 (c)**. There are two clearly identifiable trends: For $14 \text{ nm} < d_{a-Si:H} < 32 \text{ nm}$, the V_{oc} increases until it reaches a plateau value which holds for larger thicknesses. Moreover both J_{sc} and FF achieve a good performance at the optimal a-Si:H thickness of 32 nm. **Figure 6-6 (a)** illustrates the effect of thickness on J_{sc} . The poor coverage induced by a-Si:H that is too thin does not provide enough surface passivation. When $d_{a-Si:H}$ is increased from 28 to 48 nm, J_{sc} increases, before it drops drastically for $d_{a-Si:H}$ above 48 nm. We can relate these observations to the fact that a too thin a-Si:H may not be able to provide surface passivation for the arrays of SiNWs, while a too thick a-Si:H will lead to optical losses by absorption in the a-Si:H layer. The FF shows a maximum for a thickness of about 32 nm with an excellent value above 80%. On the other hand, lower FF values for thicknesses over 45 nm can be attributed to non-conformal ITO coating due to a large a-Si:H bump on the top of NWs as shown in **Figure 6-7 (d)**.

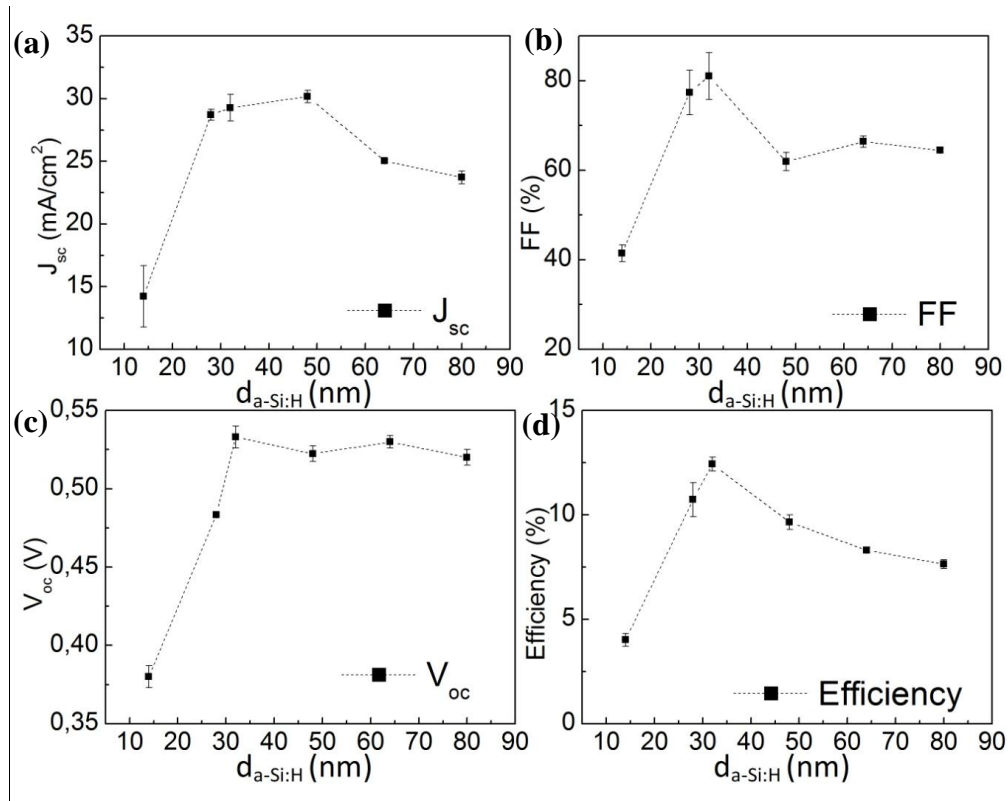


Figure 6-6: The average value and the standard deviation of J_{sc} (a), FF (b), V_{oc} (c) and η (d) as function of $d_{a-Si:H}$.

The SEM pictures of the samples D and F after a-Si:H PECVD deposition and before ITO sputtering are displayed in **Figure 6-7 (a)** and **(b)** respectively. **Figure 6-7 (c)** shows sample F after ITO deposition. The SEM pictures show that the a-Si:H coating becomes thicker with increasing deposition time, as expected. However this deposition is not uniform as shown by the bump shape of the SiNWs coated by ITO. The coating is the thickest at the top of the SiNWs, and its thickness reduces along the SiNW length from the top to the bottom. This might be explained by the challenges posed by the high aspect ratio of SiNWs. The discrepancy in the a-Si:H thickness between top and bottom of the wires increases with the deposition time. The percentage difference in thicknesses between the top and the bottom of the SiNWs reaches up to 50% for sample F while it is less than 10% for sample A. **Figure 6-7 (c)** shows that the ITO coating is not conformal as well and large bumps are formed at the top of the SiNWs (**Figure 6-7 (d)**). For sample F, the bumps are very large and touch each other. For some SiNWs, the ITO does not reach the bottom of the SiNWs, which may explain the decrease in FF discussed above.

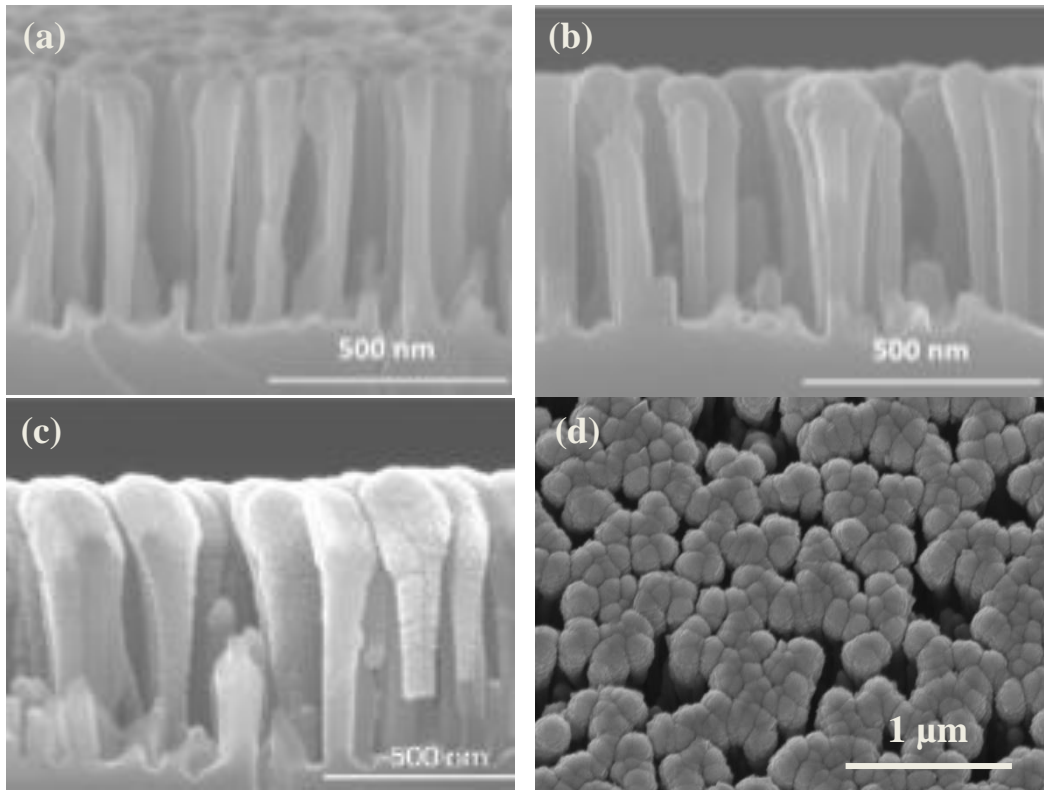


Figure 6-7: SEM pictures of SiNW solar cells after a-Si:H PECVD deposition of sample D (a) and sample F (b) before ITO deposition and sample F (c) after ITO deposition cross-section and (d) after ITO deposition top-view.

The stronger absorption loss at the front part of the cells with a thicker a-Si:H film is confirmed by the EQE measurements shown in **Figure 6-5 (b)**. The blue response is strongly reduced with increasing $d_{\text{a-Si:H}}$, indicating that a significant portion of the light is absorbed by a-Si:H near the top part of the cells, but does not contribute to the collected current. However, for wavelengths (λ) between 800 nm and 1000 nm, we observe higher EQE response for cells from samples B, C, D and E compared to cells from sample A with the thinnest a-Si:H layer. The higher performance in the long wavelength regime is explained by the reduced surface recombination due to a proper surface passivation in combination with the light trapping capability of SiNWs. As for sample F, we observe an overall weaker EQE response as the thicker a-Si:H introduces substantial optical losses. Moreover, we suspect that the large bumps observed for thicker a-Si:H deposition are making the conformal deposition of ITO difficult (see **Figure 6-7 (c)**) and may therefore play a significant role in the reduced EQE response measured. For $\lambda > 1000$ nm, all the EQE curves are nearly identical. Note that series A displays a good EQE but a poor J(V)

characteristic. This can be attributed to the extremely thin a-SiH passivation layer for this series. In this case the passivation of the SiNWs surface is strongly deteriorated and therefore we obtain a very poor characteristic under AM1.5 illumination conditions. Yet, the EQE shows a good collection, related to the fact that this measurement is performed at much lower light intensity with a monochromatic light. In fact, case A is a typical example stressing the importance of optimizing a-Si:H thickness - too thin might be good for optics, but not necessarily for electric properties.

The quality of the passivation provided by the different thicknesses of a-Si:H was then investigated by the time resolved microwave conductivity (TRMC) technique. We have studied the effect of $d_{\text{a-Si:H}}$ deposited on the NWs using the measured TRMC signal shown in **Figure 6-8**. It is noted that the intensity of the signal increases and the decay is much slower with increasing $d_{\text{a-Si:H}}$. The best effective lifetime is achieved for $d_{\text{a-Si:H}} = 32$ nm (sample C), the same thickness as for the best V_{oc} , confirming the proper passivation by a-Si:H for sample C. For thicker a-Si:H layers ($d_{\text{a-Si:H}} = 64$ nm and $d_{\text{a-Si:H}} = 80$ nm), the signal is very weak and we were not able to fit the data. The variations observed in the decay time and the shape of the curves of the different TRMC signals imply different passivation qualities and/or junction properties. A low TRMC signal might result from two main phenomena: the electron-hole recombination and carrier transfer from amorphous to crystalline layer. Devices with $d_{\text{a-Si:H}} = 14$ nm, $d_{\text{a-Si:H}} = 28$ nm and $d_{\text{a-Si:H}} = 32$ nm present a principal decay mode whose kinetics can be expressed by an exponential function, as confirmed by the logarithm scale shown by the inset of **Figure 6-8**. The experimental decay is fitted by Eq. (3.8). We were able to retrieve an effective lifetime of 2.8 μs , 3.1 μs and 5.8 μs for a respective thickness of $d_{\text{a-Si:H}}$ of 14, 28 and 32 nm. For solar cells with $d_{\text{a-Si:H}} = 48$ nm, 3 decay modes can be identified: the fast initial decay followed by the slower intermediate decay and the principal decay mode, which might be explained by an excess of charge carriers stored in the thicker amorphous layer. In this experiment, the pulsed laser light entered the device through the front side of the cells, that is, through the SiNWs. We have also flipped the samples to have the laser light penetrating through the backside of the cells, which has a planar geometry. Generally, we observe a signal with a lower intensity and a slightly higher lifetime, in the order of 10 μs , compared to

measurements performed with the light is penetrating through the SiNWs side. The lower intensity in the case of laser illumination of the planar backside is explained by the higher reflectivity of the planar backside which reduces the absorption in the wafer. We have observed a slightly better effective lifetime on the backside because of reduced recombination. However, irrespective of illumination side, the effective lifetime is very small whereas for planar cells the signal is in the order of ms, independent of the illumination side. As all solar cells, including the planar ones, have the same backside, we can conclude that the recombination at the SiNW surface is the limiting factor.

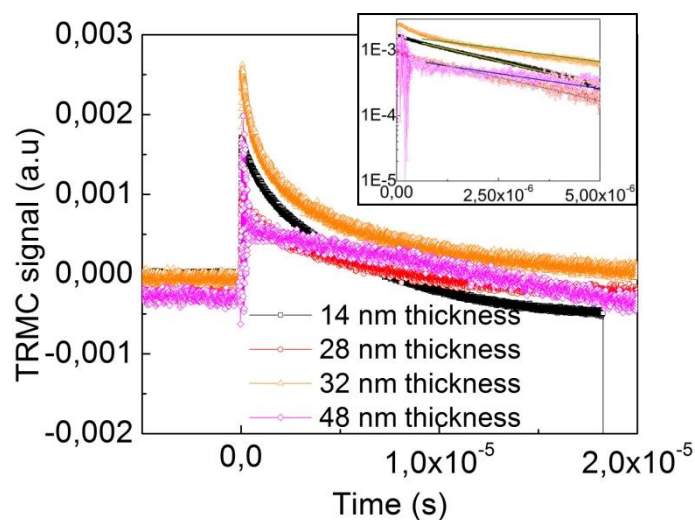


Figure 6-8: TRMC signal as a function of time for HIT solar cells with different a-Si:H thicknesses. The inset shows the signal in logarithmic scale.

We have just discussed the quality of the passivation as a function of the a-Si:H layer thickness. We will now look into detail the effect of both the intrinsic and doped layer on the performance of SiNW based HIT devices.

6.2.2.2 Effect of the doped layer

We have investigated the effect of the deposition conditions of the (p) a-Si:H layer on the performance of the HIT devices based on disordered SiNWs. As mentioned in the experimental part, the doped a-Si:H layer consists of two consecutive (p+) and (p++) a-Si:H layers, where the doping concentration is increased during the PECVD deposition in order to achieve a doping gradient. Doping is a key process that impacts the electric field and the band structure of the device [239]. A doping gradient can contribute to a reduction of the

interface defects density by maintaining a high defects formation enthalpy within (i) a-S:H. Moreover, both quasi-Fermi level splitting and band slope can be gradually adjusted by doping gradient. For example it has been shown that a gradually decreasing quasi-Fermi level split from the surface to the interior of the emitter improves the spectral response in the long wavelength region and the V_{oc} , while improved charge separation and reduced recombination can be achieved via gradually increasing band slope [239]. We present here results for solar cells which have undergone the same deposition conditions for the (i) a-Si:H layer and for which we have only varied the process conditions for the (p) a-Si:H. Therefore the solar cells only differ from their doped layer, which allow us to isolate only the effect of the (p) a-Si:H film as illustrated on the schematic in **Figure 6-9**. A thin carbon layer to prevent epitaxial growth was deposited for 1 min followed by the deposition of an (i) a-Si:H layer for 3 min (12 nm equivalent on planar).

Table 6-3 summarizes the different deposition conditions that we have tested for the (p) a-Si:H layer.

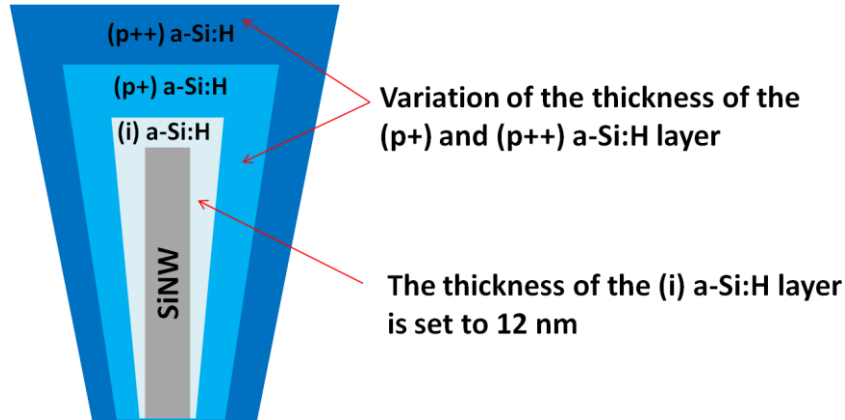


Figure 6-9: Schematic showing the details of the a-Si:H coating.

Table 6-3: Summary of various deposition conditions with details of the deposition time of every layer and average value of V_{oc} , J_{sc} , FF and η of corresponding core-shell HIT solar cells.

Samples	B	G	C	H	D
Deposition time carbon layer	1 min				
Deposition time (i) a-Si:H	3 min				

Deposition time (p+) a-Si:H	2 min	3 min	2 min	3 min	3 min
Deposition time (p++) a-Si:H	2 min	1 min	3 min	2 min	6 min
Total deposition time (p) layer	4 min	4 min	5 min	5 min	9 min
Overall thickness measured on planar Si ($d_{a-Si:H}$)	28 nm	28 nm	32 nm	32 nm	48 nm
V_{oc} (V)	0.48	0.29	0.53	0.31	0.52
J_{sc} (mA/cm ²)	28.71	29.50	29.27	29.70	30.17
FF (%)	77.33	71.94	81.05	49.34	61.91
η (%)	10.73	6.28	12.43	4.50	9.66

Consider first the samples with the same total thickness of doped layer such as sample B and G with a (p) a-Si:H deposition time of 4 min, and sample C and H with a (p) a-Si:H deposition time of 5 min. We observe that the doping gradient is playing a critical role on the performances of the devices. When the thickness (or deposition time) of the highly doped (p++) a-Si:H layer is smaller than the medium doped (p+) a-Si:H layer (i.e. $d_{(p++) a-Si:H} < d_{(p+) a-Si:H}$), the performances are systematically very poor. These poor results are explained by a significant drop of the V_{oc} from values around 0.5 V for samples with $d_{(p++) a-Si:H} > d_{(p+) a-Si:H}$ to 0.3 V for samples with $d_{(p++) a-Si:H} < d_{(p+) a-Si:H}$.

For $d_{(p++) a-Si:H} = d_{(p+) a-Si:H}$, which is the case of sample B, we did not observe this drop of V_{oc} . The J_{sc} is not impacted by the doping gradient and remains at a stable value of around 29 - 30 mA/cm².

The (J,V) curves of samples C and H are displayed in **Figure 6-10** as an example. We observe a s-shape curves for solar cells with $d_{(p++) a-Si:H} < d_{(p+) a-Si:H}$ and normal (J,V) curves for solar cells with $d_{(p++) a-Si:H} \geq d_{(p+) a-Si:H}$. Such results might be explained by the very low doping of the emitter in the case of $d_{(p++) a-Si:H} < d_{(p+) a-Si:H}$. It has been shown that in the case of highly doped emitter, the depletion region is mainly in the (n) c-Si wafer (~400 nm) while the depletion width in the emitter is about 5 nm. However, in the case of low doped emitter, the depletion region becomes negligible on the side of the (n) c-Si wafer and only exists in the emitter region. This can explain the s-shape curves observed in the case of low-doped emitter [240]–[242].

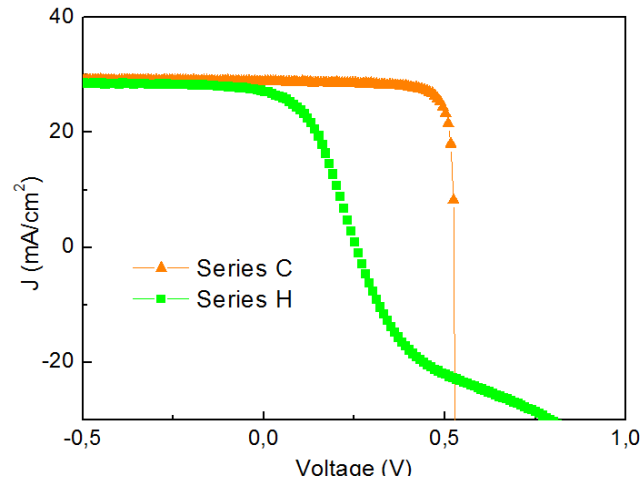


Figure 6-10: Effect of the gradient doping on (J,V) curves of HIT solar cells based on SiNWs.

These results show the importance of a proper design of the doping gradient of the amorphous layer in order to achieve highly efficient solar cells. We next consider samples B, C and D with $d_{(p++)} \text{ a-Si:H} \geq d_{(p+)} \text{ a-Si:H}$. We observe that there is an optimum thickness for the (p) a-Si:H layer in terms of V_{oc} and FF . For fixed values of the (i) a-Si:H layer, we observe first an increase and then stabilization of the V_{oc} which is consistent with our previous analysis on the optimization of the passivation scheme as a function of the overall thickness of a-Si:H. When the doped amorphous layer is too thick, we observe a drop in the FF which can be attributed to the non-conformal a-Si:H and ITO coatings due to the formation of large a-Si:H bumps on the top of the NWs. **Figure 6-11** shows the effect of increasing the thickness of the doped a-Si:H layer, (p) a-Si:H, on the EQE response of the solar cells with the (p) a-Si: layer thickness being the total thickness of the (p+) and (p++) a-Si:H layers. We observe a slight decrease in the EQE response over the short wavelength region with increasing thickness of the doped (p) a-Si:H layer, because of the absorption loss in the doped amorphous layer. The EQE response in the long wavelength regime is not affected by the thickness of the (p) a-Si:H layer and the EQE curves display the same trend.

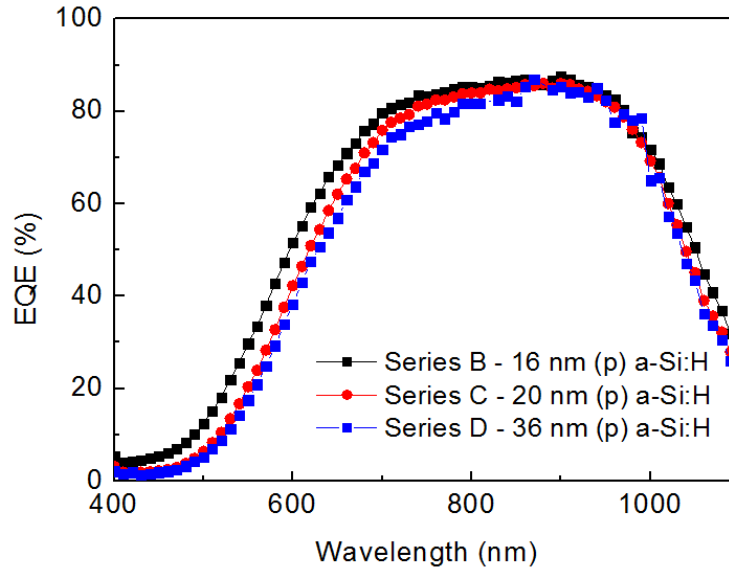


Figure 6-11: Effect of the gradient doping on the EQE of HIT solar cells based on SiNWs.

6.2.2.3 Effect of the intrinsic layer

We will now analyze the effect of the thickness of the intrinsic layer on the performance of HIT solar cells based on disordered SiNWs. We present here results for solar cells which have undergone the same deposition conditions for the (p) a-Si:H layer. Therefore they only differ from the thickness of their intrinsic layer, which allow us to isolate the effect of (i) a-Si:H. A thin carbon layer to prevent epitaxial growth was deposited for 1 min before the deposition of the (i) a-S:H layer. The doped layer consists of the consecutive deposition of (p+) a-Si:H for 2 min and (p++) a-Si:H for 3 min. **Table 6-4** summarizes the different deposition conditions that we have tested.

Table 6-4: Summary of various deposition conditions with details of the deposition time of every layer and average value of V_{oc} , J_{sc} , FF and η of corresponding core-shell HIT solar cells.

Samples	I	C	J	K
Deposition time carbon layer	1 min	1 min	1 min	1 min
Deposition time (i) a-Si:H	2 min	3 min	4 min	5 min
Deposition time (p+) a-Si:H	2 min	2 min	2 min	2 min
Deposition time (p++) a-Si:H	3 min	3 min	3 min	3 min

Overall thickness measured on planar Si ($d_{\text{a-Si:H}}$)	28 nm	32 nm	36 nm	40 nm
V_{oc} (V)	0.44	0.53	0.51	0.504
J_{sc} (mA/cm ²)	28.58	29.27	28.1	28.96
FF (%)	74.29	81.05	68.95	70.13
η (%)	9.34	12.43	9.82	10.24

The (i) a-Si:H layer is used for surface passivation. Indeed, it has been proven that the insertion of a thin intrinsic layer of a-Si:H improves drastically the performances of heterojunction solar cells. The thickness of the (i) a-Si:H layer has to be carefully tuned to ensure both low electrical resistance and uniform passivation. When the thickness of the (i) a-Si:H layer is too small (for example, sample I, which an equivalent 8 nm of (i) a-Si:H layer on planar Si), we are not able to achieve good V_{oc} . On the other hand, V_{oc} above 0.5V is obtained for solar cells with an (i) a-Si:H deposition time longer than 2 min. Indeed SiNWs have a high aspect ratio structure with a significant surface ratio compared to their planar reference counterparts. Therefore a thicker (i) a-Si:H is required to passivate uniformly all the SiNWs' surface. The increase in V_{oc} with increasing thickness of (i) a-Si:H indicates reduced surface recombination at c-Si / (p) a-Si:H interface. We observe an optimum V_{oc} and FF at 3 min (i) a-Si:H deposition time. A thicker (i) a-Si:H layer may also impact the charge carrier transport. Indeed as the conductivity of (i) a-Si:H layer is low, a thicker (i) a-Si:H will reduce the V_{oc} . The FF appears to be strongly dependent on the thickness of the (i) a-Si:H. Tunneling or hopping hole transport are becoming more unlikely with increasing thickness of (i) a-Si:H, which can explain the decrease in FF for samples J and K. As for J_{sc} , there is no clear trend with increasing thickness of (i) a-Si:H. **Figure 6-12** shows the EQE curves of the HIT SiNWs based solar cells with increasing (i) a-Si:H thickness. The thickness of the (i) a-Si:H seems to be a critical parameter as the EQE response is impacted over the entire spectral range by the thickness, and not only in the short wavelength region. The main trend is a decrease of the EQE response in the short wavelength region with increasing thickness. As for the EQE response for $\lambda > 700$ nm, we observe that the EQE response increases from $d_{\text{(i) a-Si:H}} = 8$ nm to $d_{\text{(i) a-Si:H}} = 12$ nm and then decreases from $d_{\text{(i) a-Si:H}} > 16$ nm. Therefore the

thickness of (i) a-Si:H has to be optimized to ensure a good balance to achieve both uniform passivation and low electrical resistance.

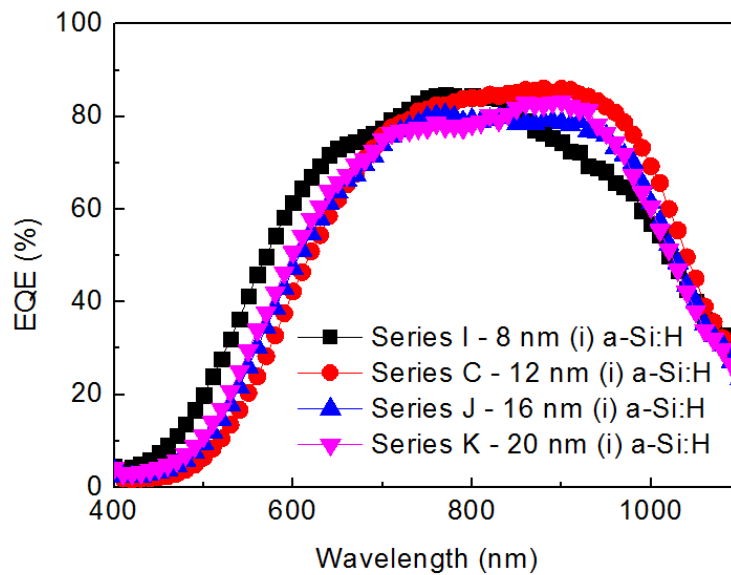


Figure 6-12: Effect of the (i) a-Si:H thickness on the EQE of HIT solar cells based on SiNWs.

6.2.3 Effect of SiNW length

The effect of SiNW length on the performance of SiNW based HIT devices is next investigated. **Table 6-5** shows the current density-voltage $J(V)$ characteristics of HIT solar cells with SiNWs length (L) of 800 nm, 1.5 μm and 10 μm , measured under 100 mW/cm^2 illumination (AM 1.5G). Cells were co-deposited in the same chamber with $d_{\text{a-Si:H}} = 28$ nm. The V_{oc} for all the cells are lower than the highest value obtained for the reference planar cell of 0.58 V. We should note that the reference planar cells were co-deposited in the same chamber as SiNW samples and naturally the deposition conditions are not optimal for them. From **Table 6-5**, the V_{oc} and FF are observed to decrease with L , attributed to the fact that it is harder to properly passivate the longer wires. This is also corroborated by the EQE measurements shown in **Figure 6-13 (a)**, where the blue response weakens with increasing L , indicating that more recombination occurs at the front part of the cells where the NWs are located. Indeed longer SiNWs result in larger surface area, which means the presence of more defects and correspondingly a higher recombination rate. Interestingly the overall EQE response for $700 \text{ nm} < \lambda < 1000 \text{ nm}$ increases for SiNWs with

intermediate lengths of 800 nm and 1.5 μm . Such improvement is explained by the enhanced light trapping capability of longer SiNWs in combination with a proper surface passivation by a-Si:H. Higher EQE response in the long wavelength regime for 1.5 μm SiNWs shows that the improvement in light trapping in longer SiNWs overcomes the losses due to higher recombination. This increase in EQE is nevertheless not observed for very long SiNWs ($L= 10 \mu\text{m}$) despite the fact that longer SiNWs have better light harvesting properties, as confirmed by the total reflectance presented in **Figure 6-13 (b)**, which was measured using a UV/Vis/NIR PE LAMBDA 750 spectrophotometer with an integrating sphere. This figure shows that SiNWs exhibit very low reflectance from the visible to near infrared range, and the reflectance reduces with SiNW length. Therefore the reduction in EQE for very long SiNWs can be explained by the fact that enhanced light trapping offered by very long SiNWs cannot counterbalance the very high recombination rate due to an insufficient surface passivation. It is also possible that such very high aspect ratio structure prevents the formation of the junction at the bottom of the NWs, which is also supported by the low V_{oc} of the cells with 10 μm long NWs (see **Table 6-5**). Likewise ITO may not reach the bottom of the wires and therefore the quality of the contacts might be degraded [243]. In **Figure 6-13 (a)**, no significant difference in EQE is observed for $\lambda > 1000 \text{ nm}$ since the longer wavelength light is absorbed deep in the substrate and hence is not much affected by the SiNWs length.

Table 6-5: Dependence of the photovoltaic parameters J_{sc} , FF , V_{oc} and η on the length of SiNWs.

Length of SiNWs	V_{oc} (V)	J_{sc} (mA/cm²)	FF (%)	η (%)
planar	0.58	29.4	60.2	10.25
0.8 μm	0.49	28.9	69.2	9.69
1.5 μm	0.37	26.59	42.33	4.16
10 μm	0.28	8.38	36.62	0.85

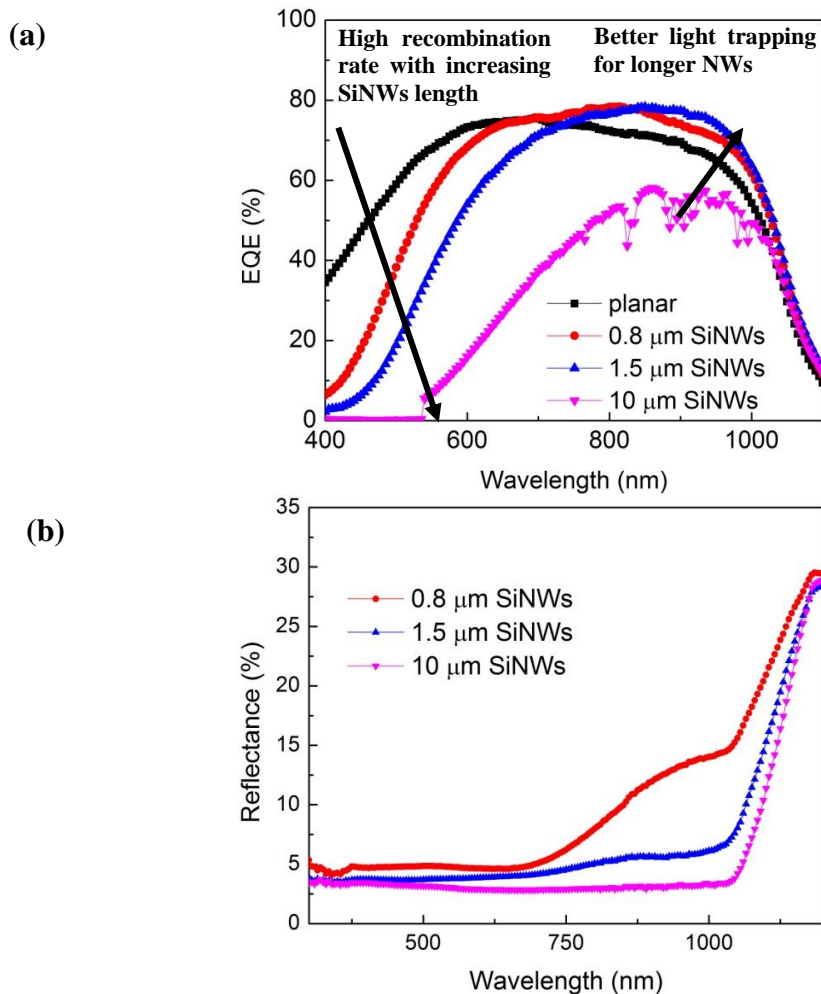


Figure 6-13: Effects of the SiNWs length on the (a) EQE and (b) reflectance of the cells.

The decrease in efficiency of HIT SiNW based solar cells with increasing SiNW length can be correlated with the TRMC signal measured on samples with different L . Indeed, for longer SiNWs the signal is weaker and the decay is much faster, indicating a decreasing carrier lifetime with increasing L as illustrated in **Figure 6-14**. We were able to fit the TRMC signals with an exponential decay with good accuracy ($\chi^2 > 0.998$ with χ^2 being the fitting error of the experimental curve by the theoretical model). To fit the experimental decay, we used Eq. (3.8). We found effective lifetimes of 12 μs , 11 μs and 6.9 μs for SiNW length of 300 nm, 500 nm and 1.5 μm , respectively. For 10 μm long SiNWs, we were unable to fit the data as the signal was too weak. For comparison, we have obtained a lifetime in the order of a millisecond for the reference planar cells. Similar to the case of SiNW HIT cells with different a-Si:H thickness, we therefore conclude that for all SiNW lengths the performance is limited by surface recombination.

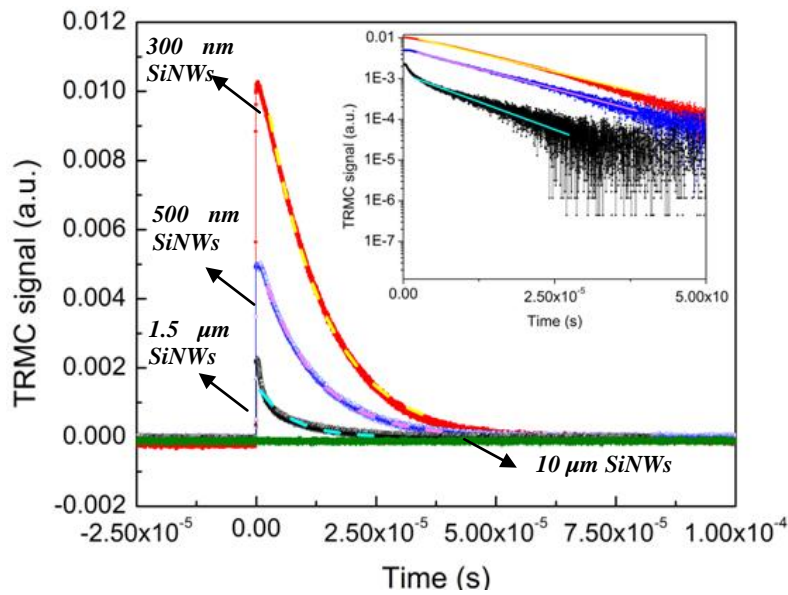
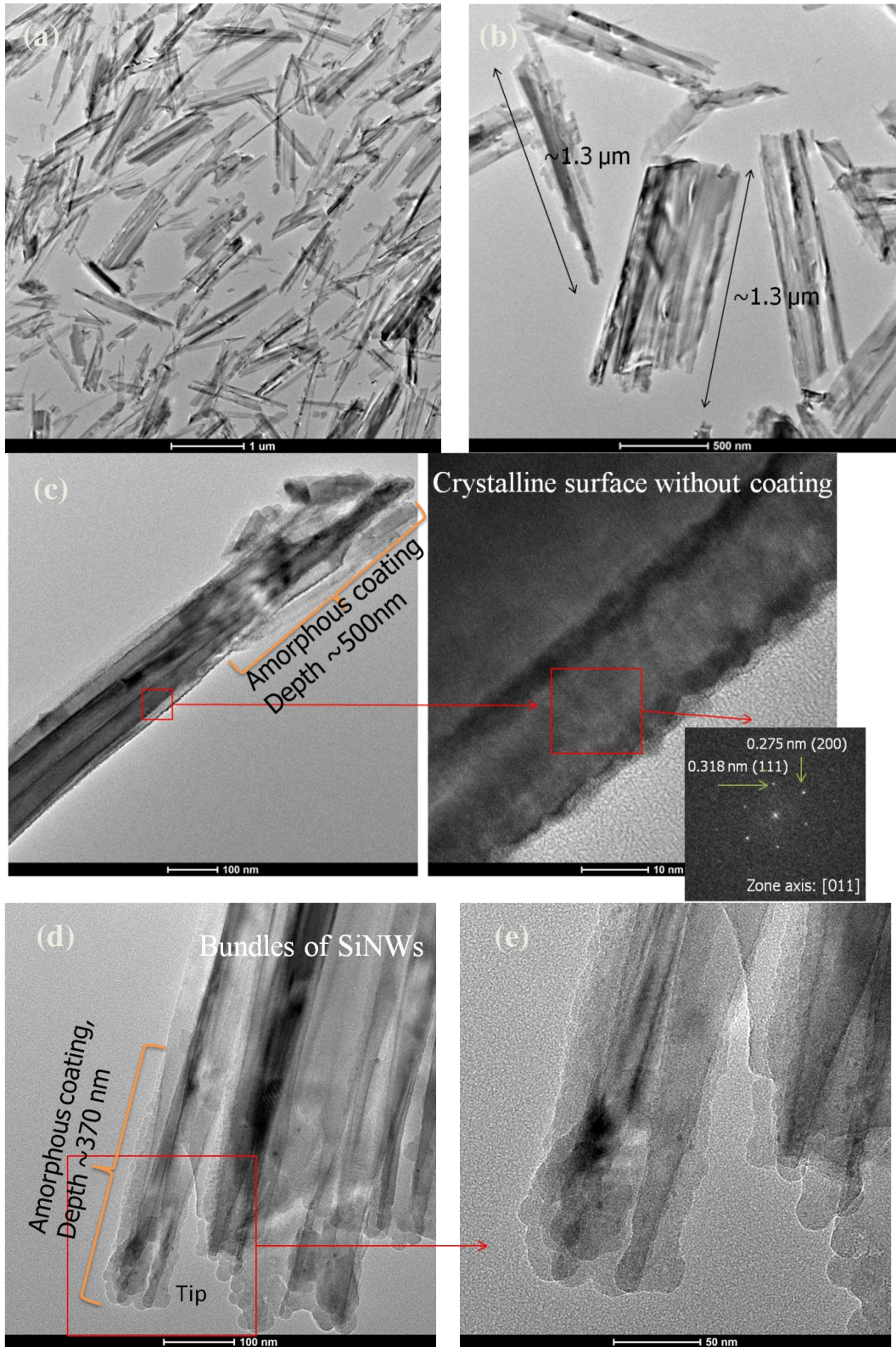


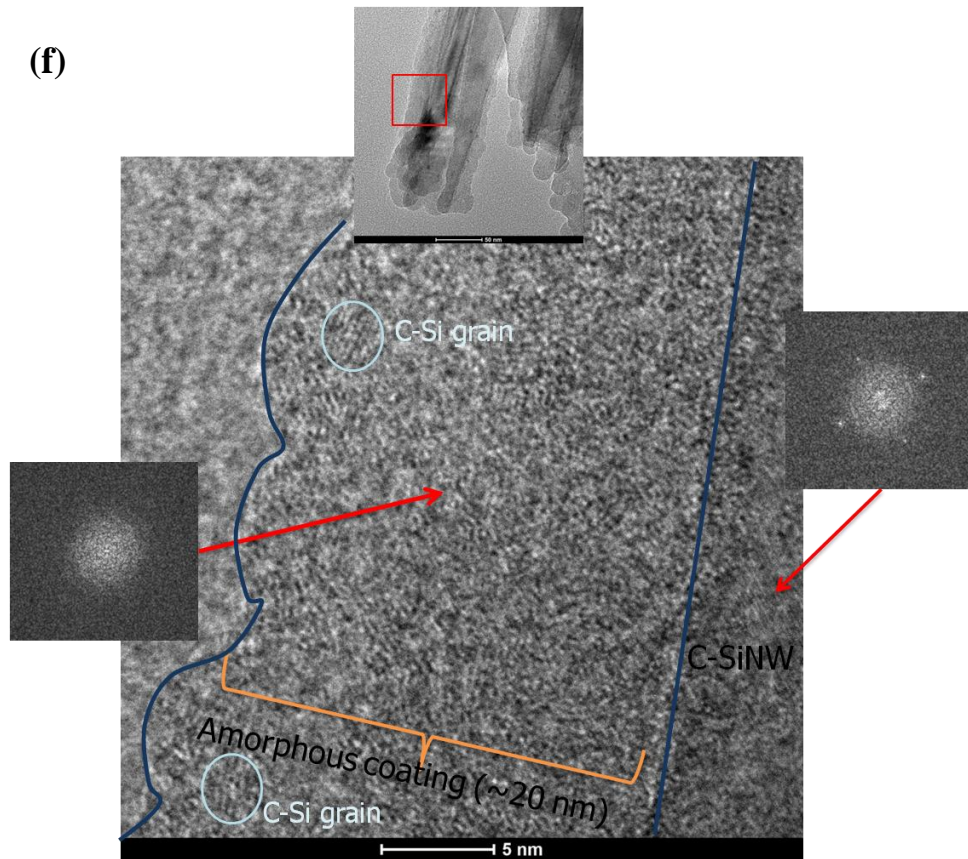
Figure 6-14: TRMC signal as a function of time for samples with different SiNW lengths.

6.2.4 TEM analysis

The coating of the disordered SiNWs by amorphous silicon was further analyzed by Transmission Electron Microscopy (TEM). TEM analysis were realized by Ms Yang Yi from DSI, Singapore. The high density of the SiNWs together with their strong agglomeration make the observation of a single SiNW challenging, as shown in **Figure 6-15 (a) and (b)**. Here SiNWs with a length of 1.3 μm fabricated by the standard MACE process are analyzed. The coating by amorphous silicon is not covering all the surface of SiNWs and the coating depth (distance from the top of SiNWs where we can observe a-Si:H coating on the surface of the SiNWs) is between 300 to 500 nm, which also explains why cells with shorter SiNWs below 500 nm perform better. Therefore, for long SiNWs, only the top part of the wire is covered by a-Si:H (**Figure 6-15 (c), (d) and (e)**). **Figure 6-15 (c)** shows TEM picture along with diffraction pattern of a SiNW not covered by a-Si:H (near the bottom part of the wire) confirming its crystallinity. The coverage of the SiNWs by a-Si:H is observed at the top part of the SiNWs, 300 to 500 nm down from the tip. The coating thickness is between 20 to 30 nm with the maximum thickness measured around the tip, which corresponds to the thickness that we have deposited by PECVD. The coating is dominated by amorphous phase but

occasionally Si nanocrystals with a size of about 4-5 nm can be observed as shown in **Figure 6-15 (f)** and **Figure 6-15 (g)**. The diffraction pattern of the coating confirms its amorphous phase. The diffraction pattern "of the wire part" includes a crystalline and amorphous phase which is explained by the superposition of the amorphous coating on the crystalline SiNW.





(g) *Nanosize Si crystals can be observed*

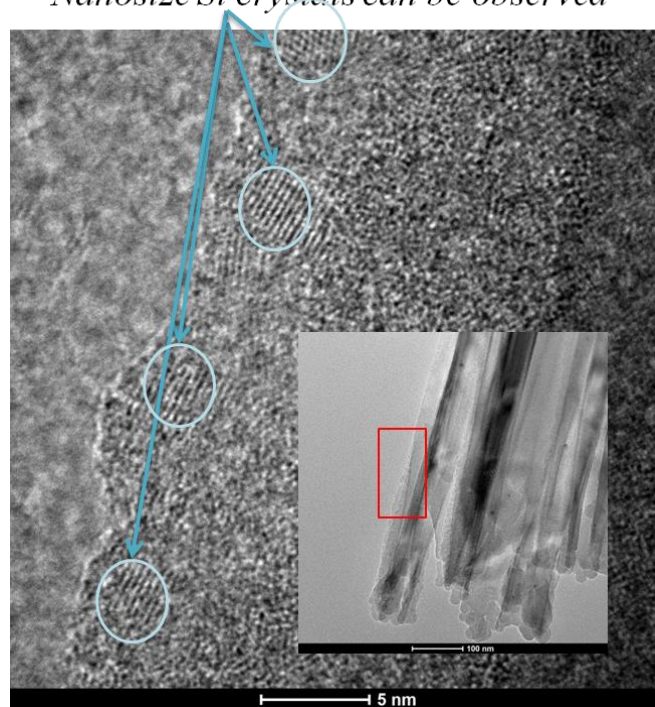


Figure 6-15: TEM analysis of disordered SiNWs. SiNWs agglomerate (a) and (b). Only the tip of the wire is covered by a-Si:H and the coating depth by a-Si:H is between 370- 500 nm (c), (d) and (e). Small crystal grains can be found within the amorphous coating (f) and (g).

6.2.5 Electron Beam Induced Current (EBIC) microscopy

As SiNW based HIT devices show reduced performances compared to their reference counterparts, a legitimate question arises: are SiNWs really contributing to the generated current, i.e. are SiNWs electrically active? To answer this question, SiNW based solar cells were characterized by the electron beam induced current (EBIC) technique [170]. The electron beam focused in a less than 10 nm^2 spot scans the sample surface while building the SEM image and measuring the induced current at each point giving the corresponding EBIC map. Note that the volume of excitation is much bigger than the beam size, even for low acceleration voltages. The influence of the electron beam energy was first investigated. **Figure 6-16** shows EBIC mappings of the cross-section of a HIT solar cell based on sample C (see **Table 6-1**), at different acceleration voltages of 3 keV (a), 5 keV (b) and 10 keV (c). We have used the software Casino [244] to estimate the excitation volume for different acceleration voltages. Our simulation shows that the excitation volume is a sphere with its center close to the surface, and sphere radius increases with the electron beam energy from 60 nm at 3 keV to 300 nm at 5 keV and finally to 1 μm at 10 keV. The dimensions of the excitation volume, calculated from modeling, are displayed in the inset of **Figure 6-16**. At low acceleration voltage, the signal from SiNWs is small and the EBIC mapping is slightly distorted because of charging effects that cause the image to drift as shown in **Figure 6-16 (a)**. The EBIC signal increases at higher acceleration voltage. The maximal EBIC signal is generated in the c-Si wafer, close to the SiNWs /substrate interface.

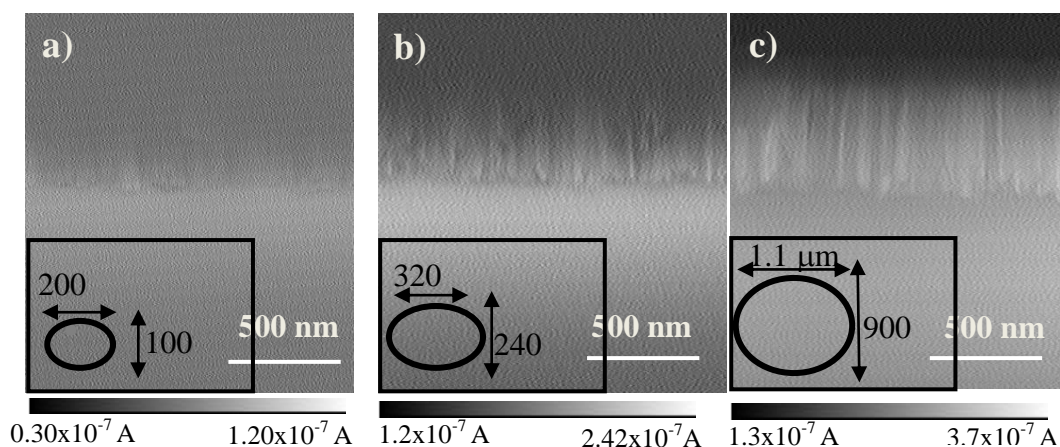


Figure 6-16: EBIC mapping of the HIT SiNW cross-section under various accelerating voltages (a) 3 keV, (b) 5 keV and (c) 10 keV.

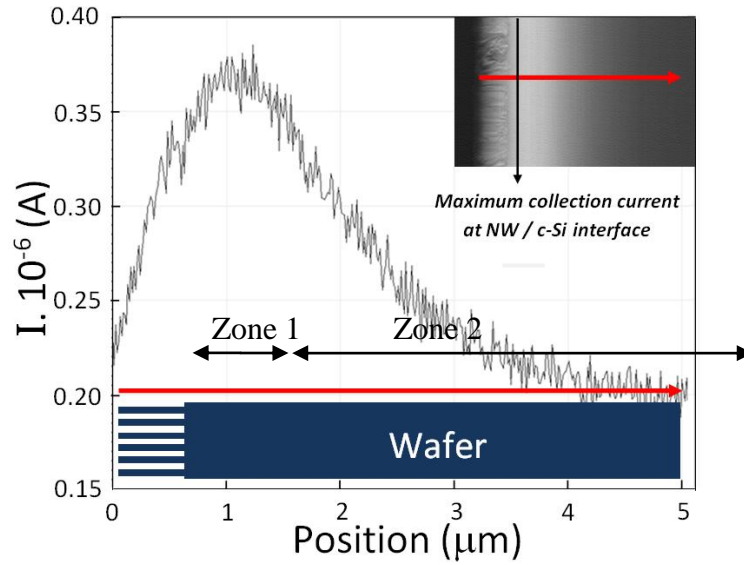


Figure 6-17: EBIC current profile at 10 keV as a function of position of the beam on the sample C with the corresponding EBIC mapping in the inset. The red arrow in the inset indicates the corresponding signal position on the sample. A cross-section schematic of the structure is displayed at the bottom.

Figure 6-17 shows a typical EBIC signal profile measured on the cross-section of a HIT solar cell based on disordered SiNWs (sample C) when the electron beam scans the sample from the top of the wires down into the substrate. The red arrow in the inset indicates the corresponding position on the sample where the EBIC profile has been extracted. The EBIC signal is the highest when the electron beam impinges the c-Si wafer at about 100 nm from the SiNW/c-Si interface, and it decays as the excitation moves further away from the interface, towards the nanowires or the bulk wafer. The e-beam current I_{ebic} and the diffusion length L are expected to follow the relationship given by Ioannou and Dimitriadis [245]:

$$I_{ebic} = \frac{A \exp\left(\frac{-x}{L}\right)}{x^{3/2}} \quad 6.4$$

where A is a constant, L is the diffusion length and x is the distance between the junction and the electron beam.

By plotting:

$$y = \ln(x^{3/2} I_{ebic}) \quad 6.5$$

as a function of x , we obtain a straight line and the diffusion length L can be extracted from the slope that is equal equal to $1/L$.

The data from zone 2, i.e. the silicon substrate, is plotted in **Figure 6-17** and compared with Eq. 5.5 in **Figure 6-18**. A good agreement between the fitted theoretical and experimental results is observed, with $\chi^2 > 0.995$. From this adjustment, we obtained an effective diffusion length of 3 μm .

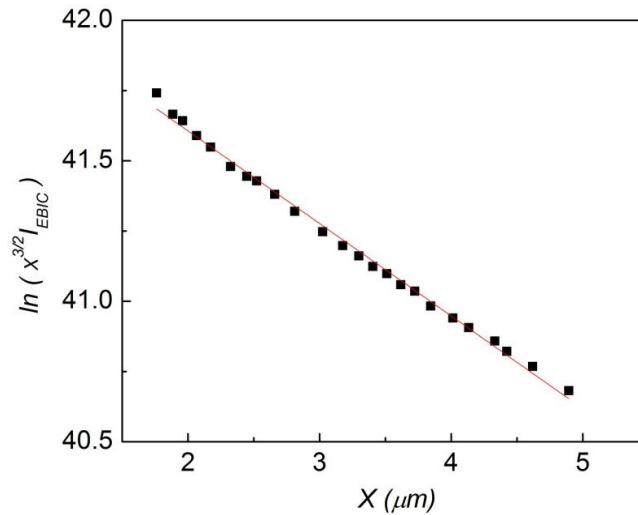


Figure 6-18: Equation (4) as a function of x , the distance from the junction, obtained from experimental data of zone 2 in Figure 6-17.

The SiNWs are covered with ITO to collect the current in the EBIC set up. However, even a thin ITO layer reflects and absorbs a non-negligible amount of impinging electrons and therefore has an impact on the EBIC measurements that we need to consider when analyzing the results. The effect of ITO on the EBIC signal is shown in **Figure 6-19 (a), (b) and (c)**. **Figure 6-19** shows a high magnification cross-section SEM image of a 500 nm long NWs (a) and the corresponding EBIC mapping image at 10 keV (b), the beam being perpendicular to the axis of the nanowires. The SiNW is partially covered by a 200 nm thick layer of ITO which acts as an electron barrier layer and reduces the signal intensity generated by the SiNWs since a darker contrast is observed in the zone covered by ITO. This is not the case for the bare bulk underlying wafer as we can observe in **Figure 6-19 (b)**. The reduction of the signal due to the presence of the ITO layer is clearly observed in **Figure 6-19 (c)**, where the wafer and the bottom of the SiNW, which is not covered with ITO have similar intensities while a decrease in the signal is observed on the portion of the SiNW covered by ITO.

To confirm these observations, we have estimated the volume of excitation at 10 keV for a planar silicon substrate and a planar silicon substrates covered by 100 nm and 200 nm of ITO by the Casino software. As shown in **Figure 6-20**, the excitation volume increases with reducing ITO thickness. The penetration depth inside a bare silicon substrate is about 900 nm, which is reduced to 550 nm and 350 nm in the presence of 100 nm and 200 nm thick ITO film respectively, inclusive of the ITO thickness. As mentioned earlier, the ITO coating is not uniform over the wires, as shown in **Figure 6-3 (b)** and **Figure 6-7 (c)**. Indeed, the ITO coating appears as a bump on the top of SiNWs whose thickness reduces along their length. This is due to the difficulty in coating conformally high aspect ratio SiNWs by sputtered ITO. Therefore the effect of ITO on the measured data might be more prominent at the top of the NWs where the ITO thickness is larger. In conclusion the EBIC current generated by the SiNWs is underestimated because of their ITO coating.

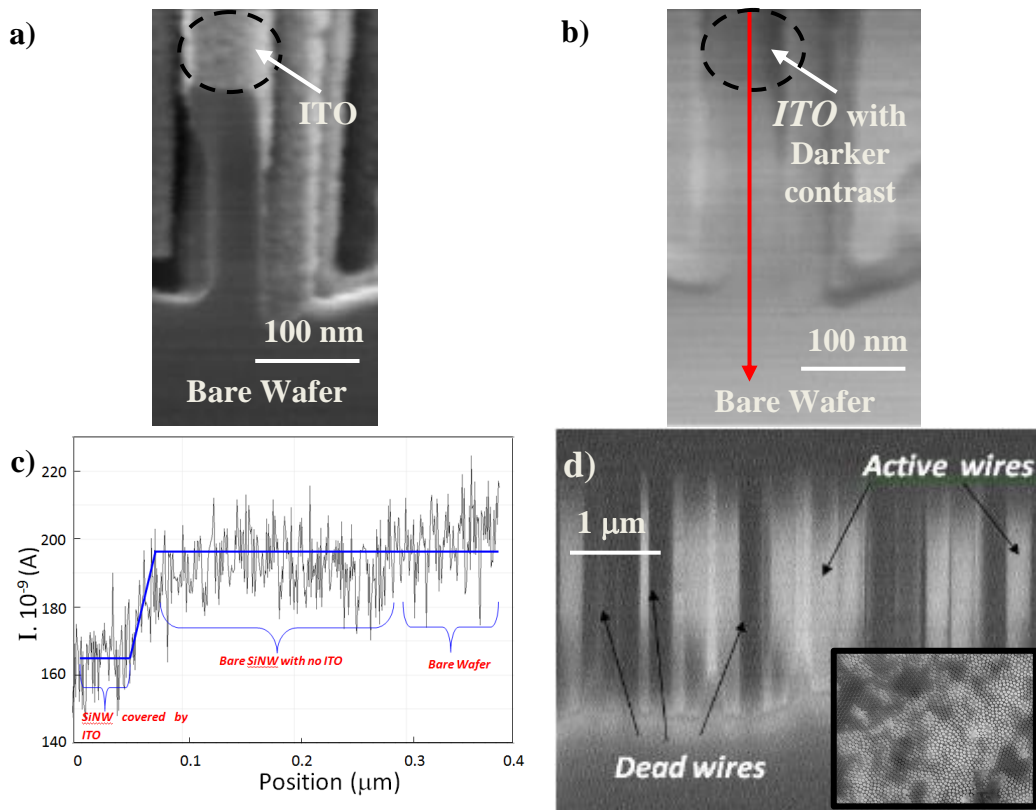


Figure 6-19: (a) Cross-section SEM image of the bottom of a SiNW partially covered by ITO and (b) corresponding EBIC mapping with the red arrow indicating the corresponding signal position on the sample and (c) the corresponding EBIC current profile at 10 keV as a function of the position of the beam on the sample. (d) Cross-section EBIC mapping of samples with “dead” and electrically active SiNWs. The inset shows the EBIC top-view mapping confirming that only few nanowires are active.

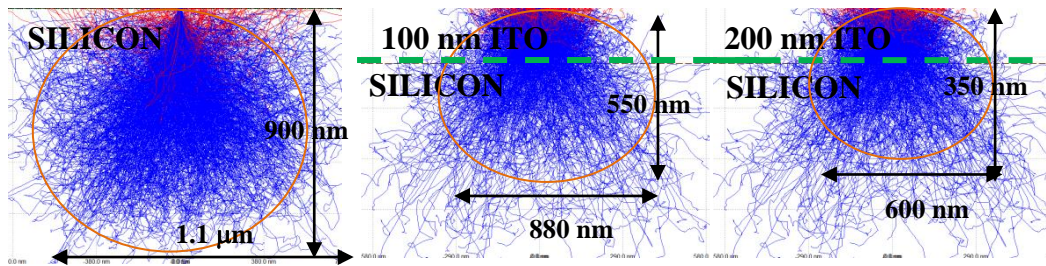


Figure 6-20: Modeling of the volume of excitation produced by a 10 keV electron beam impinging on a 550 μm c-Si substrate with (a) no ITO, (b) 100 nm of ITO and (c) 200 nm of ITO.

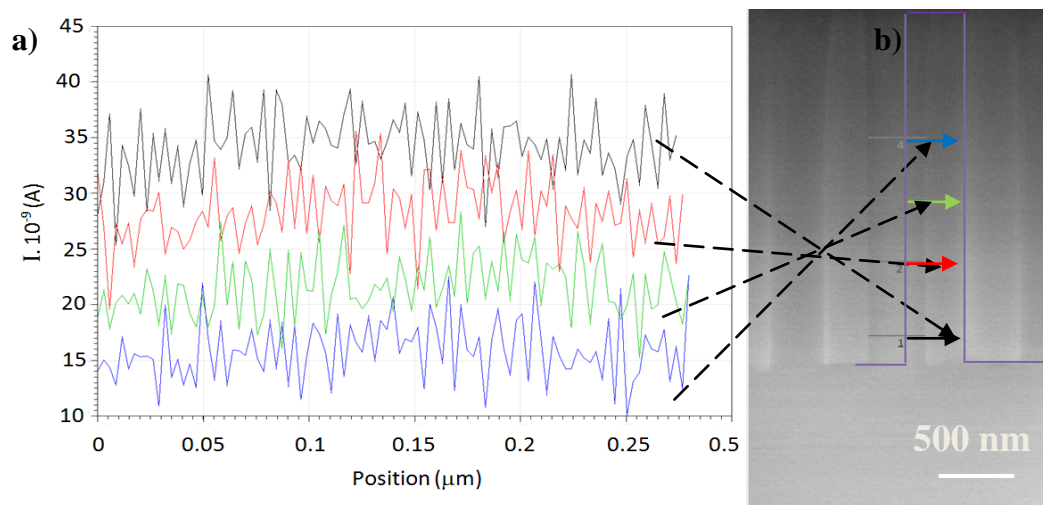


Figure 6-21: EBIC current profiles (a) and cross-section EBIC current mapping (b). The 4 different arrows indicate the localization of the different EBIC profiles measured on the sample.

A noteworthy observation is the confirmation of the electrical activity of SiNWs, as assessed by the EBIC current profile, although the SiNWs are generating less current than the underlying bulk wafer. Indeed, for comparison an EBIC mapping of a solar cell, whose SiNWs have undergone a thermal oxidation treatment, is displayed in **Figure 6-19 (c)**. More details on the fabrication and effects of this process can be found in section **6.3.6** of this thesis. This solar cell reveals “dead” SiNWs (e.g not electrically active with dark contrast) and active SiNWs (bright contrast) while for our standard SiNWs solar cells, we observe bright contrast for all the SiNWs and the EBIC signal is uniform over the entire sample.

The nanoscale resolution provided by the EBIC measurements allows us to further analyze the carrier collection along the radial direction. This is

illustrated in **Figure 6-21** showing the EBIC mapping at 10 keV of a long single nanowire of about 2 μm length. We can observe that the signal decreases in the axial direction towards the SiNW top, which means that the SiNW top part is contributing less to the current than its bottom part and leads to a reduction in efficiency.

Overall, we observe that the SiNWs can generate and separate carriers, but are less effective than the underlying bulk wafer. Moreover, the EBIC signal is very uniform for SiNWs over the entire sample and therefore every SiNW is contributing equally to the total generated current.

6.2.6 Transfer of the SiNWs based HIT solar cells concept to the thin film technology

As mentioned previously, the final objective of incorporating SiNWs into HIT devices is to use thinner Si wafers. With this objective in mind, we have fabricated HIT devices based on SiNWs prepared on a 5 μm thick commercial epitaxial silicon layer. The characteristics of the epitaxial thin film are as follows: thickness of 5 μm (+/- 0.5 μm), n-type doping (2-4 $\Omega\cdot\text{cm}$) and grown on a highly doped n-type silicon wafer (0.001-0.005 $\Omega\cdot\text{cm}$).

With a doping concentration in the order of $1 \times 10^{20} \text{ cm}^{-3}$, the minority carrier diffusion length in the highly doped n-type substrate is less than 0.3 μm [246]. Therefore the n++ substrate is acting as a conducting contact and its contribution to the photocurrent can be neglected. Hence, we can use this sample to simulate a silicon thin film with an effective absorbing thickness of 5 μm . This assumption is confirmed by the cross-section EBIC picture of the solar cell device as shown in **Figure 6-22**, where we can clearly see that the highly doped wafer does not significantly contribute to the current and that only the epitaxial film is electrically active. These experiments provide a proof of concept to establish the feasibility of using thin film technology for HIT solar cells based on SiNWs. The SiNWs used for the purpose of this experiment have a length of 500 nm. Planar cells based on the 5 μm Si epitaxial films were also fabricated in parallel to serve as a reference. Twenty one SiNWs cells and twenty one planar cells were fabricated for this experiment.

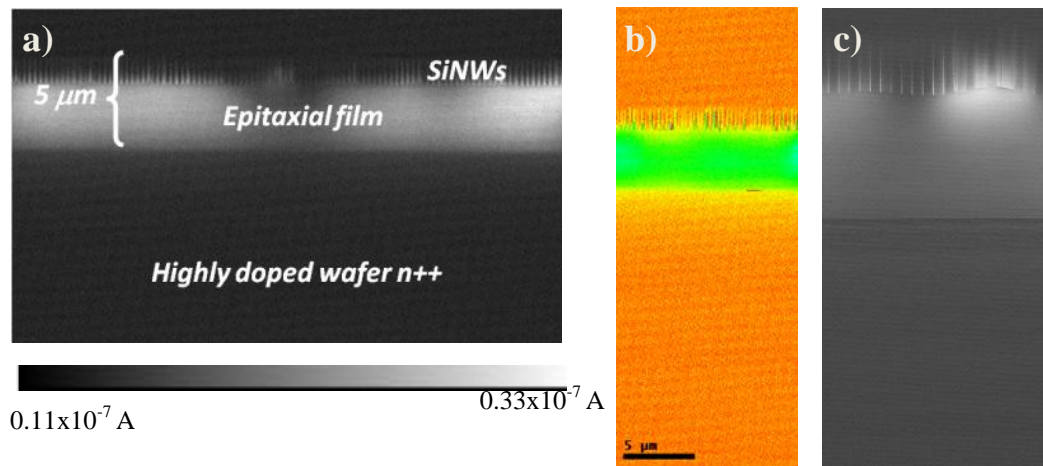


Figure 6-22: EBIC mapping of SiNW solar cells based on 5 μm epitaxial film with low magnification in (a) grey and (b) rainbow magnification and (c) high magnification .

Figure 6-23 (a) shows the $J(V)$ curves of the reference planar and SiNW based HIT devices fabricated on a 5 μm Si absorbing layer under 100 mW/cm^2 illumination (AM 1.5G). The average photovoltaic parameters of J_{sc} , V_{oc} , FF , and PCE are summarized in **Table 6-6**. Despite the gain due to light trapping in the near-IR, the efficiency of the SiNWs cells is lower than that of the planar counterpart, due to a sharp drop in V_{oc} , as well as a significant drop in J_{sc} . This is mainly induced by the high recombination rate at the SiNWs surface in the front part of the cell, as confirmed by the EQE measurements shown in **Figure 6-23 (b)**. Interestingly, the FF is higher for the SiNW cells. The PCE of our cells are limited by their low J_{sc} which we can attribute to the insufficient light absorption for the 5 μm thin film. Moreover there is almost no reflection between the epitaxial film and the supporting bulk wafer, which limits light trapping capabilities within the epitaxial film. To improve the performances of such devices, a thicker epitaxial film can be used. We can also consider transferring this device to a substrate which is either textured or is acting as a back reflector in order to promote light absorption within the thin film.

Table 6-6: Photovoltaic parameters for reference planar cells and SiNWs based solar cells on 5 μm epitaxial layer.

Solar cells	V_{oc} (V)	J_{sc} (mA/cm^2)	FF (%)	η (%)
Reference planar cell	0.63	18.4	70.2	8.06
500 nm SiNWs cell	0.512	12.4	74.8	4.74

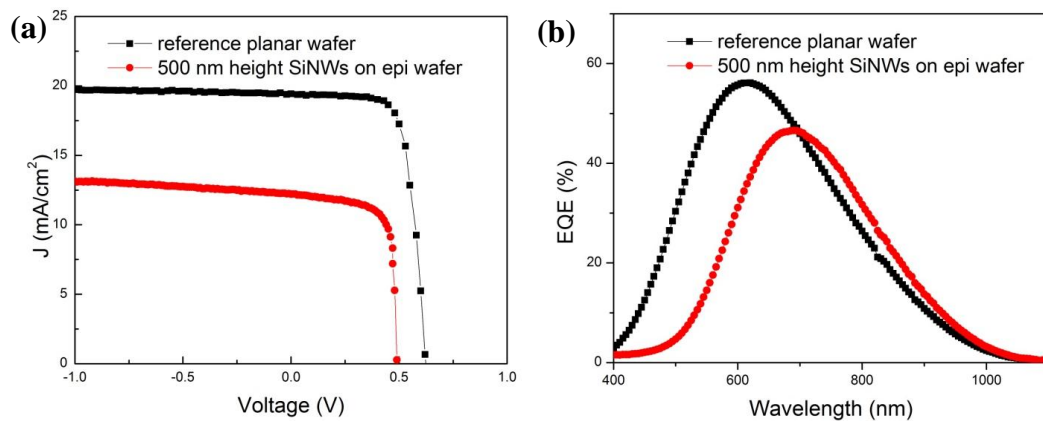


Figure 6-23: EQE (a) and (I,V) (b) curves of reference planar cell and SiNWs based solar cells on 5 μm Si epitaxial thin film.

6.3 Comparison between Ordered and Disordered SiNWs

6.3.1 Morphology of core-shell HIT solar cells based on ordered SiNWs

As mentioned in Chapter 3, we have fabricated two types of SiNWs: random and ordered arrays. The motivation to work on ordered SiNWs arrays was to achieve a proper passivation of the SiNWs surface. Indeed, SiNWs fabricated by the standard MACE process are really dense. SiNWs are packed very close to each other, which may prevent the proper deposition of a-Si:H at the bottom of the wires. Therefore these NWs represent a major challenge for a proper surface passivation. In this work, we couple low-cost nanosphere lithography with MACE in order to achieve highly ordered SiNW arrays with various geometries (in terms of pitch, length, and diameter) which allow the control of the space between the SiNWs. Ordered SiNW arrays are promising candidates for HIT devices as the passivation might be easier since the space between the NWs can be adapted to the passivation scheme. Therefore we have fabricated a large set of ordered SiNWs arrays which were subsequently used for HIT devices. **Figure 6-24** shows the SEM pictures of HIT solar cells based on ordered arrays of SiNWs after the deposition of the amorphous layer. We can clearly identify a-Si:H on the top of the wires while we were unable to observe it on the SEM cross-section image.

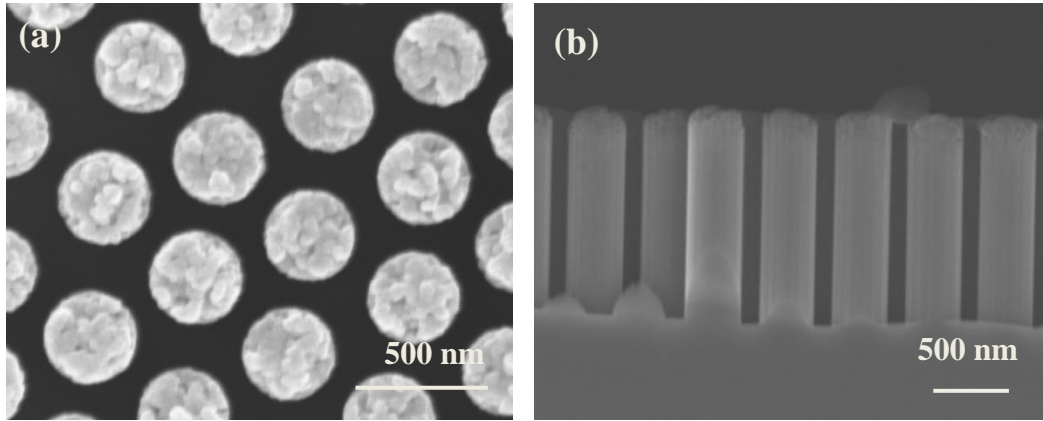


Figure 6-24: SEM picture of ordered arrays of SiNWs (pitch 550 nm, diameter of 345 nm , length of 1.2 μm) after a-Si:H deposition and before ITO deposition (a) top-view (b) cross-section

We also show the effect of ITO deposition on ordered arrays of SiNWs. We already observed the non-conformity of the ITO deposition on disorder SiNWs. The almost perfect geometry of the array of SiNWs fabricated by MACE assisted by nanosphere lithography allows us to study more accurately the morphological changes of the SiNW array with increasing thickness of ITO. **Figure 6-25** shows top-view (a), (b), (c) and (d) and cross-section view (e) of an array of SiNWs coated with different thicknesses of ITO. In **Figure 6-25 (e)**, we have placed on top of each other the cross-section SEM image of the same SiNW with different thicknesses of ITO to follow more accurately the morphological changes induced by increasing thickness of ITO. The coverage by ITO is not uniform for ordered SiNWs: large bumps are observed at the top of the SiNWs as shown in **Figure 6-25 (e)** while the thickness of ITO decreases from the top to the bottom of the wire. For thicker layers of ITO, tops of the SiNWs touch each other as we can observe from the top-view image of the arrays covered by 100 nm of ITO (see **Figure 6-25 (d)**).

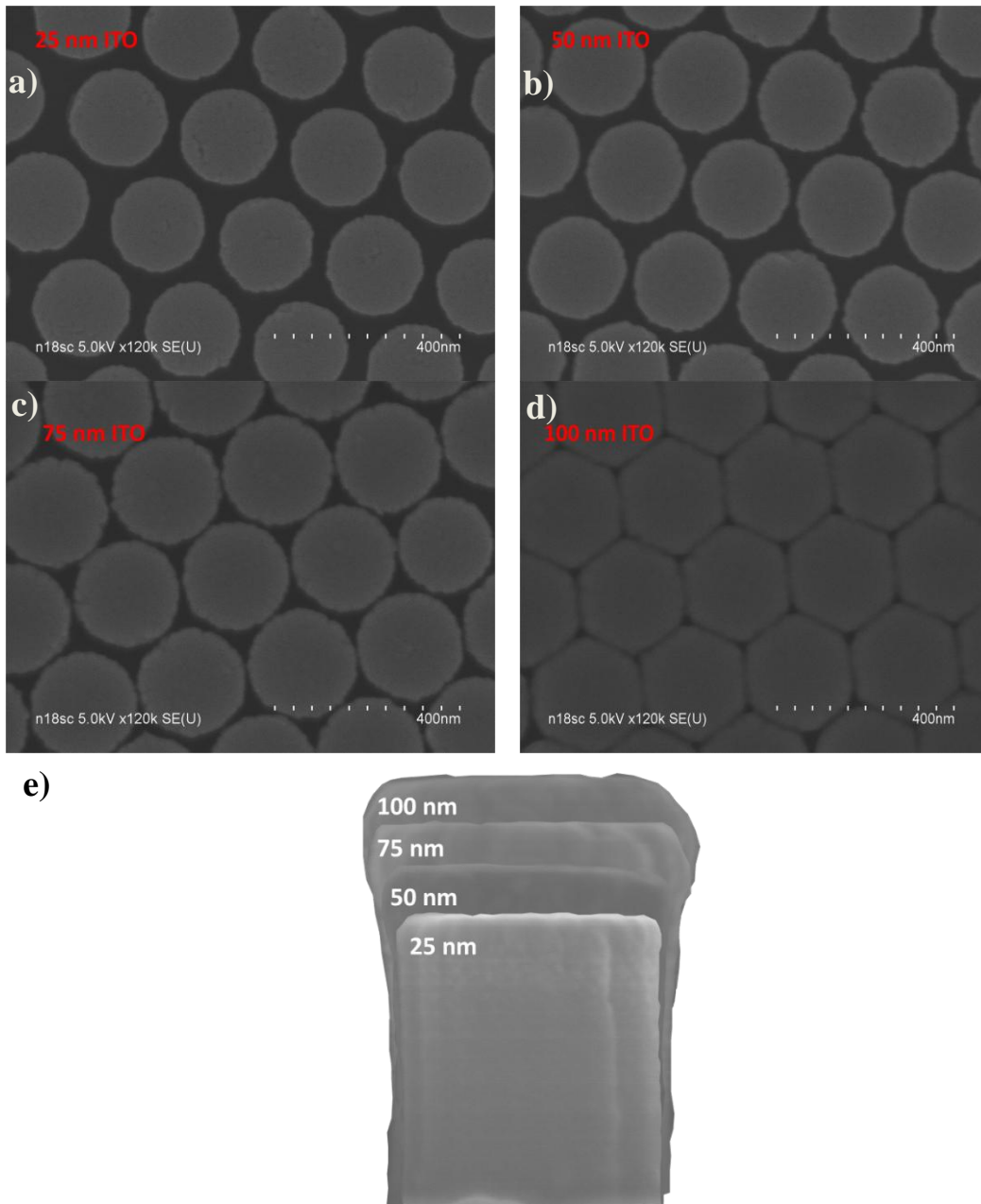


Figure 6-25: Top-view SEM image of ordered arrays of SiNWs covered with a thickness of ITO of (a) 25 nm, (b) 50 nm, (c) 75 nm and (d) 100 nm. (e) shows the cross-section of a single SiNW with various thicknesses of ITO.

6.3.2 Solar cells performance of core-shell HIT solar cells based on ordered SiNWs

We have fabricated a large number of solar cells based on these ordered SiNW arrays. However, the efficiency of such devices is systematically lower than that of devices based on random SiNWs. Irrespective of the thickness of amorphous silicon used, the V_{oc} does not exceed 0.38V in the best case. **Table 6-7** summarizes the average performances obtained for different geometry of

SiNWs arrays. We detail the type of substrate used, the pitch, length and diameter of the SiNWs as well as the thickness of a-Si:H deposition. These results are measured for at least 6 solar cells of each type of device.

Table 6-7: Summary of geometrical characteristics of SiNW arrays and average value of V_{oc} , J_{sc} , FF and η of corresponding core-shell heterojunction solar cells.

Substrate N-type	1-3	1-3	5 μm	5 μm	1-3	1-3
	$\Omega.\text{cm}$	$\Omega.\text{cm}$	Epi 2-4 $\Omega.\text{cm}$	Epi 2-4 $\Omega.\text{cm}$	$\Omega.\text{cm}$	$\Omega.\text{cm}$
Pitch (nm)	550	550	550	550	240	330
Diameter (nm)	300	300	300	300	180	240
Length (nm)	500	500	500	500	250	1700
$d_{\text{a-Si/H}}$ (nm)	14	18	14	18	32	36
V_{oc} (V)	0.33	0.36	0.3	0.32	0,27	0.32
J_{sc} (mA/cm²)	29.49	31.14	17.53	16.65	29,11	20.81
FF (%)	41.44	47	39.94	40.74	40,75	63.93
η (%)	4.02	5.3	2.15	2.27	3.24	4.3

HIT solar cells based on ordered SiNW arrays are characterized by their poor FF and their extremely low V_{oc} compared to those based on random SiNWs with V_{oc} of up to 0.53 V. However, their J_{sc} shows better performance than their random counterparts, with 31 and 32.6 mA/cm² achieved for 500 nm long ordered SiNWs. This is confirmed by the EQE measurements shown in **Figure 6-26**, where we compare the EQE response between a reference planar cell, and cells with 500 nm disordered SiNWs and 500 nm ordered SiNWs. These cells were co-deposited in the same reactor chamber. The thickness of the a-Si:H coating is about 14 nm. We observe that ordered SiNWs have a high EQE response over the entire spectral range. There is no significant drop in the EQE response in the short wavelength range as we generally observed for disordered SiNWs. While the EQE response of ordered SiNWs arrays is very similar to that of the reference planar cell in the short wavelength range, it is drastically improved in the long wavelength range, similar to that observed for cell with random SiNWs.

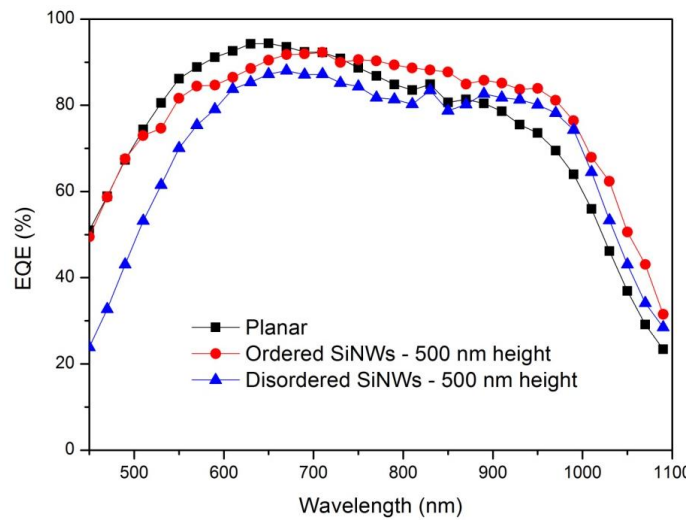


Figure 6-26: Comparison of EQE response for different C-Si substrates: reference planar cells, ordered SiNW arrays cells, disordered SiNW arrays cells.

Likewise, ordered SiNWs performed much better than random SiNWs in terms of J_{sc} for HIT solar cells based on epitaxial Si thin film of 5 μm . Indeed, in section 6.2.6, we show that the J_{sc} of a HIT solar cells based on epitaxial film decreases from 18.4 mA/cm^2 for a reference planar cell to 12.4 mA/cm^2 for disordered SiNWs cell. We do not observe this significant drop for ordered SiNWs cell, whose J_{sc} is very similar to that of planar solar cells, as shown in the EQE response in Figure 6-27. Ordered SiNWs improve the EQE response for $\lambda > 750 \text{ nm}$ compared to planar cells.

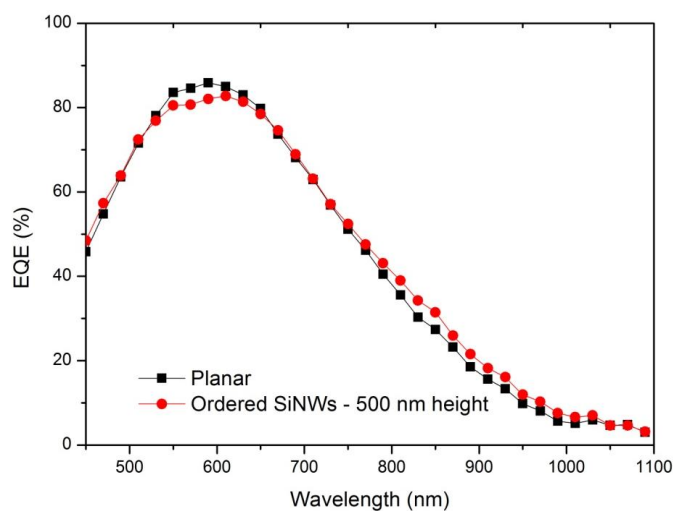


Figure 6-27: Comparison of EQE response for different epitaxial c-Si substrates: reference planar cells, ordered SiNW arrays cells, disordered SiNW arrays cells.

We believe that these poor performance for HIT solar cells based on ordered SiNWs are a direct consequence of the process based on MACE process coupled with NSL. **Figure 6-28** shows the SEM pictures with high magnification of ordered SiNWs. We can see that the surface of the SiNWs is quite rough: there are big grooves along the side of the SiNWs due to the use of a thin film gold catalyst. Moreover, the top of the wire is highly rough and the effect is becoming more important with increasing length of SiNWs. Indeed, the top of the wire is the part of the wire which has been exposed for the longest time to the etching solution. For short NWs, this top roughness is less prominent, as shown in the inset of **Figure 6-28 (b)**. We suspect that this roughness induced much more defects on the surface of ordered SiNWs compared to random SiNWs, and account for the low efficiency measured for cells with ordered SiNWs.

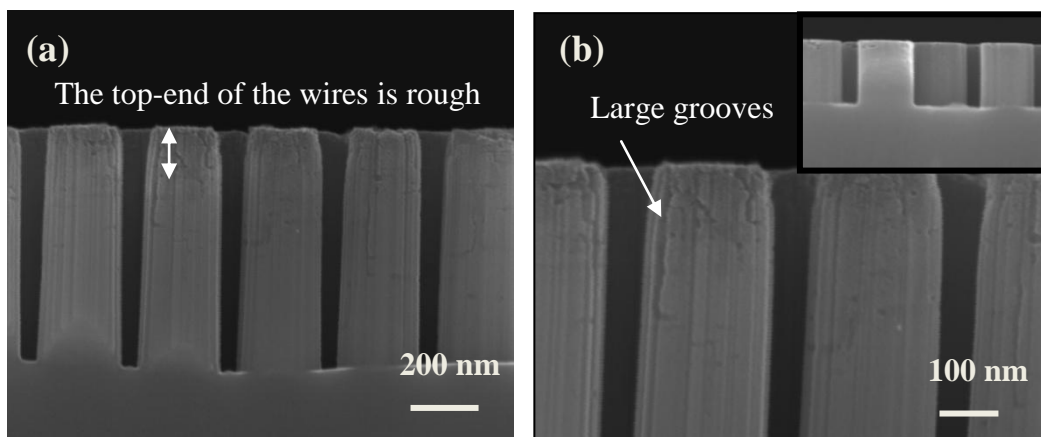


Figure 6-28: Cross-section SEM picture of ordered arrays of SiNWs (pitch 330 nm, diameter 220 nm, length 700 nm) (a) at low and (b) high magnification. The inset (b) shows that the top of the wire is less damaged for short SiNWs (250 nm height).

The fabrication of the ordered arrays of SiNWs was assisted by gold catalyst. However, gold is known to induce band gap states which can be detrimental to solar cells performance. A possible diffusion of gold during the fabrication process cannot be ignored, although SiNWs were fabricated at room temperature. Therefore we have analyzed ordered SiNWs by Electron Loss Energy Spectroscopy (EELS) inside a TEM system. We did not find any evidence of the presence of gold catalyst. Only the peak of silicon at 99 eV and

oxygen at 532 eV were detected as shown in **Figure 6-29**. Nevertheless we cannot exclude contamination by gold in concentration below the resolution of the equipment.

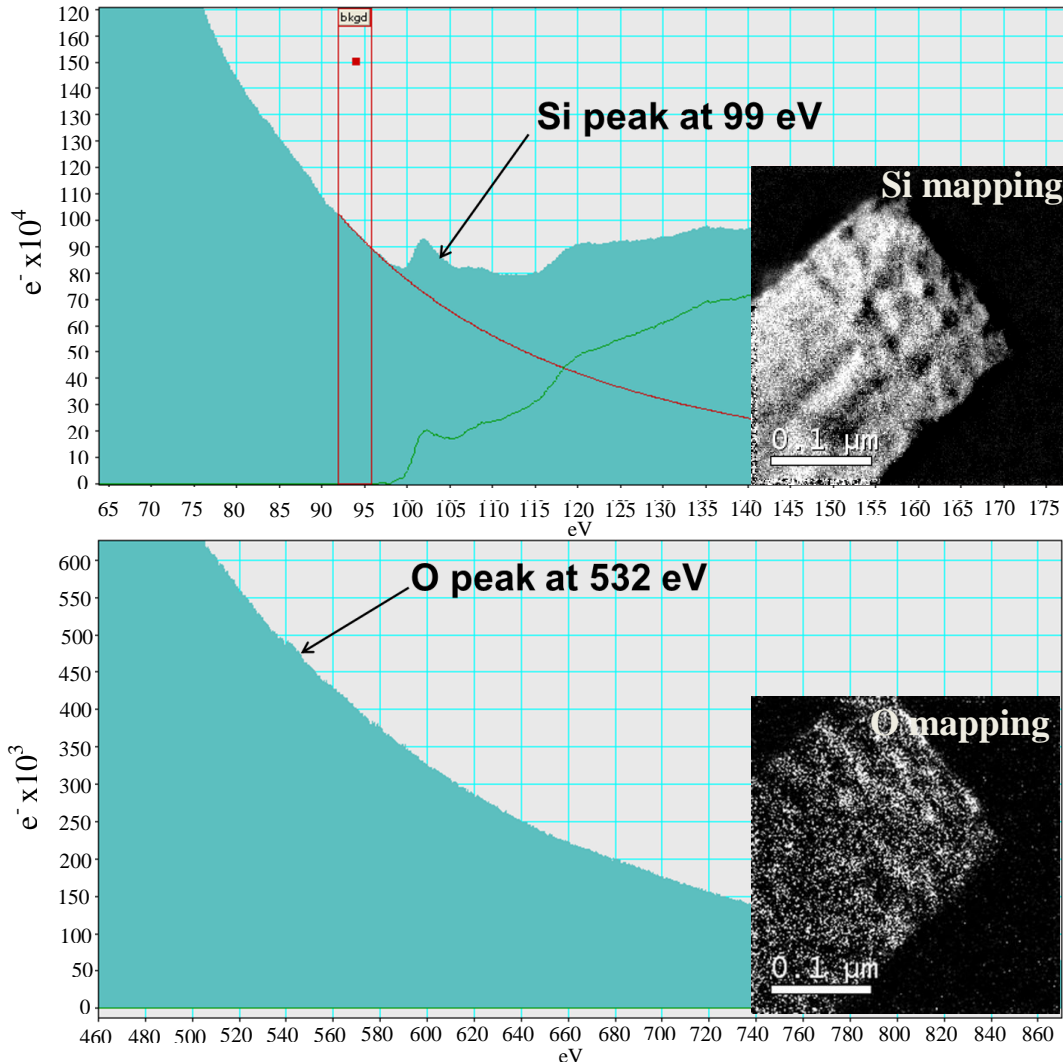


Figure 6-29: EELS analysis of ordered SiNW arrays.

6.3.3 TEM analysis of core-shell HIT solar cells based on ordered SiNWs

The TEM analysis of the SiNWs can reveal additional information to understand the poor performances of HIT devices based on ordered SiNWs. We have analyzed ordered SiNWs with and without a-Si:H coating. **Figure 6-30** shows the TEM pictures of bare SiNWs before the deposition of a-Si:H. TEM pictures were taken by Ms Ileana Florea from LPICM. The SiNWs are covered by a thin layer of oxide of 5-6 nm. We would like to highlight that the ordered

SiNWs are too thick for TEM to achieve very high resolution. We observe that the tip of the SiNW is porous, as a result of the long exposition time of the top part of the SiNWs to the etching solution. As a consequence, the tip was being etched and became porous. The TEM diffraction patterns of the tip and body of SiNWs provides us with information on structural details and defects of the zones observed. We have analyzed both the tip and the body of the SiNWs and obtained their respective diffraction pattern: diff 1 and diff 2. We can clearly see the crystalline structure of the body part of the SiNW. We also observe that the porous tip is also crystalline and forms small grains clearly visible in the diffraction pattern diff 2.

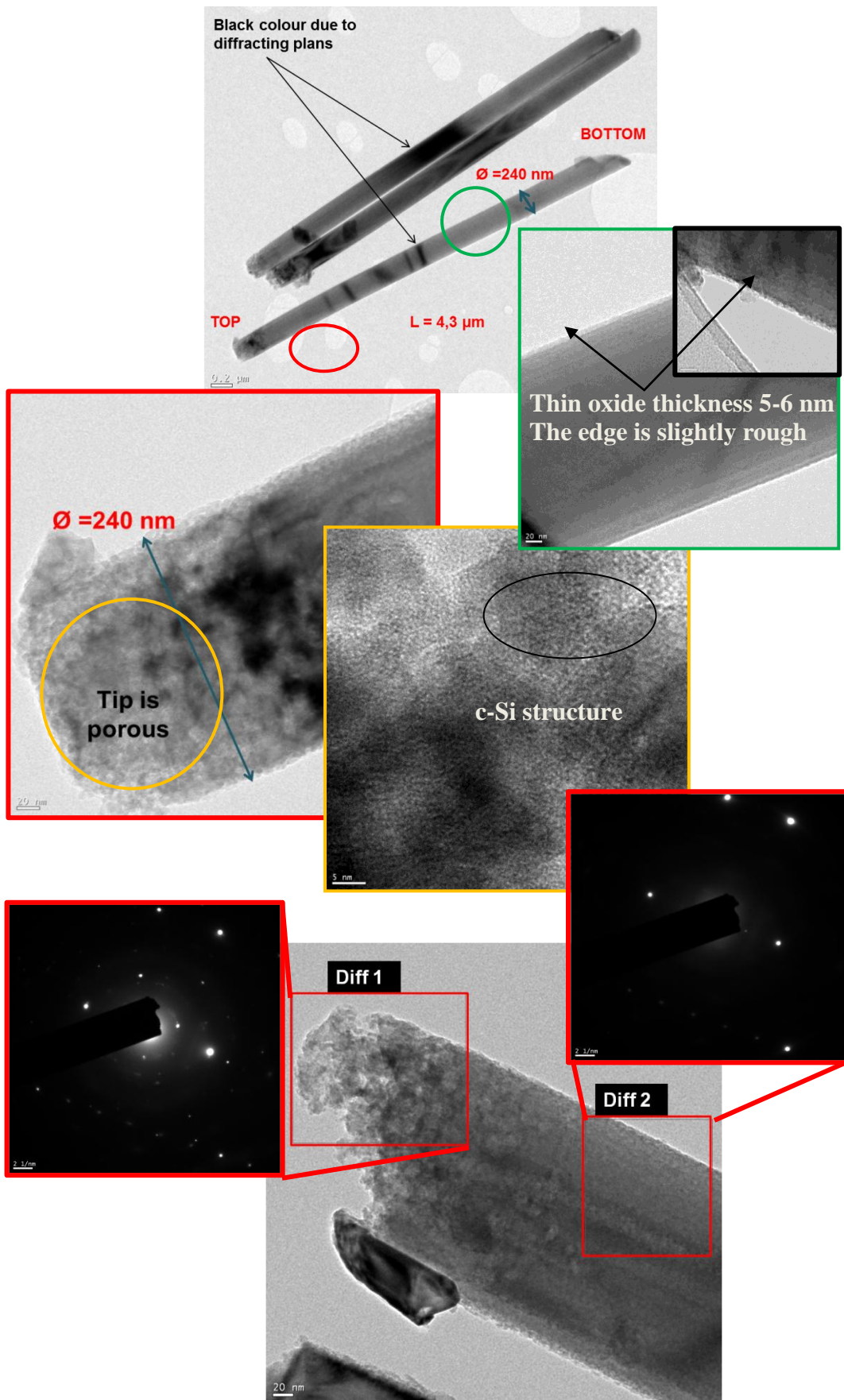


Figure 6-30: TEM analysis of ordered SiNW before a-Si:H coating.

We then study TEM pictures of a-Si:H coated SiNWs in order to understand the morphology of the coating by a-Si:H. The TEM pictures were taken by Ms Yang Yi from DSI, Singapore. SiNWs with a length of 1.2 μm , a diameter of 330 nm and a pitch of 600 nm were analyzed. **Figure 6-31** shows the TEM picture of a thick SiNW covered by (i) a-Si:H and (p) a-Si:H. We observe that the coating is not uniform over the length which is related to the difficulty to coat conformally high aspect ratio structures. The amorphous coating is very thick at the tip of the nanowire (about 40 nm) and becomes ultrathin near the bottom (**Figure 6-31 (a)** and **Figure 6-31 (b)**). The total diameter of the SiNW including the amorphous coating is 405 nm at the top of the wire and it decreases to about 335 nm at the bottom. Nevertheless, despite the non-conformity of the coating, it appears that the SiNWs is covered with a-Si:H along almost its entire length with a coating depth (distance from the top of SiNWs where we can observe a-Si:H coating on the surface of the SiNWs) of about 1.1 μm . The coating by a-Si:H has a columnar structure as illustrated in **Figure 6-31 (c)** and **Figure 6-31 (d)** which can be attributed to the initial surface roughness of ordered SiNWs as shown in **Figure 6-28**. We did not observe this columnar structure for disordered SiNWs. Moreover, small crystal grains are observed at the bottom of the wires as shown in **Figure 6-31 (e)**. This picture emphasizes the key role played by the a-SiC:H layer during the PECVD deposition to prevent epitaxial growth. Indeed, a-SiC:H layer may not completely reach the bottom of the wire and it may be too thin or not even deposited at the bottom of the SiNW. In that case, it cannot prevent the growth of a thin epitaxial layer. Therefore we observe crystal grains grown at the bottom part of the SiNW. Moreover, if we look at the tip of the NWs, we can observe a dark zone, which corresponds to the porous part of the SiNW. We did not observe this dark contrast for non-coated SiNWs by a-Si:H. We suspect the porosity of the tip to be responsible for this particular feature. Indeed, during the PECVD deposition, some radicals might diffuse and penetrate through the porous structure, resulting in the deposition of an amorphous phase inside the tip of the SiNW. The dark contrast can therefore be attributed to the dense defect/amorphous phase of Si, the electron beam being scattered by the amorphous phase. We suspect that the porosity of the tip accounts for the poor performances of the HIT devices based on ordered SiNWs.

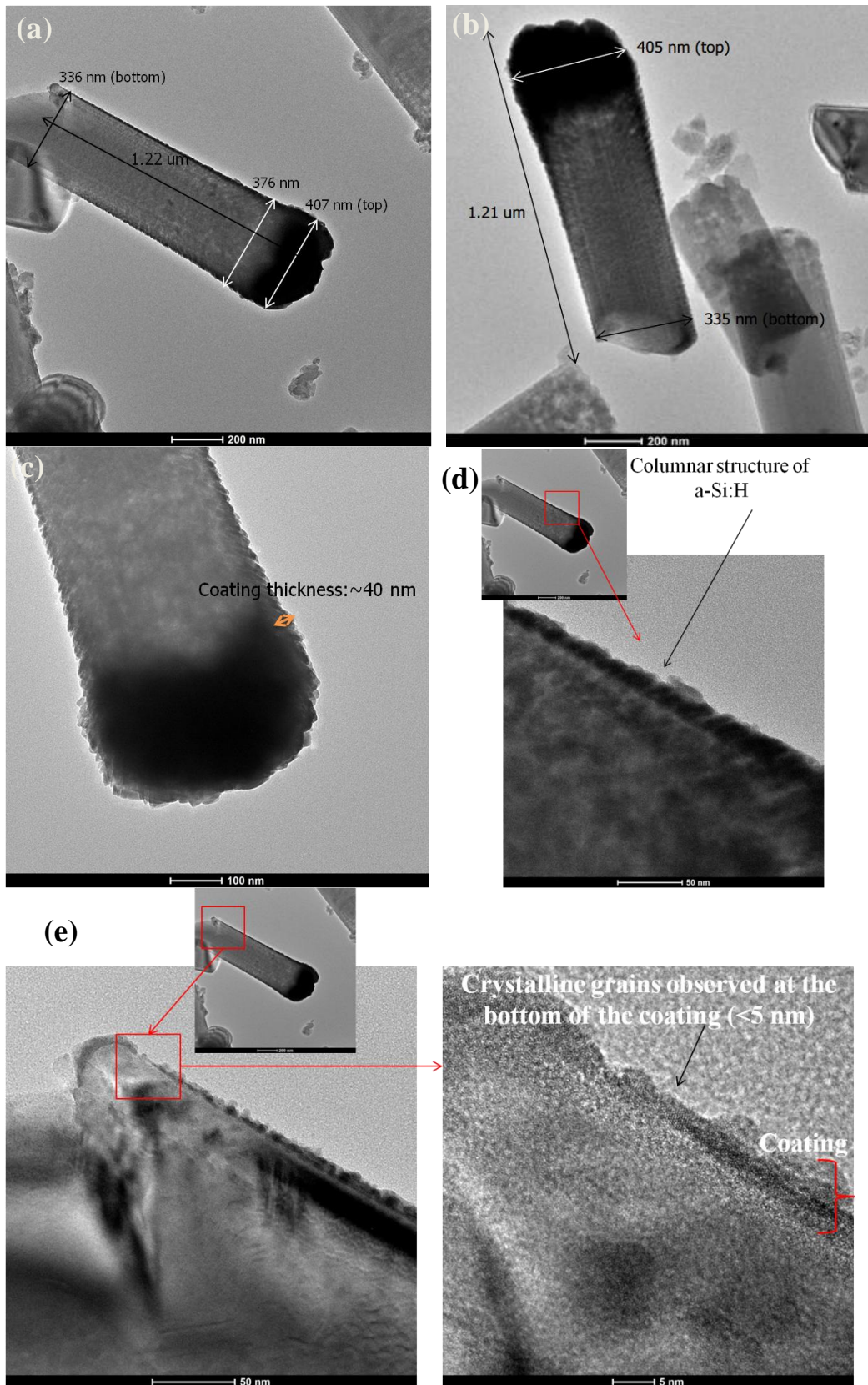


Figure 6-31: TEM analysis of ordered SiNW after a-Si:H coating. The coating of SiNWs by a-Si:H is not uniform (a), (b), it is maximum at the tip of the SiNW (c) and present a columnar structure (c) and (d). Finally, some crystalline grains are observed at the bottom of the coating (e).

6.3.4 EBIC of ordered SiNWs

EBIC characterization of HIT solar cells based on ordered SiNWs is also performed. We have investigated two types of arrays: short and long ordered SiNWs. Short SiNWs are characterized by a pitch of 500 nm, a diameter of 280 nm and a height of 460 nm. Long SiNWs have a pitch of 500 nm, a diameter of 300 nm and a length of 1.7 μm . We have modeled the interaction between the beam of electrons and the SiNW array with the software Casino for the two different geometries (short and long SiNWs) at different accelerating voltage. Results of the modeling for the short SiNWs geometry are displayed in **Figure 6-32**. We show results for a beam of electrons (10 nm) interacting with the SiNW located in the middle of a hexagonal arrangement of SiNWs. The electrons are penetrating deeper inside the structure and their scattering is enhanced with increasing accelerating voltage. **Figure 6-32 (a), (b)** and **(c)** shows the top-view EBIC mapping of the short ordered SiNW arrays at different electron gun energies. The SiNWs appear like a dark contrast over a brighter substrate, indicating that they are generating less current than the underlying wafer. Another interesting feature is the uniformity of the signal.

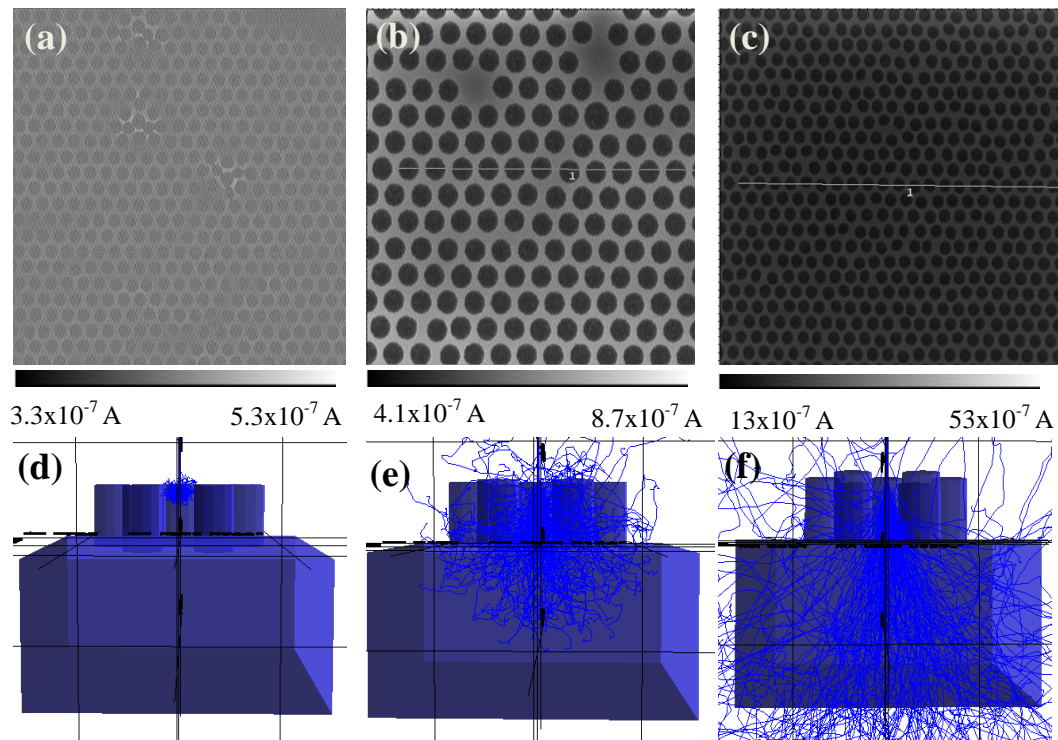


Figure 6-32: Top-view EBIC mapping of ordered SiNWs arrays (pitch of 500 nm, diameter of 280 nm and height of 460 nm) at different gun energies: 3 keV (a), 10 keV (b) and 20 keV (c) with the corresponding modeling (d), (e) and (f).

Figure 6-33 shows the EBIC cross-section mapping of short and long SiNWs for 2 different gun energies (5 and 10 keV). As mentioned previously, the SiNWs are covered by a thick layer of 200 nm of ITO which acts as an electron stopping layer and therefore reduces the signal generated by the SiNWs. Hence the darker area clearly visible in **Figure 6-33 (b)** at the bottom and around the SiNW. For short SiNWs, the signal is uniform from the top to the bottom of the wire. As for long SiNWs, we observe a decrease in the EBIC signal in the axial direction towards the SiNW top, which means that the SiNW top part is contributing less to the current than its bottom part. As for disordered SiNWs, the maximal EBIC signal is generated close to the SiNWs /substrate interface.

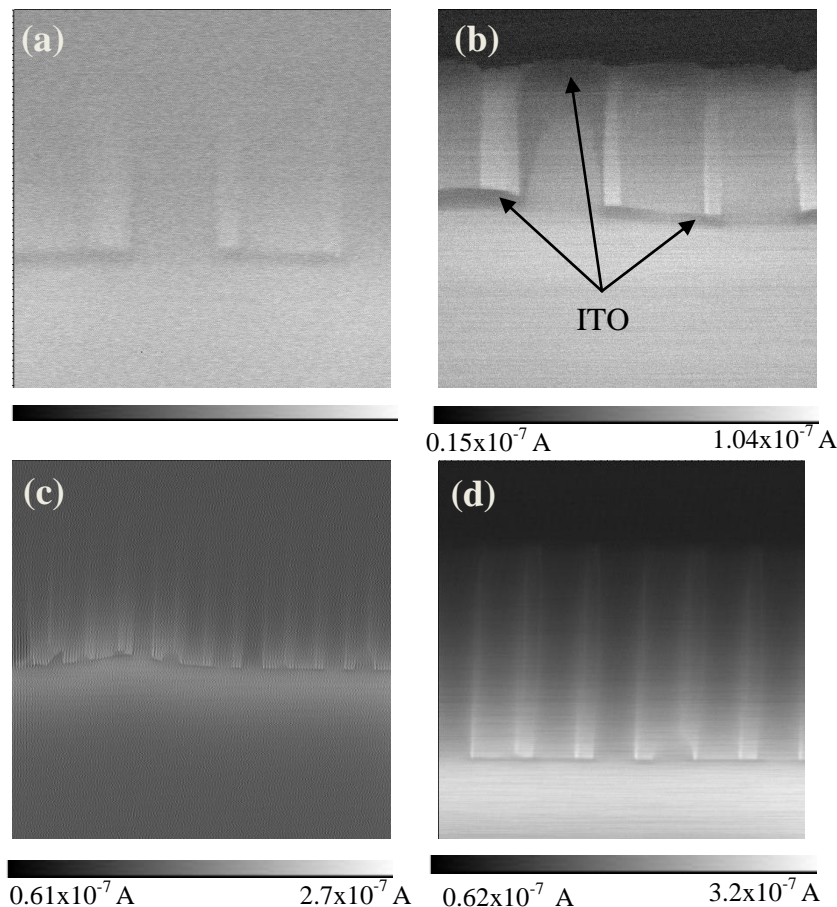


Figure 6-33: Cross-section EBIC mapping of short (a), (b) and long (c), (d) ordered SiNWs arrays at 2 different gun energies: 5 keV (a), (c) and 10 keV (b), (d)

Giving a numerical estimation of the current loss inside the SiNWs with respect to the bulk wafer is difficult as complex phenomenon of electrons

scattering are taking place. **Figure 6-34** shows the top-view EBIC mapping of ordered SiNWs arrays with different lengths. We observe an increasing contrast between the dark SiNWs and the white underlying wafer with increasing length of the SiNWs. With respect to the underlying bulk wafer, an average current loss of 23%, 29% and 36% was calculated for 500 nm, 1.7 μm and 3 μm long SiNWs respectively.

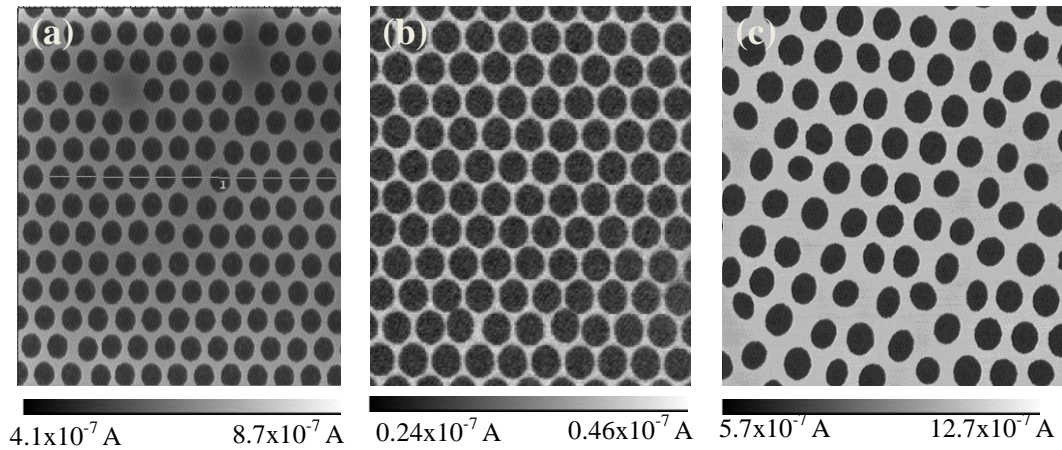


Figure 6-34: Top-view EBIC mapping of ordered SiNWs arrays with a length of (a) 500 nm, (b) 2.2 μm and (c) 3 μm .

EBIC characterization of HIT solar cells based on ordered SiNWs shows similar behavior as for disordered SiNWs. We observe the same order of current (10^{-7} A) for both disordered and ordered SiNW arrays. Ordered SiNWs are active electrically although they are generating less current than the underlying bulk wafer. Finally, the uniformity of the SiNWs over the entire sample is well assessed.

6.3.5 Change of Catalyst

In order to eliminate completely the risk of contamination by gold, we change the gold catalyst to silver when fabricating SiNWs by the MACE process assisted by NSL. As the surface roughness of the SiNW is certainly dependent on the catalyst used, it is interesting to see the effect on the morphology induced by the change of catalyst. We therefore repeated the same fabrication process presented in Chapter 3 and only switched the catalyst from gold to silver.

As shown in **Figure 6-35**, we successfully fabricated the silver etching mask with a well defined template. However the process got more complicated during the next wet etching step. We were not able to produce ordered arrays of SiNWs: the silver catalyst seems to diffuse too fast. As a consequence, the etching mask can only hold for a few seconds before most of the wafer surface starts to be etched. The localization of the etching, defined by the etching mask, is not truly respected. As a consequence the geometry of the array formed was not controlled as illustrated in **Figure 6-35**.

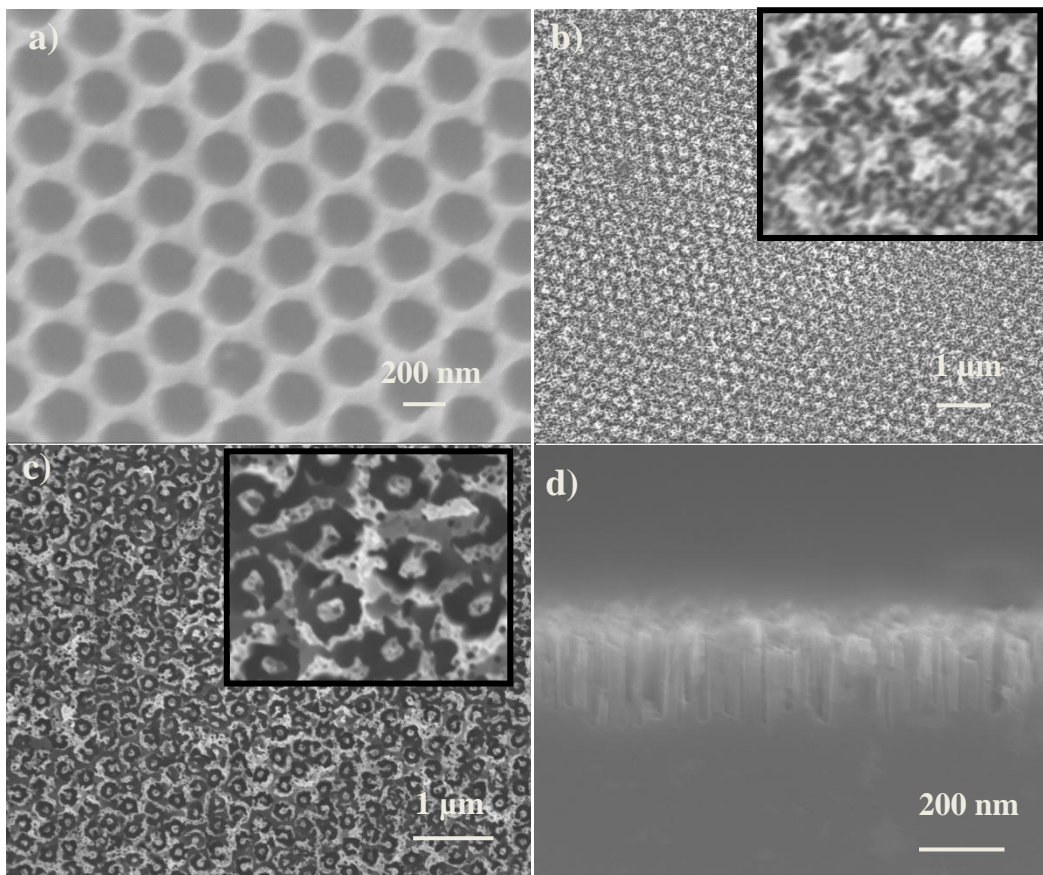


Figure 6-35: (a) Top-view SEM image of the silver etching mask after the removal of the PS spheres. (b) Top view SEM image after 20 s wet chemical etching and removal of silver film (c)) Top view SEM image after 45 s wet chemical etching and removal of silver film (d) Cross-section SEM picture of SiNWs fabricated by MACE assisted by NSL with silver catalyst after 1 min etching.

6.3.6 Effect of oxidation treatment

The objective of this treatment is to remove the defects and porosity at the surface of the SiNWs. As illustrated in **Figure 6-36**, the objective is to oxidize first the defective surface of SiNWs over several tens of nanometers.

The second step involves the removal of this oxidized layer, in order to achieve a smooth surface with reduced surface defects.

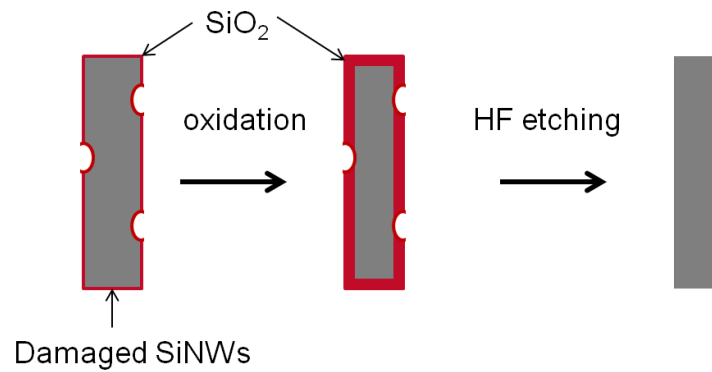


Figure 6-36: Illustration of the oxidation process

SiNW arrays with different geometries in terms of pitch, diameter or length were used. The oxide layer was formed by thermal oxidation under pure O₂ flux at 1050 °C. The oxidation rate was 4 nm/min. Different thickness of oxide layers were investigated.

For example, **Figure 6-37** shows SiNW arrays with a pitch of 800 nm and a length of 2.7 μm before and after the thermal oxidation treatment. Prior to oxidation, the initial diameter was 630 nm. The SiNW arrays were thermally oxidized for 15 minutes and the oxidized layer was subsequently etched away by a 5% HF bath. The new diameter after the oxidation process was reduced to 570 nm. The samples were then transferred to the ARCAM reactor for deposition of the (i) and (p) a-Si:H layer to form the heterojunction.

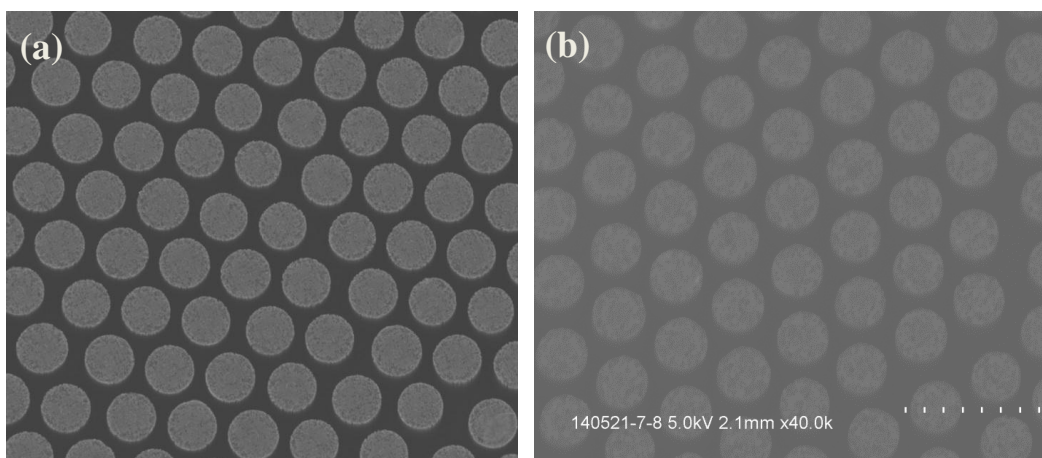


Figure 6-37: Top-view SEM picture of ordered arrays of SiNWs (pitch 800 nm, length of 2.7 μm) before (a) and after (b) oxidation process.

Table 6-8 summarizes the average performance of solar cells, with and without an oxidation pre-surface treatment.

Table 6-8: Effect of oxidation treatment: summary of geometrical characteristics of SiNW arrays and average value of V_{oc} , J_{sc} , FF and η of corresponding core-shell heterojunction solar cells.

Sample	No oxidation	60 nm oxidation	No oxidation	30 nm oxidation	No oxidation	30 nm oxidation
	N -Si wafer, 1-3 Ω .cm	N -Si wafer, 1-3 Ω .cm	5 μ m Epi wafer, 2-4 Ω .cm	5 μ m Epi wafer, 2-4 Ω .cm	5 μ m Epi wafer, 2-4 Ω .cm	5 μ m Epi wafer, 2-4 Ω .cm
Substrate						
Pitch (nm)	240	240	550	550	330	330
Diameter (nm)	180	180	300	300	200	200
Length (nm)	250	250	500	500	600	600
$d_{a-Si/H}$ (nm)	32	32	32	32	32	32
V_{oc} (V)	0,27	0,22	0,24	0,23	0,28	0,28
J_{sc} (mA/cm²)	29,11	13,98	15,38	8,20	14,03	5,74
FF (%)	40,75	46,97	48,21	39,85	44,20	51,71
η (%)	3,24	1,50	1,67	0,69	1,74	0,82

Unfortunately, the process degrades the performances of the cell. We observe that the J_{sc} of the devices cells which underwent the oxidation pre-surface treatment, is reduced while the V_{oc} remains stable for small thickness (30 nm equivalent on planar) of oxidized layer and reduces for larger thickness of oxide layer (60 nm equivalent on planar).

The EQE measurements of the oxidized and non-oxidized sample show us very interesting phenomena as displayed in **Figure 6-38**. We display the data for SiNW arrays with a pitch of 800 nm, a length of 2.7 μ m and a diameter of 570 nm after oxidation treatment. The EQE response for non-oxidized samples is null in the short wavelength regime while the response in the middle and long-wavelength regime is significant, indicating that mainly the wafer is generating current. This is explained by the quite long SiNWs used which are responsible for important recombination in the front part of the cell. In comparison, oxidized sample present a much stronger response in the short wavelength regime but no response in the long wavelength regime, indicating that only SiNWs are active while the wafer is electrically "dead". The oxidation process seems to have "wake up" SiNWs which are giving now a strong response. Unfortunately, we have lost signal from the underlying bulk wafer.

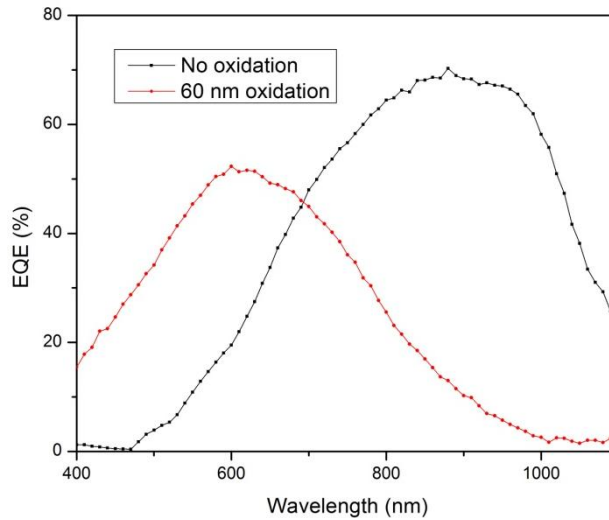


Figure 6-38: Effect of oxidation treatment on EQE

To confirm these results, EBIC measurements were carried out on oxidized and non-oxidized samples. As shown by the EBIC data in **Figure 6-39 (a)**, non-oxidized samples follow a similar trend as with previous EBIC measurements of SiNWs samples: the SiNWs are darker than the underlying bulk wafer (**Figure 6-39 (a)**). On the contrary, samples which underwent the oxidation treatment present areas where the SiNWs are active (white area) and some areas where SiNWs are inactive (black area) while the bulk wafer is dark (**Figure 6-39 (b)**). Such behavior is also observable on the cross section picture of the oxidized samples as displayed in **Figure 6-40**.

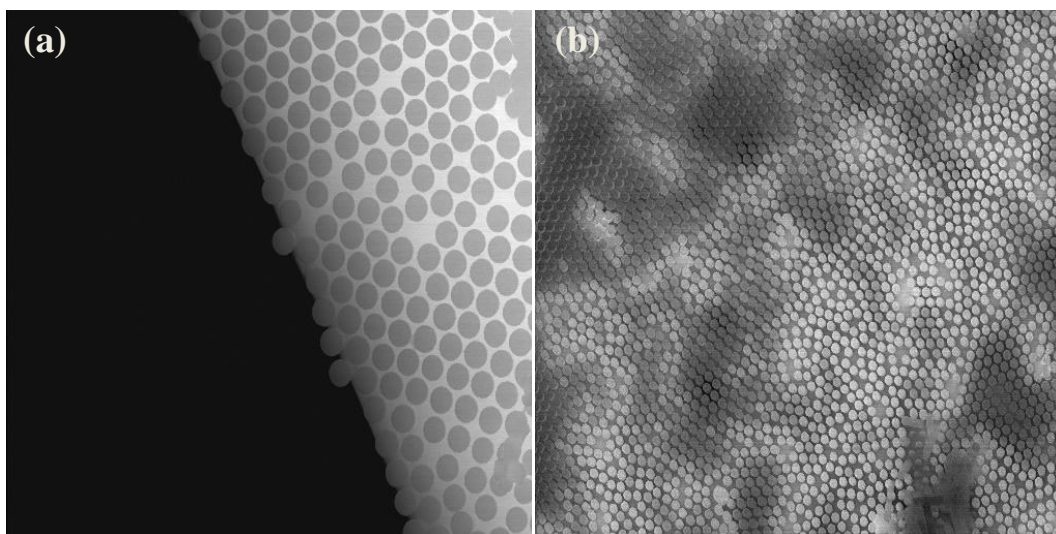


Figure 6-39: Top-view EBIC mapping before (a) and after (b) oxidation pre-treatment.

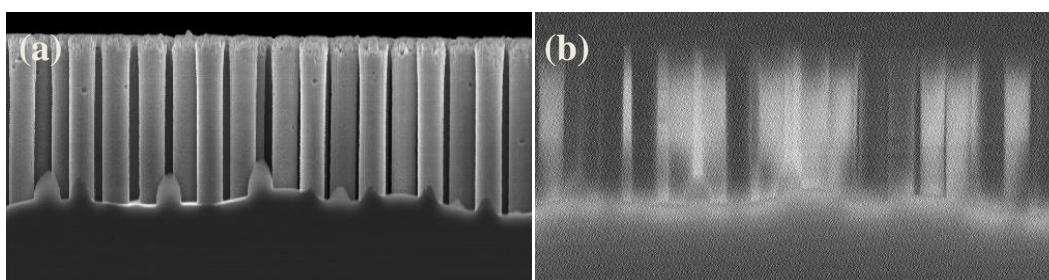


Figure 6-40: Cross-section SEM pictures (a) and corresponding EBIC mapping (b) of samples which underwent an oxidation pre-treatment

The main finding about this oxidation process is the possibility to improve drastically the response of SiNWs, especially for long wires. More investigation needs to be carried out in order to explain why the bulk wafer became electrically non-active. If we managed to solve this issue, we will be able to increase significantly the EQE response over the whole spectral range.

Conclusion

We have investigated HIT devices based on random SiNW arrays fabricated by wet etching. The simplicity of the fabrication process exposed here coupled with the excellent FF (more than 80%) of the fabricated device proves the potential of using SiNWs for cheap and highly efficient HIT solar cells on low-cost thin films. The process optimization is essential in order to get a proper surface passivation. If the amorphous layer is too thin, it is impossible to cover conformally the extra surface induced by SiNWs. However, if too thick, the absorption in the amorphous layer reduces the intensity of the current generated by the devices because of strong absorption losses. By optimizing the deposition conditions, a remarkable efficiency of 12.9% was achieved for such kind of devices. The effect of the length of SiNWs was investigated. Only short SiNWs ($< 1 \mu\text{m}$) are suitable for PV applications as the performances degrade for long SiNWs. Indeed, long SiNWs are more difficult to passivate with a-Si:H. The poor passivation results in a larger amount of surface defects responsible for a shorter carrier lifetime and subsequent degradation of the performances. The current generated by the SiNWs was mapped using EBIC microscopy. We have observed that SiNWs are electrically active but generate

less current than the underlying bulk wafer due to strong carrier recombination at the nanowires surface. The effect is becoming more ubiquitous with increasing length. Moreover, we have proven that HIT cells based on SiNWs can be successfully transferred to the thin film technology. An efficiency of 4.74% was obtained for a silicon thin film with an effective absorbing thickness of 5 μm incorporating SiNWs. We have also investigated HIT solar cells based on ordered SiNW arrays. The performance of this type of device is poor which might be related to the porosity of the tip of the wire and a higher surface roughness.

Looking ahead, there is still room for improvement. The process conditions can be refined to achieve higher efficiency. Moreover contacts still need to be improved as thick ITO layers (200 nm) were used for all these experiments. New surface treatment may also boost the efficiency of this kind of devices.

Chapter 7 : Hybrid Solar Cells based on SiNWs and Advanced Concepts

In this chapter, we investigate the potential of SiNWs for another kind of device, namely, hybrid solar cells. Hybrid solar cells are devices that result from the combination of two types of materials: organic and inorganic, hence the name "hybrid" [23], [191]. We will discuss the performance of hybrid devices based on disordered and ordered SiNWs. We will also discuss the possibility to transfer this kind of device to a-Si:H thin film and we will report on the fabrication of ordered and disordered a-Si:H nanowires (a-Si:H NWs). Finally a detailed study of the role of LiF/Al cathode for a-Si:H thin film based solar cells will be carried out.

7.1 Hybrid Solar cells based on Disordered and Ordered SiNWs

Figure 7-1 shows the schematic architecture of our hybrid device. SiNWs are coated by a thin layer of PEDOT:PSS and the device is completed by a Titanium/Palladium/Silver (Ti/Pd/Ag) back contact and a front silver grid electrode.

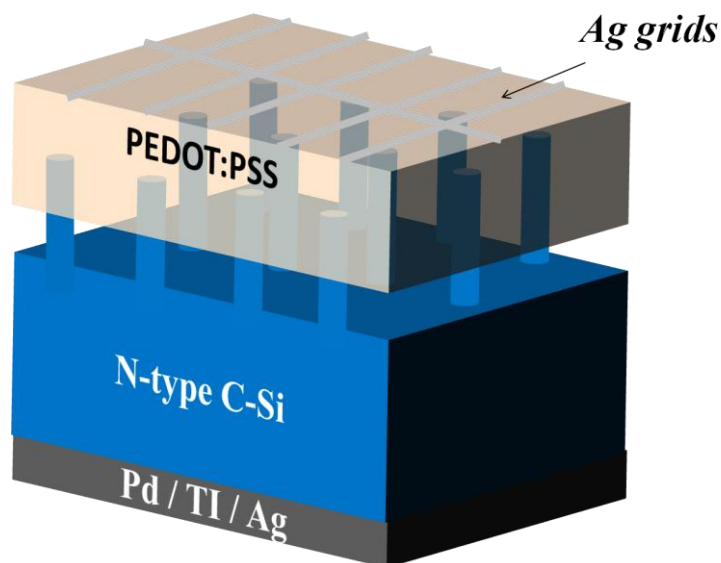


Figure 7-1: Schematic detailing the architecture of the hybrid device

7.1.1 Experiments

SiNWs were fabricated via the standard MACE process and by the MACE process assisted by NSL. These methods of fabrication have been introduced in section 3.1 and Chapter 4 of this thesis. Single-crystal n-type wafers [100] with a resistivity of 1-3 $\Omega\cdot\text{cm}$ were used for these experiments. SiNWs were subsequently dipped into a 5% HF bath for 5 min in order to remove the thin native oxide layer. Following this step, a Titanium/Palladium/Silver (Ti/Pd/Ag ; 50 nm : 50 nm : 1 μm) back contact was deposited via e-beam evaporation. Ti/Pd/Ag stack is a common electrode that has been shown to make good contact with n-type Si wafer (U.S. Pat. No. 3,686,036 - [247]). Ti can result in low contact resistance ($<10^{-5}$ $\Omega\cdot\text{cm}^2$) for wafers with doping level above 10^{19} cm^{-3} . Moreover Ti promotes adhesion of the back contact and reduces the native SiO_2 layer. Pd improves the adhesion between Ti and Ag and plays the role of a diffusion barrier. After the back contact deposition, a thin layer of PEDOT:PSS of about 80 nm was spin coated on the top of the SiNWs at 1800 rpm. The solution of PEDOT:PSS (PH 1000 – Heraeus Clevios) was doped with 5 wt% dimethyl sulfoxide (DMSO) and 1 wt% Triton X-100 (Aldrich) and was stirred for 4 hours via a magnetic bar. DMSO was used to increase the conductivity of PEDOT:PSS and Triton X-100 to improve its wettability. After the spin coating, the samples were directly annealed at 105°C for 8 minutes. PEDOT:PSS is a transparent and conducting mixture of polymers. It is composed of two polymers: a sulfonated polystyrene (PSS) and a conjugated polymer Poly(3,4-ethylenedioxythiophene), commonly named PEDOT. PEDOT is made of repetitive unit of the monomer EDOT. PSS plays the role of dopant for PEDOT, making PEDOT both conductive and soluble. Sulphonic acid group of PSS are deprotonated, giving a H^+ to the monomer EDOT which opens up one of its $\text{C}=\text{C}$ π bonding, resulting in the bonding of a C with the H^+ [248]. By removing electrons, PEDOT shows a net positive charge that will attract the negative sulfonate group of deprotonated PSS [248]. PEDOT and PSS align along each other and become intertwined. The unpaired electron remaining on the PEDOT is delocalized on the conjugating backbone and is therefore highly mobile, resulting in the strong conductivity of PEDOT [248]. With proper additives, conductivity of PEDOT

as high as 1000 S/cm can be achieved [249]. After the spin coating step, a 1.5 μm front silver grid contact was evaporated on top of the PEDOT:PSS layer. The front grid electrode induces about 12% power loss of the incident light because of shadowing effect. Devices with a size of 0.95 cm^2 are obtained. A reference planar cell was co-deposited at the same time. The process flow is summarized in **Figure 7-2** below.

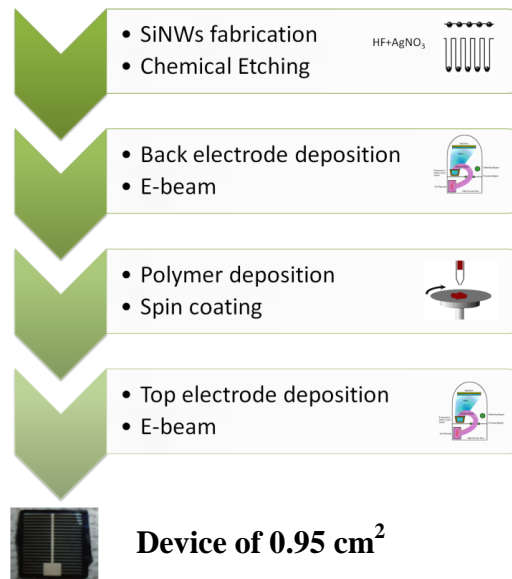


Figure 7-2: Process flow of hybrid solar cells

7.1.2 Discussion

We have fabricated hybrid solar cells on various substrates : disordered SiNWs with different lengths and ordered SiNWs with various geometries.

Table 7-1 summarizes the geometrical characteristics of the SiNW arrays and the average photovoltaic performance obtained.

The three ordered SiNWs arrays (labelled as A, B and C shown in Table 6.1) were characterized by UV/Vis/NIR spectrophotometer (PerkinElmer) using an integrating sphere at the angle of incidence (AOI) of 8°. The total reflectance was measured in the spectral region between 370 nm to 1100 nm and the results are shown in **Figure 7-3**. We observe an increase in J_{sc} for cells where there is a reduced reflectance. Therefore, for samples of about the same height, the J_{sc} of the ordered arrays of SiNWs is directly related to the reflectance.

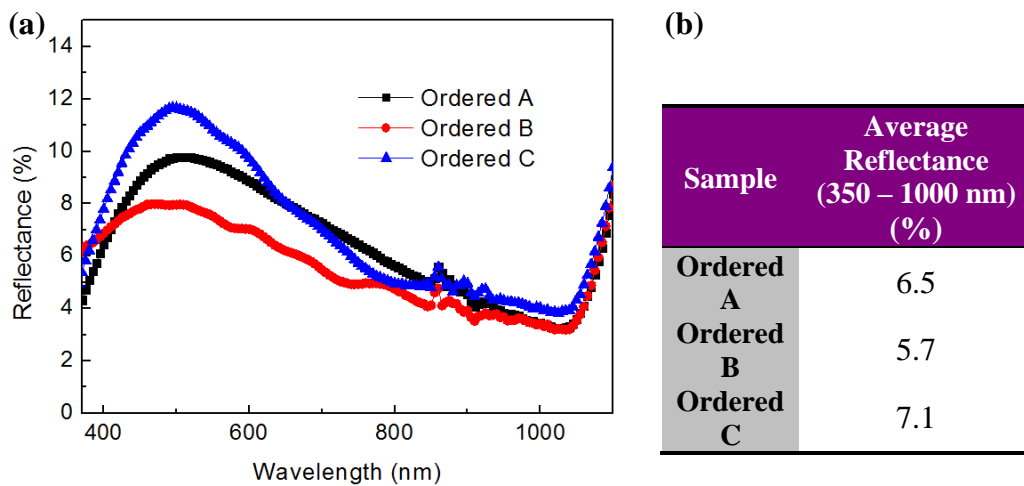


Figure 7-3: EQE response of the three arrays of ordered SiNW arrays A, B and C and (b) the corresponding average reflectance on the spectrum range 350-1100 nm.

Figure 7-4 shows the (J,V) curves and EQE of all the cells. **Figure 7-4 (a)** shows the (J,V) curves of the hybrid solar cells under dark and standard illumination conditions. Hybrid solar cells exhibit normal (J,V) curves, except for the ordered array C which presents a small s-shape curve under dark and illuminated conditions. The SiNWs have reduced EQE response in the short wavelength region compared to the reference planar cells, indicating that strong recombination is occurring in the front part of the cells. For both ordered and disordered SiNWs, we observe a reduction in the EQE response in the short wavelength region with increasing length of SiNWs, since the recombination is expected to increase with the length of the SiNWs. The SiNWs improve the spectral response in the long wavelength region as compared to planar cells, thanks to their good light trapping properties as we have observed previously for HIT devices.

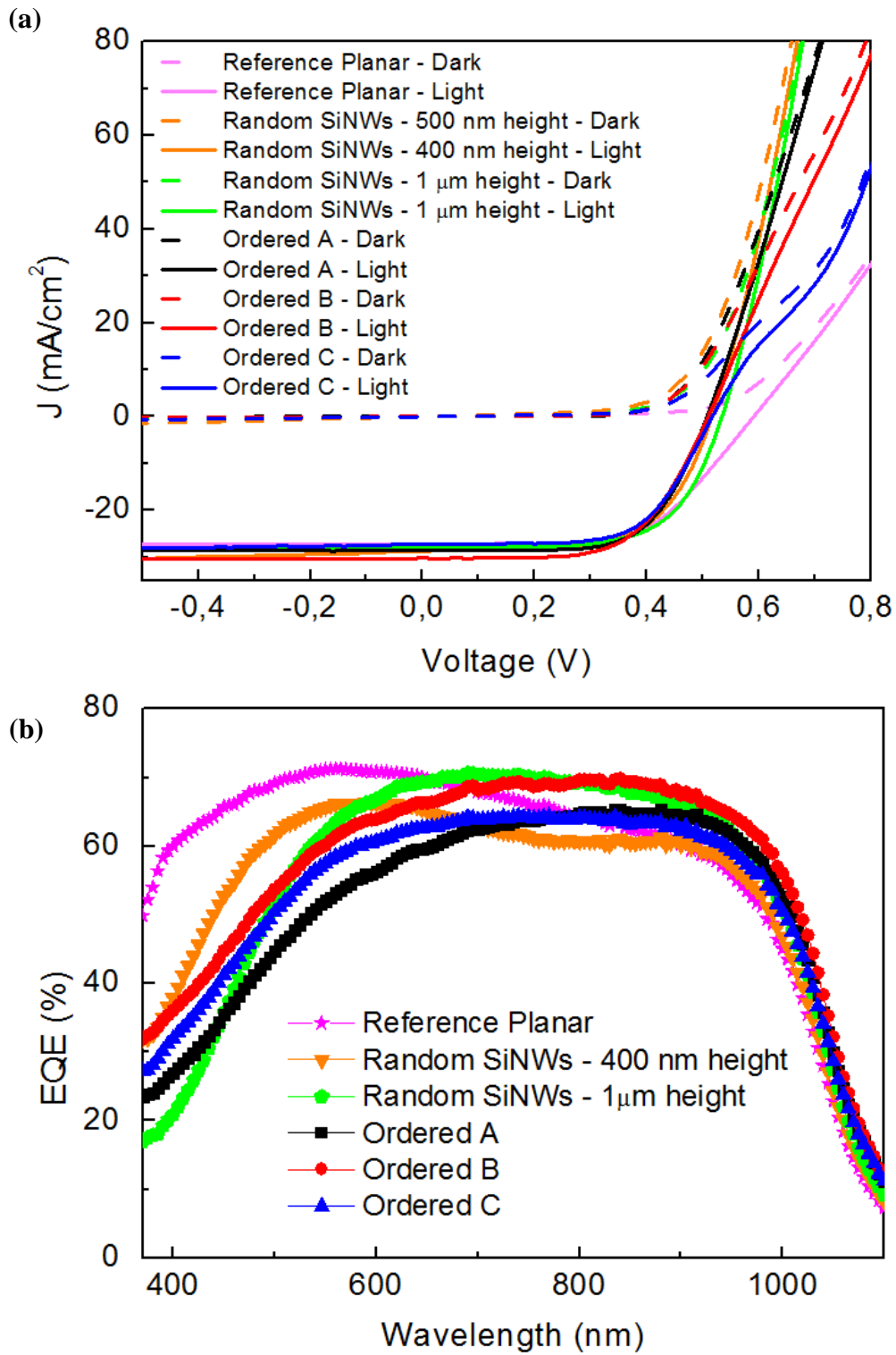


Figure 7-4: (a) (J,V) and (b) EQE of hybrid devices based on disordered and ordered SiNWs.

Figure 7-5 shows the energy band diagram of the hybrid device with the corresponding charge transport mechanism. We observe that the level of the Highest Occupied Molecular Orbital (HOMO) of the PEDOT:PSS (5 eV) is well matched with the valence band of silicon (5.17 eV) which ensures good charge carriers separation. Holes are therefore injected in the PEDOT:PSS and electrons are collected at the Ti/Pd/Ag contact.

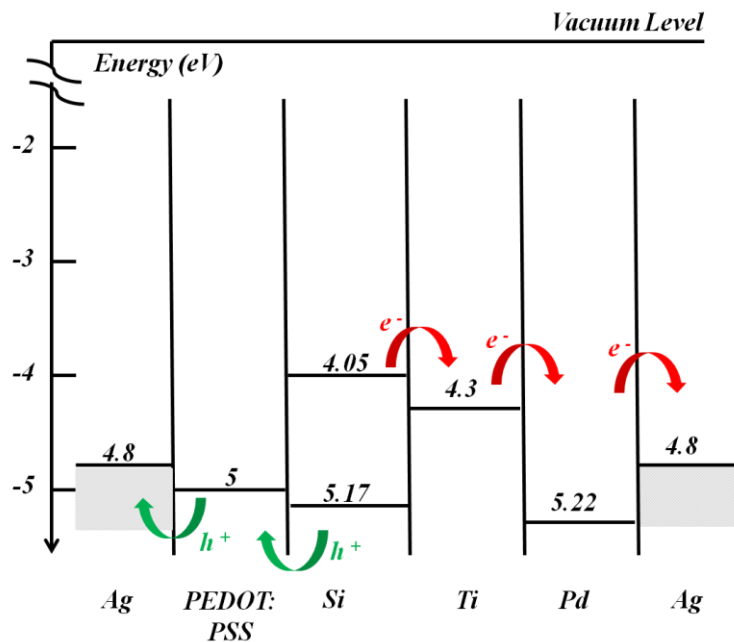


Figure 7-5: Band diagram of the hybrid device

We have also analyzed the morphology of the PEDOT:PSS coating on the array of SiNWs. **Figure 7-6** show cross-section (a), (b), top-view (c), and inclined (d) (30°) SEM images of ordered arrays of SiNWs coated with PEDOT:PSS. We observe that the PEDOT:PSS film cannot penetrate deep inside the SiNWs structure and therefore cannot reach the bottom of the wire as show in **Figure 7-6** (a), (b) and (d). We measure an average penetration depth between 300 to 550 nm according to the available space between the SiNWs. The polymer film is forming a canopy lying on the top of the array as illustrated in the SEM picture in **Figure 7-6** (d). Therefore the coating by PEDOT:PSS is incomplete which limits the area of the p-n junction formed. It also means that a significant portion of the SiNWs surface is not passivated. Improving conformal coating by the polymer solution will increase significantly the area of the p-n junction and can therefore potentially boost the efficiency of hybrid

solar cells. Finding a simple way to force the polymer film down to the bottom of the structure is highly desirable.

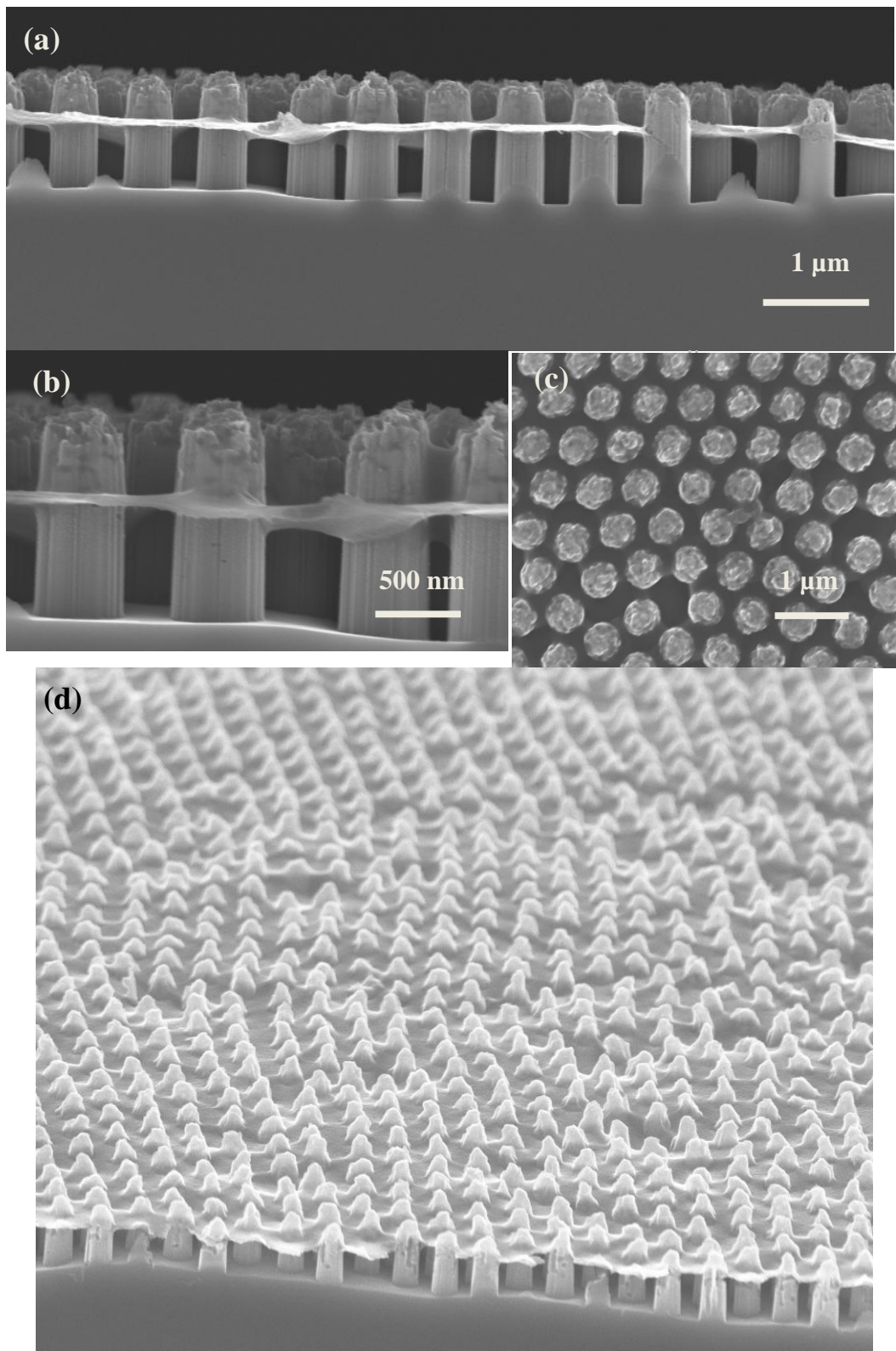


Figure 7-6: Cross-section view (a), (b), Top-view (c) and Inclined-view (d) SEM pictures of SiNWs coated with PEDOT:PSS

7.1.3 Low-Pressure-Assisted-Deposition

A new method to promote infiltration of the polymer between the SiNWs has been implemented. This method consists of using vacuum suction to pull the polymer film down the SiNWs. This is simply done by loading the sample inside a vacuum chamber and pumping down to 200 mTorr. This way, the polymer film is drawn into the wire structure by capillary action as there is no more air between the SiNWs to counterbalance the force. Specifically three different methods have been tested to promote conformal coating of the wires by PEDOT:PSS. We will name these methods as LPAD1, LPAD2 and LPAD3, with LPAD standing for Low-Pressure-Assisted-Deposition.

In the first method LPAD1, a droplet of PEDOT:PSS is first drop casted on the top of the arrays. The sample is then loaded inside the vacuum chamber for a few seconds. After this low pressure step, the sample is spinned to remove any excess of the polymer solution. Finally the sample is dried for 8 min at 105°C. For LPAD2 and LPAD3, the PEDOT:PSS is first spin coated on the top of the SiNW arrays. In LPAD2, the sample is dried for 1 min at 105°C before being loaded inside the vacuum chamber. For LPAD3, the sample is directly being loaded inside the vacuum chamber before being dried at 105°C for 8 min. Therefore, for LPDA1, we have a larger initial volume of PEDOT:PSS compared to the standard spin coating process, while for LPAD1 and LPAD2, the thickness is kept the same as in the original recipe. **Figure 7-7** shows the results we achieved for the three methods of deposition.

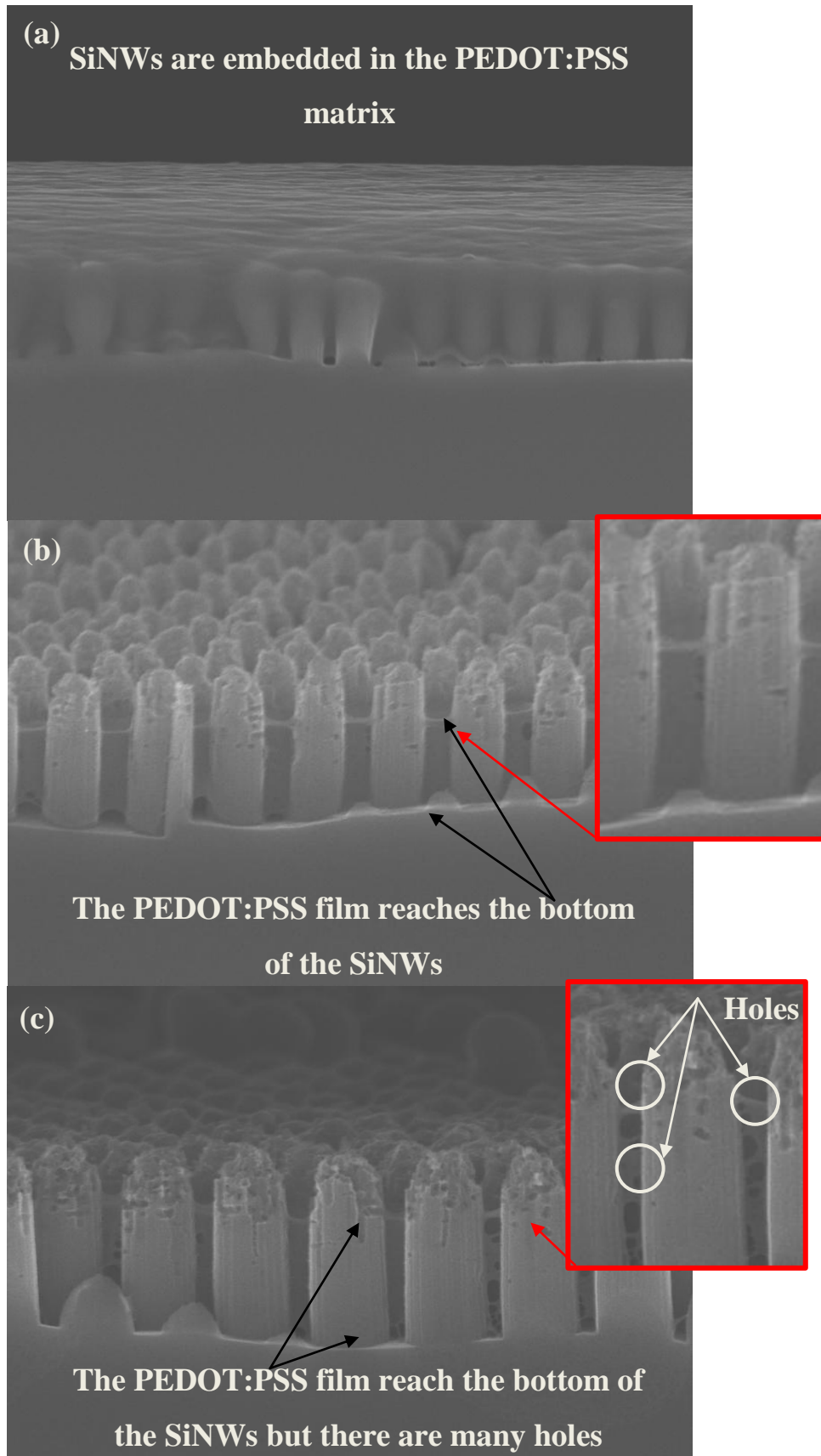


Figure 7-7: SEM pictures of ordered SiNWs after (a) LPAD1, (b) LPAD2 and (c) LPAD3.

LPAD1 allows the SiNWs to be totally embedded within the polymer matrix. The coating of the SiNWs by PEDOT:PSS is complete. However the PEDOT:PSS coverage might be too thick to ensure both reasonable transparency and collection length. This process can be optimized by tuning the volume of the initial droplet drop casted at the top of the arrays. We have also successfully made the PEDOT:PSS film reach the bottom of the SiNWs structure using LPAD2 and LPAD3. When comparing the results obtained from LPA2 and LPAD3, we observe that there are many holes in the PEDOT:PSS film using the LPAD3 technique. We believe that evaporating the solvent before the vacuum step allows the PEDOT:PSS layer to gain strength (less liquid) and to become more resistant to the vacuum suction force. The advantage of LPAD2 and LPAD3 is the possibility to tune the final thickness of the PEDOT:PSS layer by adjusting the spinning speed of the spin coater in the initial step.

This work is still under investigation. Next steps include the optimization of the LPAD process and the fabrication of hybrid devices to study the effects on performance of the different PEDOT:PSS coating morphologies. We think that this approach is very promising to enhance the efficiency of hybrid solar cells based on SiNWs.

7.2 Hybrid Solar Cells based on amorphous thin films

As for HIT devices, we aim to transfer the concept of hybrid solar cells to thin film technology. Our group has already reported efficient hybrid solar cells based on epitaxial thin film [117]. We investigate here the potential of hybrid devices based on a-Si:H thin films, which are much cheaper and easier to produce than epitaxial silicon thin films.

7.2.1 Nanostructuring of a-Si:H thin films

To transfer the concept of hybrid solar cells based on SiNWs to a-Si:H thin films, we first need to study the feasibility of nanostructuring a-Si:H by MACE or by MACE assisted by NSL. The etching procedure was therefore tested on a-Si:H thin films. Hydrogenated amorphous silicon (a-Si:H) thin films of 3.3 to 5 μm thick were deposited either on glass substrate (commercial

fluorine-doped SnO₂ (SnO₂:F) coated glass, ASAHI substrate) or on (p++) silicon substrate (0.01 -0.02 Ω.cm). The (i) a-Si:H films were deposited by RF PECVD using a mixture of silane (50 sccm, 1 Watt) with hydrogen (40 sccm) for 1 min followed by the deposition of pure silane for 4 to 7 hours. The next step in the process was the wet chemical etching of the (i) a-Si:H films. As the etching solution was based on HF, it presented a risk to the ASAHI substrate since HF can etch the glass. To prevent any damage of the substrate, we coated the side and backside of the glass substrate by a nitrocellulose solution which is resistant to HF and which can be easily removed by a concentrated nitric acid bath.

7.2.1.1 Fabrication of disordered a-Si:H NWs

The samples were dipped into an etching solution of 4.6 M HF (Sigma Aldrich) and 0.02 M AgNO₃ (Sigma Aldrich, Purity = 99.9999%) at room temperature for different times varying from 3 to 15 min. The samples were then rinsed for 5 min in DI water. The silver dendrites were subsequently removed by a 15 min HNO₃ bath (65%, sigma Aldrich). Following that the samples were rinsed thoroughly in DI water and dried under nitrogen gas environment. As illustrated in **Figure 7-8 (a)** and **(b)** the etching process is able to fabricate SiNWs on a-Si:H thin films, similar to that achieved on c-Si substrates. The fabrication of a-Si:H NWs is quite a unique concept and so far only *Douani et al.* [250] have reported on the etching of thin a-Si_{1-x}C_x:H films to fabricate NWs. As shown in **Figure 7-8 (c)**, the etch rate of a-Si:H NWs is about 48 Å/s. We have therefore confirmed the feasibility of a-Si:H NWs fabrication using the MACE process.

1 μm

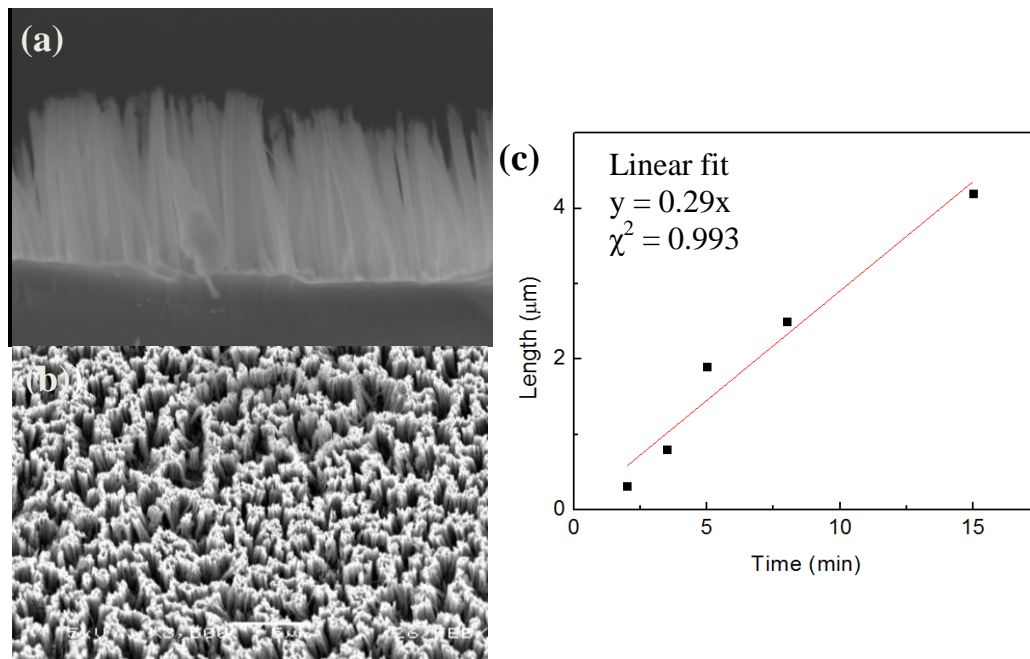


Figure 7-8: (a) Cross section view of a-Si:H nanowires. (b) Top-view of a-Si:H nanowires. (c) Length of nanowires as a function of the etching time.

We aim at nanostructuring the intrinsic layer of a-Si:H based solar cells in order to improve the harvesting capabilities of the device. We therefore need to characterize optically the arrays of a-Si:H NWs. For solar cell application, the thickness of the intrinsic layer lies in the range of 300-500 nm. On glass substrate, 10 nm (n++) a-Si:H layer followed by an (i) a-Si:H layer of 500 nm were deposited by RF PECVD following the same experimental procedure as mentioned before. The samples were then dipped into an etching solution of 4.6 M HF and 0.02 M AgNO₃ at room temperature for 2.5 minutes. The reflectance of the samples was measured before and after etching using an integrating sphere spectrophotometer system (Lambda 950/UV/Vis/NIR, PerkinElmer) with an angle of incidence (AOI) of 8°. The total reflectance was measured in the spectral region between 300 nm to 1100 nm and the results are shown in **Figure 7-9**. We observe that a-Si:H NWs are able to reduce the reflectivity of a-Si:H planar films significantly over the entire spectral range.

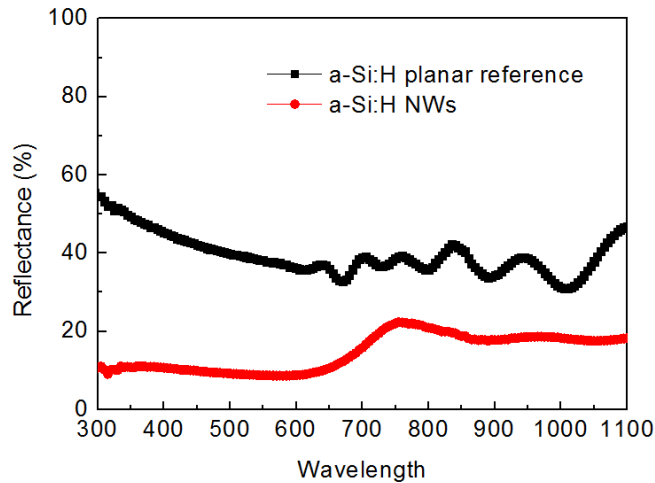


Figure 7-9: Reflectance measurement of planar a-Si:H thin films and a-Si:H nanowires.

7.2.1.2 Fabrication of ordered a-Si:H NWs

We also tested the MACE process assisted by NSL on a-Si:H thin films. We were able to fabricate ordered arrays of a-Si:H NWs, which have never been reported in the literature. We tested both gold and silver catalyst. Interestingly both catalyst worked for the fabrication of a-Si:H NWs while for c-Si substrate we were not able to obtain well defined SiNWs arrays with silver. This might be explained a different process of diffusion of Ag on c-Si and a-Si:H substrates. **Figure 7-10** shows SEM pictures of the a-Si:H NW arrays fabricated.

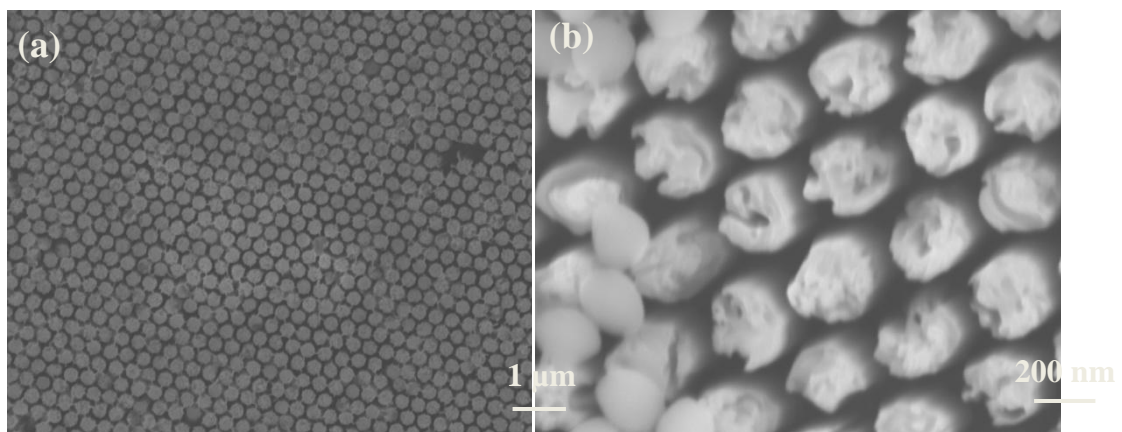


Figure 7-10: Top-view (a) and inclined 30° (b) SEM pictures of a-Si:H NWs.

7.2.2 Fabrication and characterization of hybrid solar cells based on a-Si:H

First we focused our study on planar hybrid solar cells based on a-Si:H thin film combined with an organic layer in order to develop our understanding of the a-Si:H/organic heterojunction before adding complex phenomenon due to the nanostructuration by SiNWs. Indeed, it is important to understand the physics behind the reference planar cells and to optimize the process of fabrication before adding the nanostructuration by a-Si:H NWs.

Two types of structures were considered:

- a) Combination of an n-type a-Si:H thin-film with a p-type semi-conducting polymer
- b) Combination of a p-type a-Si:H thin-film with a n-type semi-conducting polymer

7.2.2.1 (n) a-Si:H / p-type polymer

Figure 7-11 shows the configuration of the device investigated. The device has the same architecture of a standard p-i-n junction, where the (p) a-Si:H layer has been substituted by a PEDOT:PSS layer. First a 10 nm (n++) a-Si:H layer followed by an (i) a-Si:H layer of 300 nm were deposited by RF PECVD on an TCO glass substrate (commercial fluorine-doped SnO₂ (SnO₂:F) coated glass, ASAHI substrate). Two different post-treatments of the amorphous layer were tested: for one set of samples, the native oxide layer at the amorphous surface was kept intact while for the other samples the oxide layer was removed by a 5% HF bath. The polymer PEDOT:PSS (PH 1000 – Heraeus Clevis), with 5 wt% dimethyl sulfoxide (DMSO) and 1 wt% Triton X-100 (Aldrich) was subsequently spin coated on the surface. Finally a silver grid (1.5 μm thick) was evaporated on top of PEDOT:PSS by e-beam evaporation. The samples size is 0.95 cm².

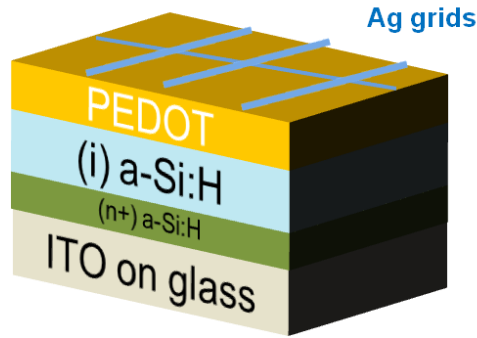


Figure 7-11: Architecture of the device studied – Hybrid thin film solar cells based on a-Si:H.

Figure 7-12 and **Table 7-2** show the current density-voltage (J-V) characteristics, EQE and photovoltaic parameters of the samples under 100 mW/cm² illumination (AM 1.5G). As shown in **Table 7-2**, the oxide layer plays a critical role in the device performance. When the native oxide layer is etched away, the efficiency of the device increases drastically from zero (0.00135%) to 1.3%. This is explained by the improvement of the V_{oc} and J_{sc} . However these solar cells give abnormal (J,V) curves. In particular, the (J,V) curve does not follow the expected diode behavior indicating presence of strong leakage currents (**Figure 7-12 (a)**). The EQE response is also very poor as shown in **Figure 7-12 (b)** where the EQE of a standard p-i-n cell is also displayed as a reference [120]. These poor performances might be explained by the band diagram alignment. The dominant charge carrier transport in p-i-n junction is drift : charge carriers generated in the (i) a-Si:H layer experience directly the electric field generated across the (i) a-Si:H layer. Therefore the driving force for charge carrier separation is the strength of this internal electric field which is determined by the work function difference between (n) a-Si:H and PEDOT:PSS. The HOMO level of PEDOT:PSS is only 5 eV which certainly leads to a small electric field within (i) a-Si:H and as a consequence inefficient charge carrier separation.

Table 7-2: Average value of V_{oc} , J_{sc} , FF and η of planar hybrid a-Si:H / PEDOT:PSS heterojunction

Sample	J_{sc} (mA/cm ²)	V_{oc} (V)	FF (%)	η (%)
(i) a-Si:H = 300 nm Thin oxide layer	0.18	0.039	18.83	0.00
(i) a-Si:H = 300 nm After HF bath	10.01	0.57	22.82	1.3

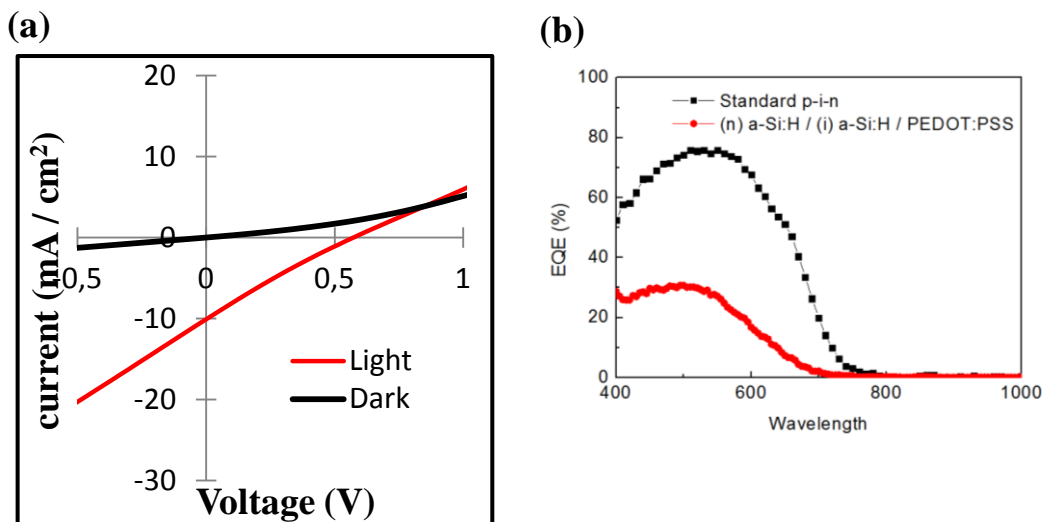


Figure 7-12: (a) (J,V) and (b) EQE planar hybrid a-Si:H / PEDOT:PSS heterojunction

7.2.2.2 (p) a-Si:H / n-type polymer

We have also investigated the inverted structure, i.e. an organic n-type semiconductor in combination with (p) a-Si:H / (i) a-Si:H. This study has been motivated by a recent work published by *Ji Hoon Seo et al.* [251], who claimed that hybrid solar cells based on a-Si:H (TCO/ (p)a-Si:H/(i)-a-Si:H/ PCBM) can achieve efficiency as high as 8.34 %.

Figure 7-13 shows the architecture of the investigated device whose structure is as follows: SnO₂:F coated glass // (p) a-Si:H // (i) a-Si:H // Organic layer (C₆₀ or PCBM) // LiF/Al electrode. On commercial fluorine-doped SnO₂ (SnO₂:F) coated glass, 10 nm of (p) a-Si:H followed by 300 nm of (i) a-Si:H were deposited by the RF PECVD technique. Two different organic materials were tested: PCBM and the buckyball fullerene C₆₀. PCBM is a

derivative of the fullerene, which has been functionalized in order to make it soluble in organic solvents. Therefore PCBM was deposited by spin coating while C₆₀ by thermal evaporation. Both are electron acceptors and are used as n-type semiconductors. Following this step, the device fabrication was completed by deposition of the cathode on top of the organic material: 1.2 nm of LiF followed by 150 nm of aluminum. LiF/Al is a common electrode used in organic solar cells and has been shown to be very suitable as a cathode for organic devices (OLED and organic photovoltaic) [252]–[262]. The device was illuminated on the side of the glass substrate and light therefore entered the device through the p-type layer.

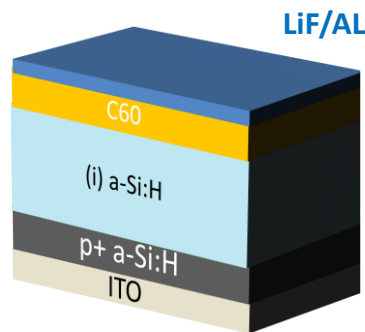


Figure 7-13: Schematic of the hybrid solar cells based on the combination of an organic layer with an amorphous thin film with a LiF/Al rear electrodes.

Three different thicknesses of C₆₀ were thermally evaporated: 30 nm, 15 nm, 5 nm, and compared with the reference cell with no C₆₀. The effect of the thickness of the organic layer on the performances of the hybrid devices is summarized in **Figure 7-14** while the performance of the devices is presented in **Table 7-3**.

Table 7-3: Effect of the thickness of C₆₀ on the average value of V_{oc} , J_{sc} , FF and η of planar hybrid a-Si:H / C₆₀ heterojunction

Cathode	V_{oc} (V)	J_{sc} (mA/cm ²)	FF (%)	η (%)
30 nm C₆₀	0,82±0.01	14.6±1.59	64.2±0.01	7.7±0.79
15 nm C₆₀	0,817±0.001	14.8±1.12	63.2±0.02	7.7±0.63
5 nm C₆₀	0.82±0.02	15.32±1.12	63.2±0.03	7.9±0.79
No C₆₀	0.85± 0.004	15.49± 0.19	63.21± 0.84	8.3±0.14

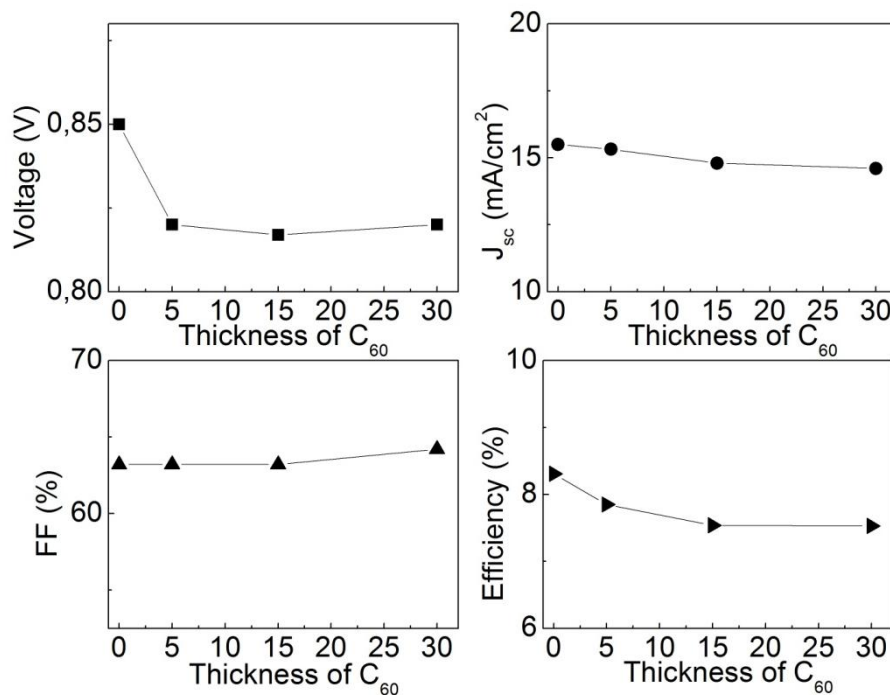


Figure 7-14: Effect of C₆₀ thickness on the performance of the solar cells.

Interestingly it appears that the presence of an organic layer is detrimental to the performance of these devices. The FF remains constant, while both J_{sc} and V_{oc} are reduced with increasing thickness of C₆₀. The reduction in J_{sc} can be explained by the absorption loss in the organic layer. The V_{oc} drops significantly, even for a small thickness of C₆₀ and remains constant upon increasing thickness of C₆₀. It indicates that more recombination is taking place in the hybrid device. It seems that the organic film only creates an additional barrier for charge carrier collection. Therefore the key interface is between the LiF/Al cathode and the amorphous layer and not with the organic layer. We observed a similar trend with PCBM. The performances are improved with the thinning of the PCBM layer and the maximum efficiency is always obtained for the device with the organic layer. Note that hybrid devices based on the combination of an organic material with a-Si:H were fabricated in controlled atmosphere: the fabrication and characterization were carried out in a glove box. The performance of such devices were degrading really fast when exposed to ambient atmosphere (less than 1 day).

These preliminary results reveal the importance of the LiF/Al - (i) a-Si:H interface. We have therefore decided to focus our next study on the

following device: SnO₂:F coated glass // (p) a-SiC:H //(i) a-Si:H // LiF/Al. This work is presented in the next section.

7.3 LiF/Al as a back contact for thin film solar cells based on a-Si:H

LiF/Al electrodes have been classically used as a cathode for enhancing the efficiency of OLED and plastic solar cell devices. A thin layer of LiF incorporated under the aluminum has been recognized to improve both the V_{oc} and FF of the devices. In this section we investigate the possibility to use this cathode in a Schottky device based on amorphous thin film. We study thin film solar cells based on a-Si:H without the use of any n-type doping layer. Upon insertion of an ultra thin (1.2 nm) insulating layer of LiF, the efficiency of the Schottky junction device has been found to increase by 98%, that is, from an initial average efficiency of 4.2% up to 8.3%. We investigate the effect of the thickness of the LiF layer and study the light stability of such devices.

7.3.1 Introduction

LiF/Al bilayer cathodes, made from the combination of a very thin insulating layer of LiF (typically about 1 to 2 nm) with a thick layer of Al, are commonly used for improving the efficiency of OLED and plastic solar cells [252]–[256], [258]–[260]. Indeed, it has been proven that the incorporation of a thin LiF layer between Al and the photoactive material can improve both the V_{oc} and FF of the cells. However, the underlying mechanisms are still not clear and several hypotheses are under investigation such as a dipole effect, a doping effect, a thermal protection effect or a passivation effect [257], [263]. Indeed, LiF has a strong dipole moment which once coupled with Al induces a vacuum level shift responsible for a more favorable band alignment [252], [254], [255]. This concept is illustrated in **Figure 7-15** for organic P3HT:PCBM solar cells. As for the doping effect, it is suggested that LiF might dissociate and dope the organic layer upon deposition of the hot aluminum atoms on the organic materials [261], [262], [264]. LiF can also play the role of an insulating buffer layer, protecting the organic material from the hot aluminum atoms during the metallic deposition. Finally one hypothesis considers direct tunneling between the (i) a-Si:H and LiF/Al electrode for small LiF thickness [263], [265].

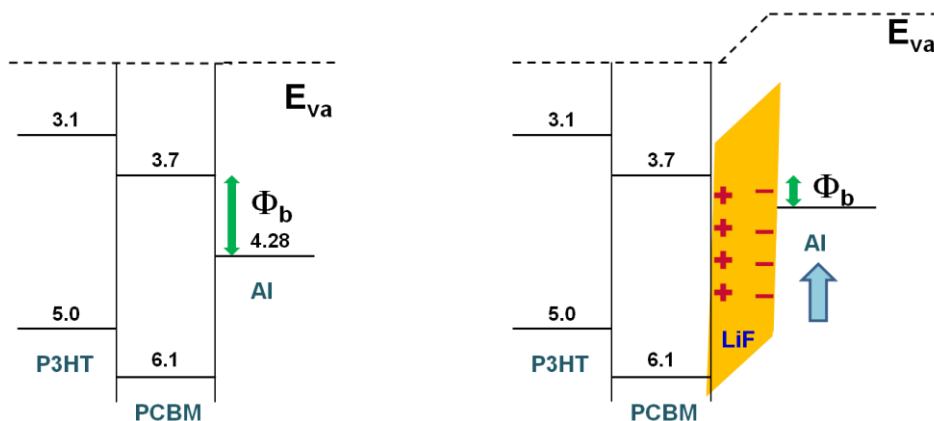


Figure 7-15: Schematic of the vacuum level shift induced by LiF/Al cathode for organic solar cells.

Although LiF/Al electrodes have been widely implemented for organic materials, few works have been published on the use of LiF/Al as a back contact for inorganic material [266], [267]. In 2011, *Liang Fang et al.* [266] studied the possibility to replace the n-type layer in a classical p-i-n a-Si:H thin film solar cells by a LiF/Al back electrode, and observed an improvement of 13% in the PCE compared to standard p-i-n junctions. Such approach is very promising as the n doped layer, whose role is to create an internal electric field within the intrinsic amorphous active layer, is considered as a “dead layer” since it does not contribute directly to the generation of current. Therefore eliminating this doped layer by an electrode with suitable work function is an exciting approach to enhance the efficiency and stability of such devices. Moreover, this would also eliminate the requirement of using toxic gas such as phosphine.

We have decided to focus our study on the combination of LiF/Al cathode with a-Si:H thin films as this design is promising for improving the performance in terms of efficiency and light stability of standard p-i-n junctions. We have therefore fabricated Schottky solar cells based on amorphous silicon thin films with both Al and LiF/Al cathodes whose structure is as follows: SnO₂:F coated glass // (p) a-SiC:H //(i) a-Si:H // LiF/Al or Al electrode. **Figure 7-16** shows the architecture of the device.

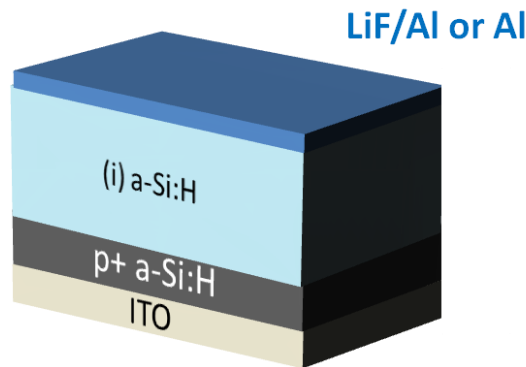


Figure 7-16: Schematic of the structure of the LiF/Al rear electrodes on (p+) a-SiC:H/(i) a-Si:H.

7.3.2 Experiments

The front electrode of the fabricated devices was a commercial fluorine-doped SnO₂ (SnO₂:F) coated glass (ASAHI substrate). The substrate was loaded into a PECVD chamber for the deposition of hydrogenated amorphous silicon carbide window layer (p) a-SiC:H and intrinsic amorphous silicon layer (i) a-Si:H. The deposition temperature was 175°C. The window layer (p) a-SiC:H was deposited at a RF power of 1 W from a gas mixture of hydrogen (H₂), silane (SiH₄), methane (CH₄) and trimethylboron (B(CH₃)₃) with an initial ratio of 40:25:100:20 for 230s, then 40:25:100:10 for the following 30s and finally 40:25:100:0 for the last 30s. A thin intrinsic amorphous silicon layer (i)-a-Si:H was then deposited using a mixture of silane (50 sccm) with hydrogen (40 sccm) at a RF power of 1 W for 1 min, followed by the deposition of pure silane for 105 min.

The samples were divided into 2 sets. For one set of samples, a 150 nm thick Al electrode was evaporated directly on the (i) a-Si:H layer, whereas for the other set, 1.2 nm of LiF was inserted between the intrinsic a-Si:H layer and the Al electrode. The electrodes were deposited by thermal evaporation through a shadow mask, and the thickness of the deposited layer was monitored by an in situ quartz crystal. The current density-voltage (J-V) characteristics of cells were measured under 100 mW/cm² illumination (AM 1.5G) with a solar simulator (Oriel AAA). The light intensity was calibrated using a Si reference cell.

7.3.3 Results and Discussion

7.3.3.1 Photovoltaic performances

Figure 7-17 shows the (J,V) curves of the two sets of samples. As depicted, there is a large difference between the samples with Al and LiF/Al cathodes. When the back electrode is made of a single Al layer, the (J,V) curve presents a S-shape instead of a proper diode behavior. The current is behaving normally at low bias and then gradually saturated when the forward bias approaches the open circuit voltage V_{oc} . Charge blocking / accumulation may be responsible for this kind of anomalous feature. The Schottky barrier height might be too large to ensure a proper charge collection. Another possibility concerns the formation upon contact of numerous induced gap states at the interface between intrinsic amorphous silicon and the metal, acting as recombination centers, hence a strong recombination loss. In contrast, the device with a LiF/Al electrode presents a proper diode behavior.

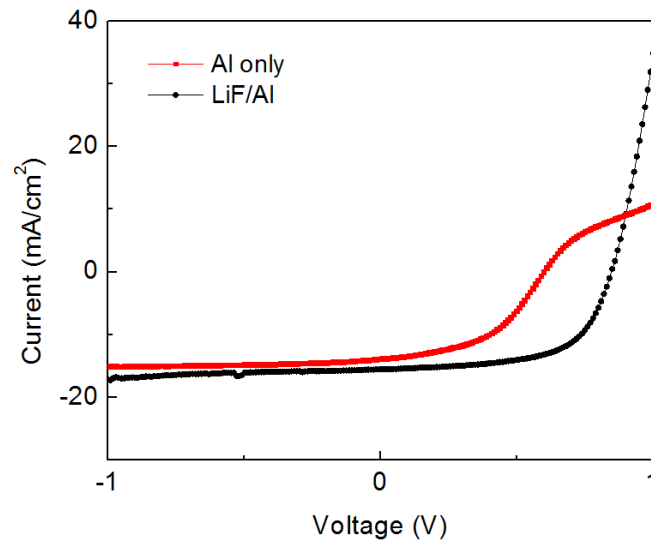


Figure 7-17: (J,V) curves of the thin film devices with LiF/Al cathode (black) and Al cathode (red).

The photovoltaic parameters (J_{sc} , FF , V_{oc} and η) are summarized in Table 7-4. We observe remarkable improvement in V_{oc} , J_{sc} , FF and efficiency of the device with a LiF/Al electrode. The V_{oc} increases by 39.2% while the photogenerated current increases by 13.5%. The series resistances and shunt resistances were extracted from the (J,V) curves. The devices with a thin LiF

interlayer present reduced series resistance (58.8 Ω) and increased shunt resistance (5364.4 Ω) which account for their improved performance. In comparison, the devices with only a single Al layer electrode show much higher series resistance (128.5 Ω) and smaller shunt resistance (1992 Ω). The reduction in series resistance and increase in shunt resistance explain the improvement in FF . The decrease in series resistance might come from direct tunneling at the LiF/Al cathode and the passivation of interfacial band gap states at the aluminum surface by LiF. As the strength of the internal electric field in the intrinsic a-Si:H layer is determined by the work function difference between (p+) a-SiC:H and the LiF/Al rear electrode, an enhanced electric field is expected for the lower workfunction LiF/Al as compared to Al alone. The better V_{oc} results from reduced shunt leakage and enhanced internal electric field.

Table 7-4: Comparison of photovoltaic parameters of thin film devices with Al cathode and LiF/Al cathode.

Cathode	V_{oc} (V)	J_{sc} (mA/cm ²)	FF (%)	η (%)
Al	0.61 \pm 0.01	13.65 \pm 0.22	50.67 \pm 2.34	4.20 \pm 0.19
LiF/Al	0.85 \pm 0.004	15.49 \pm 0.19	63.21 \pm 0.84	8.30 \pm 0.14

Moreover the photocurrent generated by the device with LiF/Al cathode is larger than that with Al back electrode. Such observation is confirmed by the External Quantum Efficiency (EQE) measurements of these two systems depicted in **Figure 7-18**, where the response of the LiF/Al devices is higher than the reference device with only aluminum as the back contact over the spectral range from 400 nm to 700 nm.

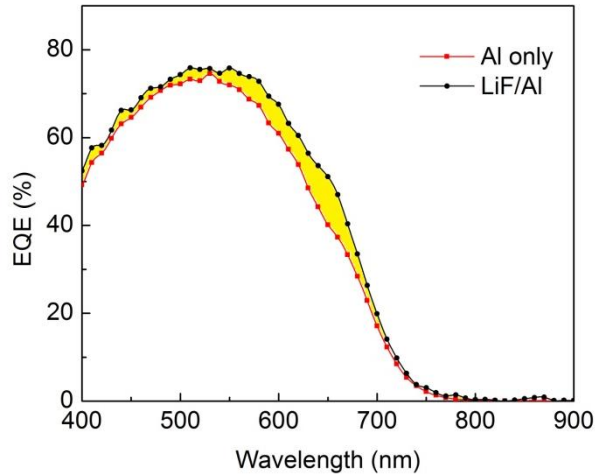


Figure 7-18: EQE curves of the thin film devices with LiF/Al cathode (black) and Al cathode (red)

This increase in the current for LiF/Al devices may come from a better absorption or collection of charges. A more favorable band alignment can make charge extraction easier. In the literature, it has also been suggested that the improvement in J_{sc} due to LiF/Al might come from an optical effect through reflectivity enhancement, therefore increasing the optical path and subsequent absorption within the device [268]. Such optical effect might partly explain the larger quantum efficiency observed for samples with a LiF/Al electrode. It was claimed that a potential increase of 7% of the photocurrent could be attributed to the increased rear electrode reflectivity [268]. In our case, we observe upon insertion of the 1.2 nm layer of LiF an increase in J_{sc} of 13.5 %. The improvement in J_{sc} can also be partially attributed to the difference in series resistance. Solar cells with a LiF/Al cathode show an average performance of 8.3% and our best cell achieve performance as high as 8.55%.

Figure 7-19 shows the proposed band diagram for the LiF/ Al device. The band diagram of a standard p-i-n junction is displayed as a reference. The electron-hole pairs are generated within the intrinsic layer and are separated by the internal electric field. When building the energy band diagram of the p-i-n junction, the fermi levels of the doped region must align. As the sandwiched intrinsic layer is free of charge, the variation of potential is determined by the doped layers and is simply calculated by subtracting from the band gap, the value of the fermi level of the n and p doped a-Si:H layer, with respect to their respective band edge E_c and E_v . We achieve a linear potential variation in the

order of 1.4-1.6 eV. As for the LiF/Al device, the electrons are collected at the LiF/Al cathode and holes are collected at the SnO₂:F electrode. Since there is no n-doped layer, the electrical field across the junction is determined by the value of the workfunction of the LiF/Al electrode. The workfunction of LiF/Al has been calculated and estimated between 2,5 – 3.5 eV [254], [269]. The potential variation at the metal/semiconductor interface is determined by equaling the workfunction of the electrode with the fermi level of the p-doped layer. We achieve a theoretical potential variation comprises between 2.1-3.1 eV. As a consequence, the electric field is larger for the device with the LiF/Al cathode than the device with the standard p-i-n architecture, making the drift process more efficient.

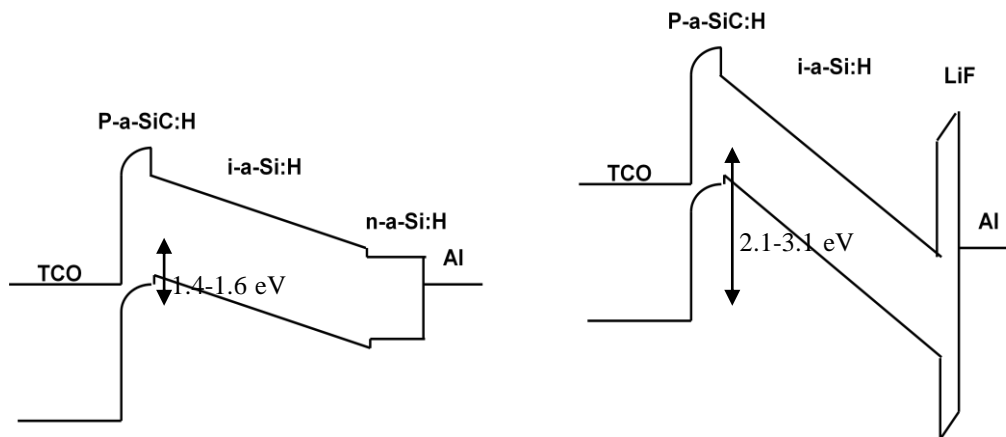


Figure 7-19: Schematic of the band diagram of p-i-n junction and a-Si:H thin film with a LiF/Al rear electrodes.

7.3.3.2 Effect of LiF thickness

The effect of the LiF thickness is also investigated. As LiF is an insulator, a variation in its thickness is expected to impact drastically the performances of the devices. Four series of samples were fabricated with varying LiF thicknesses: 1.2 nm, 5 nm, 10 nm and 50 nm. **Figure 7-20** shows the (J,V) curves of the devices and **Table 7-5** summarizes their photovoltaic parameters. In the absence of LiF or when LiF is too thick, the (J,V) curves exhibit a s-shape and flattened s-shape characteristics respectively.

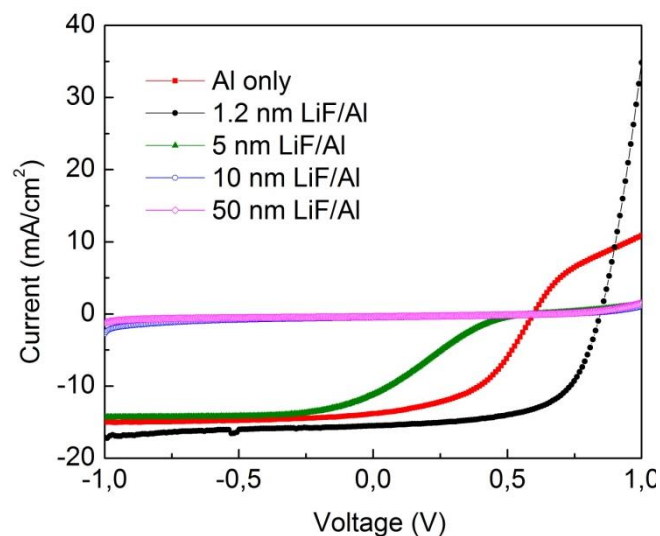


Figure 7-20: (J,V) curves of the thin film devices with LiF/Al cathode (black) and Al cathode (red).

When the thickness of LiF increases, the performances of the devices drop drastically and all photovoltaic parameters are degraded as shown in **Table 7-5**.

Table 7-5: Photovoltaic Performance - Effect of LiF thickness.

LiF thickness	V_{oc} (V)	J_{sc} (mA/cm ²)	FF (%)	η (%)
1.2 nm	0.85 ± 0.004	15.49 ± 0.19	63.21 ± 0.84	8.30 ± 0.14
5 nm	0.62±0.006	11.15±0.8	19.12±1.5	1.3±0.14
10 nm	0.61±0.06	0.52±0.05	3.4±3.4	0.01±0.08
50 nm	0.62±0.02	0.39±0.06	3.4±0.01	0.008±0.01

Indeed with increasing thickness, the morphology of the LiF film changes from a non-uniform cluster island structure to a continuous insulating layer [257]. This effect reminds us of the concept of point-contact solar cells where the contact with the metal is limited to an array of points while the regions between contacts are passivated [270]. The cells exhibit increased resistance with thicker LiF, as confirmed by the series resistances extracted from the (J,V) curves and shown in **Table 7-6**. This accounts for the very poor performances seen for cells with thicker layers of LiF.

Table 7-6: Effect of LiF thickness on the series resistances.

LiF thickness	1.2 nm	5 nm	10 nm	50 nm
R_{series} (Ω)	58.8	3095.3	6038	6642.6

7.3.3.3 Light soaking

We have investigated the effect of light soaking on the performances of the devices with LiF/Al cathodes, as displayed in **Figure 7-21** for a LiF thickness of 1.2 nm. Light degradation for this type of devices is an interesting study as the suppression of the n-type amorphous layer might improve the light stability of the device. We obtained an overall degradation of about 16-17%. We have analyzed the degradation for each photovoltaic parameter. Except the V_{oc} which first increases and remains stable, all other photovoltaic parameters have degraded. The decay curves can be divided into 2 zones, an initial fast

decay followed by a more gradual decay for a longer period of time before stabilization.

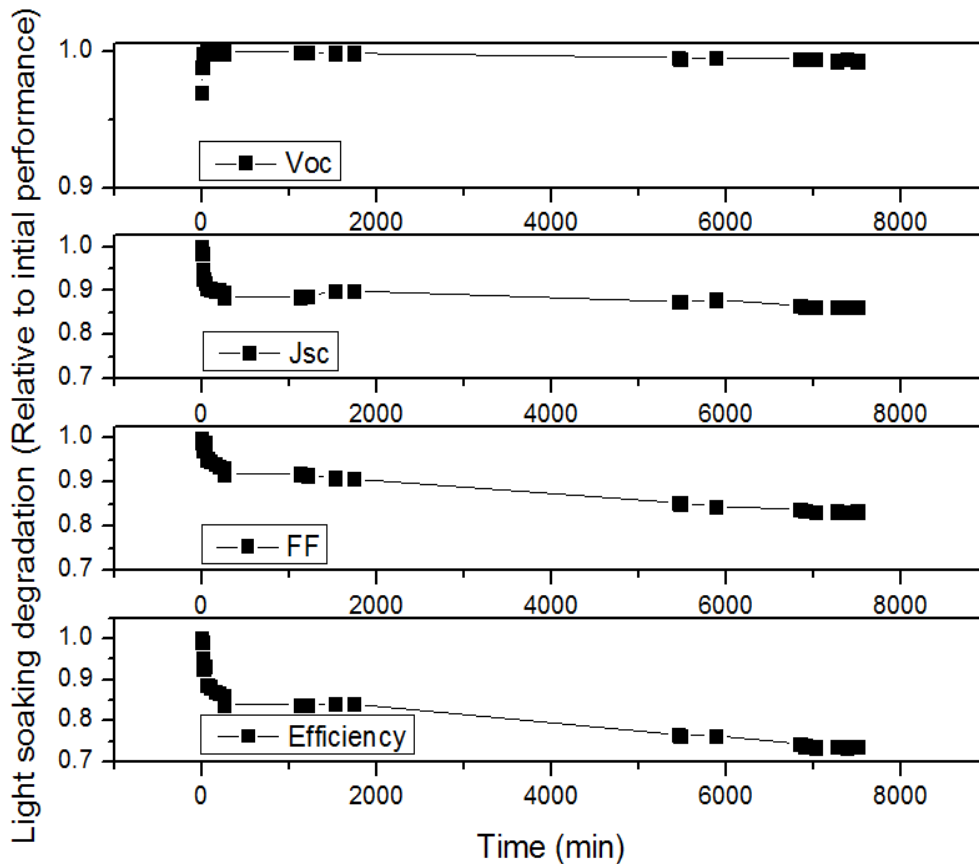


Figure 7-21: Light soaking effect on the cells' performances.

7.3.3.4 Effect of the electrode size

The effect of the electrode size on the performance of the devices is also studied. Note that the electrode size is the same as the sample size. Four series of samples with different sizes of electrodes - 0.0314 cm^2 , 0.1256 cm^2 , 0.2 cm^2 and 0.5 cm^2 - were fabricated. The effect of the electrode/sample size is shown in Figure 7-22.

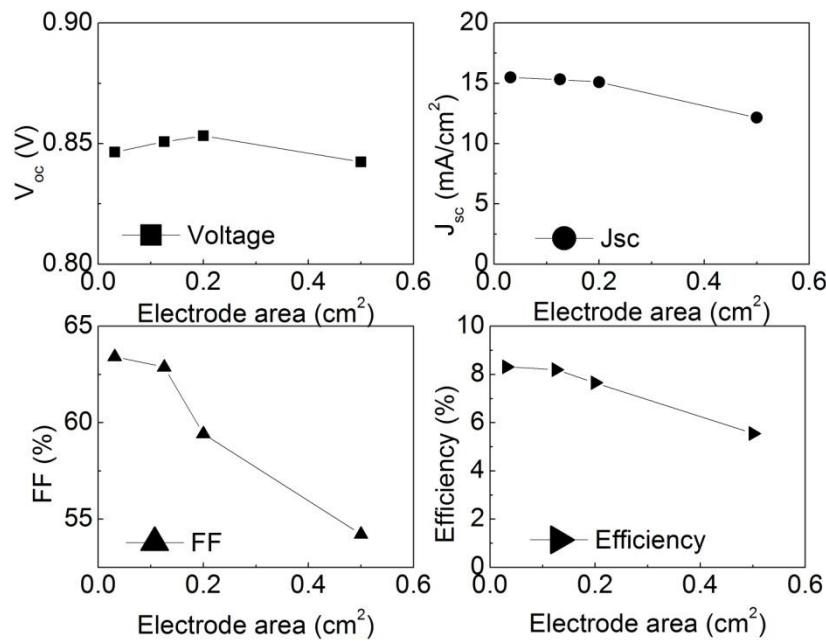


Figure 7-22: Effect of the electrode size on the solar cells' parameters

Most of the parameters degrade with increasing electrode size, except for V_{oc} which remains quite stable. The fill factor undergoes the sharpest drop while the J_{sc} decreases slightly. The series and shunt resistances were extracted from the (J,V) curves. The I_{sc} (A), R_{series} (Ω) and R_{shunt} (Ω) are area-related. For example, doubling the area of a cell should roughly decrease by half the parasitic resistances since the cross sectional area where the current can flow is multiply by two. In order to get a clear picture, we used specific resistance (per unit area in Ω/cm^2) and the data are summarized in **Table 7-7**. Interestingly the specific series resistance r_{series} decreases with the electrode area. Specific shunt resistance r_{shunt} decreases with increasing electrode size, which may account for the observed fall in FF and consequently drop in efficiency.

Table 7-7: Effect of the electrode size on the series and shunt resistances

Electrode area (cm ²)	0.0314	0.1256	0.2	0.5
r_{series} (Ω/cm^2)	132.6	58.8	32.8	24.6
r_{shunt} (Ω/cm^2)	46339	5364.4	4906.4	1688.6

In this section, we have investigated the role of LiF/Al electrode for Schottky thin films solar cells based on a-Si:H. We report an average efficiency of 8.3% for thin film solar cell based on a-Si:H without any n-type doping layer upon insertion of an ultra thin (1.2 nm) LiF insulating layer. LiF can replace the n-dead layer, which is responsible for significant optical and electrical losses in conventional p-i-n junction. Light soaking gives an average degradation of about 16-17% for this kind of devices.

Conclusion

In this chapter, we have fabricated efficient hybrid solar cells based on ordered and disordered SiNWs. Efficiency in the range of 9-9.5% were achieved for both ordered and disordered SiNWs and we do not observe any particular difference between devices made from both type of arrays. We have also developed a new method of deposition based on low-pressure which improves significantly the conformal coating of SiNWs by PEDOT:PSS. This will help to increase the area of the p-n junction while passivating parts of the SiNWs that were not coated by PEDOT:PSS. We have also investigated the potential of hybrid solar cells based on a-Si:H thin films with ordered and disordered a-Si:H NWs. We successfully fabricated both random and ordered a-Si:H NWs. Nevertheless, no convincing results were obtained with planar hybrid solar cells based on the combination of a-Si:H thin film layers with organic materials. We had a poor efficiency with PEDOT:PSS while C₆₀ and PCBM were degrading the overall performance of the device. However this work has allowed us to demonstrate the capabilities of LiF/Al electrode as a substitute of the (n) a-Si:H layer in standard p-i-n junction. Efficiency as high as 8.55% was achieved for schottky solar cells based on a-Si:H with a LiF/Al rear contact. This very simple fabrication process opens the door to highly efficient thin film solar cells without the use of the toxic phosphine gas. Next step include the fabrication of nanostructured a-Si:H thin film solar cells with LiF/Al cathode.

Chapter 8 : Conclusion and Future Work

8.1 Achievements:

In this PhD project, the potential of SiNWs for photovoltaic applications has been investigated. We have realized and optimized every step of the process, from the fabrication of the nanostructures to their implementation into different solar cells technologies, while performing a wide range of structural, optical and electrical characterization techniques to improve the understanding of SiNW arrays and solar cells.

Regarding fabrication, we have optimized the process of fabrication for disordered SiNWs by a detailed analysis of the wettability properties of both, the initial substrate before fabrication and the surface of the nanowires after fabrication. We showed that tuning the wettability properties of the initial substrate allows us to change the uniformity and the density of fabricated SiNWs, while changing the wettability of the SiNWs after fabrication impacts strongly their agglomeration. Furthermore, we have implemented a new method in NTU, EEE, to produce ordered arrays of SiNWs with excellent control over the pitch, diameter and length.

We have successfully integrated these SiNWs into HIT solar cells. A detailed study of the effects played by the thickness and the doping of the a-Si:H layer has been carried out. It has allowed us to achieve a record efficiency of 12.9% for HIT devices based on SiNWs. The devices are characterized by their excellent FF above 80% under the optimized conditions. We have also assessed, via EBIC measurements, that the SiNWs are contributing to the photogenerated current, although they are less efficient than the underlying bulk wafer. This demonstrates that the effect of SiNWs is not strictly limited to their excellent antireflective or light trapping properties.

We have also produced hybrid solar cells based on SiNWs with a good efficiency of about 9-9.5%. Interestingly, both ordered and disordered SiNWs revealed good efficiency while we were unable to achieve reasonable V_{oc} for HIT devices based on ordered SiNWs. We have developed and implemented a

new process to improve the conformal coating of the organic material around the SiNWs. We believe this technique may boost the performances of the hybrid devices. We have also fabricated hybrid solar cells based on the combination of an a-Si:H thin film with an organic material but such devices appear to have limited potential. However, through these structures, we have identified an extremely interesting effect played by the LiF/Al electrode. We have indeed shown that the latter can replace the dead n layer in standard p-i-n junction. The use of the toxic phosphine gas and the associated absorption losses in (n) a-Si:H can thus be eliminated.

Investigation of the optical properties of a large set of SiNW arrays with different geometries has proven that the optical properties strongly depend on the geometrical parameters such as the length, the diameter and density of the arrays produced. Finally, an optical model which can simulate the optical properties of a realistic SiNW array, taking into account the inherent defects due to the fabrication process, has been developed and compared with the experimental data. This statistical model is therefore a powerful tool to design and find the optimal geometrical conditions an array should respect in order to have maximal optical efficiency.

8.2 Future Work

We think that our results and techniques could lead to highly efficient SiNW solar cells based on a thin absorber layer. There is still room for a lot of improvement regarding the performance of HIT and hybrid solar cells.

The efficiency of HIT devices can be improved by tuning more finely the process conditions. The performances can be enhanced by optimizing the front and back contacts. For instance, a Ti/Pd/Ag back contact should be used for the HIT devices. Moreover, ITO should be optimized in terms of the thickness, transparency, mobility and work function. That will improve the charge collection efficiency of the devices. Another key point will be to improve the quality of the (p) layer. For example, the use of a material with larger band gap will decrease the absorption loss within this layer. Replacing the a-Si:H layers by microcrystalline ones can lead to better conductivity and

reduce absorption losses. Microcrystalline and amorphous oxide materials that are currently under development in LPICM are also of high interest since the incorporation of oxygen allow transmission over a wider spectral range and can thus potentially increase the J_{sc} . Finally, another key aspect will be to study various surface treatments to improve the quality of the surface of SiNWs. For example, we have recently developed a two-step surface treatment for removing residual silver nanoparticles left behind from the MACE process. The idea is to create first a thin oxide sacrificial layer by UV ozone followed by an HF bath to partially etch this layer. We have thus achieved a clean surface that has allowed us to improve the PCE of hybrid solar cells from 10% to 12.4% [112]. We expect that the application of such a surface treatment to SiNWs, before the fabrication of HIT solar cells, can improve drastically the performance of the cells.

We also believe that ordered SiNWs have the potential to boost the performance of HIT cells further. Indeed, the fabrication method by NSL assisted MACE is not only cost-efficient and fast, but it also provides a good control of the nanowires geometry, which is important for surface passivation. Indeed, the interspace between SiNWs can be controlled, making conformal coating of the passivation layer less challenging. Therefore we believe that some efforts should be focused on surface treatment of these wires to reduce the roughness and the porosity of the tip. We may consider to fabricate the SiNWs arrays before the removal of PS spheres. Thus the PS spheres can protect the top of the wires during the chemical etching step. This will require us to find an efficient way to remove the PS spheres at the end of the fabrication process, even when they fall and are trapped inside the array.

As for hybrid solar cells, we think that performances can also be improved by coating the organic layer by the low-pressure deposition technique developed during this thesis in order to achieve conformal coating of the wire by PEDOT:PSS. An ITO top contact for hybrid devices should also improve the collection efficiency.

Finally, the J_{sc} of solar cells based on SiNWs might be improved by using an optimized SiNW array whose geometrical parameters of pitch, length

and diameter can be computed using the optical model in order to achieve minimal reflectance. The use of a dual diameter SiNW arrays may also help to further improve the performance.

References:

- [1] U.S. Energy Information Administration (EIA), “Monthly Energy Review,” *Monthly Energy Review*, Mar-2015. [Online]. Available at: <http://www.eia.gov/>. [Accessed: 23-Jul-2015].
- [2] American Chemical Society, “Carbon dioxide from water pollution, as well as air pollution, may adversely impact oceans,” 19-Sep-2012. [Online]. Available at: <http://www.sciencedaily.com/releases/2012/09/120919125604.htm>. [Accessed: 23-Jul-2015].
- [3] M. Starr and W. Palz, *Photovoltaic Power for Europe: An Assessment Study*. Springer Science & Business Media, 1983.
- [4] International Energy Agency - Photovoltaic Power Systems Programme, “A snapshot of Global PV Markets 2014,” <http://www.iea-pvps.org>, 30-Mar-2015. [Online]. Available at: [http://www.iea-pvps.org/index.php?id=92&no_cache=1&tx_damfrontend_pi1\[showUid\]=2430&tx_damfrontend_pi1\[backPid\]=92](http://www.iea-pvps.org/index.php?id=92&no_cache=1&tx_damfrontend_pi1[showUid]=2430&tx_damfrontend_pi1[backPid]=92). [Accessed: 10-Jun-2015].
- [5] European Photovoltaic Industry Association, “Global Market Outlook - For Photovoltaics 2014-2018,” <http://www.epia.org>, 06-Dec-2014. [Online]. Available at: http://www.epia.org/fileadmin/user_upload/Publications/EPIA_Global_Market_Outlook_for_Photovoltaics_2014-2018_-_Medium_Res.pdf. [Accessed: 10-Jun-2015].
- [6] Ash Sharma - IHS, “Global Solar Installations to Grow by 30% to Reach 57 GW in 2015,” <https://technology.ihs.com>, 30-Mar-2015. [Online]. Available at: <https://technology.ihs.com/528029/global-solar-installations-to-grow-by-30-to-reach-57-gw-in-2015>. [Accessed: 10-Jun-2015].
- [7] International Energy Agency, “Medium Term Renewable Energy Market Report 2014,” <http://www.iea.org>, 04-Jan-2015. [Online]. Available at: <http://www.iea.org/Textbase/npsum/MTrenew2014sum.pdf>. [Accessed: 10-Jun-2015].
- [8] IHS Technology, “Top Solar Power Industry Trends for 2015,” <https://www.ihs.com/>, 21-May-2015. [Online]. Available at: <http://www.webcitation.org/6YhA2411f>. [Accessed: 10-Jun-2015].
- [9] Solarbuzz, “Technologies.” [Online]. Available at: <http://www.solarbuzz.com/going-solar/understanding/technologies>. [Accessed: 23-Jul-2015].
- [10] “Panasonic Press Release, 10 April 2014. Panasonic HIT® Solar Cell Achieves World’s Highest Energy Conversion Efficiency of 25.6% at Research Level | Headquarters News | Panasonic Global, (<http://panasonic.co.jp/corp/news/official.data.dir/2014/04/en140410-4/en140410-4.html>; accessed 24 April 2014).” [Online]. Available at: <http://news.panasonic.com/press/news/official.data/data.dir/2014/04/en140410-4/en140410-4.html>. [Accessed: 29-Oct-2014].
- [11] E. Wesoff, “Exclusive: First Solar’s CTO Discusses Record 18.6% Efficient Thin-Film Module : Greentech Media,” 15-Jun-2015. [Online]. Available at: <http://www.greentechmedia.com/articles/read/Exclusive-First-Solars-CTO-Discusses-Record-18.6-Efficient-Thin-Film-Mod>. [Accessed: 24-Jul-2015].
- [12] “CdTe Technology | First Solar.” [Online]. Available at: <http://www.firstsolar.com/en/technologies-and-capabilities/pv-modules/first-solar-series-3-black-module/cdte-technology>. [Accessed: 24-Jul-2015].
- [13] “ZSW: ZSW Brings World Record Back to Stuttgart.” [Online]. Available at: <http://www.zsw-bw.de/en/support/press-releases/press-detail/zsw-brings-world-record-back-to-stuttgart.html>. [Accessed: 24-Jul-2015].
- [14] “Investor Relations - Publications - Corporate News - Manz AG: New efficiency world record from exclusive research partner ZSW substantiates the technological advantage of CIGS thin film technology | Manz AG.” [Online]. Available at: <http://www.manz.com/>. [Accessed: 24-Jul-2015].
- [15] “TSMC Solar Commercial-size Modules (1.09m²) Set CIGS 16.5% Efficiency Record.” [Online]. Available at: <http://www.prnewswire.com/news-releases/tsmc-solar-commercial-size-modules-109m2-set-cigs-165-efficiency-record-300072332.html>. [Accessed: 24-Jul-2015].

- [16] J. S. Cashmore, M. Apolloni, A. Braga, O. Caglar, V. Cervetto, Y. Fenner, S. Goldbach-Aschemann, C. Goury, J. E. Hötzel, T. Iwahashi, J. Kalas, M. Kitamura, M. Klindworth, M. Kupich, G.-F. Leu, J. Lin, M.-H. Lindic, P. A. Losio, T. Mates, D. Matsunaga, B. Mereu, X.-V. Nguyen, I. Psimoulis, S. Ristau, T. Roschek, A. Salabas, E. L. Salabas, and I. Sinicco, "Record 12.34% stabilized conversion efficiency in a large area thin-film silicon tandem (MICROMORPH™) module," *Prog. Photovolt. Res. Appl.*, p. n/a–n/a, Jun. 2015.
- [17] H. Sai, T. Matsui, T. Koida, K. Matsubara, M. Kondo, S. Sugiyama, H. Katayama, Y. Takeuchi, and I. Yoshida, "Triple-junction thin-film silicon solar cell fabricated on periodically textured substrate with a stabilized efficiency of 13.6%," *Appl. Phys. Lett.*, vol. 106, no. 21, p. 213902, May 2015.
- [18] "Prof. Yan's Research Group."
- [19] "NREL: National Center for Photovoltaics Home Page." [Online]. Available at: <http://www.nrel.gov/ncpv/>. [Accessed: 24-Jul-2015].
- [20] L. He, C. Jiang, D. Lai, H. Wang, and others, "Highly efficient Si-nanorods/organic hybrid core-sheath heterojunction solar cells," *Appl. Phys. Lett.*, vol. 99, p. 021104, 2011.
- [21] E. C. Garnett, C. Peters, M. Brongersma, Y. Cui, and M. McGehee, "Silicon nanowire hybrid photovoltaics," in *Photovoltaic Specialists Conference (PVSC), 2010 35th IEEE*, pp. 000934–000938.
- [22] S. Günes and N. S. Sariciftci, "Hybrid solar cells," *Inorganica Chim. Acta*, vol. 361, no. 3, pp. 581–588, Feb. 2008.
- [23] P.-J. Alet, S. Palacin, P. Roca I Cabarrocas, B. Kalache, M. Firon, and R. de Bettignies, "Hybrid solar cells based on thin-film silicon and P3HT," *Eur. Phys. J. Appl. Phys.*, vol. 36, pp. 231–234, Jan. 2007.
- [24] A. Kojima, K. Teshima, Y. Shirai, and T. Miyasaka, "Organometal Halide Perovskites as Visible-Light Sensitizers for Photovoltaic Cells," *J. Am. Chem. Soc.*, vol. 131, no. 17, pp. 6050–6051, May 2009.
- [25] W. S. Yang, J. H. Noh, N. J. Jeon, Y. C. Kim, S. Ryu, J. Seo, and S. I. Seok, "High-performance photovoltaic perovskite layers fabricated through intramolecular exchange," *Science*, p. aaa9272, May 2015.
- [26] K.-Q. Peng and S.-T. Lee, "Silicon Nanowires for Photovoltaic Solar Energy Conversion," *Adv. Mater.*, vol. 23, pp. 198–215, Jan. 2011.
- [27] K. Peng, Y. Xu, Y. Wu, Y. Yan, S.-T. Lee, and J. Zhu, "Aligned Single-Crystalline Si Nanowire Arrays for Photovoltaic Applications," *Small*, vol. 1, pp. 1062–1067, Nov. 2005.
- [28] H. N. Cong, M. Dieng, C. Sene, and P. Chartier, "Hybrid organic-inorganic solar cells: Case of the all thin film PMeT(Y)/CdS(X) junctions," *Sol. Energy Mater. Sol. Cells*, vol. 63, no. 1, pp. 23–35, 2000.
- [29] A. P. Alivisatos, "Semiconductor Clusters, Nanocrystals, and Quantum Dots," *Science*, vol. 271, no. 5251, pp. 933–937, Feb. 1996.
- [30] D. C. Olson, S. E. Shaheen, R. T. Collins, and D. S. Ginley, "The Effect of Atmosphere and ZnO Morphology on the Performance of Hybrid Poly(3-hexylthiophene)/ZnO Nanofiber Photovoltaic Devices," *J Phys Chem C*, vol. 111, no. 44, pp. 16670–16678, 2007.
- [31] K. M. Coakley and M. D. McGehee, "Photovoltaic cells made from conjugated polymers infiltrated into mesoporous titania," *Appl. Phys. Lett.*, vol. 83, no. 16, pp. 3380–3382, Oct. 2003.
- [32] B. L. Williams, A. A. Taylor, B. G. Mendis, L. Phillips, L. Bowen, J. D. Major, and K. Durose, "Core-shell ITO/ZnO/CdS/CdTe nanowire solar cells," *Appl. Phys. Lett.*, vol. 104, no. 5, p. 053907, Feb. 2014.
- [33] R. Salazar, A. Delamoreanu, C. Levy-Clement, and V. Ivanova, "ZnO/CdTe and ZnO/CdS core-shell nanowire arrays for extremely thin absorber solar cells," *Energy Procedia*, vol. 10, pp. 122–127, 2011.
- [34] W. U. Huynh, "Hybrid Nanorod-Polymer Solar Cells," *Science*, vol. 295, pp. 2425–2427, Mar. 2002.
- [35] P. Chartier, H. Nguyen Cong, and C. Sene, "Hybrid organic-inorganic photovoltaic junctions: case of the all thin-film CdSe/poly(3-methylthiophene) junction," *Sol. Energy Mater. Sol. Cells*, vol. 52, no. 3–4, pp. 413–421, Apr. 1998.

- [36] L. B. Roberson, M. A. Poggi, J. Kowalik, G. P. Smestad, L. A. Bottomley, and L. M. Tolbert, "Correlation of morphology and device performance in inorganic-organic TiO₂-polythiophene hybrid solid-state solar cells," *Coord. Chem. Rev.*, vol. 248, no. 13-14, pp. 1491-1499, Jul. 2004.
- [37] M. Foldyna, L. Yu, and P. Roca i Cabarrocas, "Theoretical short-circuit current density for different geometries and organizations of silicon nanowires in solar cells," *Sol. Energy Mater. Sol. Cells*, vol. 117, pp. 645-651, Oct. 2013.
- [38] M. Foldyna, L. Yu, S. Misra, and P. Roca i Cabarrocas, "Light trapping enhancement in ordered and disordered silicon nanowire based solar cells," 2013, vol. 8824, p. 88240K-88240K-9.
- [39] "Impact of Both Series and Shunt Resistance | PVEducation," <http://www.pveducation.org>. [Online]. Available at: <http://www.pveducation.org/pvcdrom/solar-cell-operation/impact-of-both-resistances>. [Accessed: 10-Jun-2015].
- [40] Green, "Solar cell fill factors: General graph and empirical expressions," *Solid-State Electron.*, vol. 24, pp. 788-789, 1981.
- [41] Y. Wu, Y. Cui, L. Huynh, C. J. Barrelet, D. C. Bell, and C. M. Lieber, "Controlled Growth and Structures of Molecular-Scale Silicon Nanowires," *Nano Lett.*, vol. 4, pp. 433-436, Mar. 2004.
- [42] A. I. Hochbaum, R. Fan, R. He, and P. Yang, "Controlled Growth of Si Nanowire Arrays for Device Integration," *Nano Lett.*, vol. 5, no. 3, pp. 457-460, 2005.
- [43] J. V. Wittemann, W. Munchgesang, S. Senz, and V. Schmidt, "Silver catalyzed ultrathin silicon nanowires grown by low-temperature chemical-vapor-deposition," *J. Appl. Phys.*, vol. 107, no. 9, pp. 096105-096105, 2010.
- [44] P.-J. Alet, L. Yu, G. Patriarche, S. Palacin, and P. Roca i Cabarrocas, "In situ generation of indium catalysts to grow crystalline silicon nanowires at low temperature on ITO," *J. Mater. Chem.*, vol. 18, p. 5187, 2008.
- [45] L. Yu, B. O'Donnell, P. J. Alet, S. Conesa-Boj, F. Peiro, and J. Arbiol, "Plasma-enhanced low temperature growth of silicon nanowires and hierarchical structures by using tin and indium catalysts," *Nanotechnology*, vol. 20, p. 225604, 2009.
- [46] E. Garnett and P. Yang, "Light Trapping in Silicon Nanowire Solar Cells," *Nano Lett.*, vol. 10, no. 3, pp. 1082-1087, 2010.
- [47] K. J. Morton, G. Nieberg, S. Bai, and S. Y. Chou, "Wafer-scale patterning of sub-40 nm diameter and high aspect ratio (>50:1) silicon pillar arrays by nanoimprint and etching," *Nanotechnology*, vol. 19, p. 345301, Aug. 2008.
- [48] C.-M. Hsu, S. T. Connor, M. X. Tang, and Y. Cui, "Wafer-scale silicon nanopillars and nanocones by Langmuir-Blodgett assembly and etching," *Appl. Phys. Lett.*, vol. 93, p. 133109, 2008.
- [49] X. Li and P. W. Bohn, "Metal-assisted chemical etching in HF/H₂O produces porous silicon," *Appl. Phys. Lett.*, vol. 77, no. 16, p. 2572, 2000.
- [50] S. Kodambaka, J. Tersoff, M. C. Reuter, and F. M. Ross, "Diameter-Independent Kinetics in the Vapor-Liquid-Solid Growth of Si Nanowires," *Phys. Rev. Lett.*, vol. 96, no. 9, p. 096105, Mar. 2006.
- [51] V. G. Dubrovskii, T. Xu, Y. Lambert, J.-P. Nys, B. Grandidier, D. Stiévenard, W. Chen, and P. Pareige, "Narrowing the Length Distribution of Ge Nanowires," *Phys. Rev. Lett.*, vol. 108, no. 10, p. 105501, Mar. 2012.
- [52] W. H. Chen, R. Lardé, E. Cadel, T. Xu, B. Grandidier, J. P. Nys, D. Stiévenard, and P. Pareige, "Study of the effect of gas pressure and catalyst droplets number density on silicon nanowires growth, tapering, and gold coverage," *J. Appl. Phys.*, vol. 107, no. 8, p. 084902, Apr. 2010.
- [53] R. S. Wagner, W. C. Ellis, K. A. Jackson, and S. M. Arnold, "Study of the Filamentary Growth of Silicon Crystals from the Vapor," *J. Appl. Phys.*, vol. 35, no. 10, pp. 2993-3000, Oct. 1964.
- [54] E. Comini, C. Baratto, G. Faglia, M. Ferroni, A. Vomiero, and G. Sberveglieri, "Quasi-one dimensional metal oxide semiconductors: Preparation, characterization and application as chemical sensors," *Prog. Mater. Sci.*, vol. 54, no. 1, pp. 1-67, Jan. 2009.
- [55] S. Misra, L. Yu, M. Foldyna, and P. Roca i Cabarrocas, "High efficiency and stable hydrogenated amorphous silicon radial junction solar cells built on VLS-grown silicon nanowires," *Sol. Energy Mater. Sol. Cells*, vol. 118, pp. 90-95, Nov. 2013.

- [56] S. Misra, L. Yu, M. Foldyna, and P. Roca i Cabarrocas, "New Approaches to Improve the Performance of Thin-Film Radial Junction Solar Cells Built Over Silicon Nanowire Arrays," *IEEE J. Photovolt.*, vol. 5, no. 1, pp. 40–45, Jan. 2015.
- [57] A. J. Tavendale and S. J. Pearton, "Deep level, quenched-in defects in silicon doped with gold, silver, iron, copper or nickel," *J. Phys. C Solid State Phys.*, vol. 16, no. 9, p. 1665, Mar. 1983.
- [58] S. Misra, L. Yu, W. Chen, M. Foldyna, and P. R. i Cabarrocas, "A review on plasma-assisted VLS synthesis of silicon nanowires and radial junction solar cells," *J. Phys. Appl. Phys.*, vol. 47, no. 39, p. 393001, Oct. 2014.
- [59] S. Mitsugi, F. Koyama, and A. Matsutani, "Correlation Length Measurement of Sidewall Roughness of Dry Etched Facet and Its Effect on Reflectivity," *Opt. Rev.*, vol. 6, no. 4, pp. 378–379, Jul. 1999.
- [60] Z. Huang, N. Geyer, P. Werner, J. de Boor, and U. Gösele, "Metal-Assisted Chemical Etching of Silicon: A Review," *Adv. Mater.*, vol. 23, pp. 285–308, Jan. 2011.
- [61] K. Q. Peng, J. J. Hu, Y. J. Yan, Y. Wu, H. Fang, Y. Xu, S. T. Lee, and J. Zhu, "Fabrication of Single-Crystalline Silicon Nanowires by Scratching a Silicon Surface with Catalytic Metal Particles," *Adv. Funct. Mater.*, vol. 16, pp. 387–394, Feb. 2006.
- [62] K. Peng, Y. Wu, H. Fang, X. Zhong, Y. Xu, and J. Zhu, "Uniform, Axial-Orientation Alignment of One-Dimensional Single-Crystal Silicon Nanostructure Arrays," *Angew. Chem. Int. Ed.*, vol. 44, no. 18, pp. 2737–2742, 2005.
- [63] S. K. Srivastava, D. Kumar, P. K. Singh, M. Kar, V. Kumar, and M. Husain, "Excellent antireflection properties of vertical silicon nanowire arrays," *Sol. Energy Mater. Sol. Cells*, vol. 94, no. 9, pp. 1506–1511, Sep. 2010.
- [64] Z. Huang, H. Fang, and J. Zhu, "Fabrication of Silicon Nanowire Arrays with Controlled Diameter, Length, and Density," *Adv. Mater.*, vol. 19, no. 5, pp. 744–748, Mar. 2007.
- [65] S. C. Shiu, J. J. Chao, S. C. Hung, C. L. Yeh, and C. F. Lin, "Morphology dependence of silicon nanowire/poly (3, 4-ethylenedioxythiophene): poly (styrenesulfonate) heterojunction solar cells," *Chem. Mater.*, vol. 22, no. 10, pp. 3108–3113, 2010.
- [66] J.-Y. Jung, Z. Guo, S.-W. Jee, H.-D. Um, K.-T. Park, and J.-H. Lee, "A strong antireflective solar cell prepared by tapering silicon nanowires," *Opt. Express*, vol. 18, no. S3, pp. A286–A292, 2010.
- [67] J. Zhu, Z. Yu, G. F. Burkhard, C.-M. Hsu, S. T. Connor, Y. Xu, Q. Wang, M. McGehee, S. Fan, and Y. Cui, "Optical Absorption Enhancement in Amorphous Silicon Nanowire and Nanocone Arrays," *Nano Lett.*, vol. 9, no. 1, pp. 279–282, Jan. 2009.
- [68] E. C. Garnett, M. L. Brongersma, Y. Cui, and M. D. McGehee, "Nanowire Solar Cells," *Annu. Rev. Mater. Res.*, vol. 41, no. 1, pp. 269–295, Aug. 2011.
- [69] V. Sivakov, G. Andrä, A. Gawlik, A. Berger, J. Plentz, F. Falk, and S. H. Christiansen, "Silicon Nanowire-Based Solar Cells on Glass: Synthesis, Optical Properties, and Cell Parameters," *Nano Lett.*, vol. 9, no. 4, pp. 1549–1554, Apr. 2009.
- [70] William L. Bailey, Michael G. Coleman, Cynthia B. Harris, Israel A. Lesk, "Texture etching of silicon: method," US4137123 A, 30-Jan-1979.
- [71] E. Yablonovitch and G. D. Cody, "Intensity enhancement in textured optical sheets for solar cells," *IEEE Trans. Electron Devices*, vol. 29, no. 2, pp. 300–305, Feb. 1982.
- [72] D. M. Callahan, J. N. Munday, and H. A. Atwater, "Solar Cell Light Trapping beyond the Ray Optic Limit," *Nano Lett.*, vol. 12, no. 1, pp. 214–218, Jan. 2012.
- [73] A. Chutinan, N. P. Kherani, and S. Zukotynski, "High-efficiency photonic crystal solar cell architecture," *Opt. Express*, vol. 17, no. 11, p. 8871, May 2009.
- [74] S. E. Han and G. Chen, "Toward the Lambertian Limit of Light Trapping in Thin Nanostructured Silicon Solar Cells," *Nano Lett.*, vol. 10, no. 11, pp. 4692–4696, Nov. 2010.
- [75] Z. Yu, A. Raman, and S. Fan, "Fundamental limit of nanophotonic light trapping in solar cells," *Proc. Natl. Acad. Sci.*, vol. 107, no. 41, pp. 17491–17496, Oct. 2010.
- [76] M. A. Green, "Enhanced evanescent mode light trapping in organic solar cells and other low index optoelectronic devices," *Prog. Photovolt. Res. Appl.*, vol. 19, no. 4, pp. 473–477, Jun. 2011.
- [77] L. Hu and G. Chen, "Analysis of Optical Absorption in Silicon Nanowire Arrays for Photovoltaic Applications," *Nano Lett.*, vol. 7, no. 11, pp. 3249–3252, Nov. 2007.

- [78] J. Li, H. Yu, S. M. Wong, X. Li, G. Zhang, P. G.-Q. Lo, and D.-L. Kwong, "Design guidelines of periodic Si nanowire arrays for solar cell application," *Appl. Phys. Lett.*, vol. 95, no. 24, p. 243113, Dec. 2009.
- [79] M. Nolan, S. O'Callaghan, G. Fagas, J. C. Greer, and T. Fraunheim, "Silicon Nanowire Band Gap Modification," *Nano Lett.*, vol. 7, no. 1, pp. 34–38, Jan. 2007.
- [80] F. Sacconi, M. P. Persson, M. Povolotskyi, L. Latessa, A. Pecchia, A. Gagliardi, A. Balint, T. Fraunheim, and A. D. Carlo, "Electronic and transport properties of silicon nanowires," *J. Comput. Electron.*, vol. 6, no. 1–3, pp. 329–333, Jan. 2007.
- [81] Y. Cui, Z. Zhong, D. Wang, W. U. Wang, and C. M. Lieber, "High Performance Silicon Nanowire Field Effect Transistors," *Nano Lett.*, vol. 3, no. 2, pp. 149–152, Feb. 2003.
- [82] B. K. Teo and X. H. Sun, "Silicon-Based Low-Dimensional Nanomaterials and Nanodevices," *Chem. Rev.*, vol. 107, pp. 1454–1532, May 2007.
- [83] Y. Kobayashi and S. Adachi, "Properties of Si Nanowires Synthesized by Galvanic Cell Reaction," *Jpn. J. Appl. Phys.*, vol. 49, p. 075002, Jul. 2010.
- [84] C. Lévy-Clément, R. Tena-Zaera, M. A. Ryan, A. Katty, and G. Hodes, "CdSe-Sensitized p-CuSCN/Nanowire n-ZnO Heterojunctions," *Adv. Mater.*, vol. 17, no. 12, pp. 1512–1515, Jun. 2005.
- [85] W. U. Huynh, J. J. Dittmer, N. Tecler, D. J. Milliron, A. P. Alivisatos, and K. W. J. Barnham, "Charge transport in hybrid nanorod-polymer composite photovoltaic cells," *Phys. Rev. B*, vol. 67, no. 11, p. 115326, Mar. 2003.
- [86] Z. Fan, H. Razavi, J. Do, A. Moriwaki, O. Ergen, Y.-L. Chueh, P. W. Leu, J. C. Ho, T. Takahashi, L. A. Reichertz, S. Neale, K. Yu, M. Wu, J. W. Ager, and A. Javey, "Three-dimensional nanopillar-array photovoltaics on low-cost and flexible substrates," *Nat. Mater.*, vol. 8, no. 8, pp. 648–653, Aug. 2009.
- [87] Y. Dong, B. Tian, T. J. Kempa, and C. M. Lieber, "Coaxial Group III–Nitride Nanowire Photovoltaics," *Nano Lett.*, vol. 9, no. 5, pp. 2183–2187, May 2009.
- [88] C. Colombo, M. Heiss, M. Grätzel, and A. Fontcuberta i Morral, "Gallium arsenide pin radial structures for photovoltaic applications," *Appl. Phys. Lett.*, vol. 94, no. EPFL-ARTICLE-148563, 2009.
- [89] L. Cao, J.-S. Park, P. Fan, B. Clemens, and M. L. Brongersma, "Resonant Germanium Nanoantenna Photodetectors," *Nano Lett.*, vol. 10, no. 4, pp. 1229–1233, Apr. 2010.
- [90] W. Wei, X.-Y. Bao, C. Soci, Y. Ding, Z.-L. Wang, and D. Wang, "Direct Heteroepitaxy of Vertical InAs Nanowires on Si Substrates for Broad Band Photovoltaics and Photodetection," *Nano Lett.*, vol. 9, no. 8, pp. 2926–2934, Aug. 2009.
- [91] O. K. Varghese, M. Paulose, and C. A. Grimes, "Long vertically aligned titania nanotubes on transparent conducting oxide for highly efficient solar cells," *Nat. Nanotechnol.*, vol. 4, no. 9, pp. 592–597, Sep. 2009.
- [92] S. S. Williams, M. J. Hampton, V. Gowrishankar, I.-K. Ding, J. L. Templeton, E. T. Samulski, J. M. DeSimone, and M. D. McGehee, "Nanostructured Titania–Polymer Photovoltaic Devices Made Using PFPE-Based Nanomolding Techniques," *Chem. Mater.*, vol. 20, no. 16, pp. 5229–5234, Aug. 2008.
- [93] L. E. Greene, M. Law, B. D. Yuhas, and P. Yang, "ZnO–TiO₂ Core–Shell Nanorod/P3HT Solar Cells," *J. Phys. Chem. C*, vol. 111, no. 50, pp. 18451–18456, Dec. 2007.
- [94] K. Takanezawa, K. Tajima, and K. Hashimoto, "Efficiency enhancement of polymer photovoltaic devices hybridized with ZnO nanorod arrays by the introduction of a vanadium oxide buffer layer," *Appl. Phys. Lett.*, vol. 93, no. 6, p. 063308, Aug. 2008.
- [95] B. D. Yuhas and P. Yang, "Nanowire-Based All-Oxide Solar Cells," *J. Am. Chem. Soc.*, vol. 131, no. 10, pp. 3756–3761, Mar. 2009.
- [96] A. L. Briseno, T. W. Holcombe, A. I. Boukai, E. C. Garnett, S. W. Shelton, J. J. M. Fréchet, and P. Yang, "Oligo- and Polythiophene/ZnO Hybrid Nanowire Solar Cells," *Nano Lett.*, vol. 10, no. 1, pp. 334–340, Jan. 2010.
- [97] K. Wang, J. J. Chen, Z. M. Zeng, J. Tarr, W. L. Zhou, Y. Zhang, Y. F. Yan, C. S. Jiang, J. Pern, and A. Mascarenhas, "Synthesis and photovoltaic effect of vertically aligned ZnO/ZnS core/shell nanowire arrays," *Appl. Phys. Lett.*, vol. 96, no. 12, p. 123105, Mar. 2010.
- [98] H. Fang, X. Li, S. Song, Y. Xu, and J. Zhu, "Fabrication of slantingly-aligned silicon nanowire arrays for solar cell applications," *Nanotechnology*, vol. 19, p. 255703, 2008.

- [99] X. X. Lin, X. Hua, Z. G. Huang, and W. Z. Shen, "Realization of high performance silicon nanowire based solar cells with large size," *Nanotechnology*, vol. 24, no. 23, p. 235402, Jun. 2013.
- [100] D. Kumar, S. K. Srivastava, P. K. Singh, M. Husain, and V. Kumar, "Fabrication of silicon nanowire arrays based solar cell with improved performance," *Sol. Energy Mater. Sol. Cells*, vol. 95, no. 1, pp. 215–218, Jan. 2011.
- [101] B.-R. Huang, Y.-K. Yang, T.-C. Lin, and W.-L. Yang, "A simple and low-cost technique for silicon nanowire arrays based solar cells," *Sol. Energy Mater. Sol. Cells*, vol. 98, pp. 357–362, Mar. 2012.
- [102] J. Oh, H.-C. Yuan, and H. M. Branz, "An 18.2%-efficient black-silicon solar cell achieved through control of carrier recombination in nanostructures," *Nat. Nanotechnol.*, vol. 7, no. 11, pp. 743–748, Nov. 2012.
- [103] H. Savin, P. Repo, G. von Gastrow, P. Ortega, E. Calle, M. Garín, and R. Alcubilla, "Black silicon solar cells with interdigitated back-contacts achieve 22.1% efficiency," *Nat. Nanotechnol.*, vol. 10, no. 7, pp. 624–628, Jul. 2015.
- [104] Y. Lu and A. Lal, "High-Efficiency Ordered Silicon Nano-Conical-Frustum Array Solar Cells by Self-Powered Parallel Electron Lithography," *Nano Lett.*, vol. 10, no. 11, pp. 4651–4656, Nov. 2010.
- [105] M. Tanaka, M. Taguchi, T. Matsuyama, T. Sawada, S. Tsuda, S. Nakano, H. Hanafusa, and Y. Kuwano, "Development of New a-Si/c-Si Heterojunction Solar Cells: ACJ-HIT (Artificially Constructed Junction-Heterojunction with Intrinsic Thin-Layer)," *Jpn. J. Appl. Phys.*, vol. 31, no. 11R, p. 3518, Nov. 1992.
- [106] G. Jia, M. Steglich, I. Sill, and F. Falk, "Core-shell heterojunction solar cells on silicon nanowire arrays," *Sol. Energy Mater. Sol. Cells*, vol. 96, pp. 226–230, Jan. 2012.
- [107] G. Jia, B. Eisenhawer, J. Dellith, F. Falk, A. Thøgersen, and A. Ulyashin, "Multiple Core-Shell Silicon Nanowire-Based Heterojunction Solar Cells," *J. Phys. Chem. C*, vol. 117, no. 2, pp. 1091–1096, Jan. 2013.
- [108] G. Jia, A. Gawlik, J. Bergmann, B. Eisenhawer, S. Schonherr, G. Andra, and F. Falk, "Silicon Nanowire Solar Cells With Radial p-n Heterojunction on Crystalline Silicon Thin Films: Light Trapping Properties," *IEEE J. Photovolt.*, vol. 4, no. 1, pp. 28–32, Jan. 2014.
- [109] K. Li, X. Wang, P. Lu, J. Ding, and N. Yuan, "The influence of passivation and photovoltaic properties of α -Si:H coverage on silicon nanowire array solar cells," *Nanoscale Res. Lett.*, vol. 8, no. 1, p. 396, Sep. 2013.
- [110] M. Gharghi, E. Fathi, B. Kante, S. Sivoththaman, and X. Zhang, "Heterojunction Silicon Microwave Solar Cells," *Nano Lett.*, vol. 12, no. 12, pp. 6278–6282, Dec. 2012.
- [111] Lining He, Rusli, Changyun Jiang, Hao Wang, and D. Lai, "Simple Approach of Fabricating High Efficiency Si Nanowire/Conductive Polymer Hybrid Solar Cells," *IEEE Electron Device Lett.*, vol. 32, no. 10, pp. 1406–1408, Oct. 2011.
- [112] J. Wang, H. Wang, A. B. Prakoso, A. S. Togonal, L. Hong, C. Jiang, and Rusli, "High efficiency silicon nanowire/organic hybrid solar cells with two-step surface treatment," *Nanoscale*, vol. 7, no. 10, pp. 4559–4565, Feb. 2015.
- [113] D. Kumar, S. K. Srivastava, P. Singh, M. Husain, and V. Kumar, "Fabrication of silicon nanowire arrays based solar cell with improved performance," *Sol. Energy Mater. Sol. Cells*, vol. 95, no. 1, pp. 215–218, 2011.
- [114] E. C. Garnett and P. Yang, "Silicon Nanowire Radial p-n Junction Solar Cells," *J. Am. Chem. Soc.*, vol. 130, no. 29, pp. 9224–9225, Jul. 2008.
- [115] G. Kalita, S. Adhikari, H. R. Aryal, R. Afre, T. Soga, M. Sharon, W. Koichi, and M. Umeno, "Silicon nanowire array/polymer hybrid solar cell incorporating carbon nanotubes," *J. Phys. Appl. Phys.*, vol. 42, p. 115104, 2009.
- [116] J.-S. Huang, C.-Y. Hsiao, S.-J. Syu, J.-J. Chao, and C.-F. Lin, "Well-aligned single-crystalline silicon nanowire hybrid solar cells on glass," *Sol. Energy Mater. Sol. Cells*, vol. 93, pp. 621–624, May 2009.
- [117] L. He, C. Jiang, H. Wang, D. Lai, Y. Heng Tan, C. Seng Tan, and Rusli, "Effects of nanowire texturing on the performance of Si/organic hybrid solar cells fabricated with a 2.2 μm thin-film Si absorber," *Appl. Phys. Lett.*, vol. 100, no. 10, p. 103104, 2012.
- [118] S. Jeong, E. C. Garnett, S. Wang, Z. Yu, S. Fan, M. L. Brongersma, M. D. McGehee, and Y. Cui, "Hybrid Silicon Nanocone-Polymer Solar Cells," *Nano Lett.*, vol. 12, no. 6, pp. 2971–2976, Jun. 2012.

- [119] B. O'Donnell, L. Yu, M. Foldyna, and P. Roca i Cabarrocas, "Silicon nanowire solar cells grown by PECVD," *J. Non-Cryst. Solids*, vol. 358, no. 17, pp. 2299–2302, Sep. 2012.
- [120] A. Luque and S. Hegedus, *Handbook of photovoltaic science and engineering*. Hoboken, NJ: Wiley, 2003.
- [121] "Open course - Delft University - CH7 Thin-film Si solar cells." [Online]. Available at: http://ocw.tudelft.nl/fileadmin/ocw/courses/SolarCells/res00030/CH7_Thin_film_Si_solar_cells.pdf. [Accessed: 03-Jun-2013].
- [122] *Handbook of the Physics of Thin-film Solar Cells*. Springer Verlag, 2013.
- [123] J. C. van den Heuvel, M. J. Geerts, and J. W. Metselaar, "The relation between the optical properties and the hydrogen concentration in a-Si:H," *Sol. Energy Mater.*, vol. 22, no. 2–3, pp. 185–194, Jul. 1991.
- [124] T. Mishima, M. Taguchi, H. Sakata, and E. Maruyama, "Development status of high-efficiency HIT solar cells," *Sol. Energy Mater. Sol. Cells*, vol. 95, no. 1, pp. 18–21, Jan. 2011.
- [125] Miro Zeman, "Heterojunction silicon based solar cells," <http://www.jointsolarpanel.nl>. [Online]. Available at: http://www.jointsolarpanel.nl/fileadmin/jointsolarpanel/user/documents/seminar2009/4_Miro_Zeman_Delft_University_of_Technology.pdf. [Accessed: 12-Jun-2015].
- [126] Martin Labrune, "Silicon surface passivation and epitaxial growth on c-Si by low temperature plasma processes for high efficiency solar cells," <https://tel.archives-ouvertes.fr>. [Online]. Available at: <https://tel.archives-ouvertes.fr/pastel-00611652/document>. [Accessed: 12-Jun-2015].
- [127] Y. Liu, Y. Sun, W. Liu, and J. Yao, "Novel high-efficiency crystalline-silicon-based compound heterojunction solar cells: HCT (heterojunction with compound thin-layer)," *Phys. Chem. Chem. Phys.*, vol. 16, no. 29, pp. 15400–15410, Jul. 2014.
- [128] M. Tanaka, S. Okamoto, S. Tsuge, and S. Kiyama, "Development of hit solar cells with more than 21% conversion efficiency and commercialization of highest performance hit modules," in *Proceedings of 3rd World Conference on Photovoltaic Energy Conversion, 2003*, 2003, vol. 1, pp. 955–958 Vol.1.
- [129] Y. Tsunomura, Y. Yoshimine, M. Taguchi, T. Baba, T. Kinoshita, H. Kanno, H. Sakata, E. Maruyama, and M. Tanaka, "Twenty-two percent efficiency HIT solar cell," *Sol. Energy Mater. Sol. Cells*, vol. 93, no. 6–7, pp. 670–673, Jun. 2009.
- [130] E. Maruyama, A. Terakawa, M. Taguchi, Yukihiro Yoshimine, D. Ide, Toshiaki Baba, M. Shima, H. Sakata, and M. Tanaka, "Sanyo's Challenges to the Development of High-efficiency HIT Solar Cells and the Expansion of HIT Business," in *Conference Record of the 2006 IEEE 4th World Conference on Photovoltaic Energy Conversion, 2006*, vol. 2, pp. 1455–1460.
- [131] M. Taguchi, K. Kawamoto, S. Tsuge, T. Baba, H. Sakata, M. Morizane, K. Uchihashi, N. Nakamura, S. Kiyama, and O. Oota, "HITTM cells—high-efficiency crystalline Si cells with novel structure," *Prog. Photovolt. Res. Appl.*, vol. 8, no. 5, pp. 503–513, Sep. 2000.
- [132] T. Sawada, N. Terada, S. Tsuge, Toshiaki Baba, T. Takahama, K. Wakisaka, S. Tsuda, and S. Nakano, "High-efficiency a-Si/c-Si heterojunction solar cell," in *IEEE Photovoltaic Specialists Conference - 1994, 1994 IEEE First World Conference on Photovoltaic Energy Conversion, 1994., Conference Record of the Twenty Fourth, 1994*, vol. 2, pp. 1219–1226 vol.2.
- [133] M. Skompska, "Hybrid conjugated polymer/semiconductor photovoltaic cells," *Synth. Met.*, vol. 160, no. 1–2, pp. 1–15, 2010.
- [134] S. C. J. Meskers, J. Hübner, M. Oestreich, and H. Bässler, "Dispersive Relaxation Dynamics of Photoexcitations in a Polyfluorene Film Involving Energy Transfer: Experiment and Monte Carlo Simulations," *J Phys Chem B*, vol. 105, no. 38, pp. 9139–9149, 2001.
- [135] K. E. Ziemelis, A. T. Hussain, D. D. C. Bradley, R. H. Friend, J. Rühle, and G. Wegner, "Optical spectroscopy of field-induced charge in poly(3-hexyl thienylene) metal-insulator-semiconductor structures: Evidence for polarons," *Phys. Rev. Lett.*, vol. 66, no. 17, pp. 2231–2234, Apr. 1991.
- [136] N. T. Harrison, G. R. Hayes, R. T. Phillips, and R. H. Friend, "Singlet Intrachain Exciton Generation and Decay in Poly(p-phenylenevinylene)," *Phys. Rev. Lett.*, vol. 77, no. 9, pp. 1881–1884, 1996.

- [137] Z. Bao, A. Dodabalapur, and A. J. Lovinger, "Soluble and processable regioregular poly(3-hexylthiophene) for thin film field-effect transistor applications with high mobility," *Appl. Phys. Lett.*, vol. 69, no. 26, pp. 4108–4110, Dec. 1996.
- [138] H. Sirringhaus, N. Tessler, and R. H. Friend, "Integrated Optoelectronic Devices Based on Conjugated Polymers," *Science*, vol. 280, no. 5370, pp. 1741–1744, Jun. 1998.
- [139] L. Bozano, S. A. Carter, J. C. Scott, G. G. Malliaras, and P. J. Brock, "Temperature- and field-dependent electron and hole mobilities in polymer light-emitting diodes," *Appl. Phys. Lett.*, vol. 74, no. 8, pp. 1132–1134, Feb. 1999.
- [140] A. Babel and S. A. Jenekhe, "Electron Transport in Thin-Film Transistors from an n-Type Conjugated Polymer," *Adv. Mater.*, vol. 14, no. 5, pp. 371–374, Mar. 2002.
- [141] X. Shen, B. Sun, D. Liu, and S.-T. Lee, "Hybrid heterojunction solar cell based on organic-inorganic silicon nanowire array architecture," *J. Am. Chem. Soc.*, vol. 133, no. 48, pp. 19408–15, 2011.
- [142] E. Galopin, K. Lemmens, G. Piret, Y. Coffinier, S. Szunerits, and R. Boukherroub, "Metal-Assisted Chemical Etching of Silicon: Preparation of Silicon Nanowire Arrays," 2008.
- [143] J. R. Oh, J. H. Moon, S. Yoon, C. R. Park, and Y. R. Do, "Fabrication of wafer-scale polystyrene photonic crystal multilayers via the layer-by-layer scooping transfer technique," *J. Mater. Chem.*, vol. 21, no. 37, pp. 14167–14172, Sep. 2011.
- [144] Y. Cai and B. Zhang Newby, "Marangoni Flow-Induced Self-Assembly of Hexagonal and Stripelike Nanoparticle Patterns," *J. Am. Chem. Soc.*, vol. 130, no. 19, pp. 6076–6077, May 2008.
- [145] X. Ye and L. Qi, "Recent advances in fabrication of monolayer colloidal crystals and their inverse replicas," *Sci. China Chem.*, vol. 57, no. 1, pp. 58–69, Jan. 2014.
- [146] D. S. Raimundo, F. J. Fernandez, and W. J. Salcedo, "Self-assembled polystyrene micro-spheres applied for photonic crystals and templates fabrication," in *Proceedings-Electrochemical Society*, 2004, pp. 301–306.
- [147] A. Nuermairaiti, "Studies on the Self-organization of Colloidal Nanoparticles at Interfaces," 2010.
- [148] Daniel M. Dobkin, "Capacitive Plasmas," <http://www.enigmatic-consulting.com>. [Online]. Available at: http://www.enigmatic-consulting.com/semiconductor_processing/CVD_Fundamentals/plasmas/capacitive_plasma.html. [Accessed: 15-Jun-2015].
- [149] Michael Gedalin, "Introduction to Plasma Physics." Ben-Gurion University.
- [150] F. Paschen, "Ueber die zum Funkenübergang in Luft, Wasserstoff und Kohlensäure bei verschiedenen Drucken erforderliche Potentialdifferenz," *Ann. Phys.*, vol. 273, no. 5, pp. 69–96, Jan. 1889.
- [151] C. L. Wadhwa, *High Voltage Engineering*. New Age International, 2007.
- [152] Muso, *curve plot of Paschen's law*. 2007.
- [153] P. R. i Cabarrocas, J. B. Chévrier, J. Huc, A. Lloret, J. Y. Parey, and J. P. M. Schmitt, "A fully automated hot-wall multiplasma-monochamber reactor for thin film deposition," *J. Vac. Sci. Technol. A*, vol. 9, no. 4, pp. 2331–2341, Jul. 1991.
- [154] "Center for Nanoscale Science and Engineering," <http://www.engr.uky.edu>. [Online]. Available at: <http://www.engr.uky.edu/~cense/equipment/ebeam.html>. [Accessed: 15-Jun-2015].
- [155] "APlusPhysics - High School Physics and AP Physics Online," <http://aplusphysics.com/>. [Online]. Available at: <http://aplusphysics.com/>. [Accessed: 15-Jun-2015].
- [156] "Spin Coating|Spin Coating Application|Spin Coater Theory|Spin-Coating - Benchtop Spin Coater," <http://www.smartcoater.com>. [Online]. Available at: <http://www.smartcoater.com/spin-coating-theory/spin-coating-introduction>. [Accessed: 15-Jun-2015].
- [157] Newport, "Introduction to Solar Radiation." [Online]. Available at: <http://www.newport.com/Introduction-to-Solar-Radiation/411919/1033/content.aspx>. [Accessed: 27-Jul-2015].
- [158] ASTM - G173, "Standard Tables for Reference Solar Spectral Irradiances: Direct Normal and Hemispherical on 37° Tilted Surface." 2012.
- [159] ASTM E1021 - 15, "Standard Test Method for Spectral Responsivity Measurements of Photovoltaic Devices." .

- [160] M. Kunst, G. Müller, R. Schmidt, and H. Wetzel, "Surface and volume decay processes in semiconductors studied by contactless transient photoconductivity measurements," *Appl. Phys. A*, vol. 46, no. 2, pp. 77–85, Jun. 1988.
- [161] M. Kunst, S. von Aichberger, G. Citarella, and F. Wunsch, "Amorphous silicon/crystalline silicon heterojunctions for solar cells," *J. Non-Cryst. Solids*, vol. 299–302, Part 2, pp. 1198–1202, Apr. 2002.
- [162] M. Kunst and G. Beck, "The study of charge carrier kinetics in semiconductors by microwave conductivity measurements," *J. Appl. Phys.*, vol. 60, no. 10, pp. 3558–3566, Nov. 1986.
- [163] null Neitzert, null Hirsch, and null Kunst, "Transfer of excess charge carriers in an a-Si:H/crystalline-silicon heterojunction measured during the growth of the amorphous silicon layer," *Phys. Rev. B Condens. Matter*, vol. 48, no. 7, pp. 4481–4486, Aug. 1993.
- [164] S. Kasouit, P. Roca i Cabarrocas, and R. Vanderhaghen, "DTRMC, a probe of transverse transport in microcrystalline silicon," *Thin Solid Films*, vol. 427, no. 1–2, pp. 335–339, Mar. 2003.
- [165] A. W. Stephens, A. G. Aberle, and M. A. Green, "Surface recombination velocity measurements at the silicon–silicon dioxide interface by microwave-detected photoconductance decay," *J. Appl. Phys.*, vol. 76, no. 1, pp. 363–370, Jul. 1994.
- [166] N. Schüler, T. Hahn, K. Dornich, J. R. Niklas, and B. Gründig-Wendrock, "Theoretical and experimental comparison of contactless lifetime measurement methods for thick silicon samples," *Sol. Energy Mater. Sol. Cells*, vol. 94, no. 6, pp. 1076–1080, Jun. 2010.
- [167] "Sinton Instruments WCT-120 — The Standard Offline Wafer-Lifetime Tool." [Online]. Available at: <http://www.sintoninstruments.com/Sinton-Instruments-WCT-120.html>. [Accessed: 27-Jul-2015].
- [168] D'Acremont Alexandre, "Mesure de photoconductance résolue en temps par réflexion micro-onde." 2013.
- [169] Romain Brénot, "Correlation entre mode de croissance et propriétés de transport du silicium microcristallin, établie par réflectométrie micro-onde et ellipsométrie," <http://www.theses.fr>, 2000. [Online]. Available at: <http://www.theses.fr/2000EPXX0011>. [Accessed: 15-Jun-2015].
- [170] H. J. Leamy, "Charge collection scanning electron microscopy," *J. Appl. Phys.*, vol. 53, no. 6, p. R51, 1982.
- [171] C. Gutsche, R. Niepelt, M. Gnauck, A. Lysov, W. Prost, C. Ronning, and F.-J. Tegude, "Direct determination of minority carrier diffusion lengths at axial GaAs nanowire p-n junctions," *Nano Lett.*, vol. 12, no. 3, pp. 1453–1458, Mar. 2012.
- [172] C.-C. Chang, C.-Y. Chi, M. Yao, N. Huang, C.-C. Chen, J. Theiss, A. W. Bushmaker, S. Lalumondiere, T.-W. Yeh, M. L. Povinelli, C. Zhou, P. D. Dapkus, and S. B. Cronin, "Electrical and optical characterization of surface passivation in GaAs nanowires," *Nano Lett.*, vol. 12, no. 9, pp. 4484–4489, Sep. 2012.
- [173] M. Tchernycheva, L. Rigutti, G. Jacopin, A. de Luna Bugallo, P. Lavenus, F. H. Julien, M. Timofeeva, A. D. Bouravleuv, G. E. Cirlin, V. Dhaka, H. Lipsanen, and L. Largeau, "Photovoltaic properties of GaAsP core-shell nanowires on Si(001) substrate," *Nanotechnology*, vol. 23, no. 26, p. 265402, Jul. 2012.
- [174] P. Lavenus, A. Messanvi, L. Rigutti, A. D. L. Bugallo, H. Zhang, F. Bayle, F. H. Julien, J. Eymery, C. Durand, and M. Tchernycheva, "Experimental and theoretical analysis of transport properties of core-shell wire light emitting diodes probed by electron beam induced current microscopy," *Nanotechnology*, vol. 25, no. 25, p. 255201, Jun. 2014.
- [175] L. Yu, L. Rigutti, M. Tchernycheva, S. Misra, M. Foldyna, G. Picardi, and P. R. i Cabarrocas, "Assessing individual radial junction solar cells over millions on VLS-grown silicon nanowires," *Nanotechnology*, vol. 24, no. 27, p. 275401, Jul. 2013.
- [176] A. Gustafsson, M. T. Björk, and L. Samuelson, "Locating nanowire heterostructures by electron beam induced current," *Nanotechnology*, vol. 18, no. 20, p. 205306, May 2007.
- [177] C. Y. Chen, A. Shik, A. Pitanti, A. Tredicucci, D. Ercolani, L. Sorba, F. Beltram, and H. E. Ruda, "Electron beam induced current in InSb-InAs nanowire type-III heterostructures," *Appl. Phys. Lett.*, vol. 101, no. 6, p. 063116, 2012.
- [178] "Electron beam-induced current - Wikipedia, the free encyclopedia." [Online]. Available at: https://en.wikipedia.org/wiki/Electron_beam-induced_current. [Accessed: 15-Jun-2015].

- [179] S. Ben Hatit, M. Foldyna, A. De Martino, and B. Drévilion, "Angle-resolved Mueller polarimeter using a microscope objective," *Phys. Status Solidi A*, vol. 205, no. 4, pp. 743–747, Apr. 2008.
- [180] X. Li and P. W. Bohn, "Metal-assisted chemical etching in HF/H₂O₂ produces porous silicon," *Appl. Phys. Lett.*, vol. 77, no. 16, pp. 2572–2574, Oct. 2000.
- [181] Z. Huang, N. Geyer, P. Werner, J. de Boor, and U. Gösele, "Metal-Assisted Chemical Etching of Silicon: A Review," *Adv. Mater.*, vol. 23, no. 2, pp. 285–308, Jan. 2011.
- [182] K. Q. Peng, J. J. Hu, Y. J. Yan, Y. Wu, H. Fang, Y. Xu, S. T. Lee, and J. Zhu, "Fabrication of Single-Crystalline Silicon Nanowires by Scratching a Silicon Surface with Catalytic Metal Particles," *Adv. Funct. Mater.*, vol. 16, no. 3, pp. 387–394, Feb. 2006.
- [183] C. Li, G. Fang, S. Sheng, Z. Chen, J. Wang, S. Ma, and X. Zhao, "Raman spectroscopy and field electron emission properties of aligned silicon nanowire arrays," *Phys. E Low-Dimens. Syst. Nanostructures*, vol. 30, no. 1–2, pp. 169–173, 2005.
- [184] Z. Guo, J.-Y. Jung, K. Zhou, Y. Xiao, S. Jee, S. A. Moiz, and J.-H. Lee, "Optical properties of silicon nanowires array fabricated by metal-assisted electroless etching," 2010, p. 77721C–77721C–7.
- [185] J. Y. Jung, Z. Guo, S. W. Jee, H. D. Um, K. T. Park, M. S. Hyun, J. M. Yang, and J. H. Lee, "A waferscale Si wire solar cell using radial and bulk p–n junctions," *Nanotechnology*, vol. 21, p. 445303, 2010.
- [186] Jin-Young Jung, Zhongyi Guo, Sang-Won Jee, Han-Don Um, Kwang-Tae Park, and Jung-Ho Lee, "Optically improved solar cell using tapered silicon nano wires," in *2010 10th IEEE Conference on Nanotechnology (IEEE-NANO)*, 2010, pp. 1163–1166.
- [187] Y.-P. Zhao and J.-G. Fan, "Clusters of bundled nanorods in nanocarpet effect," *Appl. Phys. Lett.*, vol. 88, p. 103123, 2006.
- [188] C. Choi, Y. Yoon, D. Hong, K. S. Brammer, K. Noh, Y. Oh, S. Oh, F. E. Talke, and S. Jin, "Strongly superhydrophobic silicon nanowires by supercritical CO₂ drying," *Electron. Mater. Lett.*, vol. 6, no. 2, pp. 59–64, 2010.
- [189] B. Ozdemir, M. Kulakci, R. Turan, and H. E. Unalan, "Effect of electroless etching parameters on the growth and reflection properties of silicon nanowires," *Nanotechnology*, vol. 22, p. 155606, 2011.
- [190] J. J. Hill, K. Haller, B. Gelfand, and K. J. Ziegler, "Eliminating Capillary Coalescence of Nanowire Arrays with Applied Electric Fields," *ACS Appl. Mater. Interfaces*, vol. 2, pp. 1992–1998, Jul. 2010.
- [191] L. He, C. Jiang, D. Lai, H. Wang, and others, "Highly efficient Si-nanorods/organic hybrid core-sheath heterojunction solar cells," *Appl. Phys. Lett.*, vol. 99, p. 021104, 2011.
- [192] S. C. Shiu, J. J. Chao, S. C. Hung, C. L. Yeh, and C. F. Lin, "Morphology dependence of silicon nanowire/poly (3, 4-ethylenedioxythiophene): poly (styrenesulfonate) heterojunction solar cells," *Chem. Mater.*, vol. 22, no. 10, pp. 3108–3113, 2010.
- [193] J.-Y. Jung, Z. Guo, S.-W. Jee, H.-D. Um, K.-T. Park, and J.-H. Lee, "A strong antireflective solar cell prepared by tapering silicon nanowires," *Opt. Express*, vol. 18, no. S3, pp. A286–A292, 2010.
- [194] A. S. Togonal, L. He, P. Roca i Cabarrocas, and Rusli, "Effect of Wettability on the Agglomeration of Silicon Nanowire Arrays Fabricated by Metal-Assisted Chemical Etching," *Langmuir*, vol. 30, no. 34, pp. 10290–10298, Sep. 2014.
- [195] D. Langbein, "Van der Waals attraction between cylinders, rods or fibers," *Phys. Kondens. Mater.*, vol. 15, pp. 61–86, Sep. 1972.
- [196] J. Silverberg, "A model for conductive percolation in ordered nanowire arrays," *J. Appl. Phys.*, vol. 105, no. 4, pp. 044306–044306, 2009.
- [197] J. Visser, "On Hamaker constants: A comparison between Hamaker constants and Lifshitz-van der Waals constants," *Adv. Colloid Interface Sci.*, vol. 3, no. 4, pp. 331–363, Dec. 1972.
- [198] J. N. Israelachvili, *Intermolecular and surface forces*. London [u.a.]: Acad. Press, 1997.
- [199] M. Gong, X. Xu, Z. Yang, Y. Liu, H. Lv, and L. Lv, "A reticulate superhydrophobic self-assembly structure prepared by ZnO nanowires," *Nanotechnology*, vol. 20, p. 165602, 2009.
- [200] D. Chandra, J. A. Taylor, and S. Yang, "Replica molding of high-aspect-ratio (sub-)micron hydrogel pillar arrays and their stability in air and solvents," *Soft Matter*, vol. 4, p. 979, 2008.

- [201] A. del Campo and C. Greiner, “SU-8: a photoresist for high-aspect-ratio and 3D submicron lithography,” *J. Micromechanics Microengineering*, vol. 17, pp. R81–R95, Jun. 2007.
- [202] S. Niyogi and R. C. Haddon, “Behavior of fluids in nanoscopic space,” *Proc. Natl. Acad. Sci. U. S. A.*, vol. 101, no. 17, pp. 6331–6332, Apr. 2004.
- [203] T. -W Lee, O. Mitrofanov, and J. W. P. Hsu, “Pattern-Transfer Fidelity in Soft Lithography: The Role of Pattern Density and Aspect Ratio,” *Adv. Funct. Mater.*, vol. 15, no. 10, pp. 1683–1688, Oct. 2005.
- [204] D. Chandra and S. Yang, “Capillary-Force-Induced Clustering of Micropillar Arrays: Is It Caused by Isolated Capillary Bridges or by the Lateral Capillary Meniscus Interaction Force?,” *Langmuir*, vol. 25, pp. 10430–10434, Sep. 2009.
- [205] M. P. Stoykovich, H. B. Cao, K. Yoshimoto, L. E. Ocola, and P. F. Nealey, “Deformation of Nanoscopic Polymer Structures in Response to Well-Defined Capillary Forces,” *Adv. Mater.*, vol. 15, no. 14, pp. 1180–1184, Jul. 2003.
- [206] T. Tanaka, M. Morigami, and N. Atoda, “Mechanism of Resist Pattern Collapse during Development Process,” *Jpn. J. Appl. Phys.*, vol. 32, pp. 6059–6064, Dec. 1993.
- [207] P. Kralchevsky, V. Paunov, I. Ivanov, and K. Nagayama, “Capillary meniscus interaction between colloidal particles attached to a liquid–fluid interface,” *J. Colloid Interface Sci.*, vol. 151, no. 1, pp. 79–94, 1992.
- [208] N. A. Lange and J. A. Dean, *Lange’s handbook of chemistry*. New York [etc.]: McGraw-Hill, 1973.
- [209] J. Song, X. Wang, E. Riedo, and Z. L. Wang, “Elastic Property of Vertically Aligned Nanowires,” *Nano Lett.*, vol. 5, pp. 1954–1958, Oct. 2005.
- [210] M. A. Hopcroft, W. D. Nix, and T. W. Kenny, “What is the Young’s Modulus of Silicon?,” *J. Microelectromechanical Syst.*, vol. 19, pp. 229–238, Apr. 2010.
- [211] Y.-S. Sohn, J. Park, G. Yoon, J. Song, S.-W. Jee, J.-H. Lee, S. Na, T. Kwon, and K. Eom, “Mechanical Properties of Silicon Nanowires,” *Nanoscale Res. Lett.*, vol. 5, pp. 211–216, Oct. 2009.
- [212] B. Lee and R. E. Rudd, “First-principles study of the Young’s modulus of Si (001) nanowires,” *Phys. Rev. B*, vol. 75, Jan. 2007.
- [213] S. Siddiqui, J. Zhang, M. Keswani, A. Fuerst, and S. Raghavan, “Study of interaction between silicon surfaces in dilute ammonia peroxide mixtures (APM) and their components using atomic force microscope (AFM),” *Microelectron. Eng.*, Nov. 2010.
- [214] M. R. Houston, R. T. Howe, and R. Maboudian, “Effect of hydrogen termination on the work of adhesion between rough polycrystalline silicon surfaces,” *J. Appl. Phys.*, vol. 81, p. 3474, 1997.
- [215] C. Li, K. Fobelets, M. Tymieniecki, M. Hamayun, Z. Durrani, and M. Green, “Bunch-Free Electroless-Etched Si Nanowire Array,” 2011.
- [216] “Photoresists, Solvents, Etchants, Wafers, and Yellow Light - MicroChemicals GmbH.” [Online]. Available at: <http://www.microchemicals.eu/>. [Accessed: 13-Aug-2015].
- [217] F. Kozlowski, N. Lindmair, T. Scheiter, C. Hierold, and W. Lang, “A novel method to avoid sticking of surface micromachined structures,” in *The 8th International Conference on Solid-State Sensors and Actuators, 1995 and Eurosensors IX.. Transducers '95*, 1995, vol. 1, pp. 220–223.
- [218] S.-C. Shiu, S.-B. Lin, S.-C. Hung, and C.-F. Lin, “Influence of pre-surface treatment on the morphology of silicon nanowires fabricated by metal-assisted etching,” *Appl. Surf. Sci.*, vol. 257, no. 6, pp. 1829–1834, Jan. 2011.
- [219] M. G. Moharam and T. K. Gaylord, “Diffraction analysis of dielectric surface-relief gratings,” *J. Opt. Soc. Am.*, vol. 72, no. 10, p. 1385, Oct. 1982.
- [220] L. Li, “Fourier modal method for crossed anisotropic gratings with arbitrary permittivity and permeability tensors,” *J. Opt. Pure Appl. Opt.*, vol. 5, no. 4, p. 345, Jul. 2003.
- [221] “Anti-Reflection EYETRUST VISION.” [Online]. Available at: http://brickellvision.com/?attachment_id=1850. [Accessed: 23-Jul-2015].
- [222] “Astronomy 302 - Lecture 14 - Spectra,” <http://exoplanet.as.arizona.edu>. [Online]. Available at: http://exoplanet.as.arizona.edu/~lclose/a302/lecture14/lecture_14.html. [Accessed: 23-Jul-2015].
- [223] Christopher Palmer, Newport Corporation, “Diffraction Grating Handbook.” [Online]. Available at: <http://www.gratinglab.com/Information/Handbook/Handbook.aspx>. [Accessed: 23-Jul-2015].

- [224] R. C. Jones, "A New Calculus for the Treatment of Optical Systems," *J. Opt. Soc. Am.*, vol. 31, no. 7, p. 488, Jul. 1941.
- [225] H. Mueller, "The foundation of optics," *JOSA A*, vol. 38, p. 661, 1948.
- [226] M. Schubert, T. Hofmann, and C. M. Herzinger, "Generalized far-infrared magneto-optic ellipsometry for semiconductor layer structures: determination of free-carrier effective-mass, mobility, and concentration parameters in n-type GaAs," *J. Opt. Soc. Am. A*, vol. 20, no. 2, p. 347, 2003.
- [227] J. J. Gil and E. Bernabeu, "A depolarization criterion in Mueller matrices," *J. Mod. Opt.*, vol. 32, no. 3, pp. 259–261, 1985.
- [228] M. G. Moharam, E. B. Grann, D. A. Pommet, and T. K. Gaylord, "Formulation for stable and efficient implementation of the rigorous coupled-wave analysis of binary gratings," *J. Opt. Soc. Am. A*, vol. 12, no. 5, p. 1068, May 1995.
- [229] M. G. Moharam, D. A. Pommet, E. B. Grann, and T. K. Gaylord, "Stable implementation of the rigorous coupled-wave analysis for surface-relief gratings: enhanced transmittance matrix approach," *J. Opt. Soc. Am. A*, vol. 12, no. 5, p. 1077, May 1995.
- [230] P. Lalanne and G. M. Morris, "Highly improved convergence of the coupled-wave method for TM polarization," *J. Opt. Soc. Am. A*, vol. 13, no. 4, p. 779, Apr. 1996.
- [231] L. Li, "Use of Fourier series in the analysis of discontinuous periodic structures," *J. Opt. Soc. Am. A*, vol. 13, no. 9, p. 1870, Sep. 1996.
- [232] L. Li, "Formulation and comparison of two recursive matrix algorithms for modeling layered diffraction gratings," *J. Opt. Soc. Am. A*, vol. 13, no. 5, p. 1024, May 1996.
- [233] M. G. Moharam and T. K. Gaylord, "Three-dimensional vector coupled-wave analysis of planar-grating diffraction," *J. Opt. Soc. Am.*, vol. 73, no. 9, p. 1105, Sep. 1983.
- [234] L. Li, "New formulation of the Fourier modal method for crossed surface-relief gratings," *J. Opt. Soc. Am. A*, vol. 14, no. 10, p. 2758, Oct. 1997.
- [235] K. Levenberg, "A method for the solution of certain problems in least squares," *Quart Appl. Math.*, vol. 2, pp. 164–168, 1944.
- [236] D. Marquardt, "An Algorithm for Least-Squares Estimation of Nonlinear Parameters," *J. Soc. Ind. Appl. Math.*, vol. 11, no. 2, pp. 431–441, Jun. 1963.
- [237] G. E. J. Jr and F. A. Modine, "Parameterization of the optical functions of amorphous materials in the interband region," *Appl. Phys. Lett.*, vol. 69, no. 3, pp. 371–373, Jul. 1996.
- [238] G. E. J. Jr and F. A. Modine, "Erratum: "Parameterization of the optical functions of amorphous materials in the interband region" [Appl. Phys. Lett. 69, 371 (1996)]," *Appl. Phys. Lett.*, vol. 69, no. 14, pp. 2137–2137, Sep. 1996.
- [239] H.-J. Du, W.-C. Wang, B. Ma, T. Long, and J.-Z. Zhu, "Band structure adjustment of solar cells by gradient doping," *Mater. Sci. Semicond. Process.*, vol. 40, pp. 570–577, Dec. 2015.
- [240] S. M. Iftiqar, Y. Lee, V. A. Dao, S. Kim, and J. Yi, "High efficiency heterojunction with intrinsic thin layer solar cell: A short," 2013.
- [241] M. W. M. van Cleef, F. A. Rubinelli, R. Rizzoli, R. Pinghini, R. E. I. Schropp, and W. F. van der Weg, "Amorphous Silicon Carbide/Crystalline Silicon Heterojunction Solar Cells: A Comprehensive Study of the Photocarrier Collection," *Jpn. J. Appl. Phys.*, vol. 37, no. 7R, p. 3926, Jul. 1998.
- [242] N. Jensen, U. Rau, R. M. Hausner, S. Uppal, L. Oberbeck, R. B. Bergmann, and J. H. Werner, "Recombination mechanisms in amorphous silicon/crystalline silicon heterojunction solar cells," *J. Appl. Phys.*, vol. 87, no. 5, p. 2639, 2000.
- [243] I. Cosme, R. Cariou, W. Chen, M. Foldyna, R. Boukhicha, P. Roca i Cabarocas, K. D. Lee, C. Trompoukis, and V. Depauw, "Lifetime assessment in crystalline silicon: From nanopatterned wafer to ultra-thin crystalline films for solar cells," *Sol. Energy Mater. Sol. Cells*.
- [244] "Casino Software." [Online]. Available at: <http://www.gel.usherbrooke.ca/casino/index.html>. [Accessed: 26-Jun-2015].
- [245] D. E. Ioannou and C. A. Dimitriadis, "A SEM-EBIC minority-carrier diffusion-length measurement technique," *IEEE Trans. Electron Devices*, vol. 29, no. 3, pp. 445–450, Mar. 1982.
- [246] M. S. Tyagi and R. Van Overstraeten, "Minority carrier recombination in heavily-doped silicon," *Solid-State Electron.*, vol. 26, no. 6, pp. 577–597, Jun. 1983.

- [247] R. Gereth and H. Fischer, "Solar cell with metal layered contact and method of manufacture," US3686036 A, 22-Aug-1972.
- [248] A. Elschner, S. Kirchmeyer, W. Lovenich, U. Merker, and K. Reuter, *PEDOT: Principles and Applications of an Intrinsically Conductive Polymer*. CRC Press, 2010.
- [249] Clevios™, "Clevios™ Conductive Polymers." [Online]. Available at: <http://www.heraeus-clevios.com/en/conductivepolymers/pedot-pss-conductive-polymers.aspx>. [Accessed: 28-Jul-2015].
- [250] R. Douani, G. Piret, T. Hadjersi, J.-N. Chazalviel, and I. Solomon, "Formation of a-Si:H and a-Si_{1-x}C_x:H nanowires by Ag-assisted electroless etching in aqueous HF/AgNO₃ solution," *Thin Solid Films*, vol. 519, no. 16, pp. 5383–5387, Jun. 2011.
- [251] J. H. Seo, D.-H. Kim, S.-H. Kwon, Y. C. Park, H. H. Jung, H. W. Lee, J.-D. Kwon, S.-G. Park, K.-S. Nam, Y. Jeong, S. Y. Ryu, J.-W. Kang, and C. S. Kim, "Highly efficient hybrid thin-film solar cells using a solution-processed hole-blocking layer," *Phys. Chem. Chem. Phys.*, vol. 15, no. 6, p. 1788, 2013.
- [252] L. S. Hung, C. W. Tang, and M. G. Mason, "Enhanced electron injection in organic electroluminescence devices using an Al/LiF electrode," *Appl. Phys. Lett.*, vol. 70, no. 2, p. 152, 1997.
- [253] G. E. Jabbour, Y. Kawabe, S. E. Shaheen, J. F. Wang, M. M. Morrell, B. Kippelen, and N. Peyghambarian, "Highly efficient and bright organic electroluminescent devices with an aluminum cathode," *Appl. Phys. Lett.*, vol. 71, no. 13, pp. 1762–1764, Sep. 1997.
- [254] S. E. Shaheen, G. E. Jabbour, M. M. Morrell, Y. Kawabe, B. Kippelen, N. Peyghambarian, M.-F. Nabor, R. Schlaf, E. A. Mash, and N. R. Armstrong, "Bright blue organic light-emitting diode with improved color purity using a LiF/Al cathode," *J. Appl. Phys.*, vol. 84, no. 4, pp. 2324–2327, Aug. 1998.
- [255] T. Mori, H. Fujikawa, S. Tokito, and Y. Taga, "Electronic structure of 8-hydroxyquinoline aluminum/LiF/Al interface for organic electroluminescent device studied by ultraviolet photoelectron spectroscopy," *Appl. Phys. Lett.*, vol. 73, no. 19, pp. 2763–2765, Nov. 1998.
- [256] S. E. Shaheen, R. Radspinner, N. Peyghambarian, and G. E. Jabbour, "Fabrication of bulk heterojunction plastic solar cells by screen printing," *Appl. Phys. Lett.*, vol. 79, no. 18, pp. 2996–2998, Oct. 2001.
- [257] C. J. Brabec, S. E. Shaheen, C. Winder, N. S. Sariciftci, and P. Denk, "Effect of LiF/metal electrodes on the performance of plastic solar cells," *Appl. Phys. Lett.*, vol. 80, no. 7, p. 1288, 2002.
- [258] V. D. Mihailetschi, L. J. A. Koster, and P. W. M. Blom, "Effect of metal electrodes on the performance of polymer:fullerene bulk heterojunction solar cells," *Appl. Phys. Lett.*, vol. 85, no. 6, pp. 970–972, Aug. 2004.
- [259] S. O. Ryu, "Effect of Thickness Variation and LiF Interlayer of the Conjugated Polymer/Fullerene Photoactive Layers on the Optical and Electrical Performance of Solar Cell Devices," *Mol. Cryst. Liq. Cryst.*, vol. 551, no. 1, pp. 154–162, Nov. 2011.
- [260] K.-G. Lim, M.-R. Choi, H.-B. Kim, J. H. Park, and T.-W. Lee, "High-efficiency polymer photovoltaic cells using a solution-processable insulating interfacial nanolayer: the role of the insulating nanolayer," *J. Mater. Chem.*, vol. 22, no. 48, p. 25148, 2012.
- [261] E. D. Głowacki, K. L. Marshall, C. W. Tang, and N. S. Sariciftci, "Doping of organic semiconductors induced by lithium fluoride/aluminum electrodes studied by electron spin resonance and infrared reflection-absorption spectroscopy," *Appl. Phys. Lett.*, vol. 99, no. 4, p. 043305, Jul. 2011.
- [262] K. R. Choudhury, J. H. Yoon, and F. So, "Enhanced electron injection and transport with LiF doping," in *The 20th Annual Meeting of the IEEE Lasers and Electro-Optics Society, 2007. LEOS 2007*, 2007, pp. 62–62.
- [263] K.-G. Lim, M.-R. Choi, J.-H. Kim, D. H. Kim, G. H. Jung, Y. Park, J.-L. Lee, and T.-W. Lee, "Role of Ultrathin Metal Fluoride Layer in Organic Photovoltaic Cells: Mechanism of Efficiency and Lifetime Enhancement," *ChemSusChem*, vol. 7, no. 4, pp. 1125–1132, Apr. 2014.
- [264] S. K. M. Jönsson, E. Carlegrim, F. Zhang, W. R. Salaneck, and M. Fahlman, "Photoelectron spectroscopy of the contact between the cathode and the active layers in plastic solar cells: the role of LiF," *Jpn. J. Appl. Phys.*, vol. 44, no. 6R, p. 3695, 2005.
- [265] V. D. Mihailetschi, P. W. M. Blom, J. C. Hummelen, and M. T. Rispen, "Cathode dependence of the open-circuit voltage of polymer:fullerene bulk heterojunction solar cells," *J. Appl. Phys.*, vol. 94, no. 10, p. 6849, 2003.

- [266] L. Fang, S. J. Baik, S. Lim, S. Yoo, and K.-S. Lim, "Amorphous Si Rear Schottky Junction Solar Cell With a LiF/Al Back Electrode," *IEEE Trans. Electron Devices*, vol. 58, no. 9, pp. 3048–3052, 2011.
- [267] S. Kim, J. Lee, V. A. Dao, S. Lee, N. Balaji, S. Ahn, S. Q. Hussain, S. Han, J. Jung, J. Jang, Y. Lee, and J. Yi, "Effects of LiF/Al back electrode on the amorphous/crystalline silicon heterojunction solar cells," *Mater. Sci. Eng. B*, vol. 178, no. 9, pp. 660–664, May 2013.
- [268] T. Lanz, L. Fang, S. J. Baik, K. S. Lim, and B. Ruhstaller, "Photocurrent increase in amorphous Si solar cells by increased reflectivity of LiF/Al electrodes," *Sol. Energy Mater. Sol. Cells*, vol. 107, pp. 259–262, Dec. 2012.
- [269] T.-F. Guo, F.-S. Yang, Z.-J. Tsai, T.-C. Wen, S.-N. Hsieh, and Y.-S. Fu, "High-performance polymer light-emitting diodes utilizing modified Al cathode," *Appl. Phys. Lett.*, vol. 87, no. 1, p. 013504, Jul. 2005.
- [270] R. M. Swanson, "Point-contact solar cells: Modeling and experiment," *Sol. Cells*, vol. 17, no. 1, pp. 85–118, Mar. 1986.

List of Publications

Journal Papers:

[1] A. S. Togonal, L. He, P. Roca i Cabarrocas, and Rusli, "Effect of Wettability on the Agglomeration of Silicon Nanowire Arrays Fabricated by Metal-Assisted Chemical Etching," *Langmuir*, vol. 30, no. 34, pp. 10290–10298, Sep. 2014.

[2] J. Wang, H. Wang, A. B. Prakoso, A. S. Togonal, L. Hong, C. Jiang, and Rusli, "High efficiency silicon nanowire/organic hybrid solar cells with two-step surface treatment," *Nanoscale*, vol. 7, no. 10, pp. 4559–4565, Feb. 2015.

[3] Aliénor Togonal, Martin Foldyna, Wanghua Chen, Wang Jianxiong, Maria Tchernycheva, Vladimir Neplokh, Joaquim Nassar, Pere Roca i Cabarrocas and Rusli, "Core-shell heterojunction solar cells based on disordered silicon nanowire arrays," *J. Phys. Chem. C*, 2016, 120 (5), pp 2962–2972

Papers submitted, currently under review:

Togonal, A. S., Tondelier, Denis, Geoffroy, Bernard, Vanel, Jean-Charles, Bonnasieux, Yvan, Rusli, and Roca i Cabarrocas, Pere, "Effect of LiF/Al back electrode on the performance of thin film solar cells based on hydrogenated amorphous silicon"

Martin Foldyna, Aliénor Svetlana Togonal, Rusli, Pere Roca i Cabarrocas, "Optimization and optical characterization of vertical nanowire arrays for core-shell structure solar cells"

Conference papers:

[3] A. S. Togonal, M. Foldyna, J. Wang, P. Roca i Cabarrocas and Rusli, "Design and Realization of Cost-Effective Nanostructures for Enhanced Light Trapping in High Efficiency Crystalline Silicon Solar Cells," presented at the 29th European Photovoltaic Solar Energy Conference and Exhibition, Amsterdam, 2014.

[4] A. S. Togonal, D. Tondelier, B. Geoffroy, J.C. Vanel, Y. Bonnasieux, Rusli, and P. Roca i Cabarrocas, "LiF/Al as a back contact for thin film solar cells based on hydrogenated amorphous silicon," presented at the 6th World Conference on Photovoltaic Energy Conversion (WCPEC 6), Kyoto, 2014.

[5] A. S. Togonal, M. Foldyna, W. H. Chen, J. Wang, M. Tchernycheva, V. Neplokh, P. Roca i Cabarrocas and Rusli, "Performance optimization and carrier lifetime measurements of core-shell HIT solar cells," presented at the E-MRS Spring Meeting, Lille, 2015.

[6] Foldyna, Martin, Togonal, A. S., Misra, Soumyadeep, Rusli, and Roca i Cabarrocas, Pere, "Optical characterization of disordered

nanowire arrays for heterojunction solar cells.” presented at Condensed Matter in Paris, 2014.

[7] M. Foldyna, A. S. Togonal, Rusli, and P. Roca i Cabarrocas, “Optimization And Optical Characterization Of Vertical Nanowire Arrays For Core-Shell Structure Solar Cells,” presented at the Photovoltaic Technical Conference, Aix en Provence, 2015.

[8] S. Pacchini, S. Hage-Ali, A. Togonal, N. Tiercelin, P. Pernod, and P. Coquet, “Inkjet-printed elastomeric millimeter-wave devices,” in Microwave Conference (EuMC), 2014 44th European, 2014, pp. 13 – 16.

[9] D. Lai, S.C. Heng, A. S. Togonal, Y.H. Tan, L. He and C.S. Tan, “Simple Low-Cost Metallization Scheme to Improve the Efficiency of Epitaxial Emitter Solar Cells with Nanowire Texturization,” presented at the 27th European Photovoltaic Solar Energy Conference and Exhibition, Frankfurt, 2012, pp. 1648 – 1650.

Titre : Nanofils de silicium pour le solaire: du matériau à la cellule photovoltaïque

Mots clés : "Photopiles", " Nanofils", " Silicium", " Semi-conducteurs-Attaque Chimique", Agglomération, "Nanofils, Propriétés Optiques".

Résumé : Les cellules solaires à base de nanofils de silicium offrent une alternative intéressante pour la réalisation de panneaux photovoltaïques à haut rendement et à faible coût. Elles bénéficient notamment des excellentes propriétés optiques des nanofils qui forment une surface à très faible réflectivité tout en piégeant efficacement la lumière. Dans cette thèse, nous utilisons et améliorons une méthode de gravure chimique peu coûteuse et industrialisable pour la fabrication de forêts de nanofils de silicium. En adaptant la mouillabilité du substrat et des nanofils, nous avons remédié au problème d'agglomération inhérent à cette méthode lorsqu'on veut obtenir des forêts denses et désordonnées de nanofils. En combinant cette méthode de gravure chimique à la lithographie assistée par nanosphères, nous avons pu fabriquer des réseaux ordonnés de nanofils avec un contrôle précis des propriétés géométriques (diamètre des

nanofils et distance entre eux). Les propriétés optiques de ces réseaux ont été étudiées théoriquement et expérimentalement afin d'identifier les configurations optimales. Nous avons ensuite fabriqué des cellules solaires à partir de ces différents types de nanofils en les intégrant dans deux types de structures. Le premier type, des cellules solaires HIT (Hétérojonction avec couche mince Intrinsèque) à base de nanofils de silicium, a été fabriqué par RF-PECVD. L'optimisation des conditions de dépôt plasma nous a permis d'obtenir des cellules solaires hautement performantes: rendements de 12,9% et facteurs de forme au-delà de 80%. Le second type, des cellules solaires hybrides, est basé sur la combinaison d'une couche organique et des nanofils de silicium. La caractérisation des cellules fabriquées montre des rendements prometteurs. Enfin, nous présentons des résultats préliminaires pour transférer ces concepts à une technologie couches minces.

Title : Silicon Nanowires for Photovoltaics: from the material to the device

Keywords : " Solar cells", " Silicon Nanowires (SiNWs)", "Heterojunction with Intrinsic Thin layer (HIT)", "Hybrid", "Metal Assisted Chemical Etching (MACE)", "Agglomeration", "Optical Properties".

Abstract : Silicon Nanowire (SiNW) based solar cells offer an interesting choice towards low-cost and highly efficient solar cells. Indeed solar cells based on SiNWs benefit from their outstanding optical properties such as extreme light trapping and very low reflectance. In this research project, we have fabricated disordered SiNWs using a low-cost top-down approach named the Metal-Assisted-Chemical-Etching process (MACE). The MACE process was first optimized to reduce the strong agglomeration observed at the top-end of the SiNWs by tuning the wettability properties of both the initial substrate and the SiNWs surface. By combining the MACE process with the nanosphere lithography, we have also produced ordered SiNW arrays with an accurate

control over the pitch, diameter and length. The optical properties of these SiNW arrays were then investigated both theoretically and experimentally in order to identify the geometrical configuration giving the best optical performance. Disordered and ordered SiNW arrays have been integrated into two types of solar cells: heterojunction with intrinsic thin layer (HIT) and hybrid devices. SiNW based HIT devices were fabricated by RF-PECVD and the optimization of the process conditions has allowed us to reach efficiency as high as 12.9% with excellent fill factor above 80%. Hybrid solar cells based on the combination of SiNWs with an organic layer have also been studied and characterized. The possible transfer of this concept to the thin film technology is finally explored.